

Determination of displacement and evaporation/precipitation processes via Pulsed Neutron-Gamma (PNG) monitoring for CO₂ storage operations

vorgelegt von
Dipl.-Ing. (Angewandte Geophysik)
Gunther Baumann
aus Cottbus

von der Fakultät VI - Planen Bauen Umwelt
der Technischen Universität Berlin
zur Erlangung des akademischen Grades

Doktor der Ingenieurwissenschaften
- Dr.-Ing. -
genehmigte Dissertation

Promotionsausschuss:

Vorsitzender: Prof. Dr. J. Tiedemann
Berichter: Prof. Dr. W. Dominik
Berichter: Prof. Dr. F. Börner
Berichter: Prof. Dr. Dr. M. Kühn
Berichter: Dr. J. Henniges

Tag der wissenschaftlichen Aussprache: 11. Juli 2013

Berlin 2013
D 83

Acknowledgments

I especially thank my doctoral supervisor Prof. Dr. Wilhelm Dominik for the fruitful discussion regarding the thesis, the personal encouragement and the always heart-felt atmosphere. Many thanks go to Dr. Jan Henniges, my supervisor at the German Centre for Geosciences (GFZ), for the numerous discussions about the PNG results and the individual well histories at the Ketzin site. Special thanks go to Dr. Marco De Lucia for the discussions about the mutual solubility in general and evaporation/precipitation in particular; thus combining the modeler perspective on the ongoing processes with the monitoring potentials of PNG logging. Prof. Dr. Frank Börner and Prof. Dr. Michael Kühn are gratefully acknowledged for the helpful insights during the writing this thesis.

I enjoyed working together with the colleagues of the Centre for Geological Storage at the GFZ. The discussions with the colleagues of the geophysical CO₂ storage monitoring group gave insights for the thesis and different perspectives on the ongoing processes in situ. Especially, Julia Götz, Dr. Cornelia Schmidt-Hattenberger and Dr. Peter Bergmann are gratefully acknowledged. Special thanks go to Fabian Möller who organized the integrated well logging campaigns including the PNG logs at the Ketzin site without any trouble at any time. I thank different research projects for granting financial support for this thesis.

Many thanks go to Schlumberger Carbon Services in Paris. Especially, Dat Vu-Hoang, who arranged the RST data processing training, Jean Desroches, who arranged and mainly financed the second stay in Paris and Ulrike Miersemann, who processed the latest RST runs.

Peggy Beckmann, who supported the organization of the formalities for submitting the thesis and Manfred Thiel, who helped me by drawing some graphics, are gratefully acknowledged. I thank Jonathan Banks who gave valuable corrections on my English, since he reviewed the thesis as a native speaker.

I thank my parents for their love and their support and especially my beloved Rosalie, who is not a geophysicist, but meanwhile has become familiar with PNG logging.

Abstract

The storage of carbon dioxide (CO_2) in geological formations is a promising option to reduce emissions of greenhouse gases to the atmosphere. During the proposed CO_2 injection process, application of suitable techniques for monitoring of the induced changes in the subsurface is required. Existing models for the spreading of the CO_2 , as well as displacement processes or resulting issues from mutual solubility between brine and CO_2 associated with saturation changes, need to be checked.

For well logging in cased boreholes only a limited number of techniques such as radiometric pulsed neutron-gamma (PNG) logging are applicable. The main PNG derived parameters are the macroscopic capture cross section (Σ) and the neutron porosity (TPHI) of the formation. The high measurement contrast between brine and CO_2 results in a high sensitivity to evaluate saturation changes.

Previously, the conventional PNG saturation model based on a displacement process has been used for PNG interpretation in different CO_2 storage projects in saline aquifers (e.g. Murray et al., 2010; Müller et al., 2007; Sakurai et al., 2005; Xue et al., 2006). The displacement saturation model accounts for mixing of the fluids in the pore space but ignores any mutual physico-chemical interaction. In addition to the displacement process, the mutual solubility between brine and CO_2 adds further complex processes such as evaporation and salt precipitation.

Evaporation and precipitation processes are relevant in the vicinity of an injection well, where dry CO_2 enters the reservoir. Moreover, modeling results show that gravity-forced upflow of CO_2 and capillary-forced backflow of brine toward the injection point can also affect saturation changes and salt precipitation (e.g. Pruess and Müller 2009). The Σ brine value depends strongly on the brine salinity e.g. its chlorine content which makes PNG measurements suitable for evaporation and salt precipitation monitoring. Until now evaporation and precipitation processes are not considered in PNG saturation models.

For this purpose an extended PNG saturation model for NaCl-brines is developed. The extended PNG saturation model includes both the displacement and evaporation/precipitation processes weighted by their affected porosity proportions. Two scenarios are distinguished. If the repeat Σ value is smaller than the baseline Σ value, first the displacement saturation model and subsequently the evaporation/precipitation saturation model are applied to the affected porosity proportions. If the repeat Σ value is greater than the baseline Σ value, the pore fluid Σ value is increased corresponding to an increased salt load due to capillary effects. For this purpose, TPHI can be used to derive CO_2 saturation and Σ is used to derive brine and/or halite saturation.

Ketzin, the only German pilot test site for CO_2 storage in saline aquifers, has one injection and two observation wells, where an extensive PNG monitoring program is performed. For the observation well, which is further away from the injection well, the conventional displacement saturation model is valid. In contrast, the observation well closest to the injection well shows that, in addition to displacement, the evaporation/precipitation process may have occurred in some depth intervals. For the injection well, both scenarios occur. The halite saturation distribution in the injection well seems to be controlled by the combined effects of changing injection rates associated with changing brine levels, lithology heterogeneities, and different saturation changing processes such as evaporation/precipitation or capillary forces.

Such salt precipitations were previously not detected in situ in connection with CO_2 injection

in saline aquifers. In general, it can be said that PNG monitoring in combination with the extended saturation model is suited to determine displacement and evaporation/precipitation processes for CO₂ storage operations. The extended saturation model is needed, especially for injection wells. Otherwise the CO₂ saturation will be erroneously underestimated.

The depleted gas field at the Altmark site, Germany, has been proposed as a suitable geological formation for CO₂ storage operations in combination with enhanced gas recovery. The PNG monitoring potential, with considering of displacement, evaporation/precipitation processes and changing gas-water contacts, is evaluated. As a result, PNG logs can be applied for determination of changes in brine saturation and water content associated with salt precipitation, whereas changes in the gas composition are below the detection limit.

Kurzfassung

Die Speicherung von Kohlendioxid (CO_2) im geologischen Untergrund ist eine Möglichkeit, um die Emission von CO_2 in die Atmosphäre zu verringern. Während der CO_2 -Injektion ist die Überwachung der in situ ablaufenden Prozesse durch geeignete Monitoringverfahren notwendig. Bestehende Modelle zur CO_2 -Ausbreitung, sowie Verdrängungs- als auch Löslichkeitsprozesse der beteiligten Fluide untereinander, die zu Sättigungsänderungen führen, müssen überprüft werden.

Für Bohrlochmessungen in verrohrten Bohrungen können nur wenige Bohrlochmessverfahren wie die radiometrische Pulsed-Neutron-Gamma-Methode (PNG) eingesetzt werden. Die wesentlichen Parameter der PNG-Messung sind der makroskopische Einfangquerschnitt (Σ) und die Neutronenporosität (TPHI) der Formation. Der große messtechnische Kontrast zwischen Salzwasser und CO_2 geht mit einer großen Sensitivität zur Bestimmung von Sättigungsänderungen einher.

Bisher wurde das konventionelle PNG-Sättigungsmodell, basierend auf dem Verdrängungsprozess, für die Interpretation von PNG-Messungen in verschiedenen CO_2 -Speicherprojekten in salinen Aquiferen angewendet (z.B. Murray et al., 2010; Müller et al., 2007; Sakurai et al., 2005; Xue et al., 2006). Das Verdrängungsmodell berücksichtigt die Mischung von verschiedenen Fluiden im Porenraum aber keine physiko-chemischen Prozesse. Neben dem Verdrängungsprozess führt die gegenseitige Löslichkeit von Salzwasser und CO_2 zu Evaporation (Austrocknung) und Salzausfällung.

Die Austrocknungs- und Ausfällungsprozesse sind relevant für Injektionsbohrungen, wo trockenes CO_2 in die Formation injiziert wird. Weiterhin zeigen Modellierungsergebnisse, dass der gravitative Aufstieg von CO_2 und Kapillarkräfte, die zu einem Rückfluss von Salzwasser führen, die Sättigungsänderungen und Salzausfällungen beeinflussen können (z.B. Pruess and Müller 2009). Der Σ -Wert von Salzwasser hängt stark von der Salinität bzw. dem Chloridgehalt ab, weshalb PNG-Messungen für das Monitoring von Austrocknungs- und Ausfällungsprozessen geeignet sind. Bisher wurden solche Austrocknungs- und Ausfällungsprozesse in PNG-Sättigungsmodellen noch nicht berücksichtigt.

Dafür wurde ein erweitertes PNG-Sättigungsmodell für NaCl-Wässer entwickelt. Das erweiterte PNG-Sättigungsmodell beinhaltet sowohl die Verdrängungs- als auch die Austrocknungs- und Ausfällungsprozesse, jeweils gewichtet durch die dazugehörigen Porenraumanteile. Zwei Szenarien werden unterschieden. Wenn die Wiederholungsmessung kleinere Σ -Werte als die Nullmessung aufweist, wird zunächst das Verdrängungsmodell und anschließend das Austrocknungs-/Ausfällungsmodell angewendet. Wenn die Wiederholungsmessung größere Σ -Werte als die Nullmessung aufweist, ist der Σ -Wert des Porenfluids erhöht, was mit einer Erhöhung des Salzgehaltes hervorgerufen durch Kapillarkräfte zusammenhängt. Für dieses Szenario kann die CO_2 -Sättigung aus TPHI und die Salzwasser- und/oder die Halitsättigung aus Σ bestimmt werden.

Ketzin, der einzige deutsche Pilotstandort für CO_2 -Speicherung in salinen Aquiferen, hat eine Injektions- und zwei Beobachtungsbohrungen, an denen ein umfangreiches PNG-Monitoringprogramm durchgeführt wird. Für die Beobachtungsbohrung, die weiter von der Injektionsbohrung entfernt ist, ist das konventionelle Verdrängungsmodell gültig. Im Gegensatz dazu zeigt die Beobachtungsbohrung, die am nächsten an der Injektionsbohrung liegt, dass neben dem Verdrängungs- auch Austrocknungs- und Ausfällungsprozesse in einigen Teufenbereichen stattgefunden haben können. In der Injektionsbohrung treten beide Szenarien auf. Die

Verteilung der Halitsättigung in der Injektionsbohrung scheint dabei von der Kombination der Effekte aus wechselnder Injektionsrate einhergehend mit wechselnden Wasserspiegeln, Heterogenitäten in der Lithologie und verschiedenen sättigungsbeeinflussenden Prozessen wie Austrocknungs- und Ausfällungsprozesse oder Kapillarkräfte kontrolliert zu werden.

Diese Salzausfällungen wurden bisher im Zusammenhang mit der CO₂-Speicherung in salinen Aquiferen noch nicht in situ nachgewiesen. Im Allgemeinen kann gesagt werden, dass PNG-Monitoring in Kombination mit dem erweiterten Sättigungsmodell für die Bestimmung von Verdrängungs-, Austrocknungs- und Ausfällungsprozessen geeignet ist. Insbesondere für Injektionsbohrungen ist das erweiterte Sättigungsmodell von Bedeutung, da sonst die CO₂-Sättigung unterschätzt wird.

Die ausgebeutete Erdgaslagerstätte in der Altmark wird als geeignete geologische Formation für die CO₂-Speicherung zur Erhöhung der Erdgasausbeute (Enhanced Gas Recovery) angesehen. Das Potential des PNG-Monitorings unter Berücksichtigung von Verdrängungs-, Austrocknungs- und Ausfällungsprozessen und wechselnden Gas-Wasser-Kontakten ist evaluiert worden. PNG-Messungen können für die Bestimmung von Änderungen der Salzwassersättigung, des Wassergehalts einhergehend mit Salzausfällungen genutzt werden, wobei Veränderungen in der Gaszusammensetzung unterhalb der Auflösungsgrenze liegen.

Contents

Acknowledgments	i
Abstract	ii
Kurzfassung	iv
List of Figures	viii
List of Tables	xvii
1. Introduction	1
1.1. CO ₂ storage in geological formations and resulting monitoring issues	1
1.2. Integrated CO ₂ storage monitoring	1
1.3. Well logging derived CO ₂ saturation monitoring	2
1.4. Derived research objectives and structure of the thesis	3
2. Theoretical and technical aspects of PNG logging	5
2.1. Neutron properties, sources and lifetime	5
2.1.1. Neutron properties and sources	5
2.1.2. Neutron lifetime	5
2.2. Material properties for the interaction with neutrons	6
2.2.1. Capture cross sections	6
2.2.1.1. Microscopic capture cross section of molecules	6
2.2.1.2. Macroscopic capture cross section Σ of common geological materials	7
2.2.1.3. Macroscopic capture cross section of a NaCl-brine (Σ_{br})	10
2.2.2. Hydrogen Index (HI)	13
2.2.3. Characteristic length	14
2.3. PNG logging	15
2.3.1. Pulsed neutron capture (Σ) logging	15
2.3.2. Neutron porosity	18
2.4. Reservoir Saturation Tool (RST) technical parameters and data processing	19
2.4.1. Technical parameters	19
2.4.2. Data processing to derive intrinsic data	20
3. Mechanisms of saturation changes and resulting issues for PNG saturation models	23
3.1. Mechanisms of saturation changes	23
3.1.1. Processes, associated phases and resulting regions around an injection well	23
3.1.2. Influence of reservoir properties and conditions on saturation mechanisms	25
3.1.3. Effect of capillary and gravitational forces on saturation mechanisms	25
3.1.4. Salt precipitation and its impact on injectivity	26
3.2. Conventional PNG saturation models	27
3.2.1. Saturation model for EOR/EGR operations	28
3.2.2. Saturation model for CO ₂ storage operations in saline aquifers	29
3.3. Effect of mutual solubility on gaseous and aqueous phase Σ values	30

3.4.	Evaporation and salt precipitation saturation model	31
3.4.1.	Σ_{br} transformation from a concentration into a saturation based declaration	32
3.4.2.	Evaporation/precipitation saturation model using the auxiliary water density function in brine	37
3.4.3.	Evaporation/precipitation saturation model using the initial water density in brine only	44
3.4.4.	Differences between both evaporation/precipitation saturation models	46
4.	Extended PNG saturation model and resulting issues for time lapse monitoring	51
4.1.	Limitations of the conventional displacement saturation model	51
4.2.	Extended displacement and evaporation/precipitation saturation model	53
4.3.	Resulting issues for time lapse monitoring	56
4.3.1.	Displacement and subsequent evaporation/precipitation model ($\Sigma_r \leq \Sigma_b$)	58
4.3.2.	Σ_r greater than Σ_b , increased Σ pore fluid value	62
5.	PNG monitoring results at the Ketzi site	66
5.1.	Geology, fluid Σ values, well completions and injection history	66
5.1.1.	Geology, porosity distribution and examined wells	66
5.1.2.	Determination of fluid Σ values	69
5.1.3.	Well completions, injection history and changing borehole conditions .	70
5.2.	From apparent data to intrinsic data	72
5.2.1.	Apparent and field data	73
5.2.2.	Environmental corrected intrinsic data - baseline runs	81
5.2.3.	Environmental corrected intrinsic data - repeat runs	84
5.3.	Saturation profiling at the reservoir section	91
5.3.1.	Displacement saturation model	93
5.3.1.1.	Ktzi200 observation well	94
5.3.1.2.	Ktzi201 injection well	96
5.3.1.3.	Ktzi202 observation well	105
5.3.2.	Extended displacement and evaporation/precipitation saturation model	107
5.3.2.1.	Ktzi200 observation well	108
5.3.2.2.	Ktzi201 injection well	110
5.4.	Discussion of the saturation profiles	124
6.	Sensitivity study for the Altmark site	130
6.1.	Initial saturation conditions and expected saturation changes	130
6.2.	Saturation scenarios and saturation models	131
6.3.	Determination of pore fluid capture cross sections and salt precipitations . .	133
6.4.	Sensitivity study for displacement and evaporation/precipitation processes . .	134
6.4.1.	Case 1: above the initial GWC	135
6.4.2.	Case 2: below the initial GWC	135
6.4.3.	S13 injection well	137
6.5.	Summary of the sensitivity study	138
7.	Summary and Conclusion	140
A.	Appendix	144
	Bibliography	169

List of Figures

2.1.	Σ_{CO_2} versus pressure for different temperatures.	10
2.2.	Σ_{br} and ρ_{br} as a function of the NaCl-salinity X_{NaCl} in kg/kg _{sol} for different pressure and temperature conditions (25 °C, 1 bar; 30 °C, 75 bar; 30 °C, 80 bar; 35 °C, 75 bar; 40 °C, 75 bar; 40 °C, 80 bar).	12
2.3.	Σ_{br} as a sum of the concentration based NaCl (Σ_{NaCl_c}) and water values ($\Sigma_{H_2O_c}$), and the corresponding NaCl (c_{NaCl}) and H ₂ O (c_{H_2O}) concentrations as a function of the NaCl-salinity X_{NaCl} in kg/kg _{sol} (35 °C, 75 bar). c_{NaCl} in g/l results from the product of X_{NaCl} and ρ_{br} in kg/m ³	12
2.4.	HI as a function of salinity calculated after Schlumberger (1989) and Ellis et al. (1987).	14
2.5.	11/16 inch slime hole RST tool (left) and typical dual burst decay measured with RST (right) redrawn after Plasek et al. (1995).	16
2.6.	Typical count rate decay for clean fluid bearing formations redrawn and modified after Smolen (1996).	17
2.7.	Schematic representation of the RST data processing workflow modified after Plasek et al. (1995).	20
3.1.	Description of regions caused by radial CO ₂ brine displacement and evaporation/precipitation mechanisms and the corresponding phases and components around an injection well. Adapted and modified after Zeidouni et al. (2009a).	25
3.2.	The brines water density $\rho_{H_2O_{br}}$ as a function of X_{NaCl} for 35 °C and 75 bar. The curve is fitted by a fifth degree polynomial.	34
3.3.	The brines water density $\rho_{H_2O_{br}}$ as a function of S_{NaCl}/S_{H_2O} or c_{NaCl}/c_{H_2O} (upper, lower abscissa) for 35 °C and 75 bar. The curves are fitted by a fifth degree polynomial.	35
3.4.	The brine density ρ_{br} after Rowe and Chou (1970), the brine density using the pure water density for the corresponding pressure and temperature conditions $\rho_{br-pure}$ and the water density in brine $\rho_{H_2O_{br}}$ as a function of X_{NaCl} in kg/kg _{sol} for 35 °C and 75 bar. The sum of $\rho_{H_2O_{br}}$ and ρ_{NaCl} weighted by S_{H_2O} and S_{NaCl} is equal to ρ_{br} after Rowe and Chou (1970).	36
3.5.	Σ_{br} as a sum of dissolved NaCl (Σ_{NaCl_c}) and water ($\Sigma_{H_2O_c}$) (left ordinate) and the corresponding NaCl (S_{NaCl}) and H ₂ O (S_{H_2O}) saturations (right ordinate) as a function of the NaCl-salinity X_{NaCl} in kg/kg _{sol} for 35 °C and 75 bar.	37
3.6.	Evaporation/Precipitation model: <i>Brine</i> : initially composed of the water $S_{H_2O_b}$ and NaCl S_{NaCl_b} saturations. <i>During evaporation</i> : Increasing CO ₂ saturation S_{CO_2} accounts for remaining water saturation $S_{H_2O_r}$ which in turn controls the NaCl saturation in solution $S_{NaCl_{sol}}$ and accordingly the precipitated halite saturation $S_{NaCl_{pre}}$. <i>Complete evaporation</i> : S_{CO_2} and $S_{NaCl_{pre}}$ reach their maximum, and $S_{H_2O_r}$ and $S_{NaCl_{sol}}$ are equal to zero.	38

List of Figures

3.7.	The brine saturation S_{br} , remaining water saturation $S_{H_2O_r}$, dissolved NaCl saturation $S_{NaCl_{sol}}$ and precipitated halite saturation $S_{NaCl_{pre}}$ as a function of S_{CO_2} . The brine saturation S_{br} is the sum of $S_{H_2O_r}$ and $S_{NaCl_{sol}}$	41
3.8.	The brine concentration c_{br} , remaining water concentration $c_{H_2O_r}$, dissolved NaCl concentration $c_{NaCl_{sol}}$ and precipitated halite concentration $c_{NaCl_{pre}}$ as a function of the CO_2 concentration c_{CO_2} . The brine concentration c_{br} is the sum of $c_{H_2O_r}$ and $c_{NaCl_{sol}}$	42
3.9.	The Σ values of the remaining brine Σ_{br-r} , the remaining water content $\Sigma_{H_2O_r}$, the dissolved NaCl content $\Sigma_{NaCl_{sol}}$, the precipitated halite content $\Sigma_{NaCl_{pre}}$, the CO_2 content Σ_{CO_2-r} and Σ_r as a function of S_{CO_2} . The Σ values are weighted by their occupied volume fractions except $\Sigma_{br,r}$, which is additionally divided by $(S_{H_2O_r} + S_{NaCl_{sol}})$	43
3.10.	Evaporation/Precipitation model versus displacement model (subscript "dis"): The brine saturations S_{br} , S_{br-dis} , the precipitated halite saturation $S_{NaCl_{pre}}$, (left ordinate) as well as the total Σ values (Σ_r , Σ_{r-dis}) (right ordinate) as a function of S_{CO_2}	44
3.11.	The differences between the repeat Σ values ($\Delta\Sigma_r$) the water Σ values in brine ($\Delta\Sigma_{H_2O_{br}}$) as well as the water density in brine ($\Delta\rho_{H_2O_{br}}$) from the evaporation/precipitation model with the auxiliary water density function in brine ($\rho_{H_2O_{br-r}}$) or rather the constant baseline water density ($\rho_{H_2O_{br-b}}$) as a function of S_{CO_2} . ΔS_{CO_2} , the difference between the corresponding S_{CO_2} from the forward model using $\rho_{H_2O_{br-r}}$ and the calculated S_{CO_2} from the inverted model based on $\rho_{H_2O_{br-b}}$ (Equation 3.40), but using the Σ_r values from $\rho_{H_2O_{br-r}}$, is also shown.	48
3.12.	The differences between the repeat Σ values at the saturation limit ($\Delta\Sigma_r$) and the corresponding water Σ value in brine ($\Delta\Sigma_{H_2O_{br}}$) and remaining water saturations ($S_{H_2O_r}$) as a function of the initial X_{NaCl} in kg/kg _{sol} for 35 °C and 75 bar.	49
4.1.	Conventional displacement saturation model: <i>Baseline:</i> Before CO_2 injection the formation is fully brine saturated. <i>During displacement:</i> The mobile brine (ϕ_{eff}) is displaced by CO_2 and $S_{CO_{2eff}}$ is less than one during displacement. <i>Complete displacement:</i> After complete mobile brine displacement $S_{CO_{2eff}}$ is equal to one. The immobile brine (ϕ_{irr}) is unaffected by the displacement process.	52
4.2.	General extended displacement and evaporation/precipitation saturation model: <i>Baseline:</i> Before CO_2 injection the formation is fully brine saturated. <i>During displacement and evaporation/precipitation:</i> The mobile brine (ϕ_{eff}) is displaced by CO_2 and $S_{CO_{2eff}}$ is less than one during displacement. Additionally, the immobile brine (ϕ_{irr}) is evaporated associated with salt precipitation when the NaCl solubility limit is reached. <i>Complete displacement and evaporation/precipitation:</i> After complete mobile brine displacement $S_{CO_{2eff}}$ is equal to one. $S_{CO_{2irr}}$ is reduced by the occupied precipitated halite fraction. $S_{NaCl_{pre}}$ is equal to the initial NaCl saturation in ϕ_{irr}	53

List of Figures

4.3. Subsequent extended displacement and evaporation/precipitation saturation model: <i>Complete displacement, initiating evaporation</i> : The mobile brine (ϕ_{eff}) is completely displaced and $S_{CO_{2eff}}$ is equal to one. The immobile brine (ϕ_{irr}) evaporation initiates. <i>Complete displacement, further evaporation, initiating precipitation</i> : The NaCl solubility limit is reached and precipitation initiates. <i>Complete displacement and complete evaporation/precipitation</i> : $S_{CO_{2irr}}$ is reduced by the occupied precipitated halite fraction. $S_{NaCl_{pre}}$ is equal to the initial NaCl saturation in ϕ_{irr}	59
4.4. Summarizing flow-chart for the displacement and subsequent evaporation/precipitation model.	62
4.5. Summarizing flow-chart when Σ_r is greater than Σ_b for the assumed backflow rate of brine being equal to the evaporation rate.	65
5.1. Aerial view of the Ketzin site in September 2012 (Martens et al., 2013) . . .	67
5.2. Lithological composite logs, total porosity logs (TPHI) and effective porosity logs (EPhi) for all Ketzin wells after Norden et al. (2010). Neutron porosity (TPHI_b_BSAL) and formation Σ (SIGM_b_BSAL) logs from the PNG baseline runs for all Ketzin wells.	68
5.3. Cumulative CO ₂ quantity (left ordinate) and injection rate (right ordinate) since the start of injection in June 2008 until October 2012. The RST baseline and repeat runs are marked with arrows. (Data derived from Möller et al. (2012))	72
5.4. Ktzi200: MWFD, IRAT, SBNA, TRAT, SFFA and DIFF (SBNA-SFFA) logs for the baseline and six repeat runs. The brine levels for each repeat run are marked with a black bar on the left side of the first track. Lithology after Förster et al. (2010)	74
5.5. Ktzi201: MWFD, IRAT, SBNA, TRAT, SFFA and DIFF (SBNA-SFFA) logs for the baseline and five repeat runs. The brine levels for each repeat run are marked with a black bar on the left side of the first track. Lithology after Förster et al. (2010)	75
5.6. Ktzi202: MWFD, IRAT, SBNA, TRAT, SFFA and DIFF (SBNA-SFFA) logs for the baseline and five repeat runs. The brine levels for each repeat run are marked with a black bar on the left side of the first track. Lithology after Förster et al. (2010)	76
5.7. SIGM and TPHI baseline logs for all wells with different data processings (SIGM with noair, noair_OH, noair_BSAL and noair_OH_BSAL and TPHI with noair and noair_BSAL data processing). Lithology after Förster et al. (2010)	83
5.8. SIGM and TPHI logs for the baseline (SIGM and TPHI with noair_BSAL data processing) and repeat (SIGM with air_OH and TPHI with air data processing) runs for all wells. The brine levels for each repeat run are marked with a black bar on the left side of the TPHI tracks for each well. Lithology after Förster et al. (2010)	92

List of Figures

5.9. Ktzi200: Saturation profiles as fractions of ϕ_{tot} (displacement conform CO ₂ in green, apparent CO ₂ in light green and brine in blue), S_{CO_2} derived from TPHI (orange logs) (first track) and the corresponding Diff logs with solid and dotted signature (second track) for five repeat runs based on the <i>displacement saturation model</i> . The white log for each repeat run separates the mobile from the immobile brine. The brine levels for each repeat run are marked with a black bar on the right side of the second track. For the fifth and the sixth repeat run, the brine levels are above the displayed depth range. Lithology after Förster et al. (2010)	95
5.10. Ktzi201: SIGM baseline log (noair_BSAL data processing), SIGM baseline log including the flush brine salinity (SIGM_b_fl) and the SIGM repeat logs (air_OH data processing). The brine levels for each run are marked with a black bar on the right side of each track. Lithology after Förster et al. (2010)	98
5.11. Ktzi201: TPHI baseline log (noair_BSAL data processing), TPHI baseline log including the flush brine salinity (TPHI_b_fl) and the TPHI repeat logs (air data processing). The brine levels for each run are marked with a black bar on the right side of each track. Lithology after Förster et al. (2010)	100
5.12. Ktzi201: Saturation profiles as fractions of ϕ_{tot} (displacement conform CO ₂ in green, apparent CO ₂ in light green and brine in blue), S_{CO_2} derived from TPHI (orange logs) (first track) and the corresponding Diff logs with solid and dotted signature (second track) for five repeat runs based on the <i>displacement saturation model and the original brine salinity</i> . The white log for each repeat run separates the mobile from the immobile brine. The brine levels for each repeat run are marked with a black bar on the right side of the second track. Lithology after Förster et al. (2010)	101
5.13. Ktzi201: Saturation profiles as fractions of ϕ_{tot} (displacement conform CO ₂ in green, apparent CO ₂ in light green and brine in blue), S_{CO_2} derived from TPHI (orange logs) (first track) and the corresponding Diff logs with solid and dotted signature (second track) for five repeat runs based on the <i>displacement saturation model and the flush brine salinity</i> . The white log for each repeat run separates the mobile from the immobile brine. The brine levels for each repeat run are marked with a black bar on the right side of the second track. Lithology after Förster et al. (2010)	104
5.14. Ktzi202: Saturation profiles as fractions of ϕ_{tot} (displacement conform CO ₂ in green, apparent CO ₂ in light green and brine in blue), S_{CO_2} derived from TPHI (orange logs) (first track) and the corresponding Diff logs with solid and dotted signature (second track) for five repeat runs based on the <i>displacement saturation model</i> . The white log for each repeat run separates the mobile from the immobile brine. The brine levels for each repeat run are marked with a black bar on the right side of the second track. Except for the sixth repeat run, the brine levels are below the displayed depth range. Lithology after Förster et al. (2010)	106

List of Figures

5.15. Ktzi200: Saturation profiles as fractions of ϕ_{tot} (CO ₂ in green, brine in blue, halite in red) (first track), halite saturations in a smaller scale, Σ_{br} logs (second track) and the corresponding Diff logs (third track) for five repeat runs based on the <i>extended saturation model without porosity adjustment</i> . The white solid log for each repeat run separates the mobile from the immobile brine. The brine levels for each repeat run are marked with a black bar on the right side of the third track. For the fifth and the sixth repeat run, the brine levels are above the displayed depth range. Lithology after Förster et al. (2010)	109
5.16. Ktzi200: Saturation profiles as fractions of ϕ_{tot} (CO ₂ in green, brine in blue, halite in red) (first track), halite saturations in a smaller scale, Σ_{br} logs (second track) and the corresponding Diff logs (third track) for five repeat runs based on the <i>extended saturation model with porosity adjustment</i> . The white solid log for each repeat run separates the mobile from the immobile brine. The white dotted logs show the adjustment of the affected porosities. The brine levels for each repeat run are marked with a black bar on the right side of the third track. For the fifth and the sixth repeat run, the brine levels are above the displayed depth range. Lithology after Förster et al. (2010)	111
5.17. Ktzi201: Saturation profiles as fractions of ϕ_{tot} (CO ₂ in green, brine in blue, halite in red) (first track), halite saturations in a smaller scale, Σ_{br} logs (second track) and the corresponding Diff logs (third track) for five repeat runs based on the <i>extended saturation model and the original brine salinity without porosity adjustment</i> . The white solid log for each repeat run separates the mobile from the immobile brine. If $\Sigma_r > \Sigma_b$ (occur only below the brine level for the fourth and the fifth repeat runs), $S_{CO_{2eff}}$ is set to one and $S_{CO_{2irr}}$ is set zero. The brine levels for each repeat run are marked with a black bar on the right side of the third track. Lithology after Förster et al. (2010)	113
5.18. Ktzi201: Saturation profiles as fractions of ϕ_{tot} (CO ₂ in green, brine in blue, halite in red) (first track), halite saturations in a smaller scale, Σ_{br} logs (second track) and the corresponding Diff logs (third track) for five repeat runs based on the <i>extended saturation model and the original brine salinity with porosity adjustment</i> . The white solid log for each repeat run separates the mobile from the immobile brine. The white dotted logs show the adjustment of the affected porosities. If $\Sigma_r > \Sigma_b$ (occur only below the brine level for the fourth and the fifth repeat runs), $S_{CO_{2eff}}$ is set to one and $S_{CO_{2irr}}$ is set zero. The brine levels for each repeat run are marked with a black bar on the right side of the third track. Lithology after Förster et al. (2010)	115
5.19. Ktzi201: Saturation profiles as fractions of ϕ_{tot} (CO ₂ in green, brine in blue, halite in red) (first track), halite saturations in a smaller scale, Σ_{br} logs (second track) and the corresponding Diff logs (third track) for five repeat runs based on the <i>extended saturation model and the original brine salinity with porosity adjustment</i> . The white solid log for each repeat run separates the mobile from the immobile brine. The white dotted logs show the adjustment of the affected porosities. If $\Sigma_r > \Sigma_b$ (occur only below the brine level for the fourth and the fifth repeat runs), S_{CO_2} is derived from <i>TPHI</i> . The brine levels for each repeat run are marked with a black bar on the right side of the third track. Lithology after Förster et al. (2010)	117

- 5.20. Ktzi201: Saturation profiles as fractions of ϕ_{tot} (CO₂ in green, brine in blue, halite in red) (first track), halite saturations in a smaller scale, Σ_{br} logs (second track) and the corresponding Diff logs (third track) for five repeat runs based on the *extended saturation model and the flush brine salinity without porosity adjustment*. The white solid log for each repeat run separates the mobile from the immobile brine. *If $\Sigma_r > \Sigma_b$ (occur above and below the brine level for all repeat runs), $S_{CO_{2eff}}$ is set to one and $S_{CO_{2irr}}$ is set zero.* The brine levels for each repeat run are marked with a black bar on the right side of the third track. Lithology after Förster et al. (2010) 118
- 5.21. Ktzi201: Saturation profiles as fractions of ϕ_{tot} (CO₂ in green, brine in blue, halite in red) (first track), halite saturations in a smaller scale, Σ_{br} logs (second track) and the corresponding Diff logs (third track) for five repeat runs based on the *extended saturation model and the flush brine salinity with porosity adjustment*. The white solid log for each repeat run separates the mobile from the immobile brine. The white dotted logs show the adjustment of the affected porosities. *If $\Sigma_r > \Sigma_b$ (occur above and below the brine level for all repeat runs), $S_{CO_{2eff}}$ is set to one and $S_{CO_{2irr}}$ is set zero.* The brine levels for each repeat run are marked with a black bar on the right side of the third track. Lithology after Förster et al. (2010) 120
- 5.22. Ktzi201: Saturation profiles as fractions of ϕ_{tot} (CO₂ in green, brine in blue, halite in red) (first track), halite saturations in a smaller scale, Σ_{br} logs (second track) and the corresponding Diff logs (third track) for five repeat runs based on the *extended saturation model and the flush brine salinity with porosity adjustment*. The white solid log for each repeat run separates the mobile from the immobile brine. The white dotted logs show the adjustment of the affected porosities. *If $\Sigma_r > \Sigma_b$, $S_{CO_{2eff}}$ is set to one and $S_{CO_{2irr}}$ is set zero (mostly above the brine level) or S_{CO_2} is derived from TPhi (mostly below the brine level).* The brine levels for each repeat run are marked with a black bar on the right side of the third track. Lithology after Förster et al. (2010) 122
- 5.23. Ktzi201: Flush brine log, which includes the salinity equilibration (SIGM_br_fl) and the target Σ_{br} logs (SIGM_br_tar) for five repeat runs when the affected porosities are not adjusted to minimize Diff. The constant purple curve is Σ_{br-KCl} for the KCl-preflush (39.50 cu). The remaining Σ differences between SIGM_br_tar and Σ_{br-KCl} (grey shading) are the input values for the adjustment of the affected porosities. Lithology after Förster et al. (2010) 123
- 5.24. Ktzi201: Saturation profiles as fractions of ϕ_{tot} (CO₂ in green, brine in blue, halite in red) (first track), halite saturations in a smaller scale, Σ_{br} logs (second track) and the corresponding Diff logs (third track) for five repeat runs based on the *extended saturation model and the flush brine salinity with porosity adjustment*. *Instead of the SIGM_br_fl log, the SIGM_br_tar logs and the remaining Σ differences between SIGM_br_tar and Σ_{br-KCl} for five repeat runs are the input data for the simplified evaporation/precipitation saturation model.* The white solid log for each repeat run separates the mobile from the immobile brine. The white dotted logs show the adjustment of the affected porosities. *If $\Sigma_r > \Sigma_b$, $S_{CO_{2eff}}$ is set to one and $S_{CO_{2irr}}$ is set zero (mostly above the brine level) or S_{CO_2} is derived from TPhi (mostly below the brine level).* The brine levels for each repeat run are marked with a black bar on the right side of the third track. Lithology after Förster et al. (2010) 125

List of Figures

6.1.	Saturation models: Baseline: in-situ saturation condition before injection. Scenario 1: natural gas/brine displacement (ϕ_{eff}). Scenario 2: natural gas/brine displacement (ϕ_{eff}) and complete evaporation of immobile brine associated with salt precipitation (ϕ_{irr}).	131
6.2.	Σ modeling results (left ordinate) for the baseline above the initial GWC (case 1, Σ_b) and the two different scenarios (Σ_{sc1} , Σ_{sc2}) as a function of the total porosity (ϕ_{tot}) and the corresponding differences (right ordinate) between the baseline and two scenarios (Diff(b-sc1)), Diff(b-sc2)). $S_{br_{irr}}$ is set to 50 % of ϕ_{tot}	135
6.3.	Σ modeling results (left ordinate) for the baseline below the initial GWC (case 2, Σ_b) and the two different scenarios (Σ_{sc1} , Σ_{sc2}) as a function of the total porosity (ϕ_{tot}) and the corresponding differences (right ordinate) between the baseline and two scenarios (Diff(b-sc1)), Diff(b-sc2)). $S_{br_{irr}}$ is set to 50 % of ϕ_{tot}	136
6.4.	Σ modeling results for the baseline and the two different scenarios for the S13 injection well at the Altmark site. Injection intervals with high permeabilities are indicated by dotted signature. Left track: total porosity (ϕ_{tot})* and effective porosity (ϕ_{eff})*, middle track: baseline (SIGM_b) and repeat Σ (SIGM_sc1, SIGM_sc2), right track: difference between baseline and repeats (Diff_(b-sc1), Diff_(b-sc2)). * Data according to GDF-SUEZ (2009)	138
A.1.	Ktzi200: Casing scheme after Prevedel (2008)	145
A.2.	Ktzi201: Casing scheme after Prevedel (2008)	146
A.3.	Ktzi202: Casing scheme after Prevedel (2008)	147
A.4.	Ktzi200: DSIG logs with different data processings for the baseline and the five repeat runs. The brine levels for each run are marked with a black bar on the right side of each track. Lithology after Förster et al. (2010)	149
A.5.	Ktzi200: Arithmetic mean of the absolute DSIG values with different data processings for the baseline and the six repeat runs in the evaluated depth intervals.	150
A.6.	Ktzi201: DSIG logs with different data processings for the baseline and the five repeat runs. The brine levels for each run are marked with a black bar on the right side of each track. Lithology after Förster et al. (2010)	151
A.7.	Ktzi201: Arithmetic mean of the absolute DSIG values with different data processings for the baseline and the five repeat runs in the evaluated depth intervals.	152
A.8.	Ktzi202: DSIG logs with different data processings for the baseline and the five repeat runs. The brine levels for each run are marked with a black bar on the right side of each track. Lithology after Förster et al. (2010)	153
A.9.	Ktzi202: Arithmetic mean of the absolute DSIG values with different data processings for the baseline and the five repeat runs in the evaluated depth intervals.	154
A.10.	Ktzi200: SIGM baseline log (noair_BSAL data processing) and five repeat SIGM logs with different data processings. The brine levels for each run are marked with a black bar on the right side of each track. Lithology after Förster et al. (2010)	156

List of Figures

A.11.Ktzi200: TPHI baseline log (noair_BSAL data processing), open hole derived porosity log after Norden et al. (2010) and five repeat TPHI logs with different data processings. The brine levels for each run are marked with a black bar on the right side of each track. Lithology after Förster et al. (2010)	157
A.12.Ktzi200: SIGM baseline log (noair_BSAL), SIGM first repeat logs with different data processings (noair, noair_OH and noair_OH_BSAL), corresponding DSIG logs, open hole derived porosity log after Norden et al. (2010), TPHI baseline log (noair_BSAL), TPHI first repeat log with noair data processing, the corresponding saturation profile based on the <i>displacement saturation model</i> , S_{CO_2} derived from TPHI (orange logs) and the corresponding Diff log. Lithology after Förster et al. (2010)	158
A.13.Ktzi200: Arithmetic mean of the differences between the baseline and the six repeat SIGM runs, SIGM(b-rx), with different data processings in the evaluated depth intervals. Note the different scale in each depth interval.	159
A.14.Ktzi201: SIGM baseline log (noair_BSAL data processing) and five repeat SIGM logs with different data processings. The brine levels for each run are marked with a black bar on the right side of each track. Lithology after Förster et al. (2010)	160
A.15.Ktzi201: TPHI baseline log (noair_BSAL data processing), open hole derived porosity log after Norden et al. (2010) and five repeat TPHI logs with different data processings. The brine levels for each run are marked with a black bar on the right side of each track. Lithology after Förster et al. (2010)	161
A.16.Ktzi201: Arithmetic mean of the differences between the baseline and the five repeat SIGM runs, SIGM(b-rx), with different data processings in the evaluated depth intervals. Note the different scale in each depth interval.	162
A.17.Ktzi202: SIGM baseline log (noair_BSAL data processing) and five repeat SIGM logs with different data processings. The brine levels for each run are marked with a black bar on the right side of each track. Lithology after Förster et al. (2010)	163
A.18.Ktzi202: TPHI baseline log (noair_BSAL data processing), open hole derived porosity log after Norden et al. (2010) and five repeat TPHI logs with different data processings. The brine levels for each run are marked with a black bar on the right side of each track. Lithology after Förster et al. (2010)	164
A.19.Ktzi202: Arithmetic mean of the differences between the baseline and the five repeat SIGM runs, SIGM(b-rx), with different data processings in the evaluated depth intervals. Note the different scale in each depth interval.	165
A.20.Ktzi201: DTS derived temperature differences for the time period 12:03 June, 18th, 2008 to 15:37 June, 26th, 2008. Each track includes a time period of 39.0717 hours. The temperature differences result from a baseline temperature profile before and the actual derived temperature during this time period. Courtesy of Henniges, Lithology after Förster et al. (2010), TPHI and EPHI after Norden et al. (2010)	167

List of Figures

A.21.Ktzi201: Saturation profiles as fractions of ϕ_{tot} (displacement conform CO_2 in green, apparent CO_2 in light green and brine in blue), S_{CO_2} derived from TPHI with a larger scale (orange logs) (first track) and the corresponding Diff logs with solid and dotted signature (second track) for five repeat runs based on the *displacement saturation model and the original brine salinity*. The brine levels for each repeat run are marked with a black bar on the right side of each track. Lithology after Förster et al. (2010) 168

List of Tables

2.1. Microscopic capture cross section of common elements and molecules and their values normalized to hydrogen (H_{norm}) or rather water (H_2O_{norm}).	8
2.2. Microscopic and macroscopic capture cross section parameters.	9
2.3. Σ values of different fluids, minerals and rock formations compiled after Ellis and Singer (2008); Fricke and Schön (1999); Knödel et al. (1997); Serra (1984); Schlumberger (1989, 2009). The gases' Σ values are calculated after equation 2.8. The brine Σ values are given for a NaCl-brine at 200 °F (93.3 °C) and 5,000 psi (34 MPa).	9
2.4. Defining parameters for the calculation of the macroscopic capture cross section Σ_{br} for NaCl-brines based on concentrations in g/l.	13
2.5. RST apparent Σ values and ratios after Plasek et al. (1995).	21
2.6. Well completion and lithology parameters for environmental corrections after Plasek et al. (1995).	21
2.7. RST intrinsic Σ values and corresponding quantities after Plasek et al. (1995).	22
3.1. CO ₂ and H ₂ O mole fractions (y_{CO_2} , y_{H_2O}) after Spycher et al. (2003), the corresponding mass fractions (m_{H_2O} , m_{CO_2}) and Σ values (Σ_{CO_2} , Σ_{H_2O}), as well as the total Σ phase values (Σ_{gp} , Σ_{ap}), for the gaseous and aqueous phase for 35 °C and 101.3 bar. The salt component in the aqueous phase is not taken into account.	30
3.2. Summary of parameters for the saturation based brine declaration (baseline saturation model) and the the evaporation/precipitation model (repeat saturation model).	45
3.3. Summary of the corresponding auxiliary parameters for the evaporation/precipitation model.	46
4.1. Conventional and extended PNG saturation model parameters including displacement and evaporation/precipitation processes.	55
4.2. Applicable, when $\Sigma_r \leq \Sigma_b$: Saturation parameters for the different steps of the extended saturation model including the displacement and subsequent evaporation/precipitation model. The symbols \uparrow or \downarrow indicate increasing or decreasing during the displacement (1) or evaporation/precipitation process (2). 1.1 and 2.1 describe the completed displacement or evaporation/precipitation process and 2.2* and 2.3* the optional steps.	59
5.1. Capture cross sections for brine (Σ_{br}) as the sum of the capture cross sections of fresh water ($\Sigma_{H_2O_c}$) and the dissolved salts for the “true” and the NaCl-equivalent brine ($\Sigma_{salt/NaCl_{e-eq}}$) under ambient (25 °C, 1 bar) and reservoir conditions (35 °C and 75 bar), the corresponding brine densities (ρ_{br}) and total dissolved salt content (TDS). *(Data provided by Würdemann et al. (2010); adjusted by De Lucia)	70

List of Tables

5.2.	The dates on which the RST runs were carried out.	72
5.3.	Brine levels below ground level for the repeat runs in Ktzi200, Ktzi201 and Ktzi202.	77
5.4.	Main depth ranges with changes between baseline and repeat runs in Ktzi200, Ktzi201 and Ktzi202.	81
5.5.	Borehole and formation parameters for the environmental corrected intrinsic data of the baseline runs.	82
5.6.	Borehole and formation parameters for the environmental corrected intrinsic data of the repeat runs.	85
5.7.	Ktzi200: Mean S_{CO_2} in the upper (SS1) and lower (SS2) reservoir sandstone sections for six repeats based on the conventional displacement model.	96
5.8.	Ktzi201: Mean S_{CO_2} in the upper (SS1), lower (SS2) reservoir sandstone sections, the silt section (Silt) and the third reservoir sandstone section (SS3) for five repeats based on the displacement model for the original (org) and flush (flush) brine salinity.	105
5.9.	Ktzi202: Mean S_{CO_2} in the upper reservoir sandstone section (SS1) without the thin silty mudstone and sandstone layers in the lower most part (new bottom depth 636.02 m) for five repeats based on the displacement model.	107
5.10.	Ktzi200: Mean S_{CO_2} in the upper (SS1) reservoir sandstone section for five repeats based on the extended saturation model.	110
5.11.	Ktzi201: Mean S_{CO_2} in the upper (SS1) and lower (SS2) reservoir sandstone sections for five repeats based on the extended saturation model for the original and flush brine salinity data sets shown in figures 5.19 and 5.22.	124
5.12.	Salt precipitation modeling results for the Ketzin site include the input salinity (X_{NaCl}), the dry out radius (r_{dry}) and the greatest precipitated halite saturation (S_{NaCl}).	126
6.1.	Capture cross sections for brine (Σ_{br}) as the sum of the capture cross sections of fresh water ($\Sigma_{H_2O_c}$) and the dissolved salts for the “true” and the NaCl-equivalent brine ($\Sigma_{salt/NaCl_{c-eq}}$) under ambient (25 °C, 1 bar) and reservoir conditions (125 °C and 40 bar), the corresponding brine densities (ρ_{br}) and total dissolved salt content (TDS). *(Data provided by GDF-SUEZ (2009); adjusted by De Lucia et al. (2012))	133
6.2.	Σ values of different fluids and the associated saturations for the baseline (S_b) above (case 1) and below (case 2) the initial GWC and the two assumed scenarios (S_{sc1} , S_{sc2}) first pure displacement and second displacement and evaporation/precipitation. *Data according to GDF-SUEZ (2009).	134

1. Introduction

1.1. CO₂ storage in geological formations and resulting monitoring issues

The storage of carbon dioxide (CO₂) in geological formations is a promising option for reducing greenhouse gas emissions to the atmosphere and for mitigating global climate change (IPCC, 2005). Fossil-fuelled point sources such as coal fired power plants or large energy consuming industrial facilities (metal, cement, glass, paper) are especially suited for CO₂ emissions storage in geological formations. For this purpose, different techniques are used to capture the CO₂ and transport it to the injection facilities for underground storage. The challenge is to coordinate the entire chain of Carbon Capture and Storage (CCS), e.g. to match up the surface facilities for CO₂ capture and transport and the subsurface CO₂ storage in geological formations, in a safe, technically feasible and economically sustainable way.

Saline aquifers or depleted oil and gas fields in combination with enhanced oil or gas recovery (EGR/EOR) have been proposed as suitable geological settings for CO₂ storage operations. During the proposed CO₂ injection process, application of suitable techniques for monitoring of the induced changes in the subsurface is required. For CO₂ storage operations, enabling a safe and reliable operation is of prime importance. In addition, the verification of the stored amount of CO₂ and observation of possible leakages from the intended storage formations are required in the context of CO₂ storage (Benson and Cook, 2005).

Existing models for the spreading of CO₂ in the subsurface, including the position and form of the CO₂ plume, the extent of fluid mixing and issues resulting from mutual solubility between brine and CO₂, need to be checked. Monitoring the injection front aid in predicting the arrival of CO₂ at observation wells. Saturation changes can create new migration pathways, e.g. within previously flooded reservoir intervals, or indicate leakages along a wellbore or through the confining strata of the caprock. Therefore, observing the movement and the changes in saturation contained in the reservoir and the confining strata associated with well integrity are among the primary aims for monitoring.

1.2. Integrated CO₂ storage monitoring

To evaluate the induced changes in the subsurface from CO₂ storage operations, monitoring should be performed in time-lapse mode by comparing baseline measurements before CO₂ injection starts with repeated measurements during injection or after site abandonment. In general, different monitoring techniques can be applied for surface and subsurface monitoring. Surface monitoring, for instance, includes chemical soil gas analysis or satellite remote sensing to evaluate possible ground heaving or subsidence (Wildenborg et al., 2009).

For subsurface monitoring, different geophysical and geochemical techniques are used to derive relevant properties of the storage reservoir and the confining strata. These techniques cover

1. Introduction

a wide range of scales with different spatial resolutions for the derived properties. In general, the spatial resolution decreases with increasing scale. Based on petrophysical and chemical models, the derived properties are used to describe the induced changes from CO₂ storage operations.

Geophysical methods, like 2D and 3D seismics, vertical seismic profiling, moving source profiling, electromagnetic, electrical and gravitational methods cover the large "reservoir scale" with a corresponding small spatial resolution. In contrast, well logging derived properties cover the small "borehole scale" with a large spatial resolution. In addition, core and fluid sample analysis provide important properties for site characterization. The integrated combination of these different monitoring techniques with their variability in scale and spatial resolution is the basis for a comprehensive CO₂ storage monitoring program (Michael et al., 2010).

Moreover, many geophysical and geochemical monitoring experiences exist from the ground water supply, mining or hydrocarbon industry. These experiences are of great importance, because the methodological and technical background is comparable with the monitoring tasks for CO₂ storage operations.

The suitability of these different monitoring techniques and their combinations are evaluated in different ongoing CO₂ storage projects worldwide e.g. Nagaoka (Japan), Otway (Australia), Weyburn (Canada), Frio (USA), In Salah (Algeria), Sleipner (Norway), Ketzin and Altmark (Germany). These sites cover a wide range of suitable geological formations for CO₂ storage operations with specific reservoir depth, reservoir settings, pressure and temperature conditions and storage tasks (pure CO₂ storage or EGR/EOR). Later on, based on the derived CO₂ storage monitoring experiences, practical guidelines and regulatory frameworks for monitoring and verifying the safety and effectiveness of storage sites should be developed.

1.3. Well logging derived CO₂ saturation monitoring

As mentioned above, the evaluation of saturation changes is an important aim for monitoring. For the assessing static saturation conditions, a broad range of well logging methods commonly applied during oil and gas exploration can be used. For well logging in cased boreholes, however, which is the standard situation encountered under the given conditions, only a limited number of techniques are applicable.

Electromagnetic methods like induction or NMR logs need an electrically non-conductive well completion, including casing material (fiberglass) or installations behind casing (no metallic cable). Neither of these situations are commonly found in typical well completions. Only cased hole formation resistivity logs (CHFR) are applicable in steel cased wells, where the outside surface of the casing is not coated by electrical isolating materials. These logs use the metallic casing itself as a huge electrode. Thereby, the high resistivity contrast between the metallic casing and the formation leads to a small current leakage perpendicular into the formation. This contrast is the basis for CHFR measurement (Smolen, 1996). The vertical resolution of CHFR logs is quite poor compared to other common cased-hole logs (Müller et al., 2007), and often a previous mechanical scratching run to remove corrosion products is needed to improve the electrical contact between the tool electrodes and the casing.

Radiometric measurements, like pulsed neutron-gamma (PNG) logging (Chapter 2), are applicable for the standard situation encountered under the given conditions. The PNG technique uses controlled neutron bursts, which interact with the nuclei of the surrounding borehole

1. Introduction

and formation. Due to collision with these neutrons, atoms from the surrounding environment emit gamma rays. The main PNG derived parameters are the macroscopic capture cross section (Σ) and the neutron porosity (TPHI) of the formation. Σ is derived from the decline of gamma rays with time from neutron capture processes and TPHI is derived from the ratio of the total selected capture counts of the near and far detectors. In general, the Σ and TPHI readings are affected by the borehole conditions that can change between baseline and repeat measurements. Thus, changes in the Σ and TPHI readings are a combination of saturation changes in the reservoir and changes in the borehole conditions. These changing borehole conditions can result from changing brine levels (interface between CO₂ and brine) between baseline and repeat measurements. Thus, the fluids in the borehole between baseline (brine) and repeat measurements (CO₂) change. Extensive environmental corrections have to be applied in order to transfer the apparent Σ and TPHI readings into intrinsic Σ and TPHI values in order to describe the saturation changes in the reservoir without the influence of changing borehole conditions.

Monitoring saturation changes using PNG logging is of great importance in reservoir monitoring and surveillance. Thus, PNG monitoring is widely used in oil and gas fields, giving detailed information about possible changing saturation conditions due to production or injection operations (e.g. Fitz and Ganapathy, 1993; Morris et al., 2005; Smolen, 1996).

The high Σ and TPHI contrast between brine and CO₂ in combination with the high precision of typical PNG tools (0.22 cu, Plasek et al. (1995)) results in a high measurement sensitivity to saturation changes. Due to the linearity of the general PNG mixing model, the sensitivity to CO₂ saturation is also linear. This high sensitivity makes PNG monitoring favorable for saturation profiling, especially in time-lapse mode. Therefore, PNG measurements have already been applied successfully for monitoring CO₂ injection in saline aquifers (e.g. Müller et al., 2007; Sakurai et al., 2005; Murray et al., 2010; Vu-Hoang et al., 2009; Xue et al., 2006). For this purpose, the conventional PNG saturation model, based on a displacement process has been used for PNG interpretation in different CO₂ storage projects in saline aquifers. The same conventional saturation model can be used with the neutron porosity (TPHI) and instead of the brine and CO₂ Σ values with the corresponding hydrogen index (HI) values as input parameters. Thus, only mixing of the fluids in the pore space (ignoring any mutual physico-chemical interaction) is taken into account. In addition to the displacement process, the mutual solubility between brine and CO₂ adds further complex processes, such as evaporation and salt precipitation. Until now, the resulting issues from mutual solubility are not considered in PNG saturation models.

1.4. Derived research objectives and structure of the thesis

As mentioned above, along with the displacement process, the mutual solubility between brine and CO₂ adds further complex processes (Chapter 3). The evaporation of water causes an increase in the brine's salt concentration until the salt solubility limit is reached. Upon reaching the salt solubility, further water evaporation leads to salt precipitation. These evaporation and precipitation processes are relevant in the vicinity of an injection well, where dry CO₂ enters the reservoir. Such salt precipitations have already been proven in laboratory CO₂ flooding experiments (Wang et al., 2009, 2010), but were previously not detected in situ in connection with CO₂ injection in saline aquifers. Moreover, modeling results show that gravity-forced upflow of CO₂ and capillary-forced backflow of brine toward the injection point can also affect saturation changes and salt precipitation (Pruess and Müller, 2009; Pruess,

1. Introduction

2009; Zeidouni et al., 2009a). These salt precipitations are known as a possible source of formation damage, reducing formation porosity, permeability and injectivity (Kleinitz et al., 2001; Pruess, 2009).

The remaining salt content, with their usually large amount of chlorine, has a correspondingly large Σ value. Additionally, evaporation and precipitation are near wellbore processes (Hurter et al., 2007; Muller et al., 2009; Zeidouni et al., 2009a). This makes PNG measurements suitable for evaporation and salt precipitation monitoring.

For this purpose a PNG saturation model that accounts for the evaporation/precipitation process for NaCl-brines is developed (Chapter 3.4). The extended PNG saturation model includes both the displacement and evaporation/precipitation processes weighted by their affected porosity proportions (Chapter 4).

Ketzin, the only German pilot test site for CO₂ storage in saline aquifers, has one injection (Ktzi201) and two observation wells (Ktzi200 and Ktzi202), where an extensive PNG monitoring program is performed (Chapter 5). The Ktzi200 is about 50 m and the Ktzi202 is about 112 m from the injection well. The Reservoir Saturation Tool (RST), a registered trademark of Schlumberger based on the PNG method, is used at the Ketzin site. The baseline PNG runs were performed in June 2008. The first repeat run in July 2008 was only performed in Ktzi200, which is closest to the injection well. All five subsequent repeat runs were performed in all wells roughly annually. During the investigated period from June 2008 to October 2012 around 60,000 t CO₂ was injected and the injection rate was changed, which is associated with changing brine levels. The Ketzin wells are characterized by uncemented or partly cemented annuli in the reservoir section. Therefore, in addition to the changing fluids in the borehole, the fluids in the annulus change. These changes add further environmental effects that must be carefully taken into account when characterizing the saturation changes in the reservoir (Chapter 5.2).

First, the conventional displacement saturation model is applied to the PNG monitoring data of all wells (Chapter 5.3). The extended saturation model, including both the displacement and evaporation/precipitation processes, is applied to the PNG monitoring data of the injection well. Moreover, the low salinity KCl-preflush, performed in the injection well before the start of CO₂ injection in order to reduce the brine salinity and thus the amount of salt that can precipitate, is taken into account. Additionally, the extended saturation model is applied to the PNG monitoring data of the observation well Ktzi200, which is closest to the injection well.

The depleted gas field at the Altmark site, Germany, has been proposed as a suitable geological formation for CO₂ storage operations in combination with EGR. Since the Σ contrast between natural gas (predominantly composed of N₂ and CH₄) and CO₂ is low, a decreased PNG measurement sensitivity to saturation changes in depleted gas fields can be expected. Furthermore, in the vicinity of injection wells, the immobile brine evaporate, inducing salt precipitation. Moreover, due to increased reservoir pressure during CO₂ injection, the initial gas-water contact (GWC) in the formation is expected to move downward. Thus, formerly completely brine-saturated injection layers are flooded with CO₂. The PNG monitoring potential, with considering of displacement, evaporation/precipitation processes and changing GWC's, is evaluated for application under conditions similar to the Altmark site (Chapter 6). The Altmark site might be representative of many suitable locations for a commercial deployment of the EGR and CCS technologies worldwide. This chapter 6 draws extensively on the sensitivity study recently published in Baumann and Hennings (2012).

2. Theoretical and technical aspects of PNG logging

2.1. Neutron properties, sources and lifetime

2.1.1. Neutron properties and sources

Neutrons are electrically neutral elementary particles that minor interact with electrons or coulomb fields. They are unstable as free particles. The mass of a neutron is approximately equal to the mass of a proton. The interaction, therefore, of a neutron with the hydrogen nucleus is greatest.

Neutrons can be generated chemically from (α, n) -reactions. For this mechanism Am-Be sources are commonly used. Moreover, neutrons can result from spontaneous fission of unstable isotopes like Cf-252.

Along with chemical sources continuously emitted neutrons, a neutron generator can periodically generate neutrons. The periodically emitted neutrons are used for pulsed neutron gamma (PNG) logging. In a neutron generator (minitron), deuterons d from deuterium gas are accelerated in an electric field to energies of 150-400 keV. The resulting focused deuteron beam is fired at the target material tritium. As a result, about $5 \cdot 10^7$ up to 10^{13} monoenergetic (14 MeV) neutrons per second are produced (${}^2_1H + {}^3_1H \rightarrow {}^4_2\alpha + {}^1_0n$). These high energy neutrons are emitted periodically as pulsed bursts and interact with the surrounding nuclei from the borehole and the formation. The kind of interaction depends on the kinetic energy of the neutrons. Fast neutrons have energies above 100 keV, epithermal neutrons above 0.025 eV and thermal neutrons below 0.025 eV (e.g. Ellis and Singer, 2008; Knödel et al., 1997; Serra, 1984). The following chapter 2.1.2 describes the neutron lifetime from fast to thermal energy levels and their associated interactions with the surrounding nucleus.

2.1.2. Neutron lifetime

As a result of elastic scattering (${}^AZ + n \rightarrow {}^AZ + n$), the fast neutrons are slowed down by delivering kinetic energy to a nucleus analogously to a billiard ball collision. The kinetic energy loss during collision depends on the mass of the target nucleus and the angle between the scattered neutron and the incident neutron. The properties of the nucleus remain unchanged, and no emission of gamma rays occur. The energy loss caused by a neutron's collision with a hydrogen nucleus is greatest, because the mass of protons and neutrons are approximately equal.

Along with elastic scattering, an inelastic scattering process also takes place. The inelastic scattering process, (${}^AZ + n \rightarrow {}^AZ^* + n \rightarrow {}^AZ + n + \gamma$), is likely to occur for fast neutrons. During inelastic scattering, the neutron-stocked nucleus is excited. The excitation energy of the nucleus corresponds to the decrease of the kinetic energy of the scattered neutron.

2. Theoretical and technical aspects of PNG logging

The return of the excited nucleus to the ground state leads to the emission of characteristic (element specific) gamma-rays as a function of the nucleus and the excitation energy. The duration of the gamma radiation from inelastic scattering is about 10 μ s.

After the energy loss from elastic and inelastic scattering, the neutrons reach the thermal energy level. At this thermal energy level, the neutrons are probably captured by the stocked nucleus (${}^AZ + n \rightarrow {}^{A+1}Z^* \rightarrow {}^{A+1}Z + \gamma$). Therefore, the neutrons do not exist any longer. The stocked nucleus is also excited, associated with a corresponding emission of characteristic (element specific) gamma-rays upon re-excitation. This process is most likely for H and Cl, and the duration of the gamma radiation from neutron capture is, with about 1000 μ s, much greater than the gamma radiation from inelastic scattering.

On the microscopic scale, the values of the probability for the different neutron interactions are described by individual microscopic scattering cross sections with the dimension m^2 for each nucleus. The molecule's microscopic scattering cross sections result from its chemical formula.

On the macroscopic scale, the probability of chemical materials for neutron interactions is defined as the product of the microscopic scattering cross sections of the molecules forming that chemical material and their number of molecules per cubic centimeter. The macroscopic capture cross section for neutron capture is defined by Σ , which is derived from the decline of capture gamma rays with time. The element specific energy determination of the emitted gamma rays from both inelastic scattering and neutron capture is the basis for spectral analysis. The gamma rays from inelastic scattering are analyzed in the measurement of the carbon to oxygen ratio (C/O log).

(e.g. Ellis and Singer, 2008; Knödel et al., 1997; Serra, 1984; Smolen, 1996)

2.2. Material properties for the interaction with neutrons

2.2.1. Capture cross sections

A capture cross section of a nucleus with the dimension m^2 describes the ability to absorb thermal neutrons. A large capture cross section value corresponds to a high capture ability. The microscopic capture cross section is specific to elements or rather molecules, whereas the macroscopic capture cross section characterizes chemical materials by considering environmental conditions, such the density dependence on pressure and temperature.

2.2.1.1. Microscopic capture cross section of molecules

The microscopic capture cross section σ_i for an element i is a specific value for the effective cross-section area for neutron capture interactions. Thus, a molecule's microscopic capture cross section σ can be calculated from its chemical formula (Serra, 1984)

$$\sigma = \sum_i n_i \cdot \sigma_i \quad (2.1)$$

where σ_i is the microscopic capture cross section for element i in barn ($1 \text{ barn} = 10^{-24} \text{ cm}^2$) and n_i is the number of elements of type i present in the molecule. The more useful mass-normalized microscopic capture cross section σ_{m_i} in $[\text{cm}^2/\text{g}]$ for an element i results in

2. Theoretical and technical aspects of PNG logging

$$\sigma_{m_i} = \frac{\sigma_i}{A_i} \cdot N_{Av} \quad (2.2)$$

where A_i is the atomic mass for element i in g/mol and N_{Av} is the Avogadro's Number. The mass-normalized microscopic capture cross section σ_m for a molecule results in

$$\sigma_m = \sum_i n_i \cdot \sigma_{m_i} = \sum_i \frac{n_i \cdot \sigma_i}{n_i \cdot A_i} \cdot N_{Av} \quad (2.3)$$

For instance, for a molecule B_iC_j composed of two elements like pure water or halite, the mass-normalized microscopic capture cross section is calculated as follows

$$\sigma_{m_{B_iC_j}} = \frac{i \cdot \sigma_B + j \cdot \sigma_C}{i \cdot A_B + j \cdot A_C} \cdot N_{Av} \quad (2.4)$$

which results for pure water in

$$\sigma_{m_{H_2O}} = \frac{2 \cdot \sigma_H + 1 \cdot \sigma_O}{2 \cdot A_H + 1 \cdot A_O} \cdot N_{Av} \quad (2.5)$$

and for halite in

$$\sigma_{m_{NaCl}} = \frac{1 \cdot \sigma_{Na} + 1 \cdot \sigma_{Cl}}{1 \cdot A_{Na} + 1 \cdot A_{Cl}} \cdot N_{Av} \quad (2.6)$$

Table 2.1 summarizes σ_m for common elements and molecules using the element specific capture cross sections from Sears (1992) and the atomic mass from Afeefy et al. (2005). In order to compare the individual σ_m values, the element values are normalized to hydrogen (H_{norm}) and the molecule values to water (H_2O_{norm}). Comparing the element specific or molecule specific normalized values, it appears that especially hydrogen, chlorine and trace elements like boron are essential for neutron capture processes. Hydrogen and chlorine exist in reasonable quantities in rock formations (e.g. water, NaCl), making these elements eminently relevant for PNG logging. Gases, whose densities are low under common reservoir conditions, have a small effect on neutron capture probability. The macroscopic capture cross section considers the environmental conditions.

2.2.1.2. Macroscopic capture cross section Σ of common geological materials

A molecule's macroscopic capture cross section Σ in capture units ($1 \text{ cu} = 10^{-3} \text{ cm}^{-1}$) is defined as the product of the microscopic capture cross section σ of the molecule and the number of molecules of that species contained in a cubic centimeter (Ellis and Singer, 2008)

$$\Sigma = N \cdot \sigma = \frac{N_{Av} \cdot \rho_b}{A} \cdot \sigma \quad (2.7)$$

where N is the number of molecules per cm^3 , A is the molecules mass and ρ_b is the molecule's bulk density in g/cm^3 . Using the mass-normalized microscopic capture cross section σ_m ,

2. Theoretical and technical aspects of PNG logging

Table 2.1.: Microscopic capture cross section of common elements and molecules and their values normalized to hydrogen (H_{norm}) or rather water (H_2O_{norm}).

Element	$\sigma_m[\text{cm}^2/\text{g}]$	$H_{norm} [-]$	Molecule	$\sigma_m[\text{cm}^2/\text{g}]$	$H_2O_{norm} [-]$
B	42.72	215	HBO_2	10.5595	475
Cl	0.57	2.9	$NaCl$	0.3507	15.8
H	0.20	1	N_2	0.0817	3.7
K	0.032	0.16	CH_4	0.0501	2.3
Fe	0.027	0.14	H_2O	0.0222	1
Na	0.014	0.07	SiO_2	0.0017	0.08
Ca	0.007	0.03	CO_2	0.00005	0.002
Si	0.004	0.018			
C	0.0002	0.001			
O	0.000007	3.599E-05			

Σ simplifies to

$$\Sigma = \sigma_m \cdot \rho_b \cdot 1000 \quad (2.8)$$

which results for pure water (22.2 cu for 25 °C, 1 bar)

$$\Sigma_{H_2O} = \sigma_{m_{H_2O}} \cdot \rho_{H_2O} \cdot 1000 \quad (2.9)$$

and for halite (761 cu) in

$$\Sigma_{NaCl} = \sigma_{m_{NaCl}} \cdot \rho_{NaCl} \cdot 1000 \quad (2.10)$$

The microscopic and macroscopic capture cross section parameters are summarized in table 2.2.

Table 2.3 summarizes the Σ values for different pore fluids, minerals and typical rock formations. The Σ ranges for sandstone, limestone and dolomite are nearly the same. Small amounts of impurities like high Σ trace elements (e.g. boron, gadolinium) can cause the Σ difference between the main rock forming minerals quartz, calcite and dolomite and the complex rock formations. Due to the large density of the mineral anhydrite, its corresponding rock formation has large Σ values. Moreover the sulfur in anhydrite has a relatively large σ_m . Claystone composed of illite, chlorite, kaolinite or other clay minerals, with a corresponding large amount of hydrogen in the hydroxyl groups, are also characterized by high Σ values.

The gases' Σ values are calculated by adjusting the input densities as a function of pressure and temperature using the approach of Afeefy et al. (2005). In general, gases like N_2 , CH_4 or CO_2 have a small Σ value compared to liquids like water, crude oil or brine. As one can see in figure 2.1, the Σ values for CO_2 or gases in general, depend strongly on the environmental conditions, such as temperature and pressure effects on the gas' density. Obvious is the sharp Σ rise at the critical point (31 °C, 73.8 bar) that is associated with an abrupt density rise in the transition from liquid to supercritical CO_2 .

The Σ value of a rock formation composed of a matrix and a fluid filled pore space is described by its individual volume fractions and the corresponding Σ values.

Table 2.2.: Microscopic and macroscopic capture cross section parameters.

Mnemonic	Description	Unit
σ_i	microscopic capture cross section for element i	barn
n_i	number of elements type i present in molecule	-
σ_{m_i}	mass-normalized microscopic capture cross section for element i	cm ² /g
A_i	atomic mass for element i	g/mol
σ	microscopic capture cross section for a molecule	barn
σ_m	mass-normalized microscopic capture cross section for molecule	cm ² /g
A	atomic mass for a molecule	g/mol
ρ_b	bulk density	g/cm ³
N	Number of molecules per cm ³	1/cm ³
Σ	macroscopic capture cross section for a molecule	cu
N_{Av}	Avogadro's Number, 6.0221*10 ²³	1/mol

Table 2.3.: Σ values of different fluids, minerals and rock formations compiled after Ellis and Singer (2008); Fricke and Schön (1999); Knödel et al. (1997); Serra (1984); Schlumberger (1989, 2009). The gases' Σ values are calculated after equation 2.8. The brine Σ values are given for a NaCl-brine at 200 °F (93.3 °C) and 5,000 psi (34 MPa).

Fluids	Σ [cu]	Minerals/Rocks	Σ [cu]
Water (fresh)	22.2	Quarz, SiO_2	4.3
Crude oil	22	Calcite, $CaCO_3$	7.1
Brine (50 ppk)	38	Dolomite, $CaMg[CO_3]_2$	4.7
Brine (100 ppk)	58	Anhydrite, $CaSO_4$	12
Brine (150 ppk)	77	Halite, $NaCl$	754...770
Brine (200 ppk)	98	Sandstone	6-13
Brine (250 ppk)	120	Limestone	6-14
CO ₂ (35 °C, 7.5 MPa)	0.014	Dolomite	6-12
CO ₂ (125 °C, 4 MPa)	0.003	Anhydrite	13-21
N ₂ (125 °C, 4 MPa)	2.722	Claystone	25-50
CH ₄ (125 °C, 4 MPa)	0.984	Portland-Cement	13-17

2. Theoretical and technical aspects of PNG logging

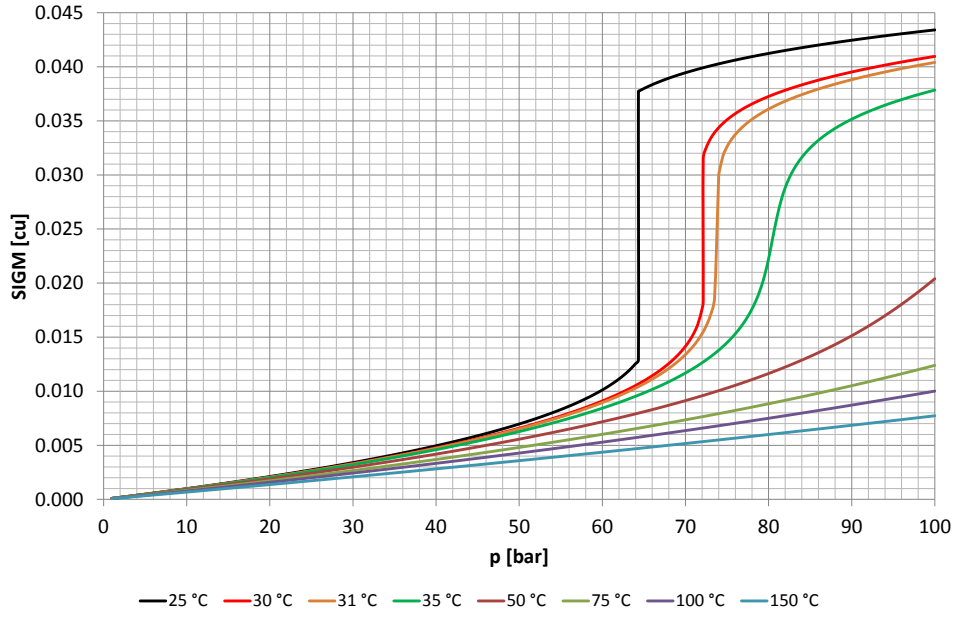


Figure 2.1.: Σ_{CO_2} versus pressure for different temperatures.

Σ_{tot} of a mixture of materials results from the sum of the volume fraction of constituent i (V_i) and the macroscopic capture cross section of constituent i (Σ_i) (Serra, 1984).

$$\Sigma_{tot} = \sum_i V_i \cdot \Sigma_i \quad (2.11)$$

2.2.1.3. Macroscopic capture cross section of a NaCl-brine (Σ_{br})

The macroscopic capture cross section for brine (Σ_{br}) can be calculated from a chemical analysis (Serra, 1984). Σ_{br} results from the sum of the capture cross sections of the solvent water $\Sigma_{H_2O_c}$ and the dissolved salts Σ_{salt} .

$$\Sigma_{br} = \Sigma_{H_2O_c} + \Sigma_{salt} = c_{H_2O} \cdot \sigma_{m_{H_2O}} + \Sigma_{salt} \quad (2.12)$$

In contrast to pure water, the subscript "c" in $\Sigma_{H_2O_c}$ specifies that this Σ value is calculated based on the water concentration c_{H_2O} in g/l of brine. Σ_{salt} is calculated from the sum of the product of the dissolved cation and anion concentrations c_i given in g/l of brine and the corresponding σ_{m_i} values.

$$\Sigma_{salt} = \sum_i (c_i \cdot \sigma_{m_i}) \quad (2.13)$$

Since most brines are dominated by NaCl and chlorine has large σ_m compared to other typical ions, a common simplification can be made by introducing a NaCl-equivalent concentration $c_{NaCl_{eq}}$. Therefore, the corresponding $\Sigma_{NaCl_{eq}}$ is equal to Σ_{salt} . This is a common assumption made in PNG interpretation (e.g. Smolen, 1996; Serra, 1984).

2. Theoretical and technical aspects of PNG logging

For a pure NaCl-brine c_{salt} simplifies to c_{NaCl} . Accordingly, Σ_{br} , simplifies to

$$\Sigma_{br} = \Sigma_{H_2O_c} + \Sigma_{NaCl_c} = c_{H_2O} \cdot \sigma_{m_{H_2O}} + c_{NaCl} \cdot \sigma_{m_{NaCl}} \quad (2.14)$$

The subscript c in Σ_{NaCl} also stands for the concentration. Σ_{NaCl_c} is calculated like Σ_{salt} but for NaCl only. The NaCl-brine density ρ_{br} in kg/m^3 is calculated after Rowe and Chou (1970), depending on the NaCl mass fraction X_{NaCl} in kg/kg_{sol} , temperature in $^{\circ}\text{C}$ and pressure in bar.

In the following, the derived ρ_{br} and all other densities are used in g/cm^3 , because this is the common unit for the Σ calculation. Moreover, the NaCl mass fraction X_{NaCl} is also called salinity and can be also described in the unit ppk ($1000 \text{ ppk} = 1 \text{ kg/kg}_{sol}$). The NaCl concentration c_{NaCl} in g/l results from the product of ρ_{br} and X_{NaCl} .

$$c_{NaCl} = \rho_{br} \cdot 1000 \cdot X_{NaCl} \quad (2.15)$$

The water concentration c_{H_2O} in g/l brine results from ρ_{br} and X_{H_2O} or c_{NaCl} .

$$c_{H_2O} = \rho_{br} \cdot 1000 \cdot (1 - X_{NaCl}) = \rho_{br} \cdot 1000 - c_{NaCl} \quad (2.16)$$

Accordingly, the sum c_{H_2O} and c_{NaCl} is equal to the brine density ρ_{br} defined after Rowe and Chou (1970).

$$\rho_{br} = \frac{c_{H_2O} + c_{NaCl}}{1000} \quad (2.17)$$

The temperature driven NaCl solubility limit is defined by Potter et al. (1977), and is used as input parameter for the maximum ρ_{br} and Σ_{br} values. The solubility limit of NaCl in water as a function of temperature is

$$NaCl [wt\%] = 26.218 + 0.0072 \cdot T + 0.000106 \cdot T^2 \quad (2.18)$$

for $0 \leq T \leq 800^{\circ}\text{C}$ (Potter et al., 1977), where 1 wt% corresponds to 0.01 X_{NaCl} .

Σ_{br} and ρ_{br} increase with increasing salinity (Figure 2.2). Since Σ_{br} is dependent strongly on the brine salinity (especially the chlorine content) PNG logs are also called chlorine logs. In general, ρ_{br} and accordingly Σ_{br} dependent slightly on pressure and temperature.

A more detailed description concerning Σ_{br} composed of Σ_{NaCl_c} and $\Sigma_{H_2O_c}$ and the corresponding NaCl and water concentrations is given in figure 2.3 for 35°C and 75 bar . With increasing c_{NaCl} , c_{H_2O} decreases slightly. This results in a decreased $\Sigma_{H_2O_c}$ value compared to the pure water value. Overall, the Σ contrast between brine and CO_2 increases with salinity. Compared to water, or even brine Σ values (compare Figure 2.2), Σ_{CO_2} is three order of magnitudes smaller, making PNG monitoring in saline aquifers favorable due to the large Σ contrast (e.g. Müller et al., 2007; Sakurai et al., 2005; Murray et al., 2010).

2. Theoretical and technical aspects of PNG logging

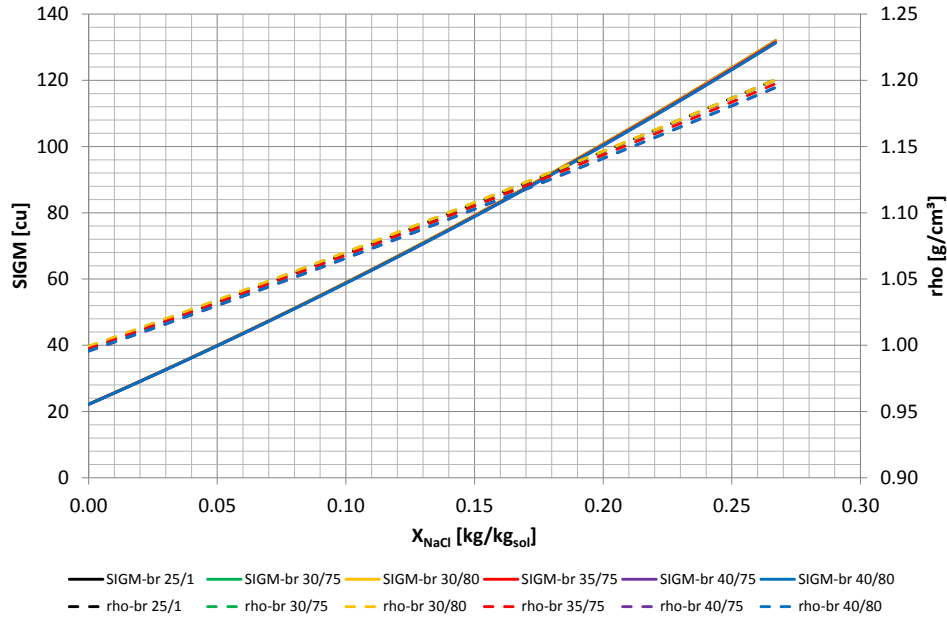


Figure 2.2.: Σ_{br} and ρ_{br} as a function of the NaCl-salinity X_{NaCl} in $\text{kg}/\text{kg}_{sol}$ for different pressure and temperature conditions (25 °C, 1 bar; 30 °C, 75 bar; 30 °C, 80 bar; 35 °C, 75 bar; 40 °C, 75 bar; 40 °C, 80 bar).

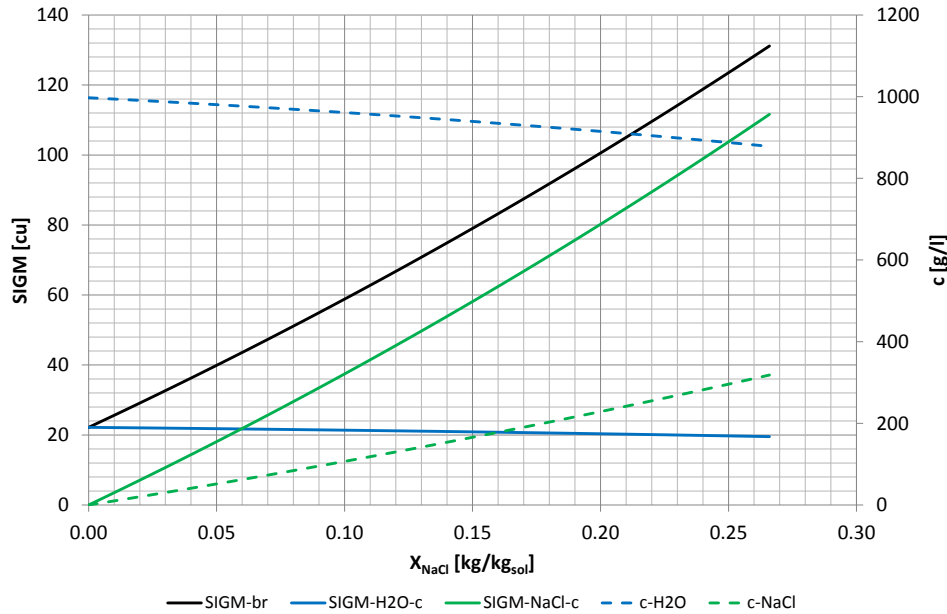


Figure 2.3.: Σ_{br} as a sum of the concentration based NaCl (Σ_{NaCl_c}) and water values ($\Sigma_{H_2O_c}$), and the corresponding NaCl (c_{NaCl}) and H_2O (c_{H_2O}) concentrations as a function of the NaCl-salinity X_{NaCl} in $\text{kg}/\text{kg}_{sol}$ (35 °C, 75 bar). c_{NaCl} in g/l results from the product of X_{NaCl} and ρ_{br} in kg/m^3 .

Table 2.4 summarizes the parameters required to calculate Σ_{br} for NaCl-brines. The column "Remarks" contains the necessary input parameters to calculate each output parameter.

Table 2.4.: Defining parameters for the calculation of the macroscopic capture cross section Σ_{br} for NaCl-brines based on concentrations in g/l.

Mnemonic	Description	Unit	Remarks
c_i	Cation and anion i concentration in brine	[g/l]	known
Σ_{salt}	Σ cation and anion fraction in brine	[cu]	c_i
$\Sigma_{NaCl_{c-eq}}$	Σ NaCl equivalent fraction in brine	[cu]	Σ_{salt}
$c_{NaCl_{eq}}$	NaCl equivalent concentration	[g/l]	$\Sigma_{NaCl_{c-eq}}$
X_{NaCl}	NaCl mass fraction, salinity (1000 ppk=1 kg/kg _{sol})	kg/kg _{sol}	known
X_{H_2O}	H ₂ O mass fraction (1 - X_{NaCl})	kg/kg _{sol}	X_{NaCl}
ρ_{br}	ρ brine, calculated after (Rowe and Chou, 1970)	[g/cm ³]	X_{NaCl} , p, T
c_{NaCl}	NaCl concentration in brine	[g/l]	X_{NaCl} , ρ_{br}
c_{H_2O}	H ₂ O concentration in brine	[g/l]	ρ_{br} , c_{NaCl}
Σ_{NaCl_c}	Σ NaCl fraction in brine	[cu]	c_{NaCl} , $\sigma_{m_{NaCl}}$
$\Sigma_{H_2O_c}$	Σ water fraction in brine	[cu]	c_{H_2O} , $\sigma_{m_{H_2O}}$
Σ_{br}	Σ brine	[cu]	$\Sigma_{H_2O_c}$, Σ_{NaCl_c}

2.2.2. Hydrogen Index (HI)

Due to the mass approximate equality of neutrons and protons, hydrogen predominantly slows down neutrons. Therefore, the hydrogen index (HI) is introduced. The hydrogen index (HI) of a material is defined as the ratio of the number of hydrogen atoms per unit volume of a material to that number in pure water at standard conditions (Serra, 1984; Ellis and Singer, 2008)

$$HI = \frac{9 \cdot n_H \cdot A_H}{\sum_i n_i \cdot A_i + n_H \cdot A_H} \cdot \rho_b = \frac{n_H \cdot A_H}{M \cdot 0.111} \cdot \rho_b \quad (2.19)$$

where ρ_b is the bulk density of the fluid in g/cm³, n_H is the number of hydrogen in the molecule, A_H is the hydrogen atomic mass and M is the molecular weight. The denominator 0.111 is the moles of hydrogen in one cubic centimeter of water. Accordingly, the HI for water is one and for CO₂ and NaCl zero, because CO₂ and NaCl contain no hydrogen.

Due to the hydrogen displacement in saline water, the HI decreases with salinity. The increasing salinity, however, cause a significant Σ increase. This, in turn tends to increase the HI. Both competing effects can be described by a modified HI based on Σ_{br} (Ellis et al., 1987).

$$HI_{br} = 1.02 - 8.44 \cdot 10^{-4} \cdot \Sigma_{br} - 1.904 \cdot 10^{-6} \cdot \Sigma_{br}^2 \quad (2.20)$$

Schlumberger (1989) modify the HI by the brine density ρ_{br} and the NaCl mass fraction X_{NaCl} in kg/kg_{sol}.

$$HI_{br} = \rho_{br} \cdot (1 - X_{NaCl}) \quad (2.21)$$

The derived HI_{br} from both equations are in good agreement with each other (Figure 2.4). For the Ketzin formation brine (compare Chapter 5.1.2) the HI is 0.92, calculated after Ellis et al. (1987).

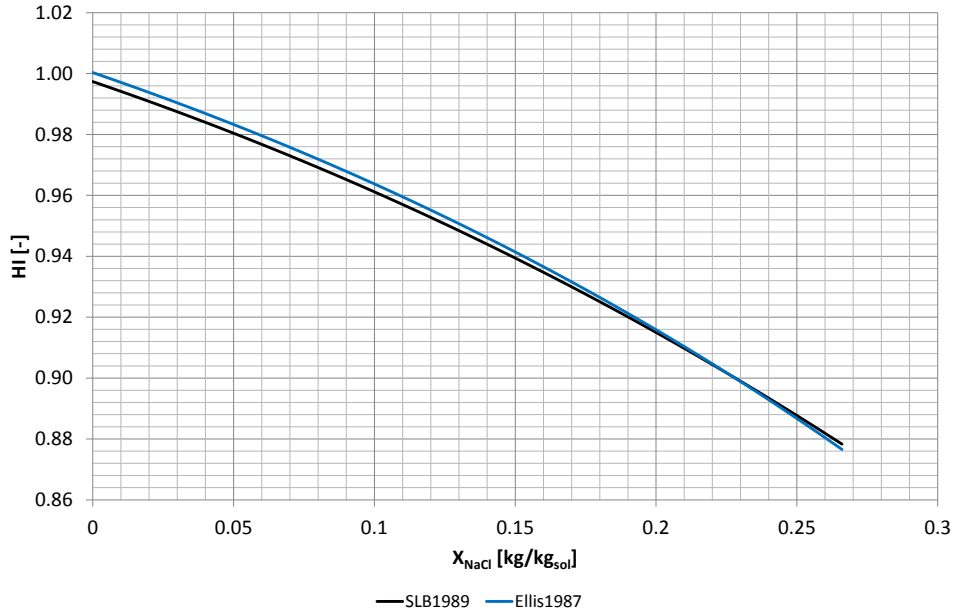


Figure 2.4.: HI as a function of salinity calculated after Schlumberger (1989) and Ellis et al. (1987).

2.2.3. Characteristic length

In addition to the microscopic and macroscopic cross sections and the HI, the characteristic lengths are also used to describe the neutron interactions with the surrounding nucleus. The slowing-down length (L_s) in cm is the distance that a neutron travels during the slowing-down phase, when the neutron's kinetic energy is reduced from the high energy level (emitted neutrons at the neutron generator) down to the lower edge of the epithermal energy level (Ellis and Singer, 2008). L_s is closely related to the ratio of the total selected capture counts from detectors at different spacings (Ellis and Singer, 2008). This ratio is used to estimate the porosity or the HI (compare Chapter 2.3.2). Thus, L_s increases with decreasing hydrogen concentration or rather decreasing HI. Moreover, the thermal neutron diffusion length (L_D) in cm is the distance that a neutron at the thermal energy level travels until it is finally captured. Thereby, the probability to absorb thermal neutrons described by Σ and the diffusion coefficient (D) in cm control L_D . D increase with decreasing porosity (Ellis and Singer, 2008). L_D increases with increasing D and decreasing Σ .

$$L_D = \sqrt{\frac{D}{\Sigma}} \quad (2.22)$$

Both, L_s and L_D can be summarized by the overall migration length (L_m) during the lifetime of a neutron. Typical L_m of neutrons in geological materials are in the order of 10 to 100 cm (McKeon and Scott, 1988).

$$L_m^2 = L_s^2 + L_D^2 \quad (2.23)$$

2.3. PNG logging

In general, neutron logs are widely used for open and cased hole well logging applications. The following section focuses on pulsed neutron gamma logging (PNG), which was introduced in the early sixties (e.g. Youmans et al., 1964; Hilchie et al., 1969). Even at that time, the potential of PNG measurements for reservoir monitoring was already recognized.

Two different modes of PNG logging for saturation evaluation can be distinguished. In the Σ logging mode, the total macroscopic capture cross section (Σ_{tot}) is determined from capture gamma rays. These also called pulsed neutron capture (PNC) logs were initially used to determine brine and oil saturations in high-salinity formations, or to characterize the residual oil saturation in log-injection-log experiments (Dewan et al., 1973). Later on they are also used to locate gas (Brimage and Blackburn, 1978). Today, PNC logs have become indispensable tools for describing changing saturation conditions due to production or injection operations, especially in time lapse mode, where runs at different time steps are compared (Morris et al., 2005). Nearby the application in the hydrocarbon industry, PNC logs are used to characterize the brine salinity through casing in caves. The brine salinity, e.g. its derived density, is used to calibrate the brines sonic velocity. A well defined brine sonic velocity improves the accuracy of cavity sonar logs, which are based on the sonic echo principle, in characterizing the shape of caves in three dimensions.

In contrast to the Σ logging mode, in C/O logging mode, the formation's carbon and oxygen concentrations, especially their ratio (COR), are determined from the inelastic gamma rays. The C/O logging mode is used to determine oil saturation in low salinity formations, since oil and freshwater have nearly the same Σ value (compare Table 2.3). In combination with information about the borehole conditions, lithology, porosity and the carbon density value (CDV), e.g. carbon concentration of the oil, the COR is used to determine the oil saturation (Murray et al., 2010).

Applicability of either the Σ or C/O methods for CO₂ storage operations in saline aquifers is determined by analyzing the measurement contrast between the examined fluids. Compared to a 25° API oil with a CDV of 0.76 g/cm³, the CDV for CO₂ is very low. Super critical CO₂ has a CDV of about 0.164 g/cm³ and aqueous media (water, brine) that do not contain carbon have a CDV of zero. Therefore, the CDV contrast between brine and CO₂ is low, explaining why qualitative determinations of CO₂ saturations with the C/O log are applicable (Murray et al., 2010).

Since the Σ contrast between CO₂ and brine is large, a good detectability of possible saturation changes can be expected in Σ logging mode, which is, therefore, more appropriate than C/O logging under the considered conditions of a saline aquifer.

2.3.1. Pulsed neutron capture (Σ) logging

Like many other well logging tools, PNG tools are constructed from a neutron source, a neutron generator, and two gamma ray detectors (compare Figure 2.5, left). Pulsed neutron capture logging tools belong to the group of PNG tools. These tools are used to measure the decline of neutron capture gamma rays with time from the borehole and the surrounding formation. Thereby, the decay of the of neutron capture gamma rays reflects the decay of the neutron population (N_t) at the time t .

2. Theoretical and technical aspects of PNG logging

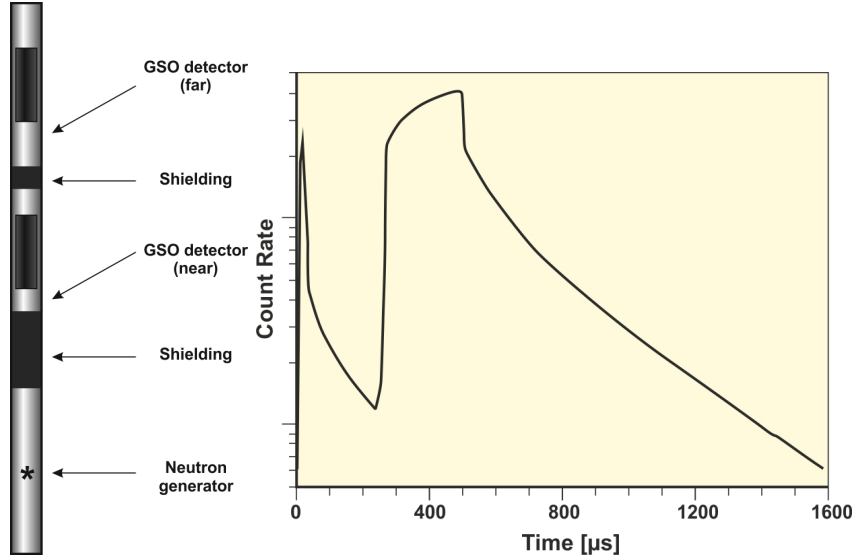


Figure 2.5.: 1¹¹/₁₆ inch slime hole RST tool (left) and typical dual burst decay measured with RST (right) redrawn after Plasek et al. (1995).

The gamma radiation decay from the formation region gives rise to only a single exponential decay,

$$N_t = N_0 \cdot e^{-\frac{t}{\tau}} = N_0 \cdot e^{-\Sigma \cdot \nu \cdot t} \quad (2.24)$$

where N_0 is the initial neutron population, t is the time in μs , τ is the decay time constant in μs and ν is the mean thermal neutron velocity (2200 m/s) (Ellis and Singer, 2008). The mean thermal neutron velocity corresponds to the thermal neutron kinetic energy of 0.025 eV. Thereby, τ is equal to the inverse product $\nu \cdot \Sigma$.

$$\tau = \frac{1}{\nu \cdot \Sigma} = \frac{4550}{\Sigma} \quad (2.25)$$

Ideally, for an infinitely homogeneous medium and a uniform distributed neutron source, the measured Σ and the intrinsic Σ value would be equal. But the effect of a localized neutron point source and the usually present Σ difference between the borehole (borehole fluid, casing, cement) and the formation result in an apparent measured Σ value which is different from the intrinsic formation Σ value (Pregg and Scott, 1986).

First, the point source character of the neutron source result in a spatial diffusion of neutrons from regions of high neutron population to regions of low neutron population (Ellis and Singer, 2008). Thus, in addition to the capture process, neutrons can also disappear from the investigation volume by diffusion. Thereby, neutrons diffuse out of the investigation volume before being captured, which result in an additional decrease of the measured capture gamma rays and a decreased observed τ value. The decreased τ value is associated with an increased Σ value compared to the value if neutron capture would be the only process (Murdoch et al., 1990).

Second, the formation decay depends on the formation fluid Σ value. Thus, the formation Σ value decreases with decreasing formation fluid Σ value, as is the case, for instance, with brine

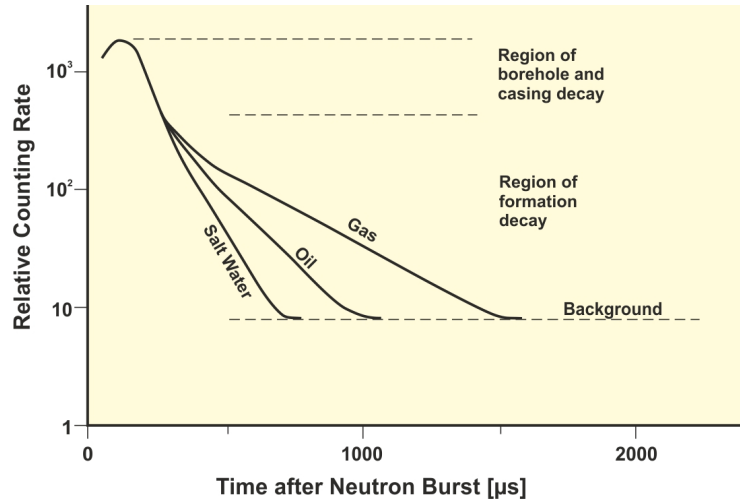


Figure 2.6.: Typical count rate decay for clean fluid bearing formations redrawn and modified after Smolen (1996).

over crude oil over gas (Figure 2.6, Formation decay). Additionally, the gamma radiation from the borehole region adds a second decay component (Figure 2.6, Borehole decay).

Both decays, from the borehole and the formation, can be described within statistical uncertainties by a sum of two exponential decay components with individual decay times τ . But as a result of the diffusion of neutrons between the borehole and formation region, this dual-exponential character is disturbed (Murdoch et al., 1990; Smith, Jr. et al., 1988). In general, the neutron diffusion effect on the Σ reading is complex and depends on the source-detector spacing, the source and detectors itself, the formation, borehole conditions and decay times (Morris et al., 2005).

On the one hand, for a borehole Σ greater than the formation Σ , neutrons diffuse inward the borehole; thus the borehole act as a sink for neutrons. As a result, the measured τ is decreased and the apparent formation Σ value is greater than the intrinsic formation Σ value. On the other hand, for a borehole Σ value close to the formation Σ or even smaller, the borehole act as a source for neutrons. Thus, the measured τ is increased and the apparent formation Σ value is smaller than the intrinsic formation Σ value (Murdoch et al., 1990).

As a result, the overall decay is complex. Thus, it is physically impossible to measure the intrinsic formation Σ value directly. Advanced electronics and processing algorithms are required to separate the borehole and diffusion effects from the apparent Σ value to get the intrinsic formation Σ value (Bonnie, 1991). The processing algorithm to correct for the environmental effects and the advanced tool electronics are discussed in chapter 2.4 for the PNG tool from Schlumberger, which is called Reservoir Saturation Tool (RST) and is a registered trademark. This tool is used for saturation profiling at the Ketzin site.

Neutron porosity is derived from the total selected counts along with the Σ value derived from decline of gamma radiation with time. The neutron porosity is discussed in the following section 2.3.2.

2.3.2. Neutron porosity

TRAT, which is the basis for the neutron porosity (TPHI), is derived from the ratio of the total selected capture counts of the near (TSCN) and far detectors (TSCF) (e.g. Plasek et al. 1995).

$$TRAT = \frac{TSCN}{TSCF} \quad (2.26)$$

In contrast to older single detector tools, the ratio from the near and far detector is less affected by borehole effects. TRAT is then corrected to the borehole conditions, predominantly the borehole size and standoff, and transformed into TPHI (e.g. Jeckovich and Olesen, 1989; Plasek et al., 1995; Ellis and Singer, 2008).

Since hydrogen, and thus water, predominantly slow down neutrons, TPHI is directly related to the HI. As long as the matrix contains no hydrogen (e.g. clean sandstone) and the porespace is saturated with freshwater, the HI and TPHI are identical (Ellis and Singer, 2008). TPHI can be expressed in terms of the HI for hydrogenous constituent materials analogous to the Σ_{tot} declaration of a mixture of materials (Ellis and Singer, 2008; Amadi and Hughes, 2008).

$$HI_{tot} = \sum_i V_i \cdot HI_i \quad (2.27)$$

The neutron porosity is usually related to limestone. As a result, all materials that have a greater L_s than limestone have apparent limestone porosities greater than the intrinsic value, while those with smaller L_s have smaller values. This is the reason why at zero porosity the limestone related neutron porosity is positive for dolomite and negative for sandstone. For this purpose correction charts, usually for sandstone and dolomite, are used to factor in these matrix effects (Ellis and Singer, 2008).

An increasing matrix density (associated with an increasing atom density) reduces the number of capture gamma rays reaching the detectors and elevates the calculated porosity. Moreover, the additional hydrogen content of hydroxyls in clay minerals decreases the count rate, also associated with an increased porosity. Both properties are true for clay minerals, which is why this phenomenon is often described as the "shale effect". As a result, the neutron porosity in shaly formations is higher than expected (Ellis and Singer, 2008).

The presence of gas, which normally contains less hydrogen than water, results in an increased L_s . This can have different effects on TSCN and TSCF. For low gas saturations both TSCN and TSCF increase, where TSCF increases slightly more than TSCN. As a result TRAT as well as the derived porosity TPHI decrease. For high gas saturations TSCF increases and TSCN decreases slightly. This effect results from the spatial distribution of thermal neutrons in the formation/borehole environment. The high gas saturation, with a corresponding large L_s for the neutrons, results in a higher count rate at the far detector and a lower count rate at the near detector. Therefore, TSCF increases and TSCN decreases slightly associated with greater TRAT and TPHI decrease compared to low gas saturations (Dunn et al., 1994, 1991; Badruzzaman et al., 2007).

If the L_s of a gas-bearing formation is longer than the L_s of the same formation with zero porosity, the derived porosity is negative (Ellis and Singer, 2008). This result from the fact, that the gas-bearing formation has a smaller bulk density than the zero porosity formation

(pure matrix density). In general, when gas is present, the resultant decrease in the porosity determination is called "gas effect" (Ellis et al., 2003, 2004).

Similarly to TRAT, the count rate ratio IRAT is derived from the selected counts of the inelastic gamma rays. Since the duration of the gamma rays from inelastic scattering ($10\mu\text{s}$) is much shorter than the duration of the gamma radiation from neutron capture ($1000\mu\text{s}$), both counts can be distinguished from one another. In contrast to TRAT, which is the ratio of the near and the far detector counts, IRAT is defined as the opposite ratio of the inelastic counts from the far (INFD) and the near detector (INND).

$$IRAT = \frac{INFD}{INND} \quad (2.28)$$

Therefore, IRAT and TRAT behave contrary. IRAT is sensitive to borehole and near borehole effects. Both counts, INFD and INND, increase in the presence of gas, where INFD increases greater than INND (Butsch and Vacca, 1990; Plasek et al., 1995). Moreover, IRAT can be used as a pseudo-density indicator, because with decreasing density decreases the neutron scattering (Badruzzaman et al., 2007). Thus, IRAT increases with decreasing borehole fluid density, which makes it useful for determining the brine level within the well.

2.4. Reservoir Saturation Tool (RST) technical parameters and data processing

As mentioned above, advanced electronics and processing algorithms are required to separate the environmental effects from the apparent Σ value to get the intrinsic formation Σ value. In this section, the data processing algorithm and technical parameters are described for today's generation Reservoir Saturation Tool (RST), which is used for saturation profiling at the Ketzin site.

2.4.1. Technical parameters

The RST uses the dual-burst neutron pulsing scheme with a short and a long neutron burst (compare Figure 2.5, right). The different length of the neutron bursts enhances the partition of the formation and borehole components of the observed neutron decay. The gamma rays acquired in the near detector after the short burst are used to analyze the borehole decay and the gamma rays in the far detector after the long burst are used to analyze the formation decay. This results in a better borehole to formation contrast, and in a lower contamination of the formation signal by the borehole signal (Steinman et al., 1988; Olesen et al., 1987).

Further hardware improvements compared to former PNG tool generations are achieved in the detector and shielding technology, or the neutron output and the shape of the neutron burst (Plasek et al., 1995; Roscoe et al., 1991). The precision or repeatability is 0.22 cu (Plasek et al., 1995). For a sufficiently high Σ contrast between the borehole and formation signal, an accuracy, e.g. the absolute error between the tool reading and the intrinsic formation Σ value, in the same range as the precision can be achieved (Plasek et al., 1995). Moreover, Jeckovich and Olesen (1989) give a threshold value of 10 cu between the borehole Σ and the formation Σ (borehole Σ higher than formation Σ) for the Thermal Decay Tool, which is

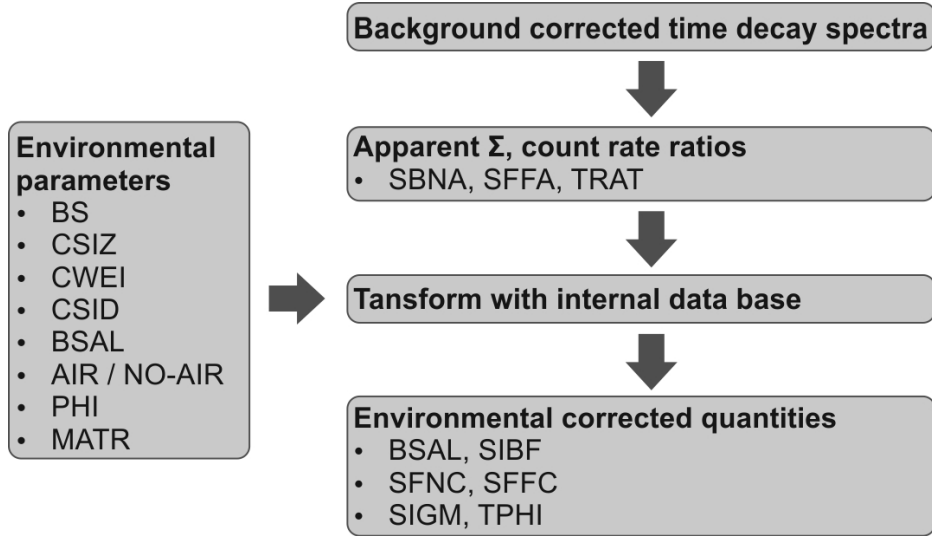


Figure 2.7.: Schematic representation of the RST data processing workflow modified after Plasek et al. (1995).

Schlumberger's PNG tool previous to the RST. This threshold value should not be exceeded for an acceptable neutron porosity (TPHI) determination. Since the formation Σ measurement (derived from far detector only) is much less sensitive to variations in the borehole than the neutron porosity measurement (derived from near and far detector), the intrinsic formation Σ is minor influenced by changing borehole conditions than the intrinsic neutron porosity.

The vertical resolution depends on the tool spacing (distance between source and detectors), the detectors themselves, the time gates and the logging speed (Serra, 1984). The RST vertical resolution is about 15 inch (38.1 cm) for a logging speed of 9 m/min (Schlumberger, 2011). The depth of investigation depends on the formation's Σ value itself and the borehole conditions (Serra, 1984). In general, decreasing formation and borehole Σ (brine/CO₂) increases the possible depth of investigation. The RST depth of investigation is about 10 to 16 inch (25.4 to 40.6 cm) (Schlumberger, 2011). For high gas saturations the depth of investigation for common PNG tools can achieve up to one meter (Knödel et al., 1997).

2.4.2. Data processing to derive intrinsic data

The key environmental effects result from the borehole conditions and neutron diffusion. These effects need to be carefully characterized by the processing algorithm in order transfer the apparent data into the intrinsic data. The processing algorithm is performed in three steps. Figure 2.7 summarizes the RST data processing workflow. In the following, the three processing steps are described in detail based on the description after Plasek et al. (1995).

First, the measured time decay gamma ray spectra is corrected for background gamma rays, especially from the clay content and "hot spot" gamma rays from, for instance, radioactive scale or marker, or activated casing.

The background corrected time decay curves are transferred to four apparent Σ values (SBNA, SBFA, SFNA, SFFA) derived from the two neutron bursts and the two detectors, that are not adjusted to the environmental conditions. Mainly SBNA, derived form the short burst at the near detector, and SFFA, derived from the long burst at the far detector, are used for

2. Theoretical and technical aspects of PNG logging

Table 2.5.: RST apparent Σ values and ratios after Plasek et al. (1995).

Mnemonic	Description	Unit
SBNA	Σ borehole near apparent, short burst near detector	[cu]
SBFA	Σ borehole far apparent, short burst far detector	[cu]
SFNA	Σ formation near apparent, long burst near detector	[cu]
SFFA	Σ formation far apparent, long burst far detector	[cu]
TRAT	Near/far capture ratio	[-]
IRAT	Far/near inelastic ratio	[-]

Table 2.6.: Well completion and lithology parameters for environmental corrections after Plasek et al. (1995).

Mnemonic	Description	Unit
BS	Borehole size	[inch]
CSIZ	Casing size	[inch]
CSID	Casing inner diameter	[inch]
CWEI	Casing weight	[lb/ft]
MATR	sandstone, limestone or dolomite matrix	[-]
AIRB	air or noair filling	[-]
BSAL	Borehole salinity, optional external knowledge	[ppk]
TPHI	Total Porosity, optional external knowledge	[V/V]

the environmental corrected intrinsic data. Moreover, the count rate ratio, TRAT, derived from the counts of the near and far detector is processed (Table 2.5). The use of count rate ratios instead of direct count rates is advantageous, because ratios are independent of a varying neutron output or alteration of the detectors. Therefore, count rate ratios improve pass-to-pass and tool-to-tool repeatability.

The computation of the environmental corrected data is mainly based on these apparent data and the borehole conditions and formation parameters. The borehole is characterized by the borehole size (BS), the well completion parameters casing size (CSIZ), casing inner diameter (CID) casing weight (CWEI) and the type of borehole fluid (air for gas above the brine level, noair and BSAL for liquids below the brine level). The formation is characterized by the total porosity (TPHI) and lithology, where one of the three possible matrices (sandstone, limestone, dolomite) can be defined (Table 2.6).

Based on an extensive measured and partially modeled database, the functionalities between the apparent and intrinsic data are parameterized. The database includes testpilot measurements with four different borehole sizes, three different casing types plus the open hole condition, three different lithologies (sandstone, limestone, dolomite), three different porosities, four different formation fluid salinities, five different borehole fluid salinities and air. All annuli are cemented with class H cement mixed with fresh water. All casings are steel and are centered in the borehole. More than 3870 database points are characterized for the wide range of operation conditions typically encountered in the field.

The tool response, e.g the apparent data, are used to interpolate within the mapped database to determine the intrinsic data. A weighted multiple linear regression (WMLR) procedure is employed for these interpolations to derive the characterizing coefficients. The equation

Table 2.7.: RST intrinsic Σ values and corresponding quantities after Plasek et al. (1995).

Mnemonic	Description	Unit
BSAL	Borehole salinity, absent value for air-filled conditions, equal to external knowledge value when predefined	[ppk]
SIBF	Borehole fluid Σ , absent value for air-filled conditions	[cu]
TPHI	Thermal decay porosity (neutron porosity), equal to external knowledge value when predefined	[V/V]
SFNC	Σ formation near detector	[cu]
SFFC	Σ formation far detector	[cu]
SIGM	Formation Σ	[cu]
DSIG	Σ difference (SFFC-SFNC)	[cu]

system is over-determined with a set of many hundred equations from the large database and only a few unknown coefficients. Moreover, many interpolations cannot readily be cast into direct analytical equations with static coefficients for this multidimensional problem. In addition, the use of static coefficients is often difficult to control when outside the range of the database. Therefore, to overcome these difficulties, the RST algorithm performs a dynamic parameterization technique without static coefficients to improve stability e.g. robustness.

The independent parameters derived from the tool response are mainly SBNA, SFFA and TRAT. The independent parameters derived from the borehole and formation conditions are the BS, CID, the casing thickness and cement sheath thickness, the lithology (sandstone, limestone, dolomite) and the borehole fluid (air, noair). Moreover, the porosity (TPHI) and borehole salinity (BSAL) can be defined by external knowledge when available, or is derived from the processing algorithm when not defined. When TPHI and BSAL are defined, their values are not derived by the processing algorithm.

Based on the forward model, the RST algorithm derives the intrinsic, e.g. environmental corrected data. The intrinsic data are the borehole salinity (BSAL) the corresponding borehole fluid Σ value (SIBF), the thermal decay porosity (TPHI), the intrinsic formation Σ values from the near and far detector (SFNC, SFFC) and the final formation Σ value (SIGM) (Table 2.7). First, BSAL and TPHI are calculated, based on the independent parameters from the tool response and the borehole and formation conditions. Subsequently, SFFC and SFNC are calculated, where in addition to the independent parameters from the tool response and the borehole and formation conditions the BSAL and TPHI values are used as input parameters (Equations 3, 4 and 5 in Plasek et al. (1995)). Therefore, especially the former derived TPHI value influences the subsequent derived SFFC and SFNC values in gas-filled borehole environments. To improve precision, the final formation Σ value (SIGM) is alpha-processed (Galford et al., 1989) from SFFA, the precise value, and SFFC, the accurate correct value.

DSIG, the difference between SFFC and SFNC, is used for log quality control, where SFNC is the near-detector analog to SFFC. DSIG close to zero provides confidence that the defined environmental parameters represent the actual logging conditions. A mismatch between SFFC and SFNC result from complex environmental conditions that are not characterized by the database. These conditions can result from washouts, eccentric casings, cement anomalies, multi casings, tubing, lithologies other than sandstone, limestone or dolomite, or a combination of all of these factors (Plasek et al., 1995). For instance, DSIG is positiv when the true BS is larger than the assumed value (Müller et al., 2007).

3. Mechanisms of saturation changes and resulting issues for PNG saturation models

3.1. Mechanisms of saturation changes

Different mechanisms lead to saturation changes. First, the injected dry CO₂ displaces in-situ pore fluids. The solubility of CO₂ (Spycher et al., 2003; Spycher and Pruess, 2005) in this brine is an important factor controlling saturation state changes. Brine density is increased by dissolving CO₂, increasing the gravity-driven movement of the brine (Ennis-King and Paterson, 2003). Moreover, the dissolved CO₂ in the brine decreases solution pH by forming carbonic acid ($H_2O + CO_2 \rightleftharpoons H^+ + HCO_3^-$), resulting in chemical reactions between brine and the reservoir matrix (Hurter et al., 2007).

Additionally, H₂O is vaporized or dissolved into CO₂. The removed H₂O causes an increase in brine salinity. Upon reaching the solubility limit, removing additional H₂O leads to salt precipitation. This process occurs in the vicinity of injection wells, where large amounts of dry CO₂ enters the reservoir. The amount of salt precipitation, defined by the pore space fraction occupied by precipitate (solid salt saturation, S_{salt}), is limited by the in-situ salt concentration of the brine (e.g. Pruess and Müller, 2009; Pruess, 2009; Zeidouni et al., 2009a,b; Hurter et al., 2007; Muller et al., 2009; Giorgis et al., 2007).

Moreover, gravity forced upflow of CO₂ and capillary forced backflow of brine towards to the injection point can increase the local solid salt saturation above the initial salt concentration. Therefore, in addition to the displacement mechanism, the effects of CO₂ solubility in brine and the action of capillary and gravitational forces affect the changing saturation states (e.g. Pruess and Müller, 2009; Pruess, 2009; Zeidouni et al., 2009a,b; Hurter et al., 2007; Muller et al., 2009; Giorgis et al., 2007). Furthermore, the mutual solubility between brine and CO₂ associated with evaporation and salt precipitation leads to different phases (gaseous, aqueous and solid) of varying compositions (CO₂, H₂O and salt) (Pruess and Müller, 2009; Pruess, 2009; Zeidouni et al., 2009a,b).

3.1.1. Processes, associated phases and resulting regions around an injection well

Pruess (2009) and Zeidouni et al. (2009a) describe the evaporation and salt precipitation process, based on mass balance and fractional flow theory. The analytical models start from the assumptions of a 1-D radial flow geometry in a homogeneous medium with uniform initial conditions. The fractional flow theory (e.g. Buckley and Leverett, 1942) describes the Darcy flow of two immiscible fluids in a homogeneous porous medium. Here, the fluid compressibility, capillary forces and interphase mass transfer are neglected. The amount of salt precipitation is

3. Mechanisms of saturation changes and resulting issues for PNG saturation models

then calculated separately based on the removed water from the aqueous phase. Accordingly, the amount of water in the gas phase is equal to the amount that is removed from the aqueous phase. The results are in excellent agreement with numerical simulations (Pruess, 2009).

Using these assumptions, the model has a similarity property. The analytical solution of this property depends on radial distance r and time t only through the similarity variable r^2/t . Here, a large t correspond to a small r and vice versa. In other words, the solid salt saturation is constant and therefore independent of space and time. The similarity property results in more than one analytical solution (saturation or concentration) at a single location. The ambiguity is resolved by the introduction of two discontinuities known as shocks (Zeidouni et al., 2009a). The two discontinuities in saturation or concentration divides the reservoir in three main regions (Zeidouni et al., 2009a). The dry-out region in the vicinity of the injection well is followed by the equilibrium region and finally the unaffected region. Both discontinuities, first at the transition from the dry-out region to the equilibrium region and second at the transition from the equilibrium region to the unaffected region, reveal the changes in the gaseous and aqueous phase between these three main regions. Overall, the mechanism of saturation changes around an injection well can be described by these five regions including the discontinuities (Zeidouni et al., 2009a). Each region is characterized by co-occurrence of different phases with different components arising from physico-chemical processes during CO_2 injection.

The dry CO_2 stream (gaseous phase) enters the reservoir at the injection point, displacing brine and evaporating water. The evaporation and salt precipitation process results from the transferred amount of water from brine to CO_2 (Pruess, 2009; Zeidouni et al., 2009a). The brine's decreasing water content is associated with salt precipitation when reaching the salt solubility limit. The water containing gaseous phase is then displaced by the fresh injected CO_2 . Therefore, the dry-out region (Figure 3.1, Region 1) is characterized by two phases (gaseous and solid) composed of two components (CO_2 and salt).

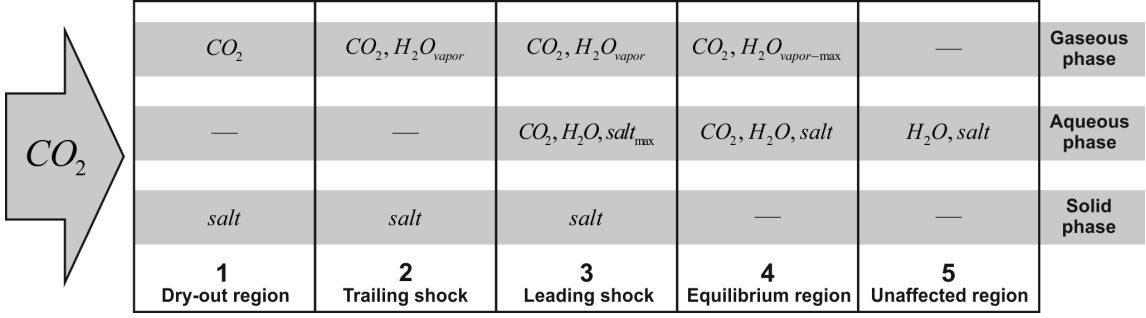
Further downstream, a second region also called trailing shock (Figure 3.1, Region 2) of two phases (gaseous and solid) and three components (CO_2 , H_2O and salt) develops (Zeidouni et al., 2009a). The additional H_2O component is caused from the water containing gaseous phase.

The third region also called leading shock (Figure 3.1, Region 3) contains all three phases (gaseous, aqueous and solid) and components (CO_2 , H_2O and salt) (Zeidouni et al., 2009a). Since both aqueous and solid phase exist together, the aqueous phase is completely salt saturated (salt_{max}). This region can be seen as a boundary between evaporation and salt precipitation further upstream toward the injection point and pure displacement further downstream.

After the third region follows the equilibrium region (Figure 3.1, Region 4), with two phases (gaseous, aqueous) and all three components (CO_2 , H_2O and salt). The gaseous phase is completely water saturated ($\text{H}_2\text{O}_{\text{max}}$), causing an equilibrium between the two phases with no mass transfer. This circumstance implies that no evaporation or salt precipitation can take place, but molecular diffusion driven salinity balance between the displaced salt saturated brine from the third region and the local brine in the equilibrium region takes place.

Downstream of the equilibrium region is the unaffected region (Figure 3.1, Region 5), where brine has not been in contact with the injected CO_2 . Therefore, only the aqueous phase composed of water and salt exist here. The injection front e.g. the spreading of the CO_2 plume (gaseous phase) is at the boundary between the equilibrium and the unaffected region. Figure 3.1 summarizes the regions around an injection well and the corresponding phases and components.

3. Mechanisms of saturation changes and resulting issues for PNG saturation models



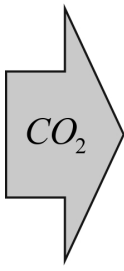
 CO_2	CO_2	CO_2, H_2O_{vapor}	CO_2, H_2O_{vapor}	$CO_2, H_2O_{vapor-max}$	—	Gaseous phase
	—	—	$CO_2, H_2O, salt_{max}$	$CO_2, H_2O, salt$	$H_2O, salt$	Aqueous phase
	$salt$	$salt$	$salt$	—	—	Solid phase
	1 Dry-out region	2 Trailing shock	3 Leading shock	4 Equilibrium region	5 Unaffected region	

Figure 3.1.: Description of regions caused by radial CO_2 brine displacement and evaporation/precipitation mechanisms and the corresponding phases and components around an injection well. Adapted and modified after Zeidouni et al. (2009a).

3.1.2. Influence of reservoir properties and conditions on saturation mechanisms

The main reservoir properties and conditions that affect the injection process and associated saturation mechanisms are pressure, temperature, porosity, permeability and brine salinity (Pruess and Müller, 2009; Pruess, 2009; Zeidouni et al., 2009a,b; Hurter et al., 2007; Muller et al., 2009; Giorgis et al., 2007). These factors define the extent of the different regions around the injection well, as well as the amount of salt precipitation.

The initial reservoir pressure and temperature conditions change depending on injection rate, radial distance to the injection point, reservoir porosity and permeability distribution. In general, the pressure and temperature dependence on the amount of salt precipitation is weak (Pruess, 2009). The pressure effects from injection do not significantly deviate the amount of salt precipitated from the amount precipitated under initial reservoir pressure conditions. The amount of salt precipitation increases almost linearly with the initial brine's salinity. An accurate estimation of S_{salt} can be performed on the basis of initial thermodynamic conditions, without having to perform numerical simulations (Pruess, 2009).

The pore size distribution control the brine's mobility and therefore the porosity fractions for displacement or for evaporation. The mobile brine is displaced in the mobile porosity fraction (ϕ_{eff}) and the immobile brine is evaporated in the immobile porosity fraction (ϕ_{irr}). Both porosity fractions summate to the total porosity ϕ_{tot} .

In addition, the multiphase flow parameters, such as aqueous and gaseous relative permeability are mainly controlled by the aqueous and gaseous phase saturations. With increasing gaseous phase saturation during CO_2 injection, the aqueous relative permeability decreases and the gaseous relative permeability increases. With decreasing aqueous relative permeability, the amount of salt precipitation increases. Thus, with increasing irreducible brine saturation $S_{br_{irr}}$, that in turn controls ϕ_{irr} ($\phi_{irr} = S_{br_{irr}} \cdot \phi_{tot}$), the amount of brine that can be displaced decreases and the fraction of brine that is removed by dissolution into the CO_2 stream increases (Pruess and Müller, 2009; Pruess, 2009; Zeidouni et al., 2009b).

3.1.3. Effect of capillary and gravitational forces on saturation mechanisms

The 1-D analytical model after Pruess (2009) or Zeidouni et al. (2009a) described above (compare 3.1.1) ignore capillary and gravitational forces. If capillary forces are neglected,

the distribution of the different saturation regions and the amount of salt precipitation are independent of the injection rate. Under the assumption of incompressible flow, only the total amount of injected CO₂ causes the saturation distribution (Pruess and Müller, 2009). The following describes the resulting issues on saturation mechanisms caused by the additional capillary and gravitational forces.

Capillary forces result from capillary pressure gradients that generate a driving force for the aqueous phase toward regions with higher gaseous phase saturations. Therefore, regions with a high contrast in aqueous and gaseous phase saturations have large corresponding capillary forces. This leads to a backflow of brine toward the injection front especially in the vicinity of the dry-out region, where capillary pressure gradients are largest. The opposing brine flow carries additional salt load into the dry-out region, which can increase the amount of salt precipitation, when the solubility limit due to evaporation is reached (Pruess and Müller, 2009). Moreover, local reservoir porosity and permeability heterogeneities (local minima) associated with low local CO₂ injection rates support capillary forces. The result is a higher amount of salt precipitation in these heterogeneous locations (Zeidouni et al., 2009a).

Gravitational forces result from density contrast between different phases. In the vicinity of an injection well, viscous forces dominate gravitational forces (Zeidouni et al., 2009a). With increasing distance from the injection front, the influence of gravitational forces become more important. With increasing distance, the lighter gaseous phase accumulates at the top of the reservoir below a natural overburden hydraulic seal. Moreover, CO₂ saturated brine in the equilibrium region or salt saturated brine in region 3 have a greater density than the original local brine. Over the long term, sinking and mixing of these heavier aqueous phases associated with a molecular diffusion driven salinity balance between salt saturated and local brine can be expected (Hurter et al., 2007).

3.1.4. Salt precipitation and its impact on injectivity

As mentioned above, the evaporation of water causes an increase in the brine's salt concentration until the temperature-dependent solubility limit is reached. Upon reaching the salt solubility, further water evaporation leads to salt precipitation. The precipitation of all dissolved NaCl in a brine solution would yield in a NaCl saturation (S_{NaCl}) of

$$S_{NaCl} = \frac{\rho_{br} \cdot X_{NaCl}}{\rho_{NaCl}} = \frac{c_{NaCl}}{\rho_{NaCl} \cdot 1000} \quad (3.1)$$

where ρ_{br} is the brine density in g/cm³, X_{NaCl} is the mass fraction of dissolved NaCl in brine, c_{NaCl} is the NaCl concentration in g/l and ρ_{NaCl} is the NaCl density in g/cm³ (extended after Battistelli et al. (1997)). In general, the solid salt saturation is independent of porosity, since the volume of precipitate is directly proportional to porosity (Pruess and Müller, 2009).

Such salt precipitations associated with CO₂ flooding have already been proven in laboratory experiments (Wang et al., 2009, 2010). Moreover, they have been observed in natural gas storage operations in saline aquifers (Lorentz and Muller, 2003). The precipitation of salt is also known as a possible source of formation damage in gas producing wells (Kleinitz et al., 2001).

The NaCl mass per unit formation volume m_{NaCl} is given by Pruess (2009).

$$m_{NaCl} = \phi_{tot} \cdot S_{NaCl} \cdot \rho_{NaCl} \quad (3.2)$$

3. Mechanisms of saturation changes and resulting issues for PNG saturation models

Therefore, the total porosity ϕ_{tot} is decreased by the halite occupied pore space.

$$\phi = \phi_{tot} \cdot (1 - S_{NaCl}) \quad (3.3)$$

The porosity reduction alone is not sufficient to account for the associated permeability effect. Permeability is also affected by the regions where precipitation occurs. Hence, details of the pore space geometry like the pore size distribution (pore bodies or pore throats) account for the distribution of precipitate and the associated permeability effect (Giorgis et al., 2007; Hurter et al., 2007). Enhanced injectivity can result in low-salinity reservoirs, and an injectivity reduction can occur in high-salinity environments (Hurter et al., 2007).

Many different models exist relating permeability to porosity (Nelson, 1994). Based on the common Kozeny-Carman sphere model (Bolton et al., 1999; Zeidouni et al., 2009a), relative permeability change ($\frac{k}{k_0}$) due to porosity change are described by:

$$\frac{k}{k_0} = \frac{(1 - S_{NaCl})^3}{\left(1 + \frac{\phi_{tot}}{1 - \phi_{tot}} \cdot S_{NaCl}\right)^2} \quad (3.4)$$

Since the amount of salt precipitation depends on the initial brine salinity, an obvious engineering idea is to flush the reservoir with low-salinity brine, or even fresh water, prior to CO₂ injection. In this connection, one should keep in mind that swelling of abundant clay minerals could occur in the reservoir. This swelling can also be associated with injectivity loss (Zeidouni et al., 2009a). In general a preflush delays the precipitation and its total amount (Pruess and Müller, 2009). Another idea is to pre-saturate the injected CO₂ in order to avoid evaporation (Muller et al., 2009). The resulting corrosive character from corbanic acid, however, makes the use of higher steel grades for the affected injection facilities necessary.

3.2. Conventional PNG saturation models

Before CO₂ storage operations were recognized as a tool for managing global climate change, CO₂ floods were already performed in the framework of enhanced oil or gas recovery projects (EOR, EGR). In fact, EOR and EGR operations are becoming increasingly important due to a rising number of nearly depleted oil and gas fields world wide. To get information about sweep efficiency, monitoring of the spreading CO₂ plume associated with saturation changes is necessary. Even during the initial development of EOR/EGR projects, the potential of PNG measurements was already recognized (Charlson et al., 1978). Today, PNG measurements have become indispensable in reservoir monitoring and surveillance. Their application in time-lapse mode (comparing runs at different time steps) gives detailed information about possible changing saturation conditions due to production or injection operations (Morris et al., 2005).

The following chapters 3.2.1 and 3.2.2 describe the conventional saturation model for EOR/EGR and for CO₂ storage operations in saline aquifers. In this context, the conventional saturation models are discussed with respect to the saturation mechanisms. As a result, the additional effects of mutual solubility in the CO₂-H₂O system are analyzed in chapters 3.3 and 3.4.

3.2.1. Saturation model for EOR/EGR operations

The bulk Σ value of a rock formation composed of a matrix and fluid filled pore space is described by its individual volume fractions and the corresponding Σ values (compare chapter 2.2.1).

$$\Sigma_{tot} = \sum_i V_i \cdot \Sigma_i \quad (3.5)$$

The simple volumetric mixing law considers the rock matrix and the fluid filled pore space. Depending on individual reservoir properties and expected saturation changes, individual expansions for multiple matrix (e.g. shale) or fluid (oil, gas, brine) components can be included in the mixing laws (e.g. Serra, 1984; Kimminau and Plasek, 1992; Smolen, 1996). For an EOR or EGR project the baseline run Σ_b before CO₂ injection results from the two phases brine and hydrocarbon

$$\Sigma_b = (1 - \phi_{tot}) \cdot \Sigma_{ma} + \phi_{tot} \cdot [S_{br_b} \cdot \Sigma_{br} + S_{hc_b} \cdot \Sigma_{hc}] \quad (3.6)$$

with

$$S_{br_b} + S_{hc_b} = 1 \quad (3.7)$$

and the repeat run Σ_r with the additional CO₂ phase

$$\Sigma_r = (1 - \phi_{tot}) \cdot \Sigma_{ma} + \phi_{tot} \cdot [S_{br_r} \cdot \Sigma_{br} + S_{hc_r} \cdot \Sigma_{hc} + S_{CO_2r} \cdot \Sigma_{CO_2}] \quad (3.8)$$

with

$$S_{br_r} + S_{hc_r} + S_{CO_2r} = 1 \quad (3.9)$$

where ϕ_{tot} is the total porosity and the subscripts ma, br, hc, and CO₂ correspond to the matrix, brine, hydrocarbon and CO₂ components, respectively (modified after Svor and Globe (1982)). The difference between equation 3.6 and 3.8 results in

$$\Sigma_b - \Sigma_r = \phi_{tot} \cdot [(S_{br_b} - S_{br_r}) \cdot \Sigma_{br} + (S_{hc_b} - S_{hc_r}) \cdot \Sigma_{hc} + S_{CO_2r} \cdot \Sigma_{CO_2}] \quad (3.10)$$

Thus, EOR or EGR operations are characterized by a three-phase system composed of hydrocarbon, brine and CO₂. The effects of mutual solubility between the different phases is generally neglected in EOR operations (Jarrell et al., 2002; Hurter et al., 2007). Thus, a pure displacement process is supposed, where the CO₂ phase can displace the brine and the hydrocarbon phases. The brine and the hydrocarbon phases have different Σ values, except for very low salinity brine and crude oil (Table 2.3). Therefore, the same changes in S_{br_r} or S_{hc_r} results in different Σ_r reading.

Hence, the equation system with the three unknown saturations (S_{br_r} , S_{hc_r} and S_{CO_2r}) is under-determined; different saturation scenarios account for the same Σ_r reading. Thus, a set

3. Mechanisms of saturation changes and resulting issues for PNG saturation models

of logging measurements to distinguish between the three phases is needed for EOR operations (Schwanitz, 1988).

Amadi and Hughes (2008) give an overview about prominent monitoring techniques for the three phase system in EOR operations. The combination of different neutron logging tools are discussed (PNG logging, C/O logging and epithermal neutron porosity). The determination of the different phases is based on their different fluid properties which are analyzed by the combination of these neutron logging tools. The monitoring techniques are based on the assumptions that the fluid properties are constant throughout, and the fluids can be tracked as separate phases. This implies, that viscous forces are dominant, and only displacement processes occur.

The fluid Σ values (Σ_{br} , Σ_{hc} and Σ_{CO_2}), ϕ_{tot} , as well as the initial baseline saturation conditions (S_{br_b} , S_{hc_b}) can be determined from a combination of open-hole logs, core and fluid sample analysis and a baseline run of two selected neutron logging tools. The repeat run after start of CO_2 injection is characterized by two unknown saturations, since the third one results directly from the other two saturations.

3.2.2. Saturation model for CO_2 storage operations in saline aquifers

For a CO_2 storage operation in a saline aquifer, the baseline model before injection results in

$$\Sigma_b = (1 - \phi_{tot}) \cdot \Sigma_{ma} + \phi_{tot} \cdot \Sigma_{br} \quad (3.11)$$

and the repeat model in

$$\Sigma_r = (1 - \phi_{tot}) \cdot \Sigma_{ma} + \phi_{tot} \cdot [S_{br} \cdot \Sigma_{br} + S_{CO_2} \cdot \Sigma_{CO_2}] \quad (3.12)$$

where ϕ_{tot} is the total porosity, and the subscripts ma, br and CO_2 correspond to the matrix, brine and CO_2 components. In contrast to EOR/EGR operations, a saline aquifer is initially characterized by only one phase, because it is completely brine saturated before injection. Thus, assuming a concurrent displacement process, the problem is reduced to a two-phase system. Therefore, S_{CO_2} can be directly calculated from the difference between equation 3.11 and 3.12.

$$S_{CO_2} = 1 - S_{br} = \frac{\Sigma_b - \Sigma_r}{\phi_{tot} (\Sigma_{br} - \Sigma_{CO_2})} \quad (3.13)$$

Similar to EOR or EGR operations, this conventional saturation model based on displacement process only is used for PNG interpretation in different CO_2 storage projects in saline aquifers (Müller et al., 2007; Sakurai et al., 2005; Murray et al., 2010). But in addition to the displacement process, the mutual solubility between brine and CO_2 adds further complex processes like evaporation and salt precipitation (compare chapter 3.1). Until now, the resulting issues from mutual solubility are not considered in PNG saturation models.

The effect of mutual solubility on the aqueous and gaseous phase Σ values is discussed in the following chapter 3.3. Salt precipitation with its large amount of chlorine has a correspondingly large Σ value (compare Table 2.3). This makes PNG measurements suitable for

evaporation and salt precipitation monitoring. The general effect of salt precipitation on PNG measurements, especially from scales, is known (Hashem and Gilchrist, 1994). Chapter 3.4 describes the PNG saturation model that accounts for the evaporation and associated salt precipitation process.

3.3. Effect of mutual solubility on gaseous and aqueous phase Σ values

The aqueous and gaseous phases in the different regions differ in terms of CO_2 and H_2O components. What effect does H_2O and CO_2 partitioning between gaseous and aqueous phase have on the total phase's Σ value?

Spycher et al. (2003) analyzed the mutual solubility from 12 to 100 °C and up to 600 bar in the CO_2 - H_2O system. The H_2O solubility in CO_2 increases with temperature. The pressure dependence is more complicated and depends on the aggregate state of CO_2 , which is also influenced by temperature.

The CO_2 solubility in H_2O decreases with temperature and increases with pressure (Spycher et al., 2003). In fact, the aqueous phase is not pure water but brine; Spycher and Pruess (2005) also analyzed the CO_2 solubility in NaCl-brines. They found that the CO_2 solubility in brine decreases with increasing salinity. To calculate the maximum effect of CO_2 in the aqueous phase on the total Σ phase value, the results from Spycher et al. (2003) for pure water are used.

The following calculation is based on the H_2O mole fraction ($y_{\text{H}_2\text{O}}$) in the gaseous phase (subscript "gp") and the CO_2 mole fraction (y_{CO_2}) in the aqueous phase (subscript "ap") for 35 °C and 101.3 bar after Spycher et al. (2003), which are representative pressure and temperature conditions for CO_2 storage operations in saline aquifers. First the mole fractions are transferred to mass fractions ($m_{\text{H}_2\text{O}}$, m_{CO_2}) using atomic mass from Afeefy et al. (2005). Afterwards the H_2O and CO_2 Σ values are calculated based on capture cross section calculation for molecules (Equation 2.7). The sum of the individual H_2O and CO_2 Σ values results in the total phase Σ values (Σ_{gp} , Σ_{ap}). Table 3.1 summarizes the mole fractions of gaseous and aqueous phase and the corresponding calculated Σ values.

Table 3.1.: CO_2 and H_2O mole fractions (y_{CO_2} , $y_{\text{H}_2\text{O}}$) after Spycher et al. (2003), the corresponding mass fractions ($m_{\text{H}_2\text{O}}$, m_{CO_2}) and Σ values (Σ_{CO_2} , $\Sigma_{\text{H}_2\text{O}}$), as well as the total Σ phase values (Σ_{gp} , Σ_{ap}), for the gaseous and aqueous phase for 35 °C and 101.3 bar. The salt component in the aqueous phase is not taken into account.

Gaseous phase	value	Aqueous phase	value
$y_{\text{H}_2\text{O}}$ [mol/mol _{gp}]	0.00407	y_{CO_2} [mol/mol _{ap}]	0.002288
$m_{\text{H}_2\text{O}}$ [g/g _{gp}]	0.00166	m_{CO_2} [g/g _{ap}]	0.05294
$\Sigma_{\text{H}_2\text{O}}$ [cu]	3.7E-05	Σ_{CO_2} [cu]	3.0E-07
Σ_{CO_2} [cu]	0.037	$\Sigma_{\text{H}_2\text{O}}$ [cu]	22.21
Σ_{gp} [cu]	0.037	Σ_{ap} [cu]	22.21

$\Sigma_{\text{H}_2\text{O}}$ in the gaseous phase is 3.7E-05 cu, and Σ_{CO_2} in the aqueous phase is 3.0E-07 cu. These values are either three or six orders of magnitudes smaller than the values of the individual

main component in each phase. Moreover, these values are significantly smaller than typical precision of PNG tools (0.22 cu; Plasek et al. (1995)). In summary, the influence on PNG measurements from mutual solubility in the gaseous and aqueous phase can be neglected. Or in other words PNG measurements are not suited to distinguish between the H₂O saturated gaseous or CO₂ saturated aqueous phase and pure CO₂ or brine. Thus, the gaseous phase in region one up to region four can be treated equally by assuming pure CO₂. Moreover, the CO₂ component in the aqueous phase can be neglected in region three and four. The salt saturated aqueous phase and the associated precipitated solid phase are discussed separately in the following chapter 3.4.

3.4. Evaporation and salt precipitation saturation model

From the PNG methodologic point of view, both the gaseous and the aqueous phase can be simplified by assuming pure CO₂ or pure brine, because the cumulative effects of all components on the total Σ can be neglected (compare Chapter 3.3). Henceforth, therefore, the term "brine" refers to the aqueous phase and the "CO₂" to the gaseous phase. The following evaporation and salt precipitation saturation model build up is simplified by the following assumptions.

On the one hand, the pressure and temperature effect on the amount of salt precipitation is weak (Pruess, 2009). On the other hand, ρ_{br} and accordingly Σ_{br} depend slightly on pressure and temperature (compare Figure 2.2). For instance, for an injection pressure of five bar greater than the initial reservoir pressure (75 bar), the Σ_{br} increase compared to that value for the initial reservoir pressure is below the typical accuracy of PNG tools. Moreover, the relative effect on Σ_{CO_2} is greater, since the density change of gases is more affected by pressure and temperature (compare Figure 2.1). But the effects of changing temperature and pressure on Σ_{CO_2} , however, are negligible compared to the large effect of Σ_{br} . Therefore, pressure and temperature correspond to the initial reservoir conditions and are assumed to be constant throughout.

The chemical composition of the reservoir brine should generally be well known and is one key parameter for the amount of salt precipitation and the corresponding Σ_{br} value. Capillary and gravitational forces are neglected, but they can increase the amount of salt precipitation. Thus, every solid salt saturation greater than that determined by the initial conditions is a result of these forces.

The following PNG saturation model describes the evaporation and salt precipitation in pure brine only. Thus, porosity is equal to one. The input parameters to derive Σ_{br} are the brine salinity X_{NaCl} and the brine density ρ_{br} that is controlled by the pressure and temperature conditions. To describe the model based on a real-world example the Ketzin site conditions are used ($X_{NaCl} = 0.193$, 35°C, 75 bar, compare Chapter 5.1.2).

Later on, this submodel is included in the bulk saturation model. Chapter 4 discuss the extended PNG saturation model that include both the displacement and evaporation/precipitation fraction weighted by their affected porosity proportions and the rock matrix fraction.

3.4.1. Σ_{br} transformation from a concentration into a saturation based declaration

Σ_{br} for a NaCl-brine is the sum of Σ_{NaCl_c} and $\Sigma_{H_2O_c}$, which are calculated from the water and NaCl concentrations in brine (compare Equation 2.14). As mentioned above (compare Chapter 3.1.4), the precipitation of all dissolved NaCl, S_{NaCl} , results from c_{NaCl} and halite density. Accordingly, based on this boundary condition for complete evaporation, Σ_{NaCl_c} can be also described by the corresponding S_{NaCl} and the halite Σ value Σ_{NaCl} . This gives the following relation for Σ_{NaCl_c}

$$\Sigma_{NaCl_c} = c_{NaCl} \cdot \sigma_{m_{NaCl}} = S_{NaCl} \cdot \Sigma_{NaCl} \quad (3.14)$$

As mentioned in equation 2.10, Σ_{NaCl} for pure halite is:

$$\Sigma_{NaCl} = \sigma_{m_{NaCl}} \cdot \rho_{NaCl} \cdot 1000 \quad (3.15)$$

Therefore, Σ_{NaCl_c} can be alternatively calculated as follows:

$$\Sigma_{NaCl_c} = c_{NaCl} \cdot \sigma_{m_{NaCl}} = S_{NaCl} \cdot \sigma_{m_{NaCl}} \cdot \rho_{NaCl} \cdot 1000 \quad (3.16)$$

Thus, the Σ_{NaCl_c} declaration by the concentration (c_{NaCl}) is equivalent to a saturation declaration (S_{NaCl} and ρ_{NaCl}) when assuming pure halite. From the PNG methodological point of view, it is irrelevant whether the salts are dissolved in brine or precipitated in the pore space, because the original NaCl content e.g. number of NaCl molecules in the pore space remain constant. Therefore, precipitated or dissolved NaCl give the same Σ reading. In other words, brine is alternatively specified by pure water with halite crystals, since this model results in the same Σ reading based on "real" brine with dissolved NaCl e.g. Na^+ cations and Cl^- anions.

Therefore, the concentration based brine Σ values, Σ_{NaCl_c} and $\Sigma_{H_2O_c}$, are described by corresponding volume fractions of a mixture of materials (Serra, 1984). The volume fractions or rather saturations S_{NaCl} and S_{H_2O} are apparent values, because brine is a solution, as opposed to the assumed separated components. Nonetheless, they are helpful alternative values to create a model that could be used to account for evaporation and precipitation processes based on the general PNG mixing law. In addition, the halite density is used for this model, because this value is also true for the boundary condition of complete evaporation (Equation 3.1).

Σ_{br} based on S_{NaCl} and S_{H_2O} results in

$$\begin{aligned} \Sigma_{br} &= \Sigma_{H_2O_c} + \Sigma_{NaCl_c} = S_{H_2O} \cdot \Sigma_{H_2O_{br}} + S_{NaCl} \cdot \Sigma_{NaCl} \\ &= S_{H_2O} \cdot \sigma_{m_{H_2O}} \cdot \rho_{H_2O_{br}} \cdot 1000 + S_{NaCl} \cdot \sigma_{m_{NaCl}} \cdot \rho_{NaCl} \cdot 1000 \end{aligned} \quad (3.17)$$

with Σ_{NaCl} the halite Σ value and $\Sigma_{H_2O_{br}}$ the water Σ value in brine. The subscript "br" in $\Sigma_{H_2O_{br}}$ and $\rho_{H_2O_{br}}$ specifies the relation to brine. The resulting sum of S_{NaCl} and S_{H_2O} must be equal to one in this binary system.

$$1 = S_{H_2O} + S_{NaCl} \quad (3.18)$$

3. Mechanisms of saturation changes and resulting issues for PNG saturation models

Accordingly ρ_{br} , which is defined by Rowe and Chou (1970), results in

$$\rho_{br} = \frac{c_{H_2O} + c_{NaCl}}{1000} = S_{H_2O} \cdot \rho_{H_2O_{br}} + S_{NaCl} \cdot \rho_{NaCl} \quad (3.19)$$

where ρ_{NaCl} correspond to halite density (2.165 g/cm³; e.g. Serra (1984)) and $\rho_{H_2O_{br}}$ to an auxiliary water density in brine. Using the pure water density for the corresponding pressure and temperature conditions (0.997 g/cm³; Rowe and Chou (1970) or Afeefy et al. (2005)) would result in too large S_{H_2O} value; the total saturation would have to be greater than one to reach the known brine density. Since the sum of S_{NaCl} and S_{H_2O} must be equal to one and ρ_{NaCl} corresponds to constant halite density, the auxiliary water density in brine is introduced to account for the brine density. Accordingly S_{NaCl} and S_{H_2O} result in

$$S_{NaCl} = \frac{\Sigma_{NaCl_c}}{\Sigma_{NaCl}} = \frac{\Sigma_{br} - \Sigma_{H_2O_c}}{\Sigma_{NaCl}} = \frac{c_{NaCl} \cdot \sigma_{m_{NaCl}}}{\sigma_{m_{NaCl}} \cdot \rho_{NaCl} \cdot 1000} = \frac{c_{NaCl}}{\rho_{NaCl} \cdot 1000} \quad (3.20)$$

$$S_{H_2O} = \frac{\Sigma_{H_2O_c}}{\Sigma_{H_2O_{br}}} = \frac{\Sigma_{br} - \Sigma_{NaCl_c}}{\Sigma_{H_2O_{br}}} = \frac{c_{H_2O} \cdot \sigma_{m_{H_2O}}}{\sigma_{m_{H_2O}} \cdot \rho_{H_2O_{br}} \cdot 1000} = \frac{c_{H_2O}}{\rho_{H_2O_{br}} \cdot 1000} \quad (3.21)$$

In combination with equations 2.15, 2.16, 3.18, 3.19, 3.20 and 3.21, $\rho_{H_2O_{br}}$ can be specified by the saturations (S_{NaCl} and S_{H_2O}), by the concentrations (c_{H_2O} and c_{NaCl}) or the salinity (X_{NaCl}) and the brine and halite density (ρ_{br} and ρ_{NaCl}).

$$\rho_{H_2O_{br}} = \frac{\rho_{br} - S_{NaCl} \cdot \rho_{NaCl}}{S_{H_2O}} = \frac{c_{H_2O}}{\left(1000 - \frac{c_{NaCl}}{\rho_{NaCl}}\right)} = \frac{\rho_{br} \cdot (1 - X_{NaCl})}{\left(1 - \frac{\rho_{br} \cdot X_{NaCl}}{\rho_{NaCl}}\right)} \quad (3.22)$$

Using $\rho_{H_2O_{br}}$, $\Sigma_{H_2O_{br}}$ accounts also for the brine's density increase with increasing salinity

$$\Sigma_{H_2O_{br}} = \sigma_{m_{H_2O}} \cdot \rho_{H_2O_{br}} \cdot 1000 \quad (3.23)$$

The following figures 3.2 and 3.3 describe $\rho_{H_2O_{br}}$ as a function of the salinity X_{NaCl} , of the saturation ratio S_{NaCl}/S_{H_2O} and the concentration ratio c_{NaCl}/c_{H_2O} . The use of the saturation or concentration ratio is advantageous for the following evaporation/precipitation model build up, because the remaining NaCl content in solution is determined by the remaining water content. Thus, the ratios describe the ability to keep NaCl in solution by the remaining water content.

Figure 3.2 describes $\rho_{H_2O_{br}}$ as a function of X_{NaCl} . $\rho_{H_2O_{br}}$ is equal to pure water density (0.997 g/cm³) for $X_{NaCl} = 0$ and increases with increasing X_{NaCl} . The functionality between $\rho_{H_2O_{br}}$ and X_{NaCl} can be calculated by a fifth degree polynomial with a $R^2=1.000$ where ρ_{br} and ρ_{NaCl} are the input parameters.

3. Mechanisms of saturation changes and resulting issues for PNG saturation models

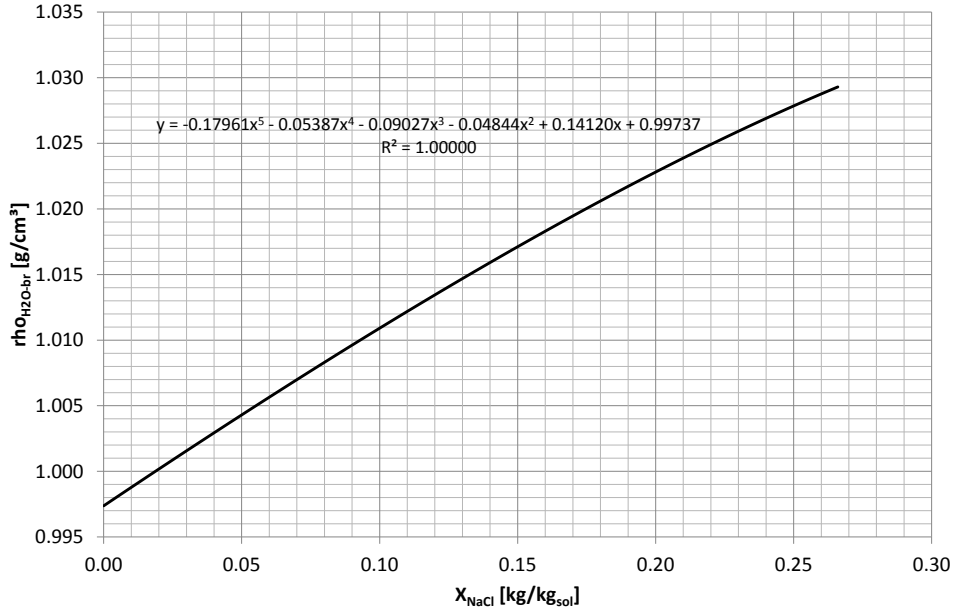


Figure 3.2.: The brines water density $\rho_{H_2O_{br}}$ as a function of X_{NaCl} for 35 °C and 75 bar. The curve is fitted by a fifth degree polynomial.

Figure 3.3 (upper abscissa) describes $\rho_{H_2O_{br}}$ as a function of the ratio S_{NaCl}/S_{H_2O} . $\rho_{H_2O_{br}}$ increases with increasing S_{NaCl}/S_{H_2O} . The functionality between $\rho_{H_2O_{br}}$ and S_{NaCl}/S_{H_2O} is calculated by a fifth degree polynomial with a $R^2=1.000$ where ρ_{br} and ρ_{NaCl} are the input parameters. In the following, this polynomial is called the auxiliary water density function in brine and is used to calculate $\rho_{H_2O_{br}}$ as a function of S_{NaCl}/S_{H_2O} . $\rho_{H_2O_{br}}$ can be also described by the concentration ratio c_{NaCl}/c_{H_2O} (Figure 3.3 , lower abscissa). Also here a fifth degree polynomial fits the curve with a $R^2=1.000$.

The concentrations and saturations depend on each other by the individual component densities ($c_i = S_i \cdot \rho_i \cdot 1000$). As a result of this mass and volume fraction equivalent, all polynomials result in the same $\rho_{H_2O_{br}}$ value. Moreover, all polynomials are only valid for 35°C and 75 bar. Thus, for other pressure and temperature conditions or rather other ρ_{br} the coefficients of the polynomials change.

3. Mechanisms of saturation changes and resulting issues for PNG saturation models

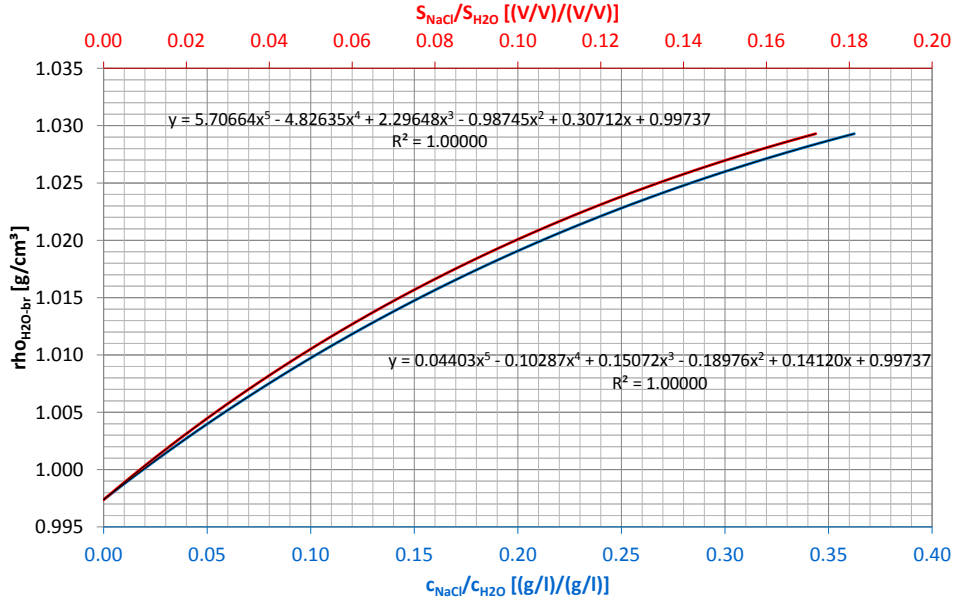


Figure 3.3.: The brines water density $\rho_{H_2O_{br}}$ as a function of S_{NaCl}/S_{H_2O} or c_{NaCl}/c_{H_2O} (upper, lower abscissa) for 35 °C and 75 bar. The curves are fitted by a fifth degree polynomial.

Figure 3.4 illustrates the brine density ρ_{br} after Rowe and Chou (1970), the brine density using the pure water density for the corresponding pressure and temperature conditions $\rho_{br-pure}$ (0.997 g/cm³) and the water density in brine $\rho_{H_2O_{br}}$ as a function of X_{NaCl} for 35 °C and 75 bar. ρ_{br} , $\rho_{br-pure}$ as well as $\rho_{H_2O_{br}}$ are equal to pure water (0.997 g/cm³, $X_{NaCl} = 0$) and increase with increasing salinity. $\rho_{br-pure}$ is always smaller than ρ_{br} , which would imply a too large S_{H_2O} to reach ρ_{br} . The sum of $\rho_{H_2O_{br}}$ and ρ_{NaCl} (2.165 g/cm³) weighted by S_{H_2O} and S_{NaCl} is equal to ρ_{br} after Rowe and Chou (1970) (Equation 3.19). Therefore, the auxiliary water density function in brine accounts for the additional brine density increase that is not taken into account using the pure water density for the corresponding pressure and temperature conditions. The additional brine density increase results from the effect of volume change upon mixing where H₂O and NaCl in solution occupy a less volume than the sum of the volumes of the assumed separated components.

3. Mechanisms of saturation changes and resulting issues for PNG saturation models

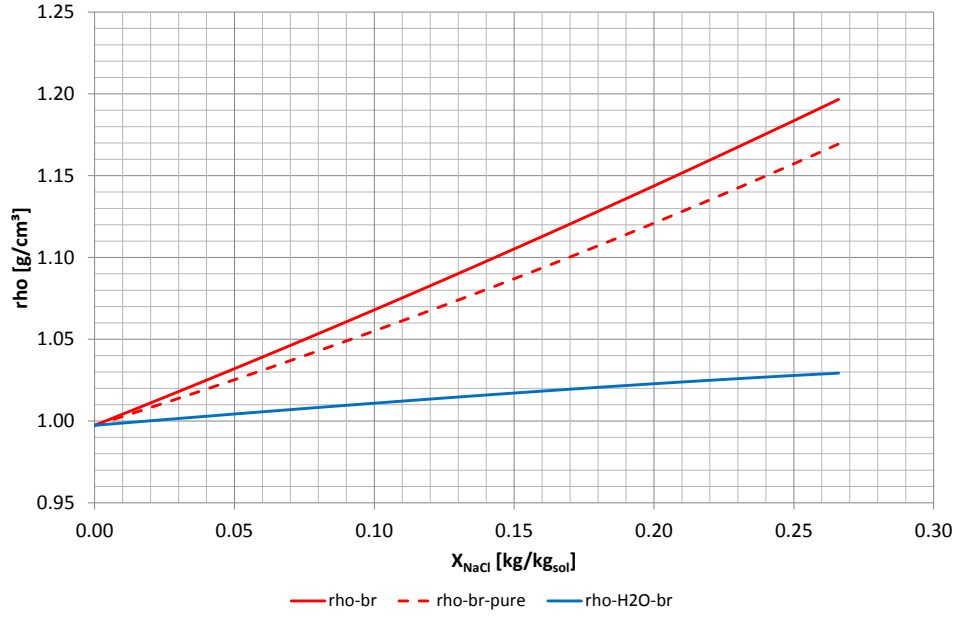


Figure 3.4.: The brine density ρ_{br} after Rowe and Chou (1970), the brine density using the pure water density for the corresponding pressure and temperature conditions $\rho_{br-pure}$ and the water density in brine $\rho_{H_2O_{br}}$ as a function of X_{NaCl} in kg/kg_{sol} for 35 °C and 75 bar. The sum of $\rho_{H_2O_{br}}$ and ρ_{NaCl} weighted by S_{H_2O} and S_{NaCl} is equal to ρ_{br} after Rowe and Chou (1970).

Figure 3.5 summarizes Σ_{br} composed of Σ_{NaCl_c} and $\Sigma_{H_2O_c}$ and the corresponding saturations S_{NaCl} and S_{H_2O} as a function of X_{NaCl} . S_{NaCl} increases with increasing salinity, or rather increasing Σ_{NaCl_c} . Analogous to $\Sigma_{H_2O_c}$ (compare Figure 2.3), S_{H_2O} decreases slightly with increasing salinity. The sum of S_{NaCl} and S_{H_2O} is always one, as defined in equation 3.18.

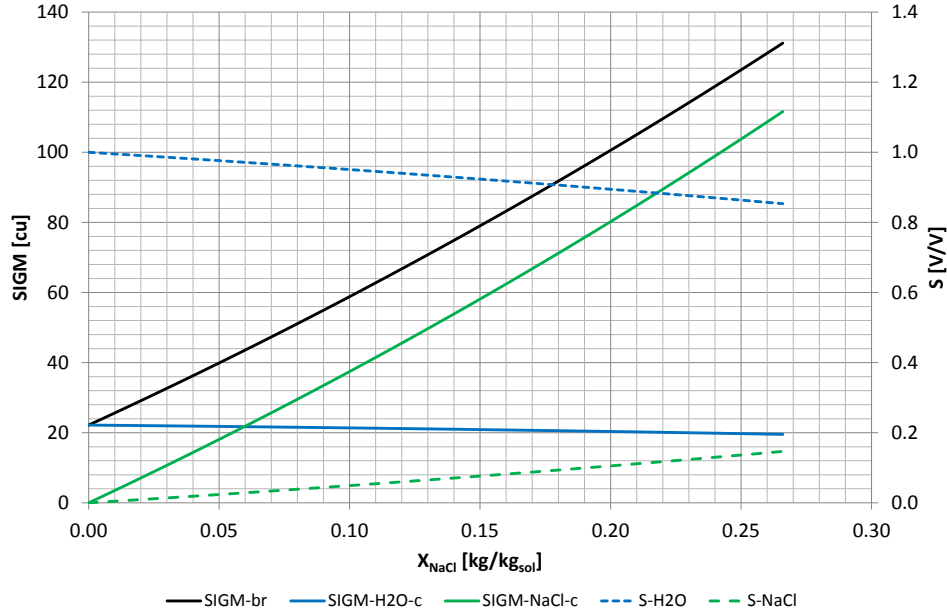


Figure 3.5.: Σ_{br} as a sum of dissolved NaCl (Σ_{NaCl_c}) and water ($\Sigma_{H_2O_c}$) (left ordinate) and the corresponding NaCl (S_{NaCl}) and H₂O (S_{H_2O}) saturations (right ordinate) as a function of the NaCl-salinity X_{NaCl} in kg/kg_{sol} for 35 °C and 75 bar.

3.4.2. Evaporation/precipitation saturation model using the auxiliary water density function in brine

Transferring the concentration based Σ values, Σ_{NaCl_c} and $\Sigma_{H_2O_c}$, into a volume fraction based declaration makes it possible to describe the evaporation/precipitation processes by the aid of the general PNG mixing law. Based on the results from chapter 3.3, the evaporation/precipitation process can be simplified by assuming pure CO₂ or rather pure brine, because the effect on Σ reading, including all components in each phase, can be neglected. The water evaporation results in a "free" volume fraction which is occupied by CO₂. Thus, from the PNG methodological point of view, the evaporation/precipitation process can be described by volume and mass exchange between water and CO₂, combined with a criterion for the NaCl solubility limit to factor in precipitation. The volume and mass depend on each other by the individual component saturations and densities ($c_i = S_i \cdot \rho_i \cdot 1000$), analogous to the NaCl mass per unit formation volume (Pruess, 2009), but with porosity equal to one. The CO₂ and NaCl densities are constant throughout, whereas the auxiliary water density in brine $\rho_{H_2O_{br}}$ increases with increasing salinity due to the effect of volume change upon mixing.

The evaporation/precipitation model is based on a mass and volume fraction equivalent defined by the equations 3.17, 3.18 and 3.19. Based on these concepts, the following describes the evaporation/precipitation model by the aid of saturations, which analogously applies for the concentrations. Figure 3.6 summarizes the initial (baseline) brine saturations as well as the saturations during and after complete evaporation.

3. Mechanisms of saturation changes and resulting issues for PNG saturation models

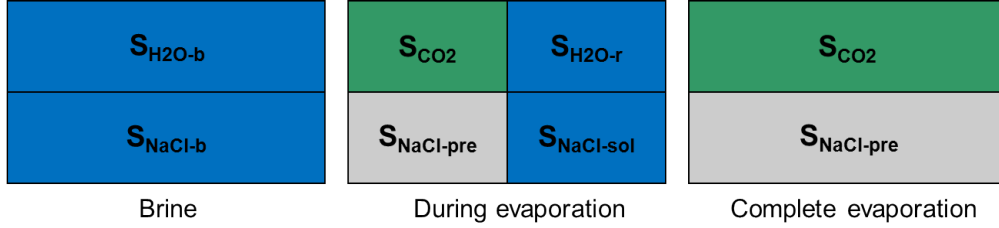


Figure 3.6.: Evaporation/Precipitation model: *Brine*: initially composed of the water $S_{H_2O_b}$ and NaCl S_{NaCl_b} saturations. *During evaporation*: Increasing CO_2 saturation S_{CO_2} accounts for remaining water saturation $S_{H_2O_r}$ which in turn controls the NaCl saturation in solution $S_{NaCl_{sol}}$ and accordingly the precipitated halite saturation $S_{NaCl_{pre}}$. *Complete evaporation*: S_{CO_2} and $S_{NaCl_{pre}}$ reach their maximum, and $S_{H_2O_r}$ and $S_{NaCl_{sol}}$ are equal to zero.

The initial (baseline) water and NaCl saturations, $S_{H_2O_b}$ and S_{NaCl_b} , (Figure 3.6, Brine) are defined by the chemical brine composition and the initial reservoir pressure and temperature conditions. The injected CO_2 stream evaporates the water and takes it away into the reservoir. This transport is associated with a decreasing initial water saturation and an increasing brine salinity. The remaining water saturation $S_{H_2O_r}$ results in

$$S_{H_2O_r} = S_{H_2O_b} - S_{CO_2} \quad (3.24)$$

where S_{CO_2} is the CO_2 saturation. Upon reaching the NaCl solubility limit, further evaporation leads to salt precipitation. The temperature driven NaCl solubility limit $c_{NaCl_{lim}}$ (0.266 kg/kg_{sol} or 318.30 g/l for 35°C, 75 bar) is defined by Potter et al. (1977), and is further used as input parameter for the brine density $\rho_{br_{lim}}$ (1.197 g/cm³) determined after Rowe and Chou (1970). The corresponding maximal Σ brine value, $\Sigma_{br_{lim}}$, is 131.15 cu.

The saturation based NaCl solubility limit $S_{NaCl/H_2O_{lim}}$ is declared by the ratio

$$S_{NaCl/H_2O_{lim}} = \frac{S_{NaCl_{lim}}}{S_{H_2O_{lim}}} \quad (3.25)$$

Accordingly, the concentration based NaCl solubility limit $c_{NaCl/H_2O_{lim}}$ results from

$$c_{NaCl/H_2O_{lim}} = \frac{c_{NaCl_{lim}}}{c_{H_2O_{lim}}} = \frac{S_{NaCl_{lim}} \cdot \rho_{NaCl} \cdot 1000}{S_{H_2O_{lim}} \cdot \rho_{H_2O_{br-lim}} \cdot 1000} \quad (3.26)$$

Here, $\rho_{H_2O_{br-lim}}$ can be calculated with the auxiliary water density functions in brine as a function of $S_{NaCl_{lim}}/S_{H_2O_{lim}}$ or $c_{NaCl/H_2O_{lim}}$. As a result of the mass and volume fraction equivalent, both calculations result in the same value of 1.029 g/cm³. $S_{NaCl/H_2O_{lim}}$ is 0.172 and $c_{NaCl/H_2O_{lim}}$ is 0.362 for these pressure and temperature conditions (35 °C, 75 bar).

During the evaporation process after reaching the solubility limit, both NaCl-saturated brine and precipitated halite exist together. The remaining water saturation $S_{H_2O_r}$ accounts for the dissolved NaCl saturation $S_{NaCl_{sol}}$ and for the precipitated halite saturation $S_{NaCl_{pre}}$ (Figure 3.6, During evaporation). NaCl remains in solution as long as $S_{NaCl/H_2O_{lim}}$ is not exceeded. The following conditional statement describes $S_{NaCl_{sol}}$ by $S_{NaCl/H_2O_{lim}}$ and $S_{H_2O_r}$

3. Mechanisms of saturation changes and resulting issues for PNG saturation models

$$\begin{aligned}
 & \text{IF} && (S_{H_2O_r} \cdot S_{NaCl/H_2O_{lim}} \leq S_{NaCl_b}) && (3.27) \\
 & \text{THEN} && (S_{NaCl_{sol}} = S_{H_2O_r} \cdot S_{NaCl/H_2O_{lim}}) \\
 & \text{ELSE} && (S_{NaCl_{sol}} = S_{NaCl_b})
 \end{aligned}$$

Dissolved plus precipitated NaCl is equal to the initial NaCl saturation.

$$S_{NaCl_b} = S_{NaCl_{sol}} + S_{NaCl_{pre}} \quad (3.28)$$

$S_{NaCl_{pre}}$ results from S_{NaCl_b} and $S_{NaCl_{sol}}$

$$S_{NaCl_{pre}} = S_{NaCl_b} - S_{NaCl_{sol}} \quad (3.29)$$

The brine saturation S_{br} is the sum of $S_{NaCl_{sol}}$ and $S_{H_2O_r}$. After complete evaporation S_{CO_2} and $S_{NaCl_{pre}}$ reach their maximum, and $S_{H_2O_r}$ and $S_{NaCl_{sol}}$ are equal to zero (Figure 3.6, Complete evaporation)

Based on this evaporation/precipitation model, ρ_{br} , $\rho_{H_2O_{br}}$ and $\Sigma_{H_2O_{br}}$ are adjusted by the brine occupied pore space fraction S_{br} . These adjusted parameters for a repeat model during evaporation/precipitation are marked by the subscript "r". Extending equations 3.19, 3.22 and 3.23 by S_{br} , ρ_{br-r} results in:

$$\rho_{br-r} = \frac{c_{H_2O_r} + c_{NaCl_r}}{1000} = \frac{S_{H_2O_r} \cdot \rho_{H_2O_{br-r}} + S_{NaCl_{sol}} \cdot \rho_{NaCl}}{S_{br}} \quad (3.30)$$

$\rho_{H_2O_{br-r}}$ results in

$$\rho_{H_2O_{br-r}} = \frac{S_{br} \cdot \rho_{br-r} - S_{NaCl_{sol}} \cdot \rho_{NaCl}}{S_{H_2O_r}} \quad (3.31)$$

and $\Sigma_{H_2O_{br-r}}$ results in

$$\Sigma_{H_2O_{br-r}} = \sigma_{m_{H_2O}} \cdot \rho_{H_2O_{br-r}} \cdot 1000 \quad (3.32)$$

$S_{H_2O_r}$ and $S_{NaCl_{sol}}$ and the corresponding Σ values can be back transferred to the Σ_{br-r} value for the repeat model.

$$\Sigma_{br-r} = S_{H_2O_r} \cdot \Sigma_{H_2O_{br-r}} + S_{NaCl_{sol}} \cdot \Sigma_{NaCl} \quad (3.33)$$

Thus, Σ_{br-r} summarizes the remaining brine weighted by the water and dissolved NaCl Σ values and their occupied volume fraction. In contrast, Σ_{br-r} divided by the sum of $S_{H_2O_r}$ and $S_{NaCl_{sol}}$ reflects the remaining $\Sigma_{br,r}$ value, which increases until the NaCl solubility limit ($\Sigma_{br_{lim}}$) is reached and is constant throughout.

$$\Sigma_{br,r} = \frac{S_{H_2O_r} \cdot \Sigma_{H_2O_{br-r}} + S_{NaCl_{sol}} \cdot \Sigma_{NaCl}}{S_{H_2O_r} + S_{NaCl_{sol}}} \quad (3.34)$$

3. Mechanisms of saturation changes and resulting issues for PNG saturation models

This model accounts for the evaporation/precipitation process, including the brine density increase with increasing salinity under the assumptions of constant pressure and temperature and neglecting capillary and gravitational forces (no additional salt load). Thus, from the PNG methodological point of view it is possible to describe the dissolved and precipitated NaCl saturations controlled by $S_{H_2O_r}$ based on static thermodynamic conditions.

The baseline model Σ_b before CO₂ injection results in

$$\Sigma_b = \Sigma_{br} = S_{H_2O_b} \cdot \Sigma_{H_2O_{br-b}} + S_{NaCl_b} \cdot \Sigma_{NaCl} \quad (3.35)$$

and the repeat model Σ_r in

$$\begin{aligned} \Sigma_r &= S_{H_2O_r} \cdot \Sigma_{H_2O_{br-r}} + (S_{NaCl_{sol}} + S_{NaCl_{pre}}) \cdot \Sigma_{NaCl} \\ &\quad + (S_{H_2O_b} - S_{H_2O_r}) \cdot \Sigma_{CO_2} \\ &= \Sigma_{H_2O_r} + \Sigma_{NaCl_{sol}} + \Sigma_{NaCl_{pre}} + \Sigma_{CO_2-r} \end{aligned} \quad (3.36)$$

where the subscripts "b" and "r" correspond to the baseline and repeat model. S_{CO_2} is derived from the difference between equation 3.35 and 3.36.

$$S_{CO_2} = S_{H_2O_b} - S_{H_2O_r} = \frac{\Sigma_b - \Sigma_r + S_{H_2O_r} \cdot (\Sigma_{H_2O_{br-r}} - \Sigma_{H_2O_{br-b}})}{\Sigma_{H_2O_{br-b}} - \Sigma_{CO_2}} \quad (3.37)$$

The derivation of the equation 3.37 is given at the end of this chapter. Both salt terms in the baseline and repeat model sum to zero (compare equation 3.28). As mentioned above, the transfer from dissolved NaCl to precipitated halite controlled by $S_{NaCl/H_2O_{lim}}$ is calculated separately.

The additional brine density increase (Figure 3.4) with increasing salinity due to the effect of volume change upon mixing is described by the term $S_{H_2O_r} \cdot (\Sigma_{H_2O_{br-r}} - \Sigma_{H_2O_{br-b}})$. Since this term is not constant, S_{CO_2} can not be calculated directly. But S_{CO_2} and all other resulting saturations can be determined iteratively. The following steps summarize the forward model to solve for the saturations and corresponding Σ values of all components:

1. Transferring the initial (baseline) concentration based brine Σ values (Σ_{NaCl_c} and $\Sigma_{H_2O_c}$) into a volume fraction based declaration (S_{NaCl_b} and $S_{H_2O_b}$) by equation 3.20 and 3.21
2. Determination of the initial (baseline) $\rho_{H_2O_{br-b}}$ by the auxiliary water density function in brine as a function of $S_{NaCl_b}/S_{H_2O_b}$ and adjusting $\Sigma_{H_2O_{br-b}}$ by equation 3.23
3. Determination of all saturations and the corresponding Σ values. The evaporation/precipitation process is defined by equations 3.24, 3.25, 3.27 and 3.28, where $\Sigma_{H_2O_{br-r}}$ is adjusted at each step of increasing S_{CO_2} or rather decreasing $S_{H_2O_r}$ by $\rho_{H_2O_{br-r}}$ as a function of $S_{NaCl_{sol}}/S_{H_2O_r}$. The baseline and repeat models are defined by equations 3.35 and 3.36.

Figure 3.7 and 3.8 summarize the evaporation/precipitation process by the aid of saturations and concentrations. The concentrations specify the component masses per liter. A more detailed description of the individual Σ components is given in figure 3.9.

Intially S_{br} is equal to one, specified by in situ brine salinity as a sum of $S_{H_2O_b}$ and S_{NaCl_b} (Figure 3.7). Increasing S_{CO_2} decreases $S_{H_2O_r}$, as well as S_{br} . $S_{H_2O_r}$ accounts for dissolved

3. Mechanisms of saturation changes and resulting issues for PNG saturation models

NaCl saturation $S_{NaCl_{sol}}$ and precipitated halite saturation $S_{NaCl_{pre}}$. Upon reaching the NaCl solubility limit $S_{NaCl/H_2O_{lim}}$, dissolved NaCl is transferred to precipitated halite leading to an additional decrease in S_{br} . Finally, when all water is evaporated ($S_{br} = S_{H_2O_r} = S_{NaCl_{sol}} = 0$), $S_{NaCl_{pre}}$ is equal to the initial dissolved NaCl saturation S_{NaCl_b} . Therefore, the resulting sum of $S_{NaCl_{pre}}$ and S_{CO_2} is equal to one (Figure 3.7).

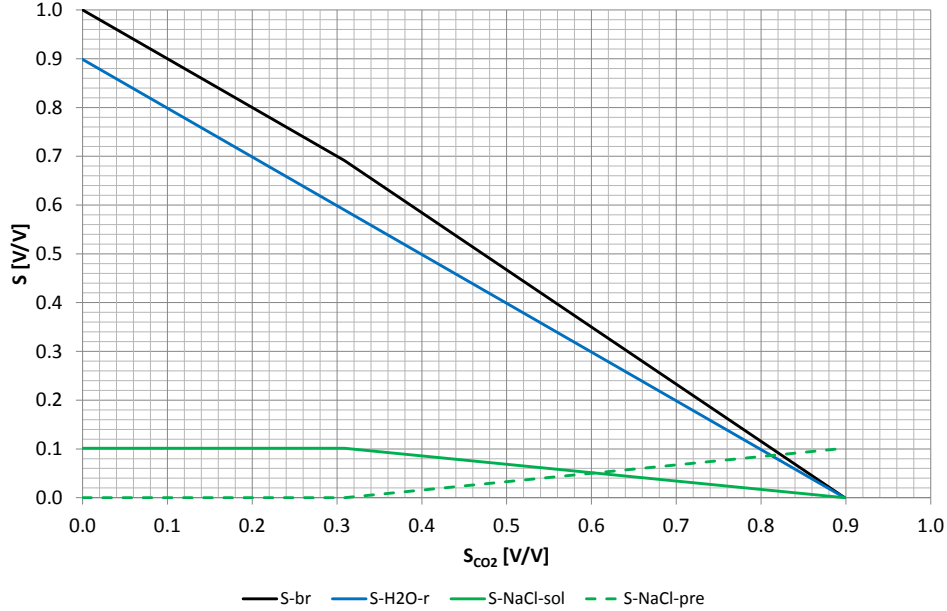


Figure 3.7.: The brine saturation S_{br} , remaining water saturation $S_{H_2O_r}$, dissolved NaCl saturation $S_{NaCl_{sol}}$ and precipitated halite saturation $S_{NaCl_{pre}}$ as a function of S_{CO_2} . The brine saturation S_{br} is the sum of $S_{H_2O_r}$ and $S_{NaCl_{sol}}$.

The concentrations behave similar to saturations (Figure 3.8). Initially c_{br} is equal to the brine density composed of the original water $c_{H_2O_b}$ and dissolved NaCl concentration c_{NaCl_b} . The remaining water concentration $c_{H_2O_r}$ accounts for dissolved NaCl concentration $c_{NaCl_{sol}}$ and precipitated halite concentration $c_{NaCl_{pre}}$, specified by the concentration based NaCl solubility limit $c_{NaCl/H_2O_{lim}}$. Accordingly, after complete evaporation ($c_{br} = c_{H_2O_r} = c_{NaCl_{sol}} = 0$), $c_{NaCl_{pre}}$ is equal to the initial dissolved NaCl concentration $c_{NaCl_{sol}}$.

3. Mechanisms of saturation changes and resulting issues for PNG saturation models

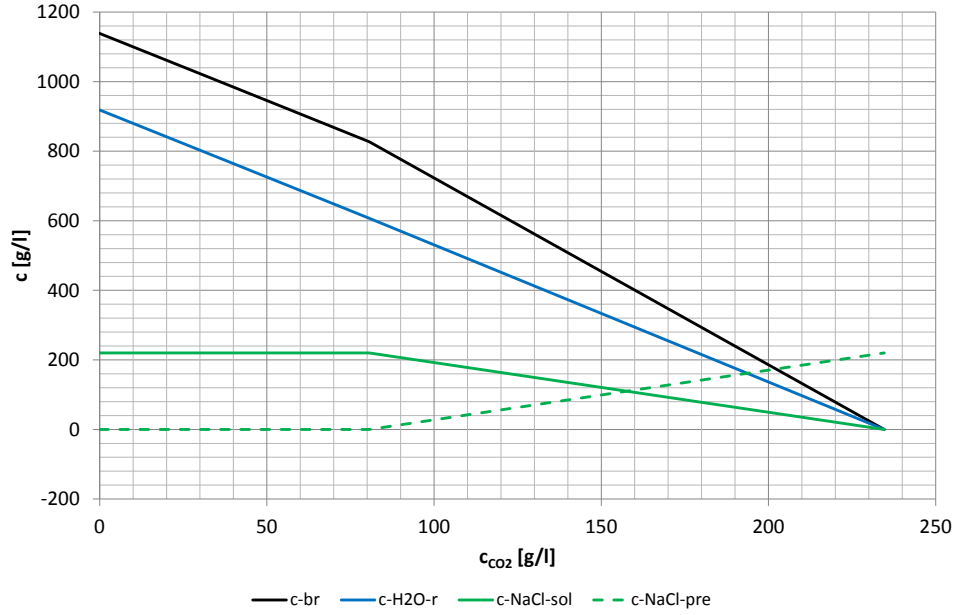


Figure 3.8.: The brine concentration c_{br} , remaining water concentration $c_{H_2O_r}$, dissolved NaCl concentration $c_{NaCl_{sol}}$ and precipitated halite concentration $c_{NaCl_{pre}}$ as a function of the CO_2 concentration c_{CO_2} . The brine concentration c_{br} is the sum of $c_{H_2O_r}$ and $c_{NaCl_{sol}}$.

Figure 3.9 summarizes the individual component Σ values and the resulting repeat Σ_r values as a function of S_{CO_2} . All Σ values are weighted by their occupied volume fractions except $\Sigma_{br,r}$, which is additionally divided by $S_{H_2O_r} + S_{NaCl_{sol}}$. Initially, Σ_r is equal to Σ_{br} , but then decreases with increasing S_{CO_2} . $\Sigma_{H_2O_r}$ decreases with Σ_{CO_2-r} increases. After complete evaporation, $\Sigma_{H_2O_r}$ is equal to zero and Σ_{CO_2} reaches its maximum. The remaining brine Σ_{br-r} , which is the sum of $\Sigma_{NaCl_{sol}}$ and $\Sigma_{H_2O_r}$, decreases with increasing S_{CO_2} and is equal to zero after complete evaporation and precipitation. In contrast, the remaining brine value $\Sigma_{br,r}$ increases with increasing S_{CO_2} . This results from the fact that the brine's volume fraction ($S_{H_2O_r} + S_{NaCl_{sol}}$) decreases with increasing S_{CO_2} . Upon reaching the NaCl solubility limit, $\Sigma_{br,r}$ reaches its maximum (131.15 cu) and is constant throughout. Moreover, upon reaching the NaCl solubility limit, dissolved NaCl is transferred to precipitated halite associated with a transferred Σ_{NaCl} value from solution, $\Sigma_{NaCl_{sol}}$, to precipitation, $\Sigma_{NaCl_{pre}}$. Σ_r is unaffected by this transformation since the total amount of NaCl is constant throughout. Hence, Σ_r changes route from the exchange between water and CO_2 only.

3. Mechanisms of saturation changes and resulting issues for PNG saturation models

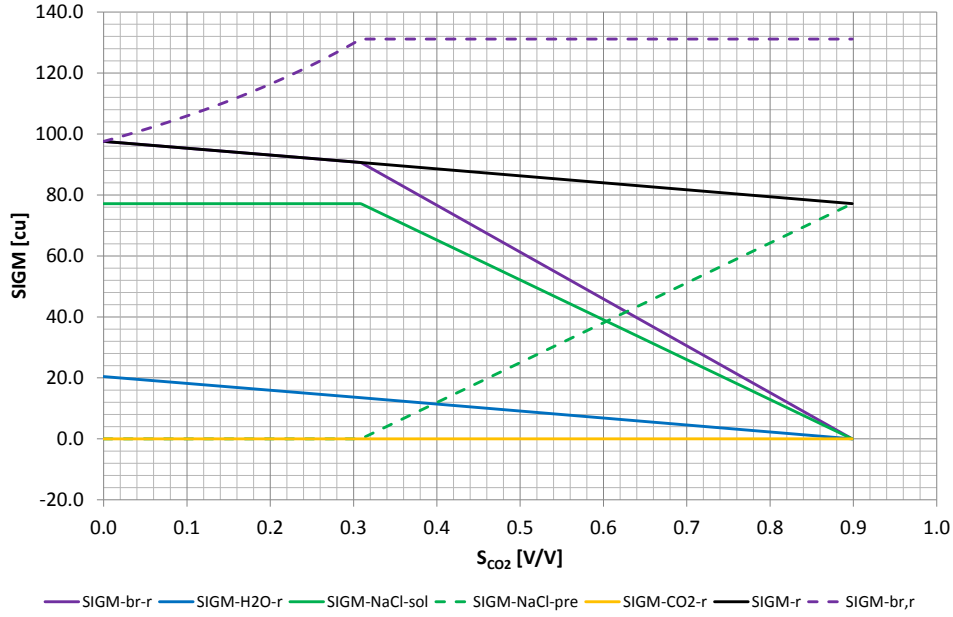


Figure 3.9.: The Σ values of the remaining brine Σ_{br-r} , the remaining water content $\Sigma_{H_2O_r}$, the dissolved NaCl content $\Sigma_{NaCl_{sol}}$, the precipitated halite content $\Sigma_{NaCl_{pre}}$, the CO_2 content Σ_{CO_2-r} and Σ_r as a function of S_{CO_2} . The Σ values are weighted by their occupied volume fractions except $\Sigma_{br,r}$, which is additionally divided by $(S_{H_2O_r} + S_{NaCl_{sol}})$.

Figure 3.10 illustrate the difference between a evaporation/precipitation and a displacement (subscript "dis") model. The displacement process is calculated with equation 3.13 for a porosity equal to one. Initially, the brine saturations (S_{br} and S_{br-dis}) and the total Σ values (Σ_r , Σ_{r-dis}) are equal. Since the total amount of NaCl is constant for the evaporation/precipitation model, Σ_r decreases less than Σ_{r-dis} . After complete evaporation or complete displacement Σ_r is greater than Σ_{r-dis} . The difference between them results from the additional Σ_{NaCl} value transferred from solution, $\Sigma_{NaCl_{sol}}$, to precipitation, $\Sigma_{NaCl_{pre}}$, during evaporation/precipitation. S_{CO_2} is finally equal to one for the displacement process. In contrast, S_{CO_2} is reduced by the occupied precipitated halite fraction, $S_{NaCl_{pre}}$, for the evaporation/precipitation process.

Physically, it is not possible to displace the immobile fluid fraction, but assuming an inverted model where the immobile brine is not evaporated but displaced, S_{CO_2} can be calculated from equation 3.13 with ϕ_{tot} equal to one. An "apparent" S_{CO_2} of 0.209 is calculated opposed to a value of 0.899 using the inverted model for the evaporation/precipitation process (equation 3.37). Therefore, neglecting evaporation/precipitation process results in an erroneous underestimation of S_{CO_2} , since the dissolved NaCl is still remaining as halite in the pore space with a corresponding higher Σ reading compared to a displacement process.

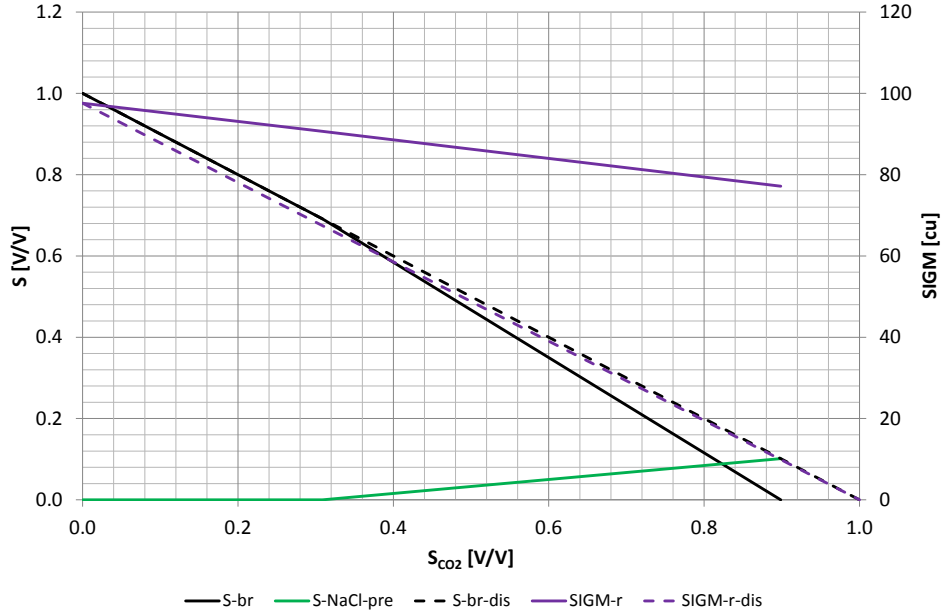


Figure 3.10.: Evaporation/Precipitation model versus displacement model (subscript "dis"): The brine saturations S_{br} , S_{br-dis} , the precipitated halite saturation $S_{NaCl_{pre}}$, (left ordinate) as well as the total Σ values (Σ_r , Σ_{r-dis}) (right ordinate) as a function of S_{CO_2} .

Table 3.2 and 3.3 summarize the parameters for the saturation based brine declaration, the evaporation/precipitation model and the corresponding auxiliary parameters. The saturation based brine declaration (Chapter 3.4.1) is the baseline saturation model marked with the subscript "b" and the evaporation/precipitation model is the repeat model marked with the subscript "r". The column "Remarks" contains the necessary input parameters to calculate each output parameter.

The following chapter 3.4.3 discusses the difference between the evaporation/precipitation model using the auxiliary water density function in brine ($\rho_{H_2O_{br}}$), the constant baseline water density ($\rho_{H_2O_{br-b}}$) and the repeat model. The constant baseline water density would simplify the model by ignoring the effect of volume change upon mixing, because the additional brine density increase with increasing salinity can be neglected, and S_{CO_2} can be calculated directly.

3.4.3. Evaporation/precipitation saturation model using the initial water density in brine only

The above described evaporation/precipitation model uses the auxiliary water density function in brine (Chapter 3.4.2). As mentioned above, using the pure water density for the corresponding pressure and temperature conditions (0.997 g/cm³, Rowe and Chou (1970) or Afeefy et al. (2005)) would result in a total saturation being greater than one in order to reach the known brine density after Rowe and Chou (1970). Therefore, the auxiliary water density in brine was introduced.

From the PNG methodological point of view, the resulting question is: what impact has an assumed constant $\rho_{H_2O_{br-b}}$ on the Σ reading and the estimated saturations? A constant

3. Mechanisms of saturation changes and resulting issues for PNG saturation models

Table 3.2.: Summary of parameters for the saturation based brine declaration (baseline saturation model) and the the evaporation/precipitation model (repeat saturation model).

Mnemonic	Description	Unit	Remarks
Saturation based Σ_{br} declaration, baseline (initial) saturation model			
ρ_{br-b}	baseline ρ brine	[g/cm ³]	c_{NaCl_b} , p, T
Σ_{br}, Σ_b	baseline Σ brine, Σ baseline	[cu]	$S_{NaCl_b}, S_{H_2O_b}$ $\Sigma_{NaCl}, \Sigma_{H_2O_{br-b}}$
S_{NaCl_b}	baseline brine NaCl fraction	[V/V]	c_{NaCl_b}, ρ_{NaCl}
c_{NaCl_b}	baseline brine NaCl concentration	[g/l]	known
ρ_{NaCl}	ρ Halite	[V/V]	2.165 g/cm ³
Σ_{NaCl}	Σ pure NaCl	[cu]	ρ_{NaCl}
$S_{H_2O_b}$	baseline brine H ₂ O fraction	[V/V]	S_{NaCl_b}
$c_{H_2O_b}$	baseline brine H ₂ O concentration	[g/l]	ρ_{br}, c_{NaCl_b}
$\rho_{H_2O_{br-b}}$	baseline ρ water in brine	[g/cm ³]	aux. water density function in brine, $S_{NaCl_b}/S_{H_2O_b}$
$\Sigma_{H_2O_{br-b}}$	baseline Σ water in brine	[cu]	$S_{H_2O_b}, \rho_{H_2O_{br-b}}$
Evaporation/precipitation saturation model, repeat saturation model			
Σ_r	Σ repeat	[cu]	$S_{CO_2}, S_{H_2O_r}, S_{NaCl_{sol}}, S_{NaCl_{pre}}$ $\Sigma_{CO_2}, \Sigma_{H_2O_{br-r}}, \Sigma_{NaCl}$
S_{CO_2}	CO ₂ saturation	[V/V]	increasing
c_{CO_2}	CO ₂ concentration	[g/l]	increasing
Σ_{CO_2}	Σ pure CO ₂	[cu]	p, T
Σ_{CO_2-r}	Σ CO ₂ remaining	[cu]	S_{CO_2}, Σ_{CO_2}
$S_{H_2O_r}$	remaining brine H ₂ O fraction	[V/V]	$S_{H_2O_b}, S_{CO_2}$
$c_{H_2O_r}$	remaining brine H ₂ O concentration	[g/l]	$c_{H_2O_b}, c_{CO_2}$
$\rho_{H_2O_{br-r}}$	ρ water in brine (remaining)	[g/cm ³]	aux. water density function in brine, $S_{NaCl_{sol}}/S_{H_2O_r}$
$\Sigma_{H_2O_{br-r}}$	Σ water in brine value (remaining)	[cu]	$\rho_{H_2O_{br-r}}$
$\Sigma_{H_2O_r}$	Σ water in brine (remaining)	[cu]	$S_{H_2O_r}, \Sigma_{H_2O_{br-r}}$
ρ_{br-r}	ρ brine (remaining)	[g/cm ³]	$c_{NaCl_{sol}}, p, T$
Σ_{br-r}	Σ brine (remaining)	[cu]	$\Sigma_{H_2O_r}, \Sigma_{NaCl_{sol}}$
$\Sigma_{br,r}$	Σ brine value (remaining), divided by the sum of $S_{H_2O_r}$ and $S_{NaCl_{sol}}$	[cu]	$\Sigma_{H_2O_r}, \Sigma_{NaCl_{sol}}$ $S_{H_2O_r}, S_{NaCl_{sol}}$
S_{br}	remaining brine fraction	[V/V]	$S_{H_2O_r}, S_{NaCl_{sol}}$
c_{br}	remaining brine concentration	[g/l]	$c_{H_2O_r}, c_{NaCl_{sol}}$
$S_{NaCl_{sol}}$	brine NaCl fraction in solution	[V/V]	$S_{H_2O_r}, S_{NaCl}/H_2O_{lim}$
$c_{NaCl_{sol}}$	brine NaCl concentration in solution	[g/l]	$c_{H_2O_r}, c_{NaCl}/H_2O_{lim}$
$\Sigma_{NaCl_{sol}}$	Σ NaCl in solution	[cu]	$S_{NaCl_{sol}}, \Sigma_{NaCl}$
$S_{NaCl_{pre}}$	halite precipitation fraction	[V/V]	$S_{NaCl_b}, S_{NaCl_{sol}}$
$c_{NaCl_{pre}}$	halite precipitation concentration	[g/l]	$c_{NaCl_b}, c_{NaCl_{sol}}$
$\Sigma_{NaCl_{pre}}$	Σ halite precipitation	[cu]	$S_{NaCl_{pre}}, \Sigma_{NaCl}$

3. Mechanisms of saturation changes and resulting issues for PNG saturation models

Table 3.3.: Summary of the corresponding auxiliary parameters for the evaporation/precipitation model.

Mnemonic	Description	Unit	Remarks
Auxiliary parameters for the evaporation/precipitation model			
$c_{NaCl_{lim}}$	NaCl concentration limit	[g/l]	Potter et al. (1977), Rowe and Chou (1970)
$\rho_{br_{lim}}$	ρ brine limit	[g/cm ³]	$c_{NaCl_{lim}}$, Rowe and Chou (1970)
$c_{H_2O_{lim}}$	H ₂ O concentration limit	[g/l]	$\rho_{br_{lim}}$, $c_{NaCl_{lim}}$
$c_{NaCl/H_2O_{lim}}$	NaCl solubility limit (conc.)	[(g/l)/(g/l)]	$c_{NaCl_{lim}}$, $c_{H_2O_{lim}}$
$S_{NaCl/H_2O_{lim}}$	NaCl solubility limit (sat.)	[V/V]	$c_{NaCl_{lim}}$, $c_{H_2O_{lim}}$, ρ_{NaCl} , $\rho_{br_{lim}}$
$\rho_{H_2O_{br-lim}}$	ρ water in brine limit	[g/cm ³]	aux. water density function in brine, $S_{NaCl_{lim}}/S_{H_2O_{lim}}$
$\Sigma_{br_{lim}}$	Σ brine, NaCl saturated	[cu]	$c_{NaCl_{lim}}$, $c_{H_2O_{lim}}$

$\rho_{H_2O_{br-b}}$ would simplify the model by assuming two "real" separated components (water and halite), that do not affect each other by their density change in solution due to the effect of volume change upon mixing.

The baseline model before CO₂ injection results in

$$\Sigma_b = S_{H_2O_b} \cdot \Sigma_{H_2O_{br-b}} + S_{NaCl_b} \cdot \Sigma_{NaCl} \quad (3.38)$$

and the repeat model in

$$\Sigma_r = S_{H_2O_r} \cdot \Sigma_{H_2O_{br-b}} + (S_{NaCl_{sol}} + S_{NaCl_{pre}}) \cdot \Sigma_{NaCl} + S_{CO_2} \cdot \Sigma_{CO_2} \quad (3.39)$$

where the repeat $\Sigma_{H_2O_{br}}$ value is calculated with the baseline $\rho_{H_2O_{br-b}}$ value (1.022 g/cm³) also. The pure water density for the corresponding pressure and temperature conditions (0.997 g/cm³, Rowe and Chou (1970) or Afeefy et al. (2005)) is not taken into account, because the initial "real" brine density after Rowe and Chou (1970) is not reached (Equation 3.19). Thus, the mass and volume fraction equivalent fails already for the baseline model using this value.

Similar to the conventional displacement model, S_{CO_2} can be directly calculated from the difference between equation 3.38 and 3.39.

$$S_{CO_2} = S_{H_2O_b} - S_{H_2O_r} = \frac{\Sigma_b - \Sigma_r}{\Sigma_{H_2O_{br-b}} - \Sigma_{CO_2}} \quad (3.40)$$

This results from the fact that the term $S_{H_2O_r} \cdot (\Sigma_{H_2O_{br-r}} - \Sigma_{H_2O_{br-b}})$ from the evaporation/precipitation model with the auxiliary water density function in brine is equal to zero, since $\Sigma_{H_2O_{br-r}}$ and $\Sigma_{H_2O_{br-b}}$ are the same.

3.4.4. Differences between both evaporation/precipitation saturation models

The following section investigates the difference between the evaporation/precipitation model using the auxiliary water density function in brine ($\rho_{H_2O_{br-r}}$) and the constant baseline water density ($\rho_{H_2O_{br-b}}$). Thus, using the auxiliary water density function in brine, $\Sigma_{H_2O_{br-r}}$ is

3. Mechanisms of saturation changes and resulting issues for PNG saturation models

adjusted at each step of increasing S_{CO_2} by $\rho_{H_2O_{br-r}}$ (step three in solving for the saturations and corresponding Σ values of all components). In contrast, using the constant baseline water density, $\Sigma_{H_2O_{br-r}}$ and $\rho_{H_2O_{br-r}}$ are equal to the baseline values.

Both evaporation/precipitation models differ by the additional brine density increase with increasing salinity described by the term $S_{H_2O_r} \cdot (\Sigma_{H_2O_{br-r}} - \Sigma_{H_2O_{br-b}})$. Initially, ($\Sigma_{H_2O_{br-r}} = \Sigma_{H_2O_{br-b}}$), and after complete evaporation, ($S_{H_2O_r} = 0$), this term is equal to zero. Accordingly, both evaporation/precipitation models are initially and after complete evaporation equal. The difference between both models during evaporation is analyzed in detail below.

Figure 3.11 illustrates the differences between the repeat Σ values ($\Delta\Sigma_r$) and the water Σ values in brine ($\Delta\Sigma_{H_2O_{br}}$) from the evaporation/precipitation model using $\rho_{H_2O_{br-r}}$, or rather $\rho_{H_2O_{br-b}}$, as a function of S_{CO_2} . Moreover, $\Delta\rho_{H_2O_{br}}$, the difference between $\rho_{H_2O_{br-r}}$ and $\rho_{H_2O_{br-b}}$, is represented. Additionally, ΔS_{CO_2} , the difference between the S_{CO_2} from the forward model using $\rho_{H_2O_{br-r}}$ and the calculated S_{CO_2} from the inverted model based on $\rho_{H_2O_{br-b}}$ (Equation 3.40) with Σ_r values from $\rho_{H_2O_{br-r}}$ is shown. Accordingly, ΔS_{CO_2} is the error in the calculated S_{CO_2} when using $\rho_{H_2O_{br-b}}$ also for the repeat model.

$\Delta\rho_{H_2O_{br}}$ and $\Delta\Sigma_{H_2O_{br}}$ behave similarly. They increase with increasing S_{CO_2} , reach their maxima when $S_{NaCl/H_2O_{lim}}$ is reached and are constant during further evaporation. $\Delta\rho_{H_2O_{br}}$ results directly from $\rho_{H_2O_{br-r}}$, since $\rho_{H_2O_{br-b}}$ is constant. Since $\Delta\Sigma_{H_2O_{br}}$ is directly controlled by $\Delta\rho_{H_2O_{br}}$, it behaves similar to $\Delta\rho_{H_2O_{br}}$.

As mentioned above, $\Delta\Sigma_r$ and ΔS_{CO_2} are initially and after complete evaporation equal to zero. $\Delta\Sigma_r$ results directly from the product of $S_{H_2O_r}$ and $\Delta\Sigma_{H_2O_{br}}$ ($\Delta\Sigma_{H_2O_{br}} = \Sigma_{H_2O_{br-r}} - \Sigma_{H_2O_{br-b}}$). $S_{H_2O_r}$ decreases continuously with increasing S_{CO_2} . $\Delta\Sigma_{H_2O_{br}}$ increases upon reaching $S_{NaCl/H_2O_{lim}}$ and is constant throughout further evaporation. Therefore, $\Delta\Sigma_r$ increases with increasing S_{CO_2} , reaches its maximum when the NaCl solubility limit is reached and decreases during further evaporation. In fact, ΔS_{CO_2} behaves similarly to $\Delta\Sigma_r$. Thus, using the initial water density in brine only results in a underestimation of S_{CO_2} during the evaporation process.

3. Mechanisms of saturation changes and resulting issues for PNG saturation models

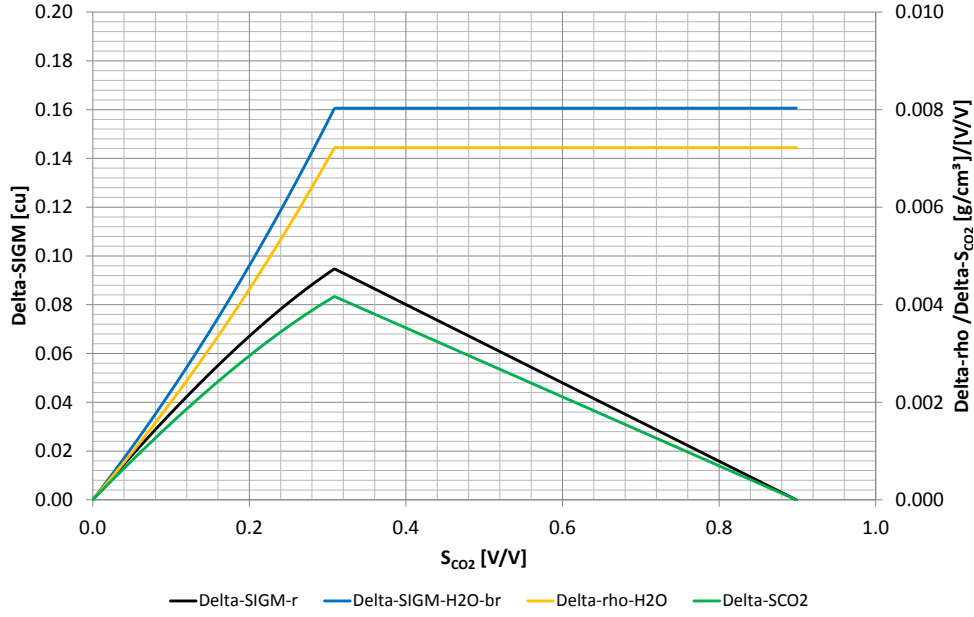


Figure 3.11.: The differences between the repeat Σ values ($\Delta\Sigma_r$) the water Σ values in brine ($\Delta\Sigma_{H_2O_{br}}$) as well as the water density in brine ($\Delta\rho_{H_2O_{br}}$) from the evaporation/precipitation model with the auxiliary water density function in brine ($\rho_{H_2O_{br-r}}$) or rather the constant baseline water density ($\rho_{H_2O_{br-b}}$) as a function of S_{CO_2} . ΔS_{CO_2} , the difference between the corresponding S_{CO_2} from the forward model using $\rho_{H_2O_{br-r}}$ and the calculated S_{CO_2} from the inverted model based on $\rho_{H_2O_{br-b}}$ (Equation 3.40), but using the Σ_r values from $\rho_{H_2O_{br-r}}$, is also shown.

For the Ketzin site conditions ($X_{NaCl} = 0.1933$, 35°C, 75 bar, compare Chapter 5.1), that are used here, the maximum $\Delta\Sigma_r$ results in 0.095 c.u (Figure 3.11) when the NaCl solubility limit is reached. Since this value is smaller than a typical PNG tool's precision (0.22 cu; Plasek et al. (1995)), the simplified evaporation/precipitation model using the initial water density in brine only is also valid for the Ketzin site conditions. The corresponding ΔS_{CO_2} is 0.004 small (Figure 3.11).

In general, as long as $S_{H_2O_r} \cdot \Delta\Sigma_{H_2O_{br}}$ is smaller than the typical PNG tool's precision, the evaporation/precipitation model using $\rho_{H_2O_{br-b}}$ only is valid. The effect of different initial brine salinities on the maximum $\Delta\Sigma_r$ is investigated. $\Delta\Sigma_r$ and the corresponding $\Delta\Sigma_{H_2O_{br}}$ and $S_{H_2O_r}$ values are analyzed as a function of the initial X_{NaCl} in kg/kg_{sol} for 35 °C and 75 bar when the solubility limit is reached. (Figure 3.12).

With increasing initial X_{NaCl} , the solubility limit is reached earlier, e.g. at lower S_{CO_2} . Thus, the remaining water saturation $S_{H_2O_r}$ increase with increasing initial X_{NaCl} (Figure 3.12, right ordinate). For X_{NaCl} close to zero, nearly all water has to be evaporated to reach the solubility limit; in turn $S_{H_2O_r}$ is close to zero. In contrast, $S_{H_2O_r}$ is equal to $S_{H_2O_b}$ for an initial X_{NaCl} equal to the NaCl solubility limit.

$\Sigma_{H_2O_{br-r}}$ reaches a maximum at the solubility limit (22.89 cu) and is then constant throughout. $\Sigma_{H_2O_{br-b}}$ increases with increasing salinity and is equal to $\Sigma_{H_2O_{br-r}}$ at the solubility limit. Therefore, $\Delta\Sigma_{H_2O_{br}}$ decreases with increasing initial X_{NaCl} (Figure 3.12, left ordinate) and is equal to zero for an initial X_{NaCl} equal to the NaCl solubility limit.

3. Mechanisms of saturation changes and resulting issues for PNG saturation models

The product of $S_{H_2O_r}$ and $\Delta\Sigma_{H_2O_{br}}$ result in $\Delta\Sigma_r$. Correspondingly, $\Delta\Sigma_r$ reaches a maximum when this product is at a maximum. The competition between the increasing $S_{H_2O_r}$ and decreasing $\Delta\Sigma_{H_2O_{br}}$ with increasing initial X_{NaCl} result in a maximum $\Delta\Sigma_r$ of 0.12 cu for X_{NaCl} equal to 0.129 kg/kg_{sol}. Thus, $\Delta\Sigma_r$ is always smaller than 0.22 cu.

Therefore, from the PNG methodological point of view, the evaporation/precipitation saturation model using $\rho_{H_2O_{br-b}}$ only is valid for different initial brine salinities for 35 °C and 75 bar. In the following chapter 4, this simplified evaporation/precipitation saturation model is used. Accordingly, the third step in solving for the saturations and corresponding Σ values of all components is simplified, because $\Sigma_{H_2O_{br-r}}$ need not to be adjusted at each step of increasing S_{CO_2} , or rather decreasing $S_{H_2O_r}$, by $\rho_{H_2O_{br-r}}$ as a function of $S_{NaCl_{sol}}/S_{H_2O_r}$.

This simplified model is chemically not correct, because the mass and volume fraction equivalent, as defined by the equations 3.17, 3.18 and 3.19, fails. During evaporation, the brine density, the corresponding Σ_{br} and finally Σ_r and S_{CO_2} are underestimated when $\rho_{H_2O_{br-b}}$ is used only.

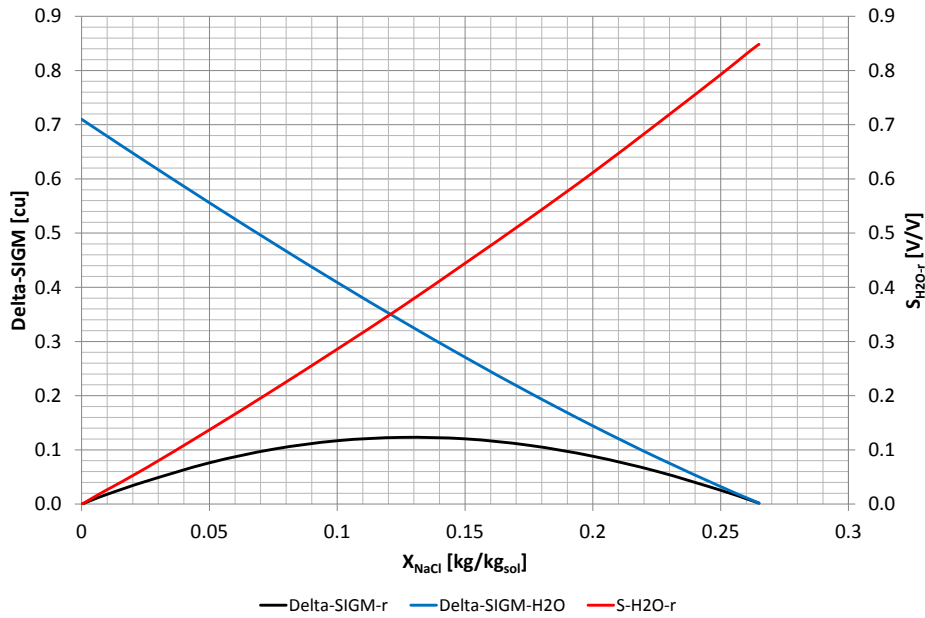


Figure 3.12.: The differences between the repeat Σ values at the saturation limit ($\Delta\Sigma_r$) and the corresponding water Σ value in brine ($\Delta\Sigma_{H_2O_{br}}$) and remaining water saturations ($S_{H_2O_r}$) as a function of the initial X_{NaCl} in kg/kg_{sol} for 35 °C and 75 bar.

Evaporation/precipitation saturation model using the auxiliary water density function in brine

Derivation of equation 3.37

$$\begin{aligned}
 \Sigma_b - \Sigma_r &= S_{H_2O_b} \cdot \Sigma_{H_2O_{br-b}} + S_{NaCl_b} \cdot \Sigma_{NaCl} \\
 &\quad - [S_{H_2O_r} \cdot \Sigma_{H_2O_{br-r}} + (S_{NaCl_{sol}} + S_{NaCl_{pre}}) \cdot \Sigma_{NaCl} + (S_{H_2O_b} - S_{H_2O_r}) \cdot \Sigma_{CO_2}] \\
 \Sigma_b - \Sigma_r &= S_{H_2O_b} \cdot \Sigma_{H_2O_{br-b}} - S_{H_2O_r} \cdot \Sigma_{H_2O_{br-r}} - S_{H_2O_b} \cdot \Sigma_{CO_2} + S_{H_2O_r} \cdot \Sigma_{CO_2} \\
 \Sigma_b - \Sigma_r &= (S_{H_2O_b} - S_{H_2O_r}) \cdot (\Sigma_{H_2O_{br-b}} - \Sigma_{CO_2}) - S_{H_2O_r} \cdot \Sigma_{H_2O_{br-r}} + S_{H_2O_r} \cdot \Sigma_{H_2O_{br-b}} \\
 \Sigma_b - \Sigma_r &= (S_{H_2O_b} - S_{H_2O_r}) \cdot (\Sigma_{H_2O_{br-b}} - \Sigma_{CO_2}) + S_{H_2O_r} \cdot (\Sigma_{H_2O_{br-b}} - \Sigma_{H_2O_{br-r}}) \\
 S_{H_2O_b} - S_{H_2O_r} &= \frac{\Sigma_b - \Sigma_r - S_{H_2O_r} \cdot (\Sigma_{H_2O_{br-b}} - \Sigma_{H_2O_{br-r}})}{\Sigma_{H_2O_{br-b}} - \Sigma_{CO_2}} \\
 S_{CO_2} &= \frac{\Sigma_b - \Sigma_r - S_{H_2O_r} \cdot (\Sigma_{H_2O_{br-b}} - \Sigma_{H_2O_{br-r}})}{\Sigma_{H_2O_{br-b}} - \Sigma_{CO_2}}
 \end{aligned}$$

4. Extended PNG saturation model and resulting issues for time lapse monitoring

Conventional and extended saturation models for saline aquifers are discussed in detail in the following section. The conventional saturation model accounts for displacement processes only, and the extended model additionally includes evaporation/precipitation process. Since these different processes lead to different saturation changes (compare Chapter 3), ϕ_{tot} is divided into fractions occupied by a mobile (ϕ_{eff}) and an immobile (ϕ_{irr}) phase (Figures 4.1 and 4.2), where ϕ_{irr} is defined by the irreducible brine saturation ($\phi_{irr} = S_{br_{irr}} \cdot \phi_{tot}$).

$$\phi_{tot} = \phi_{eff} + \phi_{irr} \quad (4.1)$$

The displacement process takes place in ϕ_{eff} and the evaporation/precipitation process in ϕ_{irr} . The saturation models are based on the general PNG mixing law (Serra, 1984). Thus, they are built up by the volume-weighted share of the individual components of the matrix and the fluids contained in ϕ_{eff} and ϕ_{irr} . Similarly, the total CO₂ saturation $S_{CO_2_{tot}}$ results from the volume weighted sum of the individual CO₂ saturations $S_{CO_2_{eff}}$ and $S_{CO_2_{irr}}$ related to ϕ_{eff} and ϕ_{irr} .

4.1. Limitations of the conventional displacement saturation model

The baseline saturation model Σ_b before injection (Figure 4.1, Baseline) is given by

$$\begin{aligned} \Sigma_b &= (1 - \phi_{tot}) \cdot \Sigma_{ma} + \phi_{eff} \cdot \Sigma_{br} + \phi_{irr} \cdot \Sigma_{br} \\ &= \Sigma_{b_{ma}} + \Sigma_{b_{eff}} + \Sigma_{b_{irr}} \end{aligned} \quad (4.2)$$

where $S_{br_{eff}}$ and $S_{br_{irr}}$ are equal to one. The repeat saturation model Σ_r during injection (Figure 4.1, During displacement and at complete displacement) results in

$$\begin{aligned} \Sigma_r &= (1 - \phi_{tot}) \cdot \Sigma_{ma} + \phi_{eff} \cdot [S_{br_{eff}} \cdot \Sigma_{br} + (1 - S_{br_{eff}}) \cdot \Sigma_{CO_2}] + \phi_{irr} \cdot \Sigma_{br} \\ &= \Sigma_{r_{ma}} + \Sigma_{r_{eff}} + \Sigma_{r_{irr}} \end{aligned} \quad (4.3)$$

The Σ matrix fractions $\Sigma_{b_{ma}}$ and $\Sigma_{r_{ma}}$ are equal since Σ_{ma} is assumed to be non-reactive and is constant throughout. Therefore, $\Sigma_{b_{ma}}$ and $\Sigma_{r_{ma}}$ can be neglected in time lapse mode.

4. Extended PNG saturation model and resulting issues for time lapse monitoring

Moreover Σ_b and Σ_r are divided into the Σ fractions corresponding to ϕ_{eff} ($\Sigma_{b_{eff}}$ and $\Sigma_{r_{eff}}$) and ϕ_{irr} ($\Sigma_{b_{irr}}$ and $\Sigma_{r_{irr}}$). Since only the displacement process occurs, and the immobile fluid proportion $S_{b_{irr}}$ cannot be reduced (Figure 4.1, Complete displacement), $\Sigma_{b_{irr}}$ and $\Sigma_{r_{irr}}$ are equal and constant throughout.

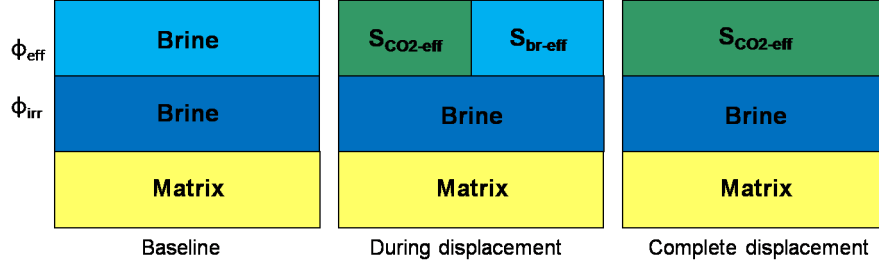


Figure 4.1.: Conventional displacement saturation model: *Baseline*: Before CO₂ injection the formation is fully brine saturated. *During displacement*: The mobile brine (ϕ_{eff}) is displaced by CO₂ and $S_{CO_{2eff}}$ is less than one during displacement. *Complete displacement*: After complete mobile brine displacement $S_{CO_{2eff}}$ is equal to one. The immobile brine (ϕ_{irr}) is unaffected by the displacement process.

The saturation conditions setup as follows

$$S_{CO_{2tot}} = S_{CO_{2eff}} = (1 - S_{br_{eff}}) \cdot \frac{\phi_{eff}}{\phi_{tot}} \quad (4.4)$$

If one starts with pure brine displacement, the difference between Σ_b and Σ_r is the difference between $\Sigma_{b_{eff}}$ and $\Sigma_{r_{eff}}$ only, since all other Σ fractions are equal and constant between baseline and repeat measurements. Therefore, Σ_b and Σ_r need not be divided into the matrix, mobile and immobile Σ fractions since the difference between them results from saturation changes in ϕ_{eff} only.

The relationship between $S_{CO_{2eff}}$ and ϕ_{eff} is obtained by

$$S_{CO_{2eff}} = 1 - S_{br_{eff}} = \frac{\Sigma_{b_{eff}} - \Sigma_{r_{eff}}}{\phi_{eff} (\Sigma_{br} - \Sigma_{CO_2})} = \frac{\Sigma_b - \Sigma_r}{\phi_{eff} (\Sigma_{br} - \Sigma_{CO_2})} \quad (4.5)$$

Accordingly, the total CO₂ saturation $S_{CO_{2tot}}$ related to ϕ_{tot} is the difference between Σ_b and Σ_r .

$$S_{CO_{2tot}} = \frac{\Sigma_b - \Sigma_r}{\phi_{eff} (\Sigma_{br} - \Sigma_{CO_2})} \cdot \frac{\phi_{eff}}{\phi_{tot}} = \frac{\Sigma_b - \Sigma_r}{\phi_{tot} (\Sigma_{br} - \Sigma_{CO_2})} \quad (4.6)$$

Thus, the simple conventional saturation model for CO₂ storage operations in saline aquifers (compare Chapter 3.2.2) without distinction between a mobile and immobile porosity fraction, is valid for a displacement process. This displacement saturation model would give rise to the Buckley and Leverett (1942) saturation profile, where the brine saturation cannot be reduced below the immobile brine saturation (Pruess, 2009). But, a $S_{CO_{2tot}}$ greater than $1 - S_{b_{irr}}$ or a $S_{CO_{2eff}}$ greater than one (boundary conditions) suggests that in addition to the displacement the evaporation/precipitation process is occurring. For this purpose, the extended displacement and evaporation/precipitation saturation model is required.

4.2. Extended displacement and evaporation/precipitation saturation model

In contrast to the conventional model, the extended baseline model includes the water fraction $S_{H_2O_b} \cdot \Sigma_{H_2O_{br-b}}$ and dissolved salt fraction $S_{NaCl_b} \cdot \Sigma_{NaCl}$ in ϕ_{irr} (Figure 4.2, Baseline). Both baseline models, conventional and extended, result in the same Σ_b value. Here, the saturation based Σ_{br} declaration is used to apply the simplified evaporation/precipitation model on the Σ fractions corresponding to ϕ_{irr} .

$$\begin{aligned} \Sigma_b &= (1 - \phi_{tot}) \cdot \Sigma_{ma} + \phi_{eff} \cdot \Sigma_{br} \\ &\quad + \phi_{irr} \cdot (S_{H_2O_b} \cdot \Sigma_{H_2O_{br-b}} + S_{NaCl_b} \cdot \Sigma_{NaCl}) \\ &= \Sigma_{b_{ma}} + \Sigma_{b_{eff}} + \Sigma_{b_{irr}} \end{aligned} \quad (4.7)$$

The simplified evaporation/precipitation model using the initial baseline water density $\rho_{H_2O_{br-b}}$ is used (Chapter 3.4.3). Accordingly, the extended repeat model includes the CO₂ fraction $S_{CO_2irr} \cdot \Sigma_{CO_2}$, the remaining water fraction $S_{H_2O_r} \cdot \Sigma_{H_2O_{br-b}}$ and the dissolved or precipitated salt fractions $(S_{NaCl_{sol}} + S_{NaCl_{pre}}) \cdot \Sigma_{NaCl}$ in ϕ_{irr} (Figure 4.2, During displacement and evaporation/precipitation and at complete displacement and evaporation/precipitation).

$$\begin{aligned} \Sigma_r &= (1 - \phi_{tot}) \cdot \Sigma_{ma} + \phi_{eff} \cdot [S_{br_{eff}} \cdot \Sigma_{br} + (1 - S_{br_{eff}}) \cdot \Sigma_{CO_2}] \\ &\quad + \phi_{irr} \cdot [S_{H_2O_r} \cdot \Sigma_{H_2O_{br-b}} + (S_{NaCl_{sol}} + S_{NaCl_{pre}}) \cdot \Sigma_{NaCl} + (S_{H_2O_b} - S_{H_2O_r}) \cdot \Sigma_{CO_2}] \\ &= \Sigma_{r_{ma}} + \Sigma_{r_{eff}} + \Sigma_{r_{irr}} \end{aligned} \quad (4.8)$$

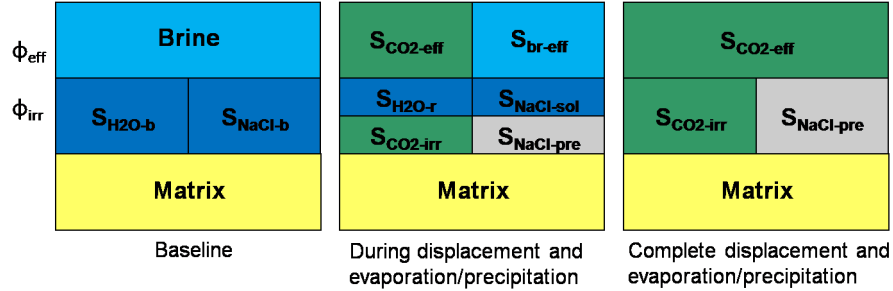


Figure 4.2.: General extended displacement and evaporation/precipitation saturation model: *Baseline*: Before CO₂ injection the formation is fully brine saturated. *During displacement and evaporation/precipitation*: The mobile brine (ϕ_{eff}) is displaced by CO₂ and S_{CO_2eff} is less than one during displacement. Additionally, the immobile brine (ϕ_{irr}) is evaporated associated with salt precipitation when the NaCl solubility limit is reached. *Complete displacement and evaporation/precipitation*: After complete mobile brine displacement S_{CO_2eff} is equal to one. S_{CO_2irr} is reduced by the occupied precipitated halite fraction. $S_{NaCl_{pre}}$ is equal to the initial NaCl saturation in ϕ_{irr} .

4. Extended PNG saturation model and resulting issues for time lapse monitoring

The saturation conditions in ϕ_{eff} and ϕ_{irr} are derived as follows,

$$S_{br_{eff}} + S_{CO_{2eff}} = 1 \quad (4.9)$$

$$S_{H_2O_r} + S_{CO_{2irr}} + S_{NaCl_{sol}} + S_{NaCl_{pre}} = 1 \quad (4.10)$$

where dissolved plus precipitated NaCl is equal to the initial NaCl saturation.

$$S_{NaCl_b} = S_{NaCl_{sol}} + S_{NaCl_{pre}} \quad (4.11)$$

$S_{NaCl_{sol}} \cdot \Sigma_{NaCl}$ and $S_{H_2O_r} \cdot \Sigma_{H_2O_{br-b}}$ can be back transferred to $S_{br_r} = S_{NaCl_{sol}} + S_{H_2O_r}$ and the corresponding Σ brine value $\Sigma_{br,r}$ (Equations 3.33 and 3.34). The total CO_2 saturation $S_{CO_{2tot}}$ is the sum of $S_{CO_{2eff}}$ and $S_{CO_{2irr}}$ weighted by their occupied porosity fractions.

$$\begin{aligned} S_{CO_{2tot}} &= (1 - S_{br_{eff}}) \cdot \frac{\phi_{eff}}{\phi_{tot}} + (S_{H_2O_b} - S_{H_2O_r}) \cdot \frac{\phi_{irr}}{\phi_{tot}} \\ &= S_{CO_{2eff}} \cdot \frac{\phi_{eff}}{\phi_{tot}} + S_{CO_{2irr}} \cdot \frac{\phi_{irr}}{\phi_{tot}} \end{aligned} \quad (4.12)$$

$S_{CO_{2eff}}$ is obtained from equation 4.5 and $S_{CO_{2irr}}$ is related to ϕ_{irr} via the evaporation/precipitation saturation model using the initial water density in brine only (compare Chapter 3.4.3)

$$S_{CO_{2irr}} = S_{H_2O_b} - S_{H_2O_r} = \frac{\Sigma_{b_{irr}} - \Sigma_{r_{irr}}}{\phi_{irr} (\Sigma_{H_2O_{br-b}} - \Sigma_{CO_2})} \quad (4.13)$$

Finally $S_{CO_{2tot}}$ results in

$$\begin{aligned} S_{CO_{2tot}} &= \frac{\Sigma_{b_{eff}} - \Sigma_{r_{eff}}}{\phi_{eff} (\Sigma_{br} - \Sigma_{CO_2})} \cdot \frac{\phi_{eff}}{\phi_{tot}} + \frac{\Sigma_{b_{irr}} - \Sigma_{r_{irr}}}{\phi_{irr} \cdot (\Sigma_{H_2O_{br-b}} - \Sigma_{CO_2})} \cdot \frac{\phi_{irr}}{\phi_{tot}} \\ &= \frac{1}{\phi_{tot}} \cdot \left(\frac{\Sigma_{b_{eff}} - \Sigma_{r_{eff}}}{(\Sigma_{br} - \Sigma_{CO_2})} + \frac{\Sigma_{b_{irr}} - \Sigma_{r_{irr}}}{(\Sigma_{H_2O_{br-b}} - \Sigma_{CO_2})} \right) \end{aligned} \quad (4.14)$$

The Σ fractions corresponding to ϕ_{eff} ($\Sigma_{b_{eff}}$ and $\Sigma_{r_{eff}}$) and ϕ_{irr} ($\Sigma_{b_{irr}}$ and $\Sigma_{r_{irr}}$) can not be distinguished with PNG measurements, but the extended saturation model can be more specified by the rate of the different saturation changing processes, which is discussed in the following chapter 4.3. The external input parameters for the extended PNG saturation model are the total porosity (ϕ_{tot}), the irreducible brine saturation ($S_{br_{irr}}$) and the fluid Σ values (Σ_{br} and Σ_{CO_2}). Table 4.1 summarizes the conventional and extended PNG saturation model parameters including displacement and evaporation/precipitation processes. The parameters for evaporation/precipitation process are based on table 3.2. The column "Remarks" contains the necessary input parameters to calculate each output parameter.

4. Extended PNG saturation model and resulting issues for time lapse monitoring

Table 4.1.: Conventional and extended PNG saturation model parameters including displacement and evaporation/precipitation processes.

Mnemonic	Description	Unit	Remarks
Reservoir and fluid properties			
ϕ_{tot}	total porosity	[V/V]	known
$S_{br_{irr}}$	irreducible brine saturation	[V/V]	known
ϕ_{irr}	immobile/irreducible porosity fraction	[V/V]	$S_{br_{irr}}, \phi_{tot}$
ϕ_{eff}	mobile/effective porosity fraction	[V/V]	ϕ_{irr}, ϕ_{tot}
Σ_{NaCl}	Σ pure NaCl	[cu]	known
Σ_{CO_2}	Σ pure CO ₂	[cu]	known
Σ_{br}	baseline Σ brine	[cu]	known
S_{NaCl_b}	baseline brine NaCl fraction	[V/V]	c_{NaCl_b}, ρ_{NaCl}
$S_{H_2O_b}$	baseline brine H ₂ O fraction	[V/V]	S_{NaCl_b}
$\Sigma_{H_2O_{br-b}}$	baseline Σ water in brine	[cu]	$\rho_{H_2O_{br-b}}$
Baseline saturation model			
Σ_b	baseline Σ total	[cu]	measured
$\Sigma_{b/r_{ma}}$	baseline/repeat Σ matrix fraction	[cu]	irrelevant in time lapse mode, $\phi_{tot}, \Sigma_{br}, \Sigma_b$
Σ_{ma}	Σ matrix	[cu]	irrelevant in time lapse mode, $\phi_{tot}, \Sigma_{b/r_{ma}}$
$\Sigma_{b_{eff}}$	baseline Σ ϕ_{eff} fraction	[cu]	ϕ_{eff}, Σ_{br}
$\Sigma_{b_{irr}}$	baseline Σ ϕ_{irr} fraction	[cu]	$\phi_{irr}, \Sigma_{H_2O_{br-b}}, \Sigma_{NaCl}$ $S_{H_2O_b}, S_{NaCl_b}$
Repeat saturation model			
Σ_r	repeat Σ total	[cu]	measured
$\Sigma_{r_{eff}}$	repeat Σ ϕ_{eff} fraction	[cu]	$\phi_{eff}, \Sigma_{br}, \Sigma_{CO_2}, S_{br_{eff}}, S_{CO_{2eff}}$
$\Sigma_{r_{irr}}$	repeat Σ ϕ_{irr} fraction	[cu]	$\phi_{irr}, \Sigma_{H_2O_{br-b}}, \Sigma_{NaCl}, \Sigma_{CO_2},$ $S_{H_2O_r}, S_{NaCl_{sol}}, S_{NaCl_{pre}}, S_{CO_{2irr}}$
$S_{CO_{2eff}}$	CO ₂ saturation ϕ_{eff} fraction	[V/V]	unknown
$S_{CO_{2irr}}$	CO ₂ saturation ϕ_{irr} fraction	[V/V]	unknown
$S_{CO_{2tot}}$	total CO ₂ saturation	[V/V]	$S_{CO_{2eff}}, S_{CO_{2irr}}$
$S_{br_{eff}}$	brine saturation ϕ_{eff} fraction	[V/V]	$S_{CO_{2eff}}$
$S_{H_2O_r}$	H ₂ O saturation ϕ_{irr} fraction	[V/V]	$S_{H_2O_b}, S_{CO_{2irr}}$
$S_{NaCl_{sol}}$	NaCl saturation in solution ϕ_{irr} fraction	[V/V]	$S_{H_2O_r}, S_{NaCl/H_2O_{lim}}$
$S_{NaCl_{pre}}$	halite saturation ϕ_{irr} fraction	[V/V]	$S_{NaCl_b}, S_{NaCl_{sol}}$
S_{br}	remaining brine fraction	[V/V]	$S_{H_2O_r}, S_{NaCl_{sol}}$
$\Sigma_{br,r}$	Σ brine value (remaining), divided by the sum of $S_{H_2O_r}$ and $S_{NaCl_{sol}}$	[cu]	$\Sigma_{H_2O_r}, \Sigma_{NaCl_{sol}}$ $S_{H_2O_r}, S_{NaCl_{sol}}$

4.3. Resulting issues for time lapse monitoring

Monitoring in time lapse mode implies a baseline run before CO₂ injection but after fluid disturbance in the formation. This fluid disturbance, associated with changing formation brine salinity, can result from a brackish water preflush, performed to minimize salt precipitation. Without a baseline log directly before start of the injection, the actual in situ saturation conditions are not determined, which unavoidably results in additional uncertainties.

Moreover, it is assumed that Σ_{ma} is non-reactive and constant, and any residual systematic errors are also constant (Kimminau and Plasek, 1992). Therefore, repeat measurements after this baseline log indicate Σ changes only when fluid contents have changed, regardless of changing borehole conditions. Borehole conditions can change between baseline and repeat measurements, because the borehole fluid content can change during production or injection processes. These changing borehole conditions (e.g. environmental effects) have to be compensated for by suitable environmental corrections applied to the apparent field Σ data to get the intrinsic Σ data. Generally, the fluid Σ values, ϕ_{tot} , the well completion details and borehole fluids should be well known (Kimminau and Plasek, 1992).

In contrast, stand-alone monitoring from a single log depends on Σ_{ma} even when it is assumed to be constant. A variable Σ_{ma} from changing lithologies will be a major uncertainty in the determination of fluid saturation changes, because Σ_{ma} is usually not well known and is thus a further unknown in the equation system (Kimminau and Plasek, 1992). In the following section only the time-lapse monitoring technique is taken into account.

If Σ_{ma} is assumed to be constant, the Σ matrix fractions Σ_{bma} and Σ_{rma} are equal and can be calculated from the baseline run and the known Σ_{br} and ϕ_{tot} values.

$$\Sigma_{bma} = \Sigma_{rma} = (1 - \phi_{tot}) \cdot \Sigma_{ma} = \Sigma_b - \phi_{tot} \cdot \Sigma_{br} \quad (4.15)$$

Moreover, Σ_{br} , ϕ_{eff} and ϕ_{irr} define the baseline Σ fractions (compare Equations 4.2 and 4.7).

$$\Sigma_b = \Sigma_{bma} + \Sigma_{beff} + \Sigma_{birr} \quad (4.16)$$

The conventional saturation model assumes a displacement process; no determinations are carried out between different porosity fractions with different possible saturation changes. Therefore, S_{CO_2} can be directly calculated from the difference between the baseline and repeat run. As mentioned above, the brine saturation can not be reduced below the irreducible brine saturation, and accordingly S_{CO_2eff} can be at most equal to one; a calculated S_{CO_2eff} greater than one suggests that evaporation is occurring along with displacement (compare Chapter 4.1).

In contrast to the conventional saturation model, the extended saturation model is divided into porosity fractions (ϕ_{eff} and ϕ_{irr}) which are affected by displacement or evaporation/precipitation. The Σ differences between baseline and repeat measurements ($\Sigma_{beff} - \Sigma_{reff}$, $\Sigma_{birr} - \Sigma_{rirr}$) result from different Σ fluid contrasts for displacement or evaporation/precipitation ($\Sigma_{br} - \Sigma_{CO_2}$, $\Sigma_{H_2O_{br-b}} - \Sigma_{CO_2}$). Therefore, different possible saturation changes in ϕ_{eff} or ϕ_{irr} can often be fit to the same Σ_r reading, and different combinations of S_{CO_2eff} and S_{CO_2irr} and their corresponding saturations are possible. But the extended saturation model can be more specified by the rate of the different saturation changing processes.

In general, the displacement and evaporation/precipitation processes occur simultaneously. For evaporation to happen, a relevant volume of dry CO₂ has to enter a brine-saturated rock

volume, thus displacing mobile brine. The dry CO₂ phase then takes up a very small mole fraction of water, in the range of 10⁻³, and the further displacement of the now wet CO₂, replaced by a new volume of dry CO₂, continues the evaporation. At each “cycle” thus the brine saturation decreases, and this effect adds up with the displacement due to the flow through the rock volume. However, the H₂O mass transfer due to mechanical displacement of the brine is one or two magnitude orders larger, at least until the brine approaches the irreducible saturation. After this point, evaporation is the only process further decreasing the brine saturation. In terms of “cycles”, i.e. the replacement of the CO₂ phase volume through dry CO₂, a few dozens suffice to reach approximately the irreducible brine saturation, and from this point on roughly thousand cycles (depending on many factors: salinity, actual irreducible brine saturation for the considered rock, relative permeabilities) are needed to complete the evaporation (Personal communication; De Lucia).

Therefore, it can be assumed at price of a small error that the mobile brine is completely displaced before the relevant evaporation/precipitation process initiates. Accordingly, first the mobile brine (ϕ_{eff}) is displaced by CO₂ and subsequently the immobile water (ϕ_{irr}) is evaporated by CO₂. The salt saturations in ϕ_{irr} ($S_{NaCl_{sol}}$, $S_{NaCl_{pre}}$) are determined from the evaporation/precipitation model, because the transfer from dissolved to precipitated NaCl is controlled by the remaining water content ($S_{H_2O_r}$), and the remaining water content is controlled by $S_{CO_2_{irr}}$.

Therefore, the evaporation/precipitation process simplifies to one unknown saturation ($S_{CO_2_{irr}}$) because the remaining water saturation ($S_{H_2O_r}$) results directly from $S_{CO_2_{irr}}$ and the initial NaCl saturation S_{NaCl_b} remains in the pore space and is transferred from solution to precipitants during the process.

Before the NaCl solubility limit is reached, the evaporation process is characterized by two phases (brine and CO₂). After the NaCl solubility limit is reached, it is characterized by three phases (brine, CO₂ and halite), and after complete evaporation by two phases (CO₂, halite). Since the brine salinity changes during evaporation until the NaCl solubility limit is reached, and complete evaporation can be seen as a special case when $S_{H_2O_r}$ is zero, the complete process can be compared with the three phase system in EOR operations. Here, a set of logging measurements is needed to distinguish between brine, CO₂ and hydrocarbon (Amadi and Hughes, 2008). Therefore, to monitor the evaporation/precipitation process directly, and to avoid ambiguities, additional information is needed.

For instance, when remaining water saturation can be excluded from external knowledge, the evaporation/precipitation process has been completed. But the evaporation/precipitation model would imply remaining water saturation before complete evaporation is reached. Thus, only a Σ fraction of additional precipitated halite can account for the modeled Σ fraction of remaining water saturation, to reach the “real” Σ reading which is greater than the model would imply for complete evaporation. The Σ fraction of the additional precipitated halite is equal to the Σ fraction of remaining water saturation. This additional halite results from back flowed brine towards the injection point (Chapter 3) with subsequent water evaporation. Therefore, the information about the remaining water saturation is required for evaporation/precipitation process. The external knowledge about the remaining water saturation could be derived from induction, NMR or neutron porosity logs. These requirements regarding the well completion and the derived information are discussed in chapter 5.3 for conditions similar to the Ketzin pilot site.

Two preconditions must be met to utilize the displacement and subsequent evaporation/precipitation process. The first precondition to examine is, whether Σ_r is smaller than the

baseline run Σ_b , because every saturation change, whether from displacement or evaporation/precipitation, results in a decreased Σ value compared to the baseline run.

$$\Sigma_r \leq \Sigma_b \quad (4.17)$$

If this precondition is not met, the repeated run is greater than the baseline run. This scenario is discussed in chapter 4.3.2.

The second precondition to examine is, whether Σ_r is greater than or equal to the minimum possible repeat value, when it is assumed that ϕ_{irr} is zero by a constant ϕ_{tot} . Thus ϕ_{irr} is transferred to ϕ_{eff} (complete displacement without evaporation/precipitation).

$$\Sigma_r \geq \Sigma_{bma} + \phi_{tot} \cdot \Sigma_{CO_2} \quad (4.18)$$

If this precondition is not met, the parameters Σ_{br} , Σ_{CO_2} , ϕ_{tot} can be regarded as valid, and the matrix has not changed, then the processed Σ_r data underestimates the "real" Σ reading. For this purpose, changing borehole conditions between baseline and repeat runs, which are not taken into account sufficiently, can account for the underestimation.

The repeat model Σ_{r_m} is marked by the subscript "m" and includes Σ_{reff} , Σ_{rirr} and the constant matrix fraction Σ_{bma} from the baseline model.

$$\Sigma_{r_m} = \Sigma_{bma} + \Sigma_{reff} + \Sigma_{rirr} \quad (4.19)$$

The equations from the extended saturation model are solved analytically, where $S_{CO_{2eff}}$, $S_{CO_{2irr}}$ and the corresponding saturations are calculated to minimize the difference between the modeled (Σ_{r_m}) and measured (Σ_r) repeat data. The following chapter 4.3.1 describes the calculation procedure for the displacement and subsequent evaporation/precipitation process.

4.3.1. Displacement and subsequent evaporation/precipitation model ($\Sigma_r \leq \Sigma_b$)

Figure 4.1 describes the displacement model and figure 4.3 the subsequent evaporation/precipitation model.

As mentioned above, the displacement and subsequent evaporation/precipitation model is applicable when $\Sigma_r \leq \Sigma_b$. First the mobile brine in ϕ_{eff} is displaced (Step 1). After reaching complete displacement (Step 1.1) the evaporation of the immobile water in ϕ_{irr} initiates (Step 2). Finally all water is evaporated (Step 2.1) and the precipitated halite saturation is equal to the initial baseline salt saturation (S_{NaCl_b}).

4. Extended PNG saturation model and resulting issues for time lapse monitoring

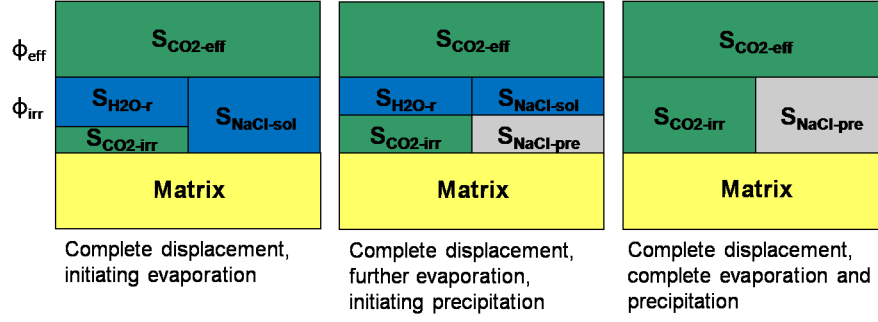


Figure 4.3.: Subsequent extended displacement and evaporation/precipitation saturation model: *Complete displacement, initiating evaporation*: The mobile brine (ϕ_{eff}) is completely displaced and S_{CO2eff} is equal to one. The immobile brine (ϕ_{irr}) evaporation initiates. *Complete displacement, further evaporation, initiating precipitation*: The NaCl solubility limit is reached and precipitation initiates. *Complete displacement and complete evaporation/precipitation*: S_{CO2irr} is reduced by the occupied precipitated halite fraction. $S_{NaClpre}$ is equal to the initial NaCl saturation in ϕ_{irr} .

Step 2.2 and 2.3 describe two cases where special adjustments are applied. If remaining water saturation during the supposed evaporation process (Step2) is excluded, the evaporation/precipitation process has been completed, and additional halite precipitation ($S_{NaClload}$) occurs (Step 2.2). If complete evaporation is reached and Σ_{r_m} is still greater than Σ_r , the affected pore space fraction ϕ_{irr} is probably overestimated (Step 2.3). The difference between the initial estimated ϕ_{irr} and the reduced value is defined by $\Delta\phi$, which describes the porosity fraction transferred from the evaporation/precipitation process ($\phi_{irr} - \Delta\phi$) to the displacement process ($\phi_{eff} + \Delta\phi$). Both calculation steps minimize the difference between Σ_{r_m} and Σ_r within reasonable external knowledge or assumptions regarding the remaining water content and the affected pore space fractions. Thus, both steps are optional. Table 4.2 summarizes the saturation parameters for the different steps of the displacement and subsequent evaporation/precipitation model.

Table 4.2.: Applicable, when $\Sigma_r \leq \Sigma_b$: Saturation parameters for the different steps of the extended saturation model including the displacement and subsequent evaporation/precipitation model. The symbols \uparrow or \downarrow indicate increasing or decreasing during the displacement (1) or evaporation/precipitation process (2). 1.1 and 2.1 describe the completed displacement or evaporation/precipitation process and 2.2* and 2.3* the optional steps.

Step	ϕ_{eff}		ϕ_{irr}			
	S_{CO2eff}	$S_{br_{eff}}$	S_{CO2irr}	S_{H2O_r}	$S_{NaCl_{sol}}$	$S_{NaCl_{pre}}$
1	\uparrow	\downarrow	0	const	const	0
1.1	1	0	0	const	const	0
2	1	0	\uparrow	\downarrow	\downarrow	\uparrow
2.1	1	0	$1 - S_{NaCl_b}$	0	0	S_{NaCl_b}
2.2*	1	0	$1 - S_{NaCl_b} + S_{NaCl_{load}}$	0	0	$S_{NaCl_b} + S_{NaCl_{load}}$
2.3*	1	0	$1 - S_{NaCl_b}$	0	0	S_{NaCl_b}
	$\phi_{eff} + \Delta\phi$		$\phi_{irr} - \Delta\phi$			

Displacement process

First the mobile brine is displaced by CO₂ (Figure 4.1, During displacement; Table 4.2, Step 1) and no evaporation/precipitation is allowed ($\Sigma_{r_{irr}} = \Sigma_{b_{irr}}$). S_{CO_2eff} is obtained from equation 4.5.

S_{CO_2eff} is equal to one for complete displacement (Figure 4.1, Complete displacement; Table 4.2, Step1.1) and $\Sigma_{r_{eff-m}}$ reaches its possible minimum ($\Sigma_{r_{eff-m}} = \phi_{eff} \cdot \Sigma_{CO_2}$). As long as S_{CO_2eff} is smaller or equal to one, only displacement takes place. The modeled repeat run Σ_{r_m} with constant $\Sigma_{b_{ma}}$ and $\Sigma_{b_{irr}}$ from the baseline model is equal to the measured repeat run Σ_r .

$$\Sigma_{r_m} = \Sigma_r = \Sigma_{b_{ma}} + \phi_{eff} \cdot [S_{br_{eff}} \cdot \Sigma_{br} + (1 - S_{br_{eff}}) \cdot \Sigma_{CO_2}] + \Sigma_{b_{irr}} \quad (4.20)$$

Evaporation/Precipitation process

Using equation 4.5, calculated S_{CO_2eff} values greater than one are possible. Hence, S_{CO_2eff} can be at most equal to one, S_{CO_2eff} is set to one. The remaining difference, $\Delta\Sigma_{r_{irr}}$, between the modeled Σ_{r_m} and the measured Σ_r value can only result from the difference between $\Sigma_{b_{irr}}$ and $\Sigma_{r_{irr}}$ described by the evaporation/precipitation model.

$$\Sigma_{r_m} - \Sigma_r = \Delta\Sigma_{r_{irr}} = \Sigma_{b_{irr}} - \Sigma_{r_{irr}} \quad (4.21)$$

$\Sigma_{r_{irr}}$ results in

$$\Sigma_{r_{irr}} = \Sigma_{b_{irr}} - \Delta\Sigma_{r_{irr}} \quad (4.22)$$

If $\Sigma_{r_{irr}} \geq \phi_{irr} \cdot [S_{NaCl_b} \cdot \Sigma_{NaCl} + (1 - S_{NaCl_b}) \cdot \Sigma_{CO_2}]$, the evaporation model can be applied directly (Figure 4.3, Complete displacement and initiating evaporation; Table 4.2, Step 2). $\Sigma_{r_{irr}}$ is described by equation 4.8 and S_{CO_2irr} is calculated from equation 4.13.

The corresponding NaCl saturations, $S_{NaCl_{sol}}$ and $S_{NaCl_{pre}}$, are determined from $S_{H_2O_r}$ based on the evaporation/precipitation model. After the solubility limit is reached, the corresponding brine salinity reaches its maximum and precipitation occurs. For complete evaporation, S_{CO_2irr} is equal to $S_{H_2O_b}$, and $S_{H_2O_r}$ is equal to zero (Figure 4.3, Complete displacement and complete evaporation; Table 4.2, Step 2.1).

The modeled repeat run Σ_{r_m} is equal to the measured repeat run Σ_r .

$$\begin{aligned} \Sigma_{r_m} = \Sigma_r = & \Sigma_{b_{ma}} + \phi_{eff} \cdot \Sigma_{CO_2} \\ & + \phi_{irr} \cdot [S_{H_2O_r} \cdot \Sigma_{H_2O_{br-b}} + (S_{NaCl_{sol}} + S_{NaCl_{pre}}) \cdot \Sigma_{NaCl} + (S_{H_2O_b} - S_{H_2O_r}) \cdot \Sigma_{CO_2}] \end{aligned} \quad (4.23)$$

During the supposed evaporation process, $\Sigma_{r_{irr}}$ includes the remaining water Σ fraction ($S_{H_2O_r} \cdot \Sigma_{H_2O_{br-b}}$). But when remaining water saturation can be excluded, the evaporation/precipitation process has been completed, and additional halite precipitation ($S_{NaCl_{load}}$) occurs (Table 4.2, Step 2.2). The Σ fraction from additional salt load ($S_{NaCl_{load}} \cdot \Sigma_{NaCl}$) is then equal to the remaining water Σ fraction ($S_{H_2O_r} \cdot \Sigma_{H_2O_{br-b}}$). Thus, $\Sigma_{r_{irr}}$ results in

$$\Sigma_{r_{irr}} = \phi_{irr} \cdot [(S_{NaCl_b} + S_{NaCl_{load}}) \cdot \Sigma_{NaCl} + (1 - S_{NaCl_b} - S_{NaCl_{load}}) \cdot \Sigma_{CO_2}] \quad (4.24)$$

4. Extended PNG saturation model and resulting issues for time lapse monitoring

Solved for $S_{NaCl_{load}}$:

$$S_{NaCl_{load}} = \frac{S_{H_2O_r} \cdot \Sigma_{H_2O_{br-b}} - (1 - S_{CO_2} - S_{NaCl_b}) \cdot \Sigma_{CO_2}}{(\Sigma_{NaCl} - \Sigma_{CO_2})} \quad (4.25)$$

If $\Sigma_{r_{irr}} < \phi_{irr} \cdot [S_{NaCl_b} \cdot \Sigma_{NaCl} + (1 - S_{NaCl_b}) \cdot \Sigma_{CO_2}]$, the minimum $\Sigma_{r_{irr}}$ value is reached, but the affected pore space fraction ϕ_{irr} is probably overestimated (Figure 4.3, Complete displacement and complete evaporation/precipitation; Table 4.2, Step 2.3).

Therefore, ϕ_{eff} and ϕ_{irr} are adjusted within the limit of ϕ_{tot} ($\phi_{tot} = \phi_{eff} + \phi_{irr}$). The difference between the initial estimated ϕ_{irr} and the reduced value is defined by $\Delta\phi$, which describes the porosity fraction transferred from the evaporation/precipitation process ($\phi_{irr} - \Delta\phi$) to the displacement process ($\phi_{eff} + \Delta\phi$). Since the displacement and evaporation/precipitation process have been completed, $S_{CO_{2eff}}$ is equal to one and $S_{CO_{2irr}}$ is $1 - S_{NaCl_b} \cdot \Sigma_{r_{irr}}$ adjusted by $\Delta\phi$ results from

$$\Sigma_{r_{irr}} = \Delta\phi \cdot \Sigma_{CO_2} + (\phi_{irr} - \Delta\phi) \cdot [S_{NaCl_b} \cdot \Sigma_{NaCl} + (1 - S_{NaCl_b}) \cdot \Sigma_{CO_2}] \quad (4.26)$$

Solved for $\Delta\phi$:

$$\Delta\phi = \frac{\phi_{irr} \cdot [S_{NaCl_b} \cdot \Sigma_{NaCl} + (1 - S_{NaCl_b}) \cdot \Sigma_{CO_2}] - \Sigma_{r_{irr}}}{[S_{NaCl_b} \cdot \Sigma_{NaCl} + (1 - S_{NaCl_b}) \cdot \Sigma_{CO_2}] - \Sigma_{CO_2}} \quad (4.27)$$

$\Delta\phi$ is always smaller or equal to ϕ_{irr} . For $\Delta\phi$ equal to ϕ_{irr} , no evaporation occurs and all brine in the complete pore space ϕ_{tot} is displaced. The modeled repeat run, Σ_{r_m} , is equal to the measured repeat run Σ_r , and results in

$$\Sigma_{r_m} = \Sigma_r = \Sigma_{b_{ma}} + (\phi_{eff} + \Delta\phi) \cdot \Sigma_{CO_2} + (\phi_{irr} - \Delta\phi) \cdot [S_{NaCl_b} \cdot \Sigma_{NaCl} + (1 - S_{NaCl_b}) \cdot \Sigma_{CO_2}] \quad (4.28)$$

The flow-chart in figure 4.4 summarizes the calculation steps for the displacement and subsequent evaporation/precipitation model.

4. Extended PNG saturation model and resulting issues for time lapse monitoring

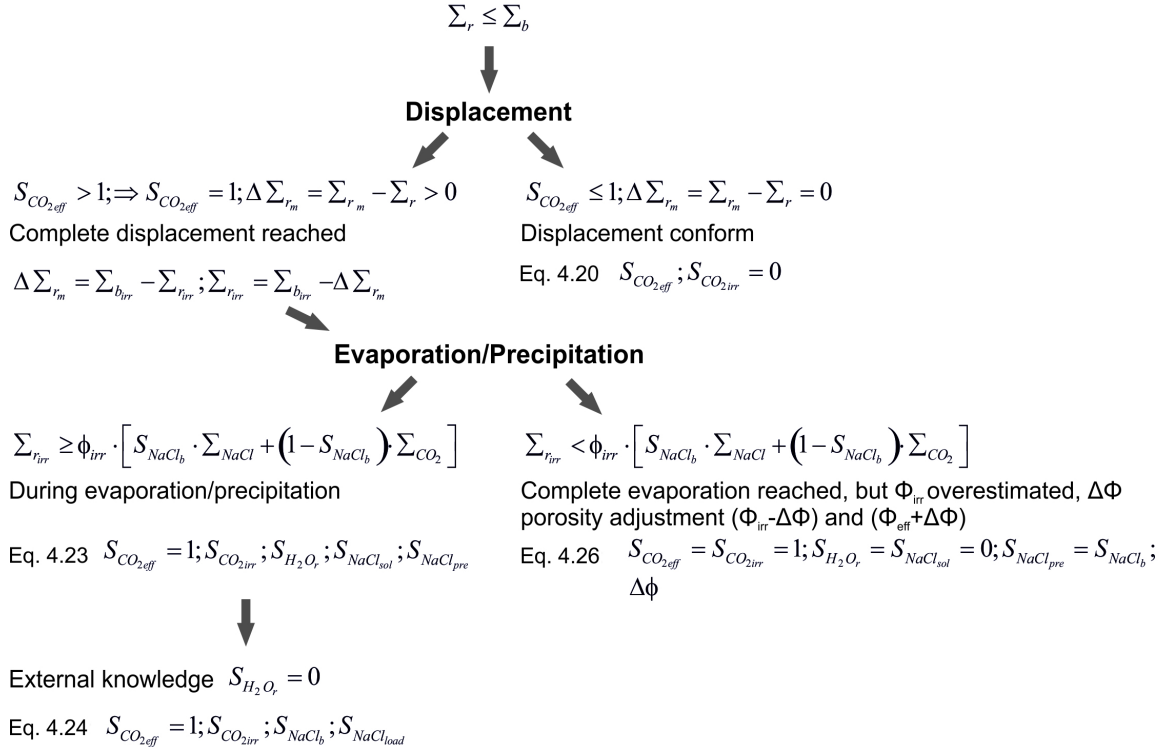


Figure 4.4.: Summarizing flow-chart for the displacement and subsequent evaporation/precipitation model.

4.3.2. Σ_r greater than Σ_b , increased Σ pore fluid value

If $\Sigma_r > \Sigma_b$, the pore fluid Σ value increases. Based on monitoring results at the Ketzin site, this situation occurs below the brine level, especially in the vicinity of the brine level, for the original formation brine salinity. Moreover, this situation occurs below and above the brine level, when the lower KCl-flush brine salinity is taken into account (Chapter 5.3.1.2).

Capillary effects result in counter imbibitions of brine towards the injection point and increase the initial salt load (Chapter 3). A high contrast in aqueous and gaseous phase saturations occurs at the brine level. Moreover, a high contrast occurs at the edge of the dry-out region. This phenomenon corresponds to large capillary forces.

During constant CO_2 injection the immobile brine is evaporated continuously, at a constant rate. As a precondition for evaporation, the mobile brine is completely displaced and S_{CO_2eff} is one. This evaporation rate describes the "free" volume fraction which is occupied by CO_2 as used in the evaporation/precipitation model. If a back flow rate of brine equal to the evaporation rate is assumed, S_{CO_2irr} is zero, because the developing "free" volume fraction from water evaporation is directly occupied by the back flowing brine. Therefore, Σ_{CO_2} in the last term of equation 4.23 is replaced by Σ_{br} .

$$\Sigma_{r_m} = \Sigma_r = \Sigma_{b_{ma}} + \phi_{eff} \cdot \Sigma_{CO_2} + \phi_{irr} \cdot [S_{H_2O_r} \cdot \Sigma_{H_2O_{br-b}} + (S_{NaCl_{sol}} + S_{NaCl_{pre}}) \cdot \Sigma_{NaCl} + (S_{H_2O_b} - S_{H_2O_r}) \cdot \Sigma_{br}] \quad (4.29)$$

4. Extended PNG saturation model and resulting issues for time lapse monitoring

Σ_{r_m} would increase continuously, because the evaporated water with a low Σ value is then replaced by the original saline brine with a higher Σ value. During this process, a diffusion driven salinity equilibration between the back flowed brine and the remaining high salinity brine (due to replaced remaining water saturation by original saline brine) can be assumed. If the brine salinity reaches the NaCl solubility limit, halite precipitation occurs. The remaining pore space fraction for the back flowed brine is then reduced by the halite occupied pore space fraction. Finally, after further counter imbibitions of brine, ϕ_{irr} is completely clogged by halite.

The general corresponding repeat model can be described by an overall summarizing Σ value (Σ_x),

$$\Sigma_{r_m} = \Sigma_r = \Sigma_{b_{ma}} + \phi_{eff} \cdot \Sigma_{CO_2} + \phi_{irr} \cdot \Sigma_x \quad (4.30)$$

where the following cases can be distinguished:

If $\Sigma_x \leq \Sigma_{br_{lim}}$, the NaCl solubility limit is not reached and no halite precipitation occurs. Equation 4.30 simplifies with a Σ_{br} value for ϕ_{irr} only which is greater than the initial Σ_{br} because of the increased salinity. The modeled repeat run, Σ_{r_m} , is equal to the measured repeat run Σ_r , and results in:

$$\Sigma_{r_m} = \Sigma_r = \Sigma_{b_{ma}} + \phi_{eff} \cdot \Sigma_{CO_2} + \phi_{irr} \cdot \Sigma_{br} \quad (4.31)$$

Σ_{br} results then in:

$$\Sigma_{br} = \frac{\Sigma_r - \Sigma_{b_{ma}} - \phi_{eff} \cdot \Sigma_{CO_2}}{\phi_{irr}} \quad (4.32)$$

If $\Sigma_x > \Sigma_{br_{lim}}$, the NaCl solubility limit is reached and halite precipitation occurs. Equation 4.30 is then modified to thermodynamically reasonable conditions, using the Σ values for NaCl saturated brine ($\Sigma_{br_{lim}}$) and halite (Σ_{NaCl}). The modeled repeat run, Σ_{r_m} is equal to the measured repeat run Σ_r .

$$\Sigma_{r_m} = \Sigma_r = \Sigma_{b_{ma}} + \phi_{eff} \cdot \Sigma_{CO_2} + \phi_{irr} \cdot [S_{NaCl} \cdot \Sigma_{NaCl} + (1 - S_{NaCl}) \cdot \Sigma_{br_{lim}}] \quad (4.33)$$

The halite saturation S_{NaCl} results then in:

$$S_{NaCl} = \frac{\Sigma_r - \Sigma_{b_{ma}} - \phi_{eff} \cdot \Sigma_{CO_2} - \phi_{irr} \cdot \Sigma_{br_{lim}}}{\phi_{irr} \cdot (\Sigma_{NaCl} - \Sigma_{br_{lim}})} \quad (4.34)$$

If $\Sigma_x = \Sigma_{NaCl}$, the complete porespace ϕ_{irr} is clogged by halite and the modeled repeat run, Σ_{r_m} , is equal to the measured repeat run Σ_r , and results in:

$$\Sigma_{r_m} = \Sigma_r = \Sigma_{b_{ma}} + \phi_{eff} \cdot \Sigma_{CO_2} + \phi_{irr} \cdot \Sigma_{NaCl} \quad (4.35)$$

If $\Sigma_x > \Sigma_{NaCl}$, the maximum possible Σ value related to ϕ_{irr} is reached. This circumstance is comparable to the situation where the minimum $\Sigma_{r_{irr}}$ value is reached, but here the affected pore space fraction ϕ_{irr} is probably underestimated. Thus, $\Delta\phi$ describes the porosity fraction

4. Extended PNG saturation model and resulting issues for time lapse monitoring

transferred from the displacement process ($\phi_{eff} - \Delta\phi$) to the evaporation/precipitation process ($\phi_{irr} + \Delta\phi$). These adjustment to the affected pore space fractions is also an optional step. Adjusting ϕ_{eff} and ϕ_{irr} within the limit of ϕ_{tot} ($\phi_{tot} = \phi_{eff} + \phi_{irr}$), Σ_{r_m} , is equal to the measured repeat run Σ_r , and results in:

$$\Sigma_{r_m} = \Sigma_r = \Sigma_{bma} + (\phi_{eff} - \Delta\phi) \cdot \Sigma_{CO_2} + (\phi_{irr} + \Delta\phi) \cdot \Sigma_{NaCl} \quad (4.36)$$

Solved for $\Delta\phi$:

$$\Delta\phi = \frac{\Sigma_r - \Sigma_{bma} - \phi_{eff} \cdot \Sigma_{CO_2} - \phi_{irr} \cdot \Sigma_{NaCl}}{\Sigma_{NaCl} - \Sigma_{CO_2}} \quad (4.37)$$

The flow-chart in figure 4.5 summarizes the calculation steps when Σ_r is greater than Σ_b .

Nearby the model assumption that $S_{CO_{2eff}}$ is one and $S_{CO_{2irr}}$ is zero, the total CO_2 saturation, $S_{CO_{2tot-TPHI}}$, can be alternatively derived from the neutron porosity. Similar to equation 4.6, $S_{CO_{2tot-TPHI}}$ can be derived from the baseline and repeat TPHI values. Instead of the brine and CO_2 Σ values, the corresponding HI values (HI_{br} and HI_{CO_2}) are used as input parameters (Chapter 2.2.2).

$$S_{CO_{2tot-TPHI}} = \frac{TPHI_b - TPHI_r}{\phi_{tot} \cdot (HI_{br} - HI_{CO_2})} \quad (4.38)$$

The conditions to be met for the application of TPHI to derive $S_{CO_{2tot-TPHI}}$ are described for the Ketzin site conditions in chapter 5.3.2.2. Similar to the situation described above, an overall summarizing Σ_x value is included to account for the increasing salinity due to capillary effects.

$$\Sigma_{r_m} = \Sigma_r = \Sigma_{bma} + \phi_{tot} \cdot [S_{CO_{2tot-TPHI}} \cdot \Sigma_{CO_2} + (1 - S_{CO_{2tot-TPHI}}) \cdot \Sigma_x] \quad (4.39)$$

Solved for Σ_x :

$$\Sigma_x = \frac{\frac{\Sigma_r - \Sigma_{bma}}{\phi_{tot}} - S_{CO_{2tot-TPHI}} \cdot \Sigma_{CO_2}}{1 - S_{CO_{2tot-TPHI}}} \quad (4.40)$$

Similar to the model described above, the following cases can be distinguished for Σ_x :

If $\Sigma_x \leq \Sigma_{brlim}$, equation 4.39 simplifies with a Σ_{br} value for Σ_x . The modeled repeat run, Σ_{r_m} , is equal to the measured repeat run Σ_r , and results in:

$$\Sigma_{r_m} = \Sigma_r = \Sigma_{bma} + \phi_{tot} \cdot [S_{CO_{2tot-TPHI}} \cdot \Sigma_{CO_2} + (1 - S_{CO_{2tot-TPHI}}) \cdot \Sigma_{br}] \quad (4.41)$$

If $\Sigma_x > \Sigma_{brlim}$, equation 4.39 is then modified to thermodynamically reasonable conditions, using the Σ values for NaCl saturated brine (Σ_{brlim}), halite (Σ_{NaCl}) and the corresponding saturations S_{brlim} and $1 - S_{brlim} = S_{NaCl}$.

$$\Sigma_x = S_{brlim} \cdot \Sigma_{brlim} + (1 - S_{brlim}) \cdot \Sigma_{NaCl} \quad (4.42)$$

4. Extended PNG saturation model and resulting issues for time lapse monitoring

Solved for S_{brlim} :

$$S_{brlim} = \frac{\Sigma_x - \Sigma_{NaCl}}{\Sigma_{brlim} - \Sigma_{NaCl}} \quad (4.43)$$

S_{brlim} adjusted to ϕ_{tot} ($S_{brlim-TPHI}$) results in:

$$S_{brlim-TPHI} = (1 - S_{CO_{2tot-TPHI}}) \cdot S_{brlim} \quad (4.44)$$

S_{NaCl} adjusted to ϕ_{tot} ($S_{NaCl-TPHI}$) results in:

$$S_{NaCl-TPHI} = (1 - S_{CO_{2tot-TPHI}}) \cdot S_{NaCl} \quad (4.45)$$

The modeled repeat run, Σ_{rm} is equal to the measured repeat run Σ_r , and results in:

$$\Sigma_{rm} = \Sigma_r = \Sigma_{bma} + \phi_{tot} \cdot [S_{CO_{2tot-TPHI}} \cdot \Sigma_{CO_2} + S_{brlim-TPHI} \cdot \Sigma_{brlim} + S_{NaCl-TPHI} \cdot \Sigma_{NaCl}] \quad (4.46)$$

The application of equations 4.41 and 4.46 are based on the following simplification. The distinctions of the different cases result from the increasing brine salinity. HI_{br} decreases with increasing salinity (Chapter 2.2.2). Therefore, using the initial HI_{br} value instead of the decreased value as input parameter in equation 4.38 results in an underestimation of $S_{CO_{2tot}}$. However, in contrast to Σ_{br} , HI_{br} is only slightly influenced by the salinity. The Ketzin NaCl-equivalent HI_{org} brine value is 0.92 (Chapter 5.3.1.2), and for a brine at the solubility limit HI_{br} is 0.88 (Equation 2.20). Thus, the "real" $S_{CO_{2tot-TPHI}}$ is 1.05 times greater than $S_{CO_{2tot-TPHI}}$, without adjusting HI_{br} . The maximum HI_{br} value for the flush brine (Chapter 5.3.1.2) is 0.98. For the flush brine the "real" $S_{CO_{2tot-TPHI}}$ is 1.11 times of $S_{CO_{2tot-TPHI}}$ without adjusting HI_{br} . As a result for both salinities, Σ_x will be underestimated. For the case $\Sigma_x \leq \Sigma_{brlim}$, the Σ_{br} value will be underestimated. For the case $\Sigma_x > \Sigma_{brlim}$, the brine saturation will be overestimated and the halite saturation will be underestimated.

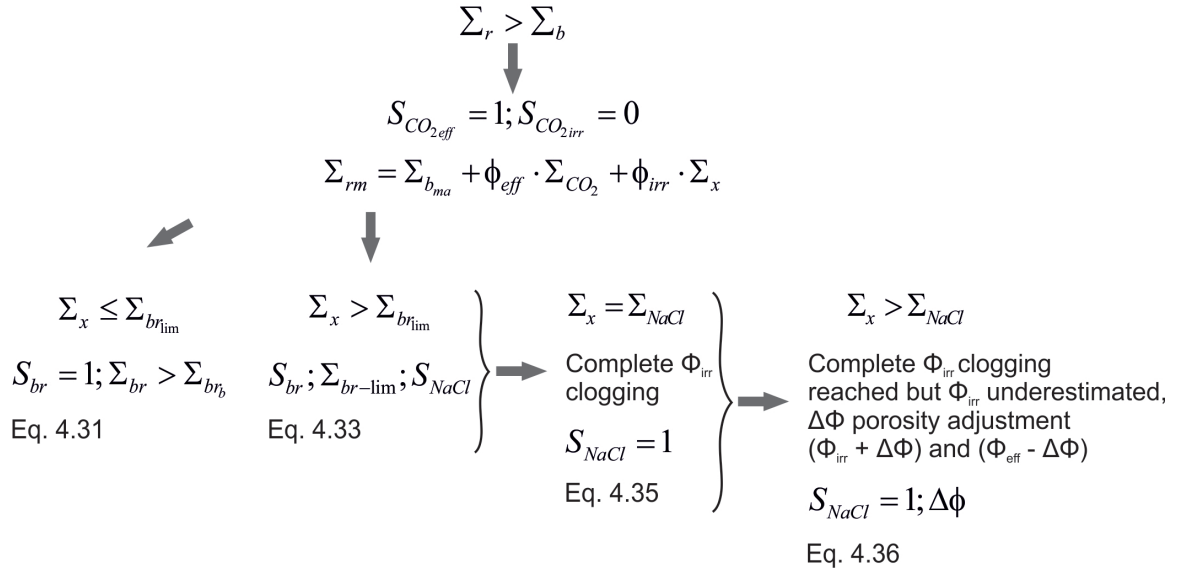


Figure 4.5.: Summarizing flow-chart when Σ_r is greater than Σ_b for the assumed backflow rate of brine being equal to the evaporation rate.

5. PNG monitoring results at the Ketzin site

The Ketzin pilot site for geological storage CO₂ in a saline aquifer is approximately 25 km west of Berlin (Figure 5.1). The general objective at the Ketzin pilot site is to understand in situ ongoing processes associated with CO₂ storage. For this purpose, an extensive monitoring program is performed, including seismic, electric and electromagnetic techniques (Juhlin et al., 2007; Ivanova et al., 2012; Schmidt-Hattenberger et al., 2011, 2012; Bergmann et al., 2012). These techniques are applied in different geometric setups like 3D seismic, vertical seismic profiling, moving source profiling, and crosshole or surface-downhole configurations.

In contrast to these methods, which cover the large "reservoir scale" associated with a small spatial resolution, well logging derived monitoring covers the small "borehole scale", with a corresponding high spatial resolution. Later on, the derived monitoring experiences from the integrated combination of these different monitoring techniques, with their variability in scale and spatial resolution, should be used for developing practical guidelines and regulatory frameworks for future (large scale) CO₂ storage operations.

5.1. Geology, fluid Σ values, well completions and injection history

5.1.1. Geology, porosity distribution and examined wells

The Ketzin pilot site is situated in the eastern part of the Roskow-Ketzin double anticline. This anticline is the result of a salt pillow intrusion, that is situated at a depth of 1500–2000 m (Förster et al., 2006). The injection reservoir (630-700 m) is the Stuttgart formation, contained within the Triassic Keuper. The heterogeneous lithology of the Stuttgart formation is characterized by a sandstone channel-facies with an alternating muddy floodplain-facies (Förster et al., 2006; Norden et al., 2010). This heterogeneous lithology results in a heterogeneous porosity and permeability distribution associated with a good and poor (high/low porosity and permeability) injection performance.

The overlaying seal of the Stuttgart formation is the Weser formation, which is characterized by mudstones, clayey siltstones, anhydrite and dolomite. Above the Weser formation is the Arnstadt formation which is characterized by a clay/carbonate playa environment, with muddy dolomite alternating with mudstones and locally thin silty-sandy intercalations (Förster et al., 2006, 2010). Both, the Weser and Arnstadt formations, with their large amount of clay minerals, are a suitable seal for the CO₂ injection reservoir.

Three vertical wells were drilled into the flank of the anticline in 2007, i.e. one injection well (Ktzi201) and two observation wells (Ktzi200 and Ktzi202). These wells penetrate into the Stuttgart formation. Ktzi200 is about 50 m and Ktzi202 is about 112 m from the injection

5. PNG monitoring results at the Ketzin site

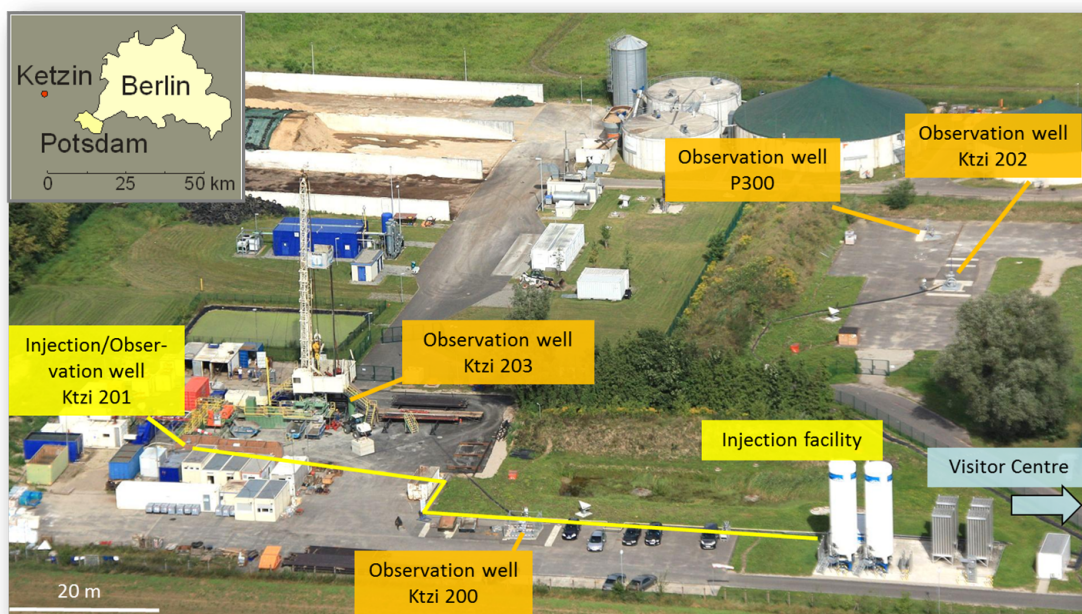


Figure 5.1.: Aerial view of the Ketzin site in September 2012 (Martens et al., 2013)

well (Figure 5.1). In summer 2011, the shallow vertical observation well P300, which is close to the Ktzi202, was drilled down to the sandstones of the first aquifer above the Stuttgart formation, enabling an above-zone monitoring of the CO₂ storage. In summer 2012, the vertical observation well Ktzi203, which is close to the injection well Ktzi201, was drilled down to the Stuttgart formation (Figure 5.1). From this well, rock cores that have been exposed to the CO₂ for about four years were taken from the storage reservoir (Martens et al., 2013). Wells Ktzi200, Ktzi201 and Ktzi202 are the focus in the flowing text, since it is in these wells that the PNG monitoring was conducted.

A detailed mineralogical/lithological composite log, including the total porosity (TPHI) and the effective porosity (EPHI), (after Norden et al., 2010) are shown in figure 5.2. The displayed depth range includes parts of the Stuttgart and the Weser formation. The permeability of the Stuttgart formation is derived from open hole NMR logs (only performed in Ktzi201), which were calibrated to the laboratory-determined permeability from rock core samples. Rock core gas permeability was determined with a nitrogen permeameter and corrected for gas-slippage effects using the Klinkenberg correction (Klinkenberg, 1941). In addition, on a subset of cores, brine permeability was measured to convert the gas permeability to brine permeability by an established correction function (Norden et al., 2010). Based on the core permeability data, the default NMR T₂ cutoff value of 33 ms for sandstones was adjusted to 10 ms. Thus, the adjusted T₂ cutoff value is the threshold that separates the immobile brine (ϕ_{irr}) from the mobile brine (ϕ_{eff}). Since the NMR log was only run in the Ktzi201, ϕ_{irr} and ϕ_{eff} for the wells Ktzi200 and Ktzi202 were obtained from a simplified model, including the measured conventional open hole logs (gamma ray, density, neutron-neutron, sonic, resistivity) and available core permeability measurements for these wells (Norden et al., 2010).

The main reservoir sandstone unit (634-651 m) of the Stuttgart formation in Ktzi201 is subdivided into two permeable sandstone layers. These layers are separated from each other by a strongly cemented sandstone layer (Norden et al., 2010). The same is true for the

5. PNG monitoring results at the Ketzin site

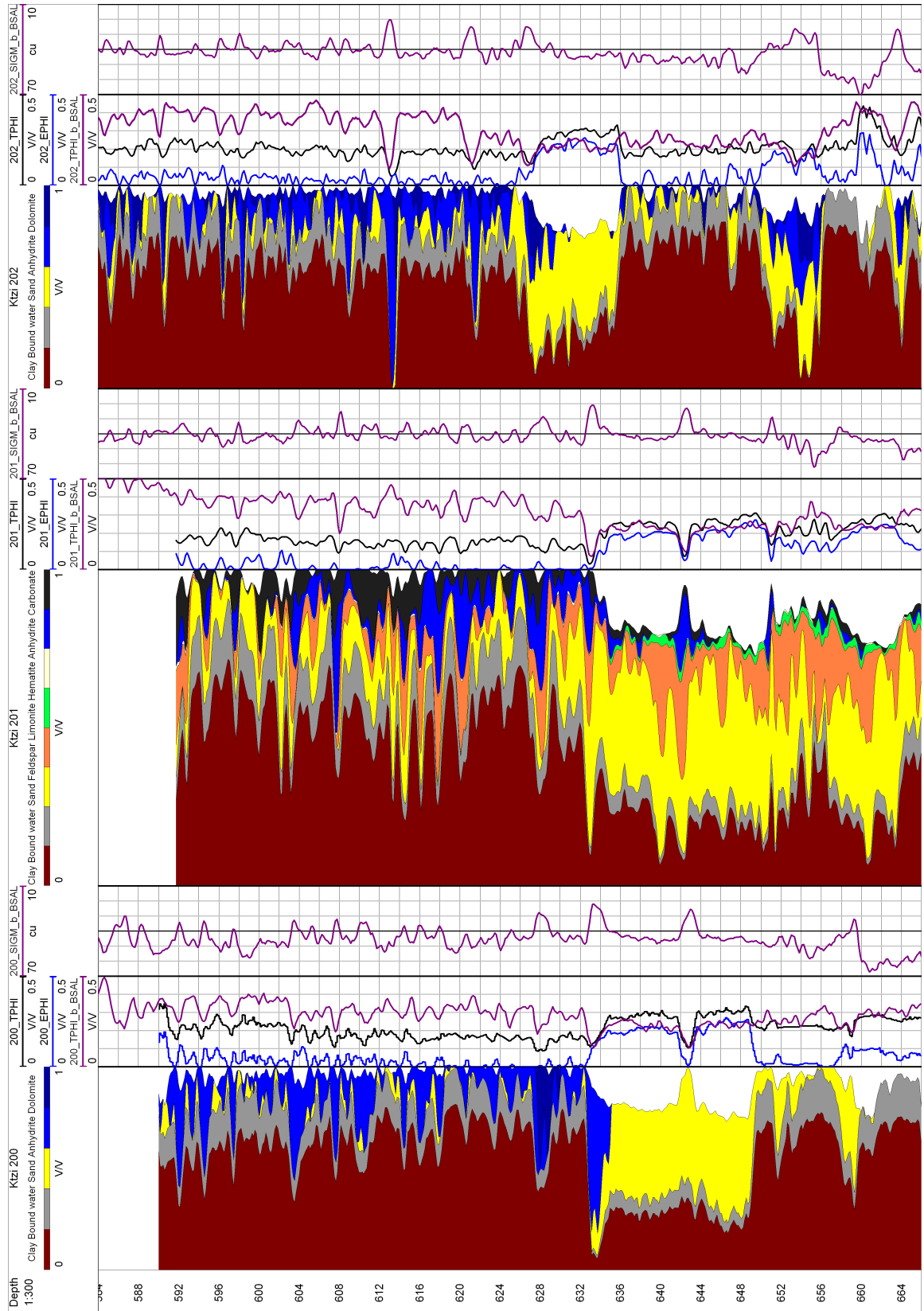


Figure 5.2.: Lithological composite logs, total porosity logs (TPHI) and effective porosity logs (EPHI) for all Ketzin wells after Norden et al. (2010). Neutron porosity (TPHI_b_BSAL) and formation Σ (SIGM_b_BSAL) logs from the PNG baseline runs for all Ketzin wells.

comparable lithological profile in Ktzi200. In this main reservoir sandstone, high effective porosity and permeability values correspond to high sand content, where cementation with anhydrite or the clay content is minor. In Ktzi201, a more fine-grained layer (siltstone) and a sandstone layer (651-664 m), also with high effective porosity and permeability, underlay the main reservoir sandstone.

In Ktzi202, the main reservoir sandstone of the Stuttgart formation is slightly shallower (627-638 m) and thinner than in Ktzi200 or Ktzi201. In general, the lithology in Ktzi202 is somewhat different from the lithology in Ktzi201 or Ktzi200, with higher clay content in the lower part of the main reservoir sandstone, associated with less porosity and permeability. Above this main reservoir sandstone is the caprock section of the Weser formation, which is characterized by a high clay content with a varying anhydrite and dolomite content. The high clay content (associated with less effective porosity and permeability), seals the underlying reservoir sandstone.

The neutron porosity (TPHI_b_BSAL) and formation Σ (SIGM_b_BSAL) logs from the PNG baseline runs for all Ketzin wells are shown in figure 5.2. TPHI_b_BSAL is shown in the porosity track and SIGM_b_BSAL is the right hand side of the porosity track for each well (processing: noir_BSAL; compare Chapter 5.2.2). Traditionally, SIGM logs are presented inversely. Thus values increase from right to left. This presentation is maintained in all the following SIGM illustrations.

Both logs depend on the geology. The Σ values of the rock matrix and the formation brine are weighted by their corresponding volume fractions. The main reservoir sandstone in all wells has a Σ range between 40-50 cu, except the interbedded, strongly cemented sandstone layer. Here, variations in TPHI and in the clay content account for the Σ changes. As a result, the cemented sandstone layer is associated with a lower porosity and a lower Σ range (10-15 cu).

TPHI_b_BSAL is in between EPHI and TPHI for all wells. In the upper part of the main reservoir sandstone in Ktzi201, TPHI_b_BSAL fits better to TPHI. The lower part fits better to EPHI. In Ktzi200 and Ktzi202, TPHI_b_BSAL fits better to EPHI. In general, the cased-hole TPHI_b_BSAL correspond well to the open-hole derived porosities in the main reservoir sandstone in all wells.

In the caprock section, the shale effect, i.e. an increased TPHI_b_BSAL reading compared to TPHI, is evident in all wells. In addition, the high anhydrite and dolomite cementation, with a corresponding low TPHI is associated with a low TPHI_b_BSAL reading. In general, the SIGM_b_BSAL logs at the caprock section are in the same range as at the reservoir section. Here, the lower TPHI (associated with a lower brine content; lower Σ reading), is compensated by the higher clay content (higher Σ reading). Similar to TPHI_b_BSAL, the SIGM_b_BSAL logs decrease where TPHI is low, due to anhydrite and dolomite cementation.

5.1.2. Determination of fluid Σ values

In the following section, the pore fluid Σ values, which are calculated based on the Σ brine calculation (Chapter 2.2.1.3), are analyzed in detail. For this purpose, the chemical brine composition from the Ketzin pilot site (Würdemann et al., 2010) is considered. Similar to many brines from the North German Basin, the Ketzin brine is dominated by chlorine. Since chlorine has a large σ_{m_i} in comparison to other dissolved ions, the Σ chlorine fraction is dominant. Overall, Σ_{salt} results in 77.31 cu, where chlorine contributes 97.9 % and sodium 1.6 % to the total value. Boric acid (HBO₂) with the trace element boron, has a Σ value

5. PNG monitoring results at the Ketzin site

Table 5.1.: Capture cross sections for brine (Σ_{br}) as the sum of the capture cross sections of fresh water ($\Sigma_{H_2O_c}$) and the dissolved salts for the “true” and the NaCl-equivalent brine ($\Sigma_{salt/NaCl_{c-eq}}$) under ambient (25 °C, 1 bar) and reservoir conditions (35 °C and 75 bar), the corresponding brine densities (ρ_{br}) and total dissolved salt content (TDS). *(Data provided by Würdemann et al. (2010); adjusted by De Lucia)

Brine	T / p	TDS	ρ_{br}	$\Sigma_{salt/NaCl_{c-eq}}$	$\Sigma_{H_2O_c}$	Σ_{br}
	[°C] / [bar]	[g/l]	[g/cm ³]	[cu]	[cu]	[cu]
“True” brine	25 / 1	224.53*	1.15	77.31	20.40	97.71
NaCl _{eq} brine	25 / 1	220.47	1.14	77.31	20.47	97.78
NaCl _{eq} brine	35 / 75	220.01	1.14	77.15	20.43	97.58

of 0.38 cu and contributes with 0.48 % to the overall Σ_{salt} value. All other remaining ions contribute less than 0.07 % to the total value.

Due to limitations in the available chemical database, a simplified chemical brine composition that neglects NH₄, Ba, Li and HBO₂ is used for chemical modeling (Personal communication; De Lucia). To compare the PNG monitoring results directly with the results from chemical models, the simplified chemical brine composition is also used. However, the large Σ difference between the simplified and original brine composition results from the boric acid (0.48 %).

Since chlorine is the dominant chemical constituent, the saturation state calculations are simplified. Σ_{salt} is presented only as the NaCl-equivalent concentration ($c_{NaCl_{eq}}$). In comparison to the “true” total salt concentration (224.53 g/l; Table 5.1), $c_{NaCl_{eq}}$ results in 220.47 g/l NaCl, which is smaller than the “true” total salt concentration. This difference results from the smaller σ_{m_i} of the other remaining ions compared to chlorine. Compensation for this discrepancy is made by decreasing the NaCl-equivalent concentration until it reaches the total Σ_{salt} value.

The brine density for the NaCl-equivalent concentration under ambient conditions (25°C, 1 bar) calculated after Rowe and Chou (1970) is at 1.14 g/cm³, close to the “true” brine density (1.15 g/cm³). To account for the Ketzin reservoir conditions (35 °C, 75 bar; Martens et al. (2013)), the brine density was also adjusted after Rowe and Chou (1970) to 1.14 g/cm³, which is approximately equal to the brine density under ambient conditions. Adjusting the brine density to reservoir conditions results in a smaller NaCl-equivalent concentration of 220.01 g/l (193 ppk). Accordingly, $\Sigma_{NaCl_{c-eq}}$ results in 77.15 cu. In Table 5.1 all relevant brine parameters are summarized. The NaCl-equivalent brine under reservoir conditions is used for all calculations involving the displacement or evaporation/precipitation processes. The Σ_{CO_2} value for the Ketzin reservoir conditions results in 0.014 cu (Figure 2.1).

5.1.3. Well completions, injection history and changing borehole conditions

Details of the well completion are given in the appendix (Figure A.1, A.2 and A.3) for wells Ktzi200, Ktzi201 and Ktzi202 respectively. The well completion below the 9 5/8 casing shoe which extends over the caprock and the reservoir section is considered in detail in the following text. The reservoir section was drilled with a 8.5 inch bit size (BS). The caliper logs show only minor washouts in the reservoir sandstones in all wells.

Due to the smart casing concept (Giese et al., 2009), that uses different sensor cables and installations behind casing for monitoring, the wells are characterized by a complex well

completion. All wells were completed with a 5.5 inch (CSIZ) coated steel production casing, with a casing weight (CWEI) of 20 lb/ft. The insulating coating is necessary to avoid an electrical short circuit between the installed ring-shaped electrodes behind the casing. These electrodes are used for the vertical resistivity array (VERA; Giese et al. (2009)).

In addition, to avoid a destruction of the installations, the wells are not cemented in the reservoir section and are, subsequently, connected with the reservoir by perforations. In contrast, the wells are characterized by an open annulus (Ktzi201 and Ktzi202) or partly cemented annulus (Ktzi200) and are hydraulically connected with the reservoir due to the installed filter screens. These filter screens are widely used in groundwater production wells. Two main filter screen sections, each with an overall length of about 10 m, are installed in the wells. Each main filter section is constructed of two filter screen elements. The upper main filter screen section is between 641.96 and 651.22 m in Ktzi200, between 632.23 and 641.56 m in Ktzi201 and between 620.77 and 629.81 m in Ktzi202. The lower main filter screen section is between 690.70 and 699.93 m in Ktzi200, between 644.88 and 654.21 m in Ktzi201 and between 645.68 and 654.71 m in Ktzi202 (Prevedel, 2008).

The annulus in Ktzi201 is not cemented between 577 and 675 m. Moreover, the annulus in Ktzi202 is not cemented between 576 and 669 m. In contrast due to a cementation failure, the annulus in Ktzi200 is cemented between 591 down to 629.5 m with a good bonding. Between 629.5 m and 640.4 m, the annulus in Ktzi200 is partly cemented and characterized by poor bonding. At the depth range between 640.4 m and 653.1 m, the annulus is filled with formation brine. Thus, both main filter screen sections are not cemented in Ktzi200. Below 653.1 m the annulus in Ktzi200 is filled with drilling mud (Prevedel, 2008). Thus, in contrast to the annuli in Ktzi201 and Ktzi202 which are not cemented, the main part of the annulus in Ktzi200 is cemented characterized by good and poor bonding.

Figure 5.3 summarizes the cumulative CO₂ quantity (left ordinate) in metric tons (t) and the injection rate (right ordinate) in metric tons per hour (t/h) during injection between June 2008 and October 2012. The RST baseline and repeat runs (compare Table 5.2) are marked with arrows. During the investigated time period, the CO₂ injection rate was changed. From June 2008 until March 2009, the injection rate was increased gradually to a maximum of 3.5 t/h. Injection then proceeded at this rate for a period of around one year (March 2009 until March 2010). Then, from March 2010 until May 2012, the injection rate was decreased down to 1.8 t/h, with short periods of an increased injection rate. Between May 2012 and October 2012 a shut-in period commenced, where the injection was stopped. These changes in the injection rate are associated with changes in the brine level within the wells (compare Table 5.3). The total injected CO₂ quantity for the investigated period is around 60,000 t.

Before starting CO₂ injection, all wells are filled with formation brine. In addition, the open annuli are also filled with formation brine before the start of CO₂ injection. The partly cemented annulus in Ktzi200 is composed of a mixture of cement, drilling mud and/or formation brine. After start of CO₂ injection, the brine in the injection well and in the annulus of Ktzi201 is displaced by the injected CO₂. The CO₂ arrived at the closest observation well (Ktzi200) after 21.7 days and 532 tons of injected CO₂, while the arrival at the observation well Ktzi202 occurred after 271 days and 11,000 tons of injected CO₂ (Schilling et al., 2009; Kempka et al., 2010). Upon arrival of the CO₂ at these observation wells, the brine within the observation wells is displaced. Moreover, in the open annuli of Ktzi200 and Ktzi202, the brine is also displaced. In the partly cemented annulus (629.5-640.4 m) of Ktzi200, the mobile fluids (brine and/or drilling mud) are displaced.

The open and partly cemented annuli in the reservoir section result in a complex well comple-

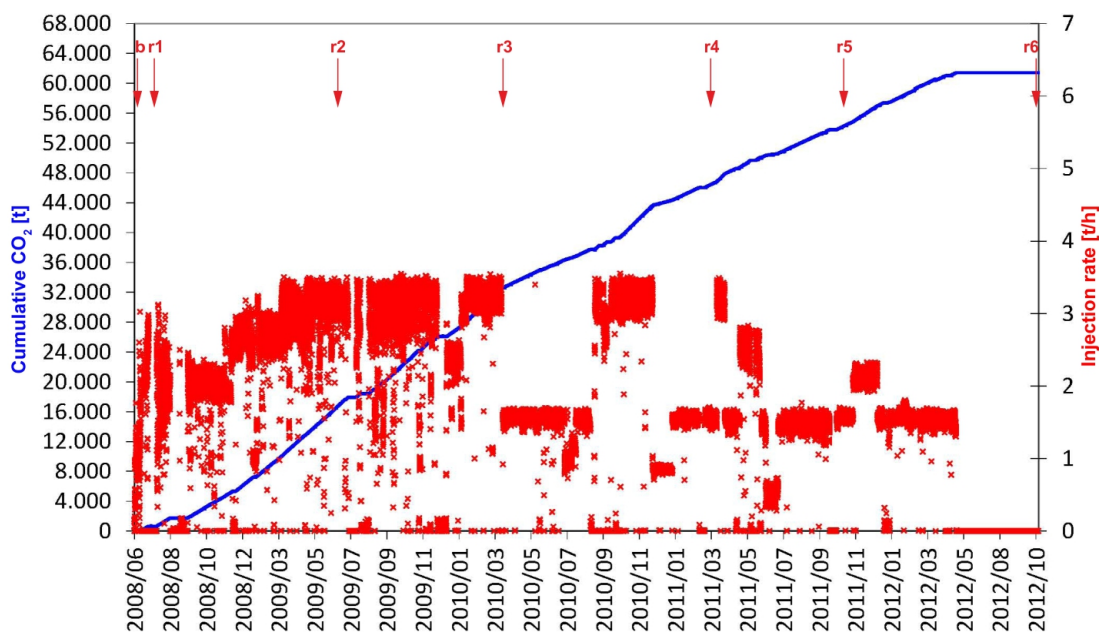


Figure 5.3.: Cumulative CO₂ quantity (left ordinate) and injection rate (right ordinate) since the start of injection in June 2008 until October 2012. The RST baseline and repeat runs are marked with arrows. (Data derived from Möller et al. (2012))

Table 5.2.: The dates on which the RST runs were carried out.

Mnemonic	Run	Ktzi200	Ktzi201	Ktzi202
b	Baseline	10.06.08	09.06.08	09.06.08
r1	Repeat 1	21.07.08	-	-
r2	Repeat 2	25.06.09	24.06.09	26.06.09
r3	Repeat 3	22.03.10	23.03.10	22.03.10
r4	Repeat 4	01.03.11	02.03.11	03.03.11
r5	Repeat 5	13.10.11	14.10.11	12.10.11
r6	Repeat 6	24.10.12	26.10.12	25.10.12

tion, because fluids in both the boreholes and the annuli change during CO₂ injection. These changing borehole conditions between baseline and repeat runs, must be carefully taken into account when characterizing the saturation changes in the reservoir.

5.2. From apparent data to intrinsic data

Table 5.2 summarizes the dates when the RST baseline and six repeat runs were carried out. The baseline runs were performed two weeks before the CO₂ injection started on June, 24th, 2008. The first repeat in July 2008 was only performed in the Ktzi200, immediately after the arrival of the CO₂ was observed in this observation well. This observation well is closest to the injection well. All additional repeat runs were performed in all wells roughly annually. The second repeat was performed in June 2009, the third repeat in March 2010, the fourth repeat in March 2011, the fifth repeat in October 2011 and the sixth repeat in October 2012.

The mnemonics for the different runs given in the first column of table 5.2 are used in the following log presentations.

The following chapter 5.2.1 discusses the apparent and field data that are not adjusted to environmental conditions. The chapters 5.2.2 and 5.2.3 discuss the environmental corrected intrinsic data that are adjusted to the borehole and formation conditions.

5.2.1. Apparent and field data

The main apparent baseline and repeat logs (MWFD, IRAT, SBNA, TRAT, SFFA and DIFF) are shown in the figures 5.4, 5.5 and 5.6 for the wells Ktzi200, Ktzi201 and Ktzi202 respectively. The MWFD logs (i.e. manometer well fluid density) are the fluid densities within the wells, and the DIFF logs are the differences between the SBNA and SFFA logs for each run. The theoretical background of all other logs is described in the chapters 2.3.2 and 2.4. The MWFD, IRAT and SBNA logs are mainly influenced by the changing brine level within the wells, where the TRAT and SFFA logs change with changing saturation conditions in the rock formation.

MWFD logs

As expected, the MWFD logs (first track) in all wells and runs show that the fluid density decreases from the baseline runs (formation brine; 1.14 g/cm^3) to the repeat runs (CO_2 ; $0.26\text{-}0.58 \text{ g/cm}^3$). The MWFD logs are averaged, which is why the density change looks very smooth. The turning point from the CO_2 density to the initial brine density is at the brine level for each run (marked by black bars on the left side of the first track). Below the brine level, all MWFD logs have the same brine density value.

Predominantly, the injection rate controls the brine level within the wells. Moreover, work on the wells (like fluid sampling or shut-in periods during the PNG well logging campaign) and thermodynamic processes like the heat pipe effect (Henninges et al., 2011) influence the brine level by changing the pressure and temperature distribution along the wellbore. Additionally, the changing pressure and temperature distribution control the CO_2 densities within the wells. However, the effect of changing density on Σ_{CO_2} is negligible compared to the large Σ_{br} value (compare Chapter 3.4).

Table 5.3 summarizes the brine levels for all repeat runs in all wells. The brine levels are described in meters below ground level and correspond to discrete RST data points.

Since the first repeat in Ktzi200 was run immediately after the arrival of the CO_2 , the brine level was, at 206.53 m below ground level, far away from the reservoir and is not included in the displayed depth range. The deepest brine levels are determined during the second repeat in Ktzi201 (652.22 m) and Ktzi200 (649.83 m), which correspond to the high injection rate during the first year of CO_2 injection. Since the CO_2 has just arrived after 271 days of injection in Ktzi202 (Kempka et al., 2010), the deepest brine level (651.41 m) was determined during the third repeat. The brine level for the second repeat is roughly 1.7 m shallower than for the third repeat in Ktzi202.

The brine level rises with decreasing injection rate. This is the case from the second repeat in Ktzi201 and Ktzi200 and from the third repeat in Ktzi202 to the subsequent repeats. A large brine level rise (from the reservoir to the caprock section) occurred from the fourth (642.98 m) to the fifth (627.28 m) and the sixth (623.77 m) repeats in Ktzi200. This brine level rise results from continuous fluid sampling, which decreases the wellhead pressure. In general, the

5. PNG monitoring results at the Ketzin site

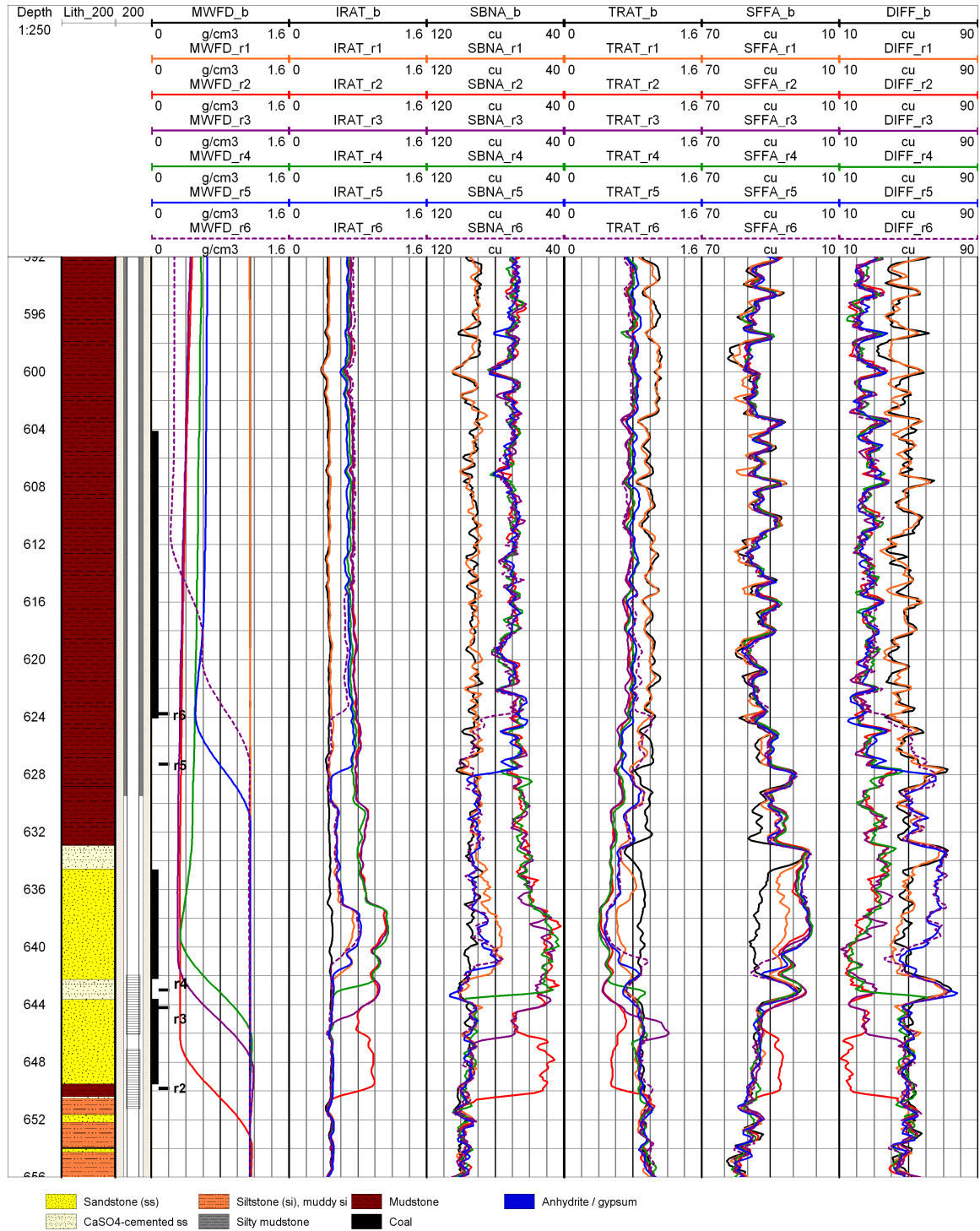


Figure 5.4.: Ktzi200: MWFD, IRAT, SBNA, TRAT, SFFA and DIFF (SBNA-SFFA) logs for the baseline and six repeat runs. The brine levels for each repeat run are marked with a black bar on the left side of the first track. Lithology after Förster et al. (2010)

5. PNG monitoring results at the Ketzin site

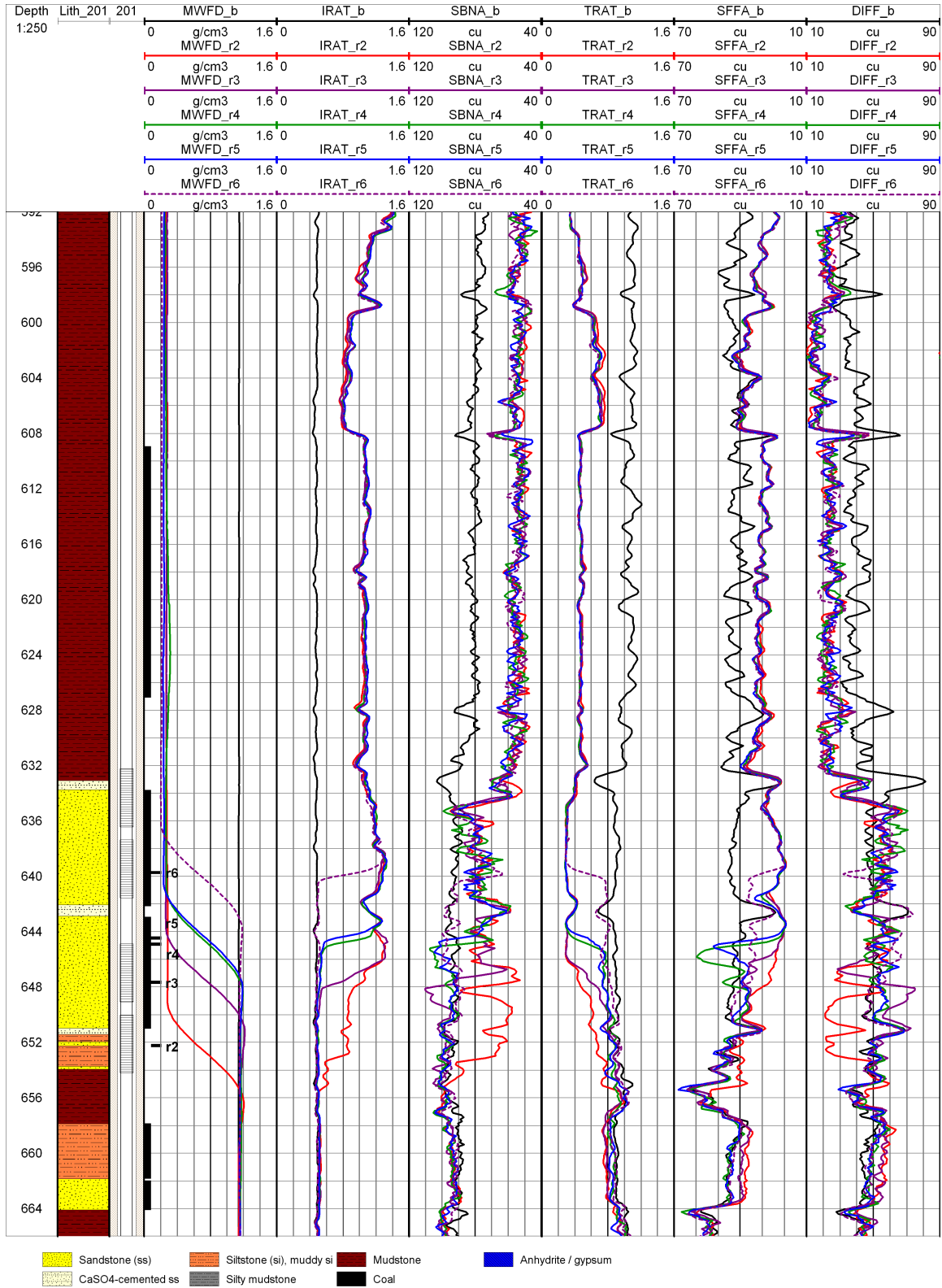


Figure 5.5.: Ktzi201: MWFD, IRAT, SBNA, TRAT, SFFA and DIFF (SBNA-SFFA) logs for the baseline and five repeat runs. The brine levels for each repeat run are marked with a black bar on the left side of the first track. Lithology after Förster et al. (2010)

5. PNG monitoring results at the Ketzin site

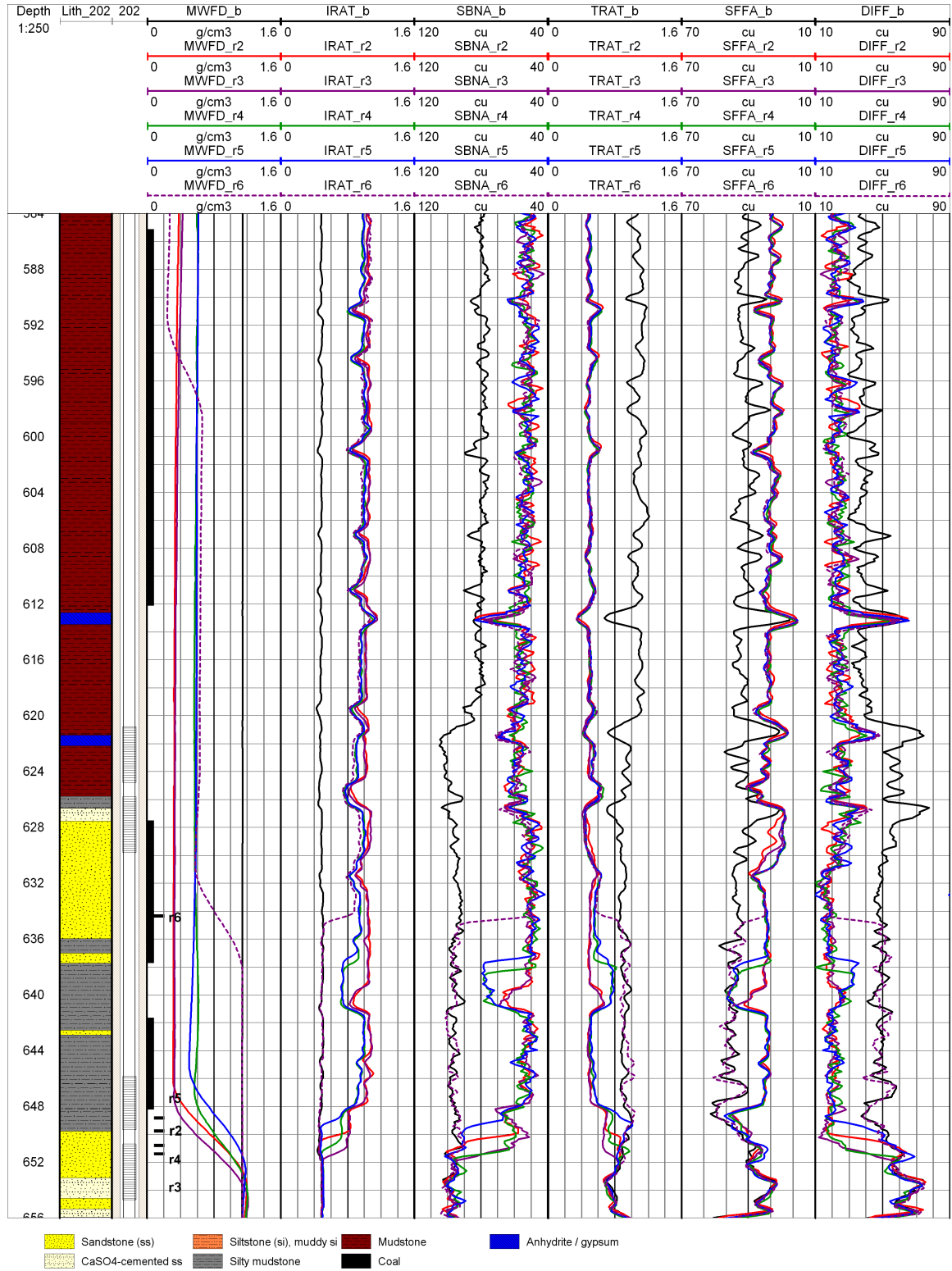


Figure 5.6.: Ktzi202: MWFD, IRAT, SBNA, TRAT, SFFA and DIFF (SBNA-SFFA) logs for the baseline and five repeat runs. The brine levels for each repeat run are marked with a black bar on the left side of the first track. Lithology after Förster et al. (2010)

Table 5.3.: Brine levels below ground level for the repeat runs in Ktzi200, Ktzi201 and Ktzi202.

Run	Ktzi200	Ktzi201	Ktzi202
	[m]	[m]	[m]
r1	206.35	-	-
r2	649.83	652.22	649.74
r3	644.19	647.65	651.41
r4	642.98	644.90	650.80
r5	627.28	644.44	648.82
r6	623.77	639.72	634.34

shallowest brine level in all wells is found for the sixth repeat (October 2012) after injection stopped in May 2012. In the following section, the IRAT, SBNA, TRAT, SFFA and DIFF logs for the reservoir section are analyzed in detail.

IRAT logs at reservoir section

The IRAT logs (second track), which are defined as the ratio of the inelastic counts from the far and the near detector, increase between the baseline (0.4-0.6) and the repeat (0.8-1.4) runs in the main reservoir sandstone. Since IRAT is more sensitive to the borehole than to the formation, the baseline IRAT logs are relatively constant in both the reservoir and the caprock section. Moreover, the absolute values in the reservoir and the caprock section are also in the same range. The repeated IRAT logs are more affected by the casing, because the presence of CO₂ in the wells and the annuli result in an increased L_s and a decreasing fluid density, which is associated with an increased depth of investigation. Thus, the repeat IRAT logs show changes at the joint assemblies in Ktzi201 and Ktzi202, where the annuli are not cemented. In general, the changing brine levels within the wells are evident in the IRAT logs and fit with the brine levels determined from the MWFD logs.

SBNA logs at reservoir section

The SBNA logs (third track) decrease between the baseline (90-100 cu) and the repeat runs in the main reservoir sandstone in all wells. The repeat SBNA logs are in the range of 40 to 55 cu in the reservoir section of the observation wells, except for the first, fifth and sixth repeat in Ktzi200. These repeats in Ktzi200 have higher SBNA values (closer to the baseline values), because the corresponding brine levels are above the reservoir section. Moreover, corresponding to the brine levels, SBNA is also decreased in the lower sandstone layer for the second and the third repeat in Ktzi200.

In Ktzi202, all repeats nearly overlap in the reservoir section. Moreover, in Ktzi202 the SBNA increase corresponds to the TRAT increase in the silty mudstone layer between 637-641 m, indicating that the silty mudstone occupies some space in the open annulus.

In the upper sandstone layer of Ktzi201, the repeat SBNA logs have a greater variability (60-100 cu) and generally higher values than the SBNA logs in the observation wells, except for the first, fifth and sixth repeat in Ktzi200. Due to the presence of CO₂ in the well, the annulus and the reservoir sandstone, the SBNA depth of investigation increases for the repeat runs compared to the baseline runs. Since the CO₂ is present in the well and in the annulus of the reservoir section of the observation wells and the injection well, the higher SBNA reading

in the upper sandstone layer in the injection well should result from the reservoir. Thus, a material with a large Σ value, like halite, could account for the increased SBNA reading in Ktzi201. The second SBNA repeat is decreased in the lower sandstone layer in Ktzi201 corresponding to the brine level, where the subsequent repeats nearly overlap with the baseline SBNA log, except for the fourth and fifth repeat between 645 and 647 m. At this depth range, the fourth and the fifth repeat SBNA logs have higher values than the baseline logs. The same is true in the corresponding SFFA logs.

TRAT logs at reservoir section

In contrast to the IRAT logs, the TRAT logs (fourth track) decrease between the baseline and the repeat runs in the main reservoir sandstone in all wells. The decrease results from the opposite ratio definition (near to far) of the TRAT logs compared to the IRAT logs. The baseline values are in the range of 0.8 to 1.0, except in the interbedded, strongly cemented sandstone layers, which have lower TRAT values. In general, TRAT and TPHI behave similarly, because TPHI is derived from TRAT. Therefore, the baseline TRAT logs are also characterized by lower values in the strongly cemented sandstone layers (0.6-0.7) and higher values in the caprock section (1.0-1.2) due to the shale effect (compare Chapter 5.1.1). The smaller repeated TRAT values compared to the baseline values in the reservoir sandstone are in the range of 0.4 to 0.6 in the observation wells (Ktzi200 and Ktzi202), and between 0.2 and 0.4 in the injection well (Ktzi201). The lowest TRAT values in Ktzi201 compared to the observation wells indicate that the lowest hydrogen content in the reservoir sandstone of the injection well.

In Ktzi200, the TRAT logs in the upper sandstone layer decrease from the first to the fourth repeat and then slightly increase from the fourth to the sixth repeat. Thus, the shallow brine level above the upper sandstone layer for the fifth and sixth repeat is not associated with a large TRAT change, indicating only minor saturation changes in the reservoir. The second repeat is decreased down to the corresponding brine level in the lower sandstone layer in Ktzi200. All subsequent repeats nearly overlap with the baseline log in the lower sandstone layer in Ktzi200.

The peak in the third TRAT repeat in Ktzi200 in the depth range at 645.0 and 646.5 m, which is greater than the baseline value, is a near wellbore effect, because the corresponding SFFA log overlaps with the baseline log. An accumulation of radioactive materials could account for the increased TRAT reading, because the corresponding gamma-ray log (not shown) is also increased within this depth range. Moreover, this peak is located in the vicinity of the corresponding brine level, that also corresponds with the boundary between the upper filter screen element and the lower filter screen element of the upper filter screen section. Due to the changing flow velocity at the joint assembly between the two filter screen elements, an accumulation of radioactive materials could be possible. However, this peak is absent in all subsequent repeats.

In Ktzi201, all repeat TRAT logs nearly overlap in the upper sandstone layer, except for the fifth and sixth repeat. The TRAT log increase from the fifth to the sixth repeat compared to the former repeats in the upper sandstone layer correspond to the brine level rise. In the lower sandstone layer of Ktzi201, the repeat TRAT logs reach their minimums during the second repeat and then increase for all subsequent repeats. The TRAT log increase in the lower sandstone layer corresponds to the rising brine level. Moreover, the second and the third repeat TRAT logs have slightly lower readings than the baseline log in the siltstone and sandstone layer between 651 and 664 m in Ktzi201.

In Ktzi202, all repeat TRAT logs nearly overlap in the main reservoir sandstone between 628 and 635 m. Moreover, the decrease in the repeat TRAT logs, compared to the baseline log, correspond to the brine levels. Thus, below the brine levels, the repeat TRAT logs overlap with the baseline log. The second and the third repeat TRAT logs are slightly increased in the silty mudstone layer between 639 and 641 m and the fourth and the fifth repeat TRAT logs are also slightly increased between 637 and 641 m. This TRAT increase can result from a formation collapse, where the silty mudstone occupies some space from the open annulus. Below the corresponding brine level, the sixth repeat nearly overlaps with the baseline log. The increased TRAT reading is not evident in the sixth repeat, because the brine level (634.34 m) has risen above this anomaly. Above the brine level, the sixth repeat TRAT log overlaps with the previous repeat TRAT logs.

SFFA logs at reservoir section

As expected, the SFFA logs (fifth track) decrease between the baseline (40-50 cu) and the repeat (20-40 cu) runs in the main reservoir sandstone in all wells. The apparent SFFA baseline logs are the basis for the intrinsic SIGM logs. Thus, the general baseline SFFA behavior is comparable to the baseline SIGM description in chapter 5.1.1. In general, the changes in the repeat SFFA logs are also comparable to the changes in the repeat TRAT logs in all wells. Thus, a decreased SFFA reading corresponds to a decreased TRAT reading.

In the upper sandstone layer of Ktzi200, the first repeat SFFA log has the lowest value reduction, whereas all subsequent repeats have higher value reductions and nearly overlap in the upper sandstone layer, indicating minor changes between these runs. In contrast to the corresponding TRAT logs, the SFFA logs are less affected by the borehole, because SFFA is derived from the far detector only, where TRAT is derived from the near and far detector. This is the reason why the TRAT logs slightly increase from the fourth to the sixth repeat, whereas the corresponding SFFA logs nearly overlap. Corresponding to the TRAT log in Ktzi200, the second repeat SFFA log is also decreased in the lower sandstone layer, and all subsequent repeats nearly overlap with the baseline log. The overlapping for the subsequent repeats indicate that, only for the second repeat, the lower sandstone layer contains CO₂, which corresponds to the high injection rate during the first year of CO₂ injection.

Corresponding to all repeat TRAT logs in Ktzi201, all SFFA logs nearly overlap in the upper sandstone layer, indicating minor saturation changes in the reservoir section between these runs. Moreover, the SFFA log increase from the fifth to the sixth repeat in the upper sandstone layer corresponds to the brine level rise. Corresponding to the repeat TRAT logs, the repeat SFFA logs reach their minimum for the second repeat and then increase for all subsequent repeats in the lower sandstone layer in Ktzi201. Between 645 and 648 m, the fourth and the fifth repeat SFFA logs are characterized by peaks that are greater than the baseline log. These peaks are in the vicinity of the corresponding brine levels. Comparable to the increased SBNA reading in the upper sandstone layer in Ktzi201, a material with a large Σ value, like halite, could account for the increased SFFA reading. Corresponding to the second and the third repeat TRAT logs, the second and the third repeat SFFA logs in Ktzi201 have slightly lower readings than the baseline log in the siltstone and sandstone layer between 651 and 664 m. Since all subsequent repeats nearly overlap with the baseline log, only for the second and the third repeat, the siltstone and sandstone layer contain CO₂.

In Ktzi202, the second and the third repeat SFFA logs have slightly higher values than the subsequent repeats in the upper part of the reservoir sandstone between 627.5 and 631 m. The fourth, fifth and sixth repeat SFFA logs nearly overlap in this depth range, indicating

minor saturation changes between these repeats. Below this depth range, the repeat SFFA logs behave similarly to the corresponding repeat TRAT logs regarding differences associated with the changing brine level and the increased reading in the silty mudstone layer between 637 and 641 m.

Diff logs at reservoir section

The Diff logs are the differences between the SBNA and SFFA logs for each run. All baseline Diff logs are characterized by a sufficiently high contrast of 40 cu or greater in the reservoir section in all wells (threshold value 10 cu; Jeckovich and Olesen (1989)). The repeat Diff logs are characterized by higher and lower readings compared to the baseline DIFF logs, depending on the brine levels and changing SFFA readings.

The first repeat DIFF log nearly overlaps with the baseline DIFF log in the reservoir section in Ktzi200, because SBNA as well as SFFA have declined approximately equally. The second, third and fourth repeat DIFF logs have the lowest values (10-40) of all repeat DIFF logs in Ktzi200, especially in the lower part of the upper sandstone layer and (for the second repeat) in the lower sandstone layer. The fifth and the sixth repeats have similar (below the corresponding brine levels) or greater (above the corresponding brine levels) values than the baseline DIFF log in the reservoir section in Ktzi200, because the brine level rise above the reservoir sandstone is associated with an increased SBNA reading although SFFA has remained unchanged. Thus, the CO₂ saturation in the upper sandstone layer has not changed. The DIFF logs overlapping of the fifth and the sixth repeats with the baseline log in Ktzi200 indicates that the CO₂ saturation has decreased to approximately zero in the lower sandstone layer.

In Ktzi202, the repeat DIFF logs are lowest (10-20 cu) compared to the DIFF logs in Ktzi200 or Ktzi201. Moreover, in Ktzi202 all repeat DIFF logs nearly overlap. However, most of these lowest repeat DIFF values are greater than the threshold value.

In Ktzi201, the repeat DIFF logs have similar or greater values than the baseline logs in the upper sandstone layer. Thus, the increased repeat SBNA reading is associated with the increased repeat DIFF reading in Ktzi201 compared to the readings in the observation wells. The repeat DIFF logs in the interbedded strongly cemented sandstone layer, the second and the third repeat DIFF logs in the lower sandstone layer have lower values than the baseline DIFF logs. In general, all repeat DIFF logs in Ktzi201 are above the threshold value.

All logs at caprock section

In Ktzi201 and Ktzi202, the changing fluids in the well and in the annulus between the baseline (formation brine) and the repeat (CO₂) logs are associated with a decreased MWFD, TRAT, SBNA, SFFA and DIFF reading and an increased IRAT reading compared to the baseline logs in the caprock section. The same is true in Ktzi200, except for all repeated SFFA logs and all logs from the first repeat nearly overlap with the baseline logs. Since the brine level is above the caprock section, no changes in any of the logs are evident between the baseline and the first repeat. Due to the cemented annulus in Ktzi200, all repeat SFFA logs nearly overlap with the baseline log, indicating minor influence of the CO₂ within the well. In general, the cemented annulus result in smaller differences between the baseline and the repeat logs in Ktzi200 than in Ktzi201 or Ktzi202, where the annuli are uncemented.

The anomaly in the depth range between 603 and 608 m in Ktzi201 can also result from a formation collapse, where the mudstone occupies some space from the open annulus. However,

5. PNG monitoring results at the Ketzin site

Table 5.4.: Main depth ranges with changes between baseline and repeat runs in Kzi200, Ktzi201 and Ktzi202.

Ktzi200			Ktzi201			Ktzi202		
[m]			[m]			[m]		
Cap	604.11	624.08	Cap	608.94	627.07	Cap	585.12	612.09
SS1	634.59	642.21	SS1	633.78	642.16	SS1	627.49	637.70
SS2	643.59	649.53	SS2	642.92	650.99	Mud	641.66	648.21
			Silt	657.86	661.82			
			SS3	661.97	664.10			

above this anomaly the repeat logs are also affected by the CO₂ within the annulus, which indicates that this formation collapse does not seal the uncemented annulus.

Due to the low permeability and effective porosity in the caprock section, it can be assumed that no saturation changes in this formation have occurred. Moreover, the obtained cap rock core samples in Ktzi203, directly above the reservoir rocks exposed to CO₂ for four years, contain no detectable amount of injected CO₂ (Personal communication; Zimmer). All repeat MWFD, IRAT, TRAT, SBNA, SFFA and DIFF logs nearly overlap in the caprock section above the brine level in all wells, except the first repeat in Ktzi200, which nearly overlap with the baseline logs due to the shallow brine level. This overlapping indicates that the boreholes and the annulus contain CO₂ for all repeat runs and no saturation changes have occurred between the different repeat runs in the caprock section.

The black bar marked depth intervals in the first track in the figures 5.4, 5.5 and 5.6 and table 5.4 summarize the depth ranges where the main changes between the baseline and repeat runs have occurred. These depth range are the upper sandstone layer (SS1) in all wells and the lower sandstone layer (SS2) in Ktzi200 and Ktzi201. In addition to changes in SS1 and SS2, changes in the more fine-grained silstone (Silt) and sandstone layer (SS3) underlying the main reservoir sandstone have occurred in Ktzi201. In Ktzi202, changes between the baseline and repeat runs have occurred in the silty mudstone (Mud).

In contrast to the reservoir section, the caprock section is characterized by changing borehole conditions only. Thus, a depth range at the caprock section (Cap) in each well is used to evaluate the effect of changing borehole conditions without changes in the formation. These caprock depth ranges have baseline SFFA values comparable to the baseline SFFA values in the reservoir depth ranges. The following chapters 5.2.2 and 5.2.3 discuss the environmental corrected intrinsic data, where the different depth ranges are analyzed in detail.

5.2.2. Environmental corrected intrinsic data - baseline runs

The measured RST response and the parameters derived from the borehole and the formation conditions are the basis for the environmental corrected intrinsic data (compare Chapter 2.4.2). The borehole and formation parameters for the baseline runs are summarized in table 5.5.

Four different data processings were performed for all baseline runs in all wells. The BS, CSIZ, CSID and CWEI are defined by the well completions (compare Chapter 5.1.3) and are constant for all baseline data processings. Since all wells are filled with brine for the baseline

5. PNG monitoring results at the Ketzin site

Table 5.5.: Borehole and formation parameters for the environmental corrected intrinsic data of the baseline runs.

Mnemonic	BS	CSIZ	CSID	CWEI	BSAL	TPHI
	[inch]	[inch]	[inch]	[lb/ft]	[ppk]	[-]
noair	8.5	5.5	4.79	20	own	own
noair_OH	8.5	5.5	4.79	20	own	OH
noair_BSAL	8.5	5.5	4.79	20	197	own
noair_OH_BSAL	8.5	5.5	4.79	20	197	OH

run, the borehole status is always "noair". Moreover, the matrix is set to "sandstone" for all runs in all wells.

The "noair" data processing is the standard processing, where BSAL and TPHI are derived from the processing algorithm (status "own" for BSAL and TPHI). The following three data processings ("noair_OH", "noair_BSAL" and "noair_OH_BSAL") include the external knowledge of the open hole logging derived total porosity after Norden et al. (2010) (status "OH" for TPHI) and/or the formation brine salinity (status "197" for BSAL). The 197 ppk corresponds to 224.85 g/l TDS in NaCl-equivalents and a Σ_{br} value of 99.23 cu. This value is close to the Ketzin formation brine value (97.58 cu, Table 5.1) and is about 90 ppk smaller than the baseline BSAL log response derived by the processing algorithm. The mnemonics for the different data processings given in the first column of table 5.5 are used in the log presentation (Figure 5.7).

Since the differences between the baseline apparent SFFA logs and the intrinsic formation SIGM_noair logs is only 0.5 cu, the general influence of the environmental corrections on the intrinsic data is low (SFFA logs not shown in figure 5.7). Moreover, the differences between the different data processings for the baseline intrinsic formation SIGM and TPHI logs are small (Figure 5.7). The SIGM_noair and SIGM_noair_OH data processings are practically equal (differences in the range of the RST precision of 0.22 cu; Plasek et al., 1995) in the reservoir section of all wells, because the open hole and the RST derived porosities are in good agreement. The effect of the open hole porosity is greater in the caprock section rather than in the reservoir section, because, due to the shale effect, the RST derived porosity is greater than the open hole porosity. Thus, using the smaller open hole porosities results in a decreased SIGM value. SIGM_noair_OH is about 0.6 cu smaller than SIGM_noair in the caprock section. Due to the decreased BSAL value, the SIGM_noair_BSAL logs are about 1.2 cu smaller than the SIGM_noair logs.

The baseline TPHI logs include the noair and noair_BSAL data processings only, because the processed TPHI logs using the open hole porosity are equal to the open hole porosity. As with SIGM, TPHI decreases with decreasing BSAL. The TPHI_noair_BSAL logs are about 0.02 smaller than the standard TPHI_noair logs.

The log quality control is performed by evaluating the corresponding DSIG logs with different data processings, which are shown in the figures A.4, A.6 and A.8 given in the appendix for the wells Ktzi200, Ktzi201 and Ktzi202 respectively. DSIG close to zero provides confidence that the defined environmental parameters represent the actual logging conditions (compare Chapter 2.4.2). For this purpose, the arithmetic mean of the absolute DSIG values in the evaluated depth ranges is used. Using the DSIG values itself instead of the absolute DSIG values would decrease the arithmetic mean. The bar charts (a) in the figures A.5, A.7 and

5. PNG monitoring results at the Ketzin site

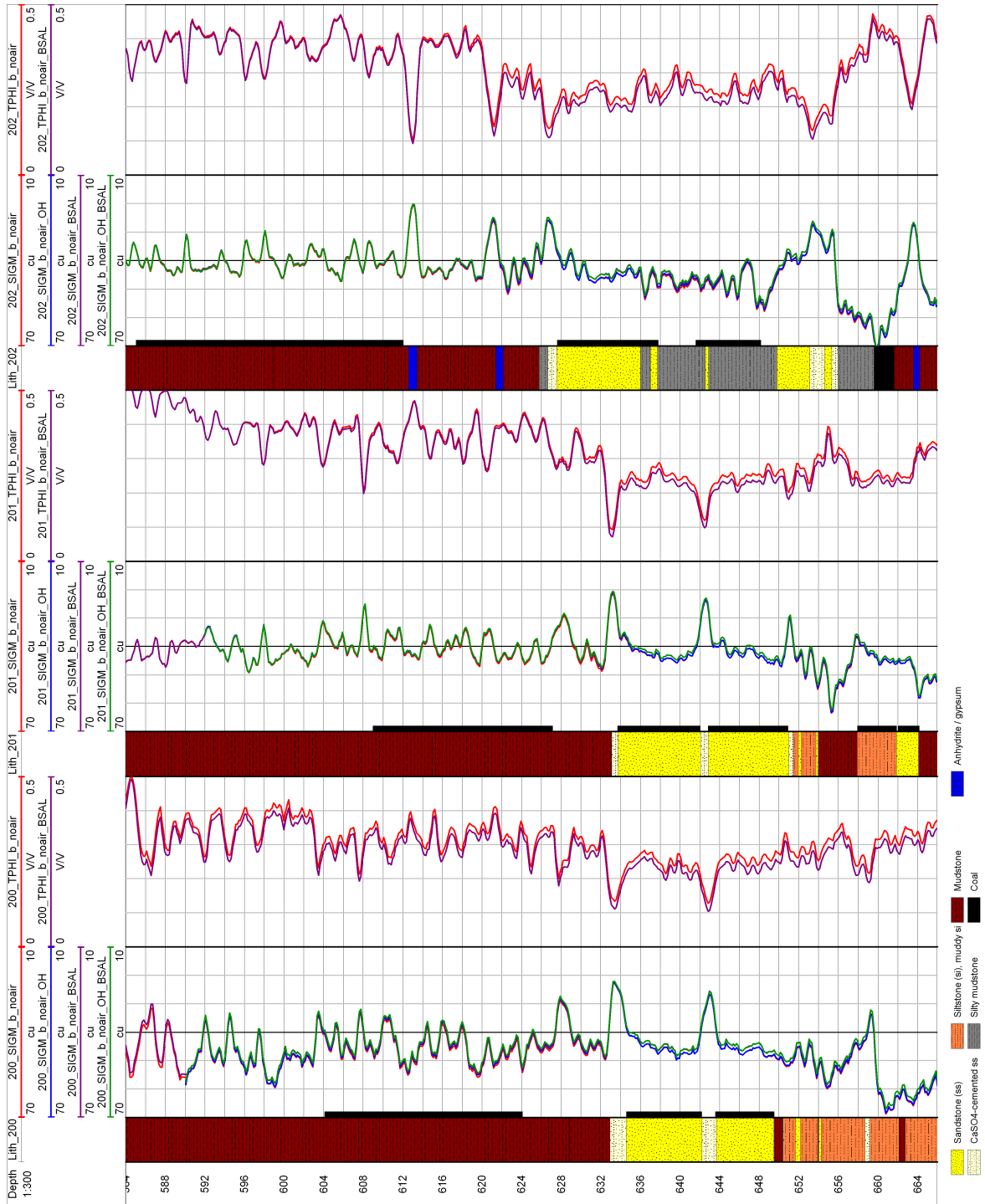


Figure 5.7.: SIGM and TPHI baseline logs for all wells with different data processings (SIGM with noair, noair_OH, noair_BSAI and noair_OH_BSAI and TPHI with noair and noair_BSAI data processing). Lithology after Förster et al. (2010)

A.9 given in the appendix summarize the arithmetic mean of the absolute DISG values with different data processings for the baseline runs in the evaluated depth ranges.

DSIG is closest to zero for the noair_BSAL data processings in the reservoir section in all wells. Due to the shale effect in the caprock section, DSIG is closest to zero for the noair_OH_BSAL data processings in all wells. Since the difference between the noair_BSAL and noair_OH_BSAL is only 0.2 cu, and the focus for saturation profiling is on the reservoir section, the noair_BSAL data processing is used for the final baseline logs in both the reservoir and the caprock section of all wells. Similar to the baseline SFFA logs, the baseline SIGM_noair_BSAL logs in the selected caprock depth ranges have values comparable to the baseline SIGM_noair_BSAL values in the selected reservoir depth ranges.

5.2.3. Environmental corrected intrinsic data - repeat runs

In contrast to the baseline runs, the repeat runs are characterized by changing fluids in both the boreholes and the annuli. Thus, the borehole parameters change. Above the brine level, the borehole and the annuli are filled with CO₂ (borehole status "air") and below the brine level with formation brine (borehole status "noair"). The RST processing algorithm assumes cemented annuli where no fluid exchange can occur (compare Chapter 2.4.2). Thus, the borehole status "air" accounts for the CO₂ within the well, but not for the CO₂ in uncemented annuli. Therefore, the borehole effect resulting from the CO₂ in uncemented or partly cemented annuli is not properly defined by the RST processing algorithm.

The borehole effect from both the CO₂ in the borehole and the annulus can be quantified by filling the borehole and annulus with brine, relogging the well and then correcting for the borehole effect from the CO₂ (Kimminau and Plasek, 1992; Hashem and Gilchrist, 1994). In fact, during this well operation the formation Σ has to be unchanged.

Advantageously, this borehole condition has occurred in Ktzi200 due to the rising brine level above the upper sandstone layer from the fourth to the subsequent repeats. Therefore, the fifth and the sixth repeat in Ktzi200 are characterized by ideal logging conditions with a large difference between SBNA and SFFA (compare DIFF logs in Figure 5.4).

There is, however, uncertainty as to whether the formation Σ changed between these runs or not. As mentioned above, the second and all subsequent repeat SFFA logs nearly overlap in the upper sandstone layer of Ktzi200, indicating minor formation Σ changes between these runs. Therefore, the task is to find a data processing for the fourth repeat nearly overlaps with the subsequent repeats in the upper sandstone layer of Ktzi200. In other words, after proper data processing, the fourth repeat and the subsequent repeats should have the same SIGM reading. This derived repeat data processing in the reservoir section of Ktzi200 should also fit to the repeat runs in the reservoir section of Ktzi201 and Ktzi202, because all wells are characterized by a partly or uncemented annulus in the reservoir section.

Moreover, borehole effects decrease as the formation Σ (i.e. SIGM) decreases (Kimminau and Plasek, 1992). As mentioned above, the selected caprock depth ranges have baseline SIGM values comparable to the baseline SIGM values in the reservoir sections. Additionally, no saturation changes occurred between the different repeat runs in the caprock section. Therefore, the depth range at the caprock section in each well are used to evaluate the borehole effect without "real" SIGM (without saturation changes in the caprock formation) changes.

Table 5.6.: Borehole and formation parameters for the environmental corrected intrinsic data of the repeat runs.

Mnemonic	BS	CSIZ	CSID	CWEI	TPHI
	[inch]	[inch]	[inch]	[lb/ft]	[-]
air	8.5	5.5	4.79	20	own
air_OH	8.5	5.5	4.79	20	OH
air_8.5	8.5	8.5	8.06	20	own
air_OH_8.5	8.5	8.5	8.06	20	OH

The repeat SIGM should decrease in the reservoir section, because the reservoir formation contains CO₂. In contrast, the repeat SIGM in the caprock section should remain unchanged, because the caprock formation contains no CO₂. Both, the reservoir and caprock section are characterized by CO₂ in all wells and in the open annuli of Ktzi201 and Ktzi202, which is associated with a decreased SBNA reading. Therefore, a greater borehole effect (i.e. greater correction necessary) can be expected in the caprock section (SIGM constant, SBNA decreased) rather than in the reservoir section (SIGM decreased, SBNA decreased) in all wells. Moreover, the borehole effect in the caprock section should be smaller in Ktzi200 (cemented annulus) than in Ktzi201 and Ktzi202 (uncemented annulus). In general, depending on the brine level, the nature of the annulus and the lithology, different data processings are required.

For this purpose, four different data processings were performed. The borehole and formation parameters for the repeat runs are summarized in table 5.6. Similar to the baseline runs, the matrix is set to "sandstone" for all repeat runs in all wells. The "air" data processing (borehole status "air" above and "noair" below the brine level) is the standard data processing, where BSAL (below brine level only) and TPHI are derived from the processing algorithm. Similar to the baseline runs data processing, the repeat runs data processing include the open hole porosity ("air_OH").

An idea to account for the CO₂ in the open annuli is setting the CSIZ equal to the BS by a constant CWEI ("air_8.5"). The CWEI is defined as constant, because the casing itself has not changed. Therefore, with increasing CSIZ, the CID increases as well. For this "pseudocasing", the CO₂ in the annulus is regarded as CO₂ in the borehole without any cementation in the annulus. Thus, the borehole status "air" should better account for the CO₂ in both the borehole and the annulus. Additionally, the open hole porosity is taken into account ("air_OH_8.5") for the "pseudocasing". The mnemonics for the different data processings given in the first column of table 5.6 are used in the log presentations.

The repeat SIGM and TPHI logs with different data processings are shown in the figures A.10, A.11, A.14, A.15, A.17 and A.18 given in the appendix for the wells Ktzi200, Ktzi201 and Ktzi202 respectively. Due to limitations in the log visualization software, the baseline logs are named like the corresponding repeat logs (bx). Nevertheless, all baseline logs are identical in each well. In contrast to the processed baseline runs, the processed repeat runs differ greatly. In the following section, the data processing for the repeat runs in all wells are discussed in detail.

First repeat in Ktzi200

Since the first repeat was only performed in the Ktzi200, the SIGM, DSIG and TPHI logs with different data processings, and the corresponding saturation profile are presented sep-

arately (Figure A.12). Due to the shallow brine level for the first repeat in Ktzi200, the borehole status is set to "noair" in both the caprock and reservoir section. Similar to the baseline run data processings, the noair, noair_OH and noair_OH_BSAL data processings were performed for the first repeat. In general, the difference between the different data processings for the first repeat intrinsic formation SIGM and TPhi logs are small (Figure A.12). DSIG is closest to zero for the noair_OH_BSAL data processing in both the reservoir and the caprock section in Ktzi200 (Bar chart (b) in Figure A.5). Therefore, the noair_OH_BSAL data processing is used for the first repeat run in Ktzi200. The corresponding saturation profile based on the displacement model is discussed in chapter 5.3.1.1.

In the following section, the second and all subsequent repeat TPhi and SIGM logs with different data processings are discussed in detail for the caprock and the reservoir section of all wells. The repeat TPhi logs include the "air" and "air_8.5" data processings only, because the processed TPhi logs using the open hole porosity are equal to the open hole porosity.

TPHI in caprock section

In the cemented caprock section of Ktzi200, the TPhi_air logs are close to the baseline TPhi_noair_BSAL logs. In contrast, in the uncemented caprock section of Ktzi201 and Ktzi202, the TPhi_air logs are much smaller than the baseline TPhi_noair_BSAL logs. TPhi_air_8.5 is much greater than TPhi_air and also greater than the baseline TPhi_noair_BSAL logs in the caprock section of all wells. The "pseudocasing", used for the TPhi_air_8.5 data processing suggests the processing algorithm a much greater borehole effect, which is why the TPhi_air_8.5 logs are significantly greater. Since the annulus is cemented in the caprock section of Ktzi200, TPhi_air_8.5 has the largest values (close to 0.6) compared to the values in Ktzi201 and Ktzi202 (0.45-0.5). Moreover, the TPhi_air_8.5 log is, with 0.6, much greater than the baseline TPhi_noair_BSAL logs and nearly constant in the caprock section. The reason for this is that the cemented annulus does not fit to the "pseudocasing" definition in Ktzi200, where the TPhi_air data processing fits best in the caprock section. In contrast, in Ktzi201 and Ktzi202 (uncemented caprock section) the TPhi_air_8.5 logs are closest to the baseline TPhi_noair_BSAL logs of all data processings, indicating the best TPhi data processing for the caprock section.

TPHI in reservoir section

The smaller repeat TPhi_air values compared to the baseline TPhi_noair_BSAL values in the reservoir section are in the range of -0.05 to 0.25 in the observation wells (Ktzi200 and Ktzi202) and between -0.25 and 0.05 in the injection well (Ktzi201). The negative porosity values in Ktzi201 and partially in Ktzi200, which are initially hard to imagine, correspond to the low TRAT values. These negative values are an effect of both the CO₂ containing annulus and the low hydrogen (brine) content in the reservoir formation. The lowest TPhi values in Ktzi201 compared to the observation wells correspond to the lowest hydrogen (brine) content in the injection well (Ktzi201).

In the reservoir section of Ktzi200 and Ktzi202, the TPhi_air_8.5 logs are greater than the baseline TPhi_noair_BSAL logs. Because of the lowest hydrogen content in the reservoir section of Ktzi201 compared to the reservoir section of the observation wells (Ktzi200 and Ktzi202), the TPhi_air_8.5 logs are correspondingly smaller in Ktzi201 than in Ktzi200 or Ktzi202. Moreover, the TPhi_air_8.5 logs are partially also greater than the baseline TPhi_noair_BSAL logs in the reservoir section of Ktzi201. The unrealistic situation that the TPhi_air_8.5 logs are greater than the baseline TPhi_noair_BSAL logs shows that

smaller corrections are necessary in the reservoir section rather than in the caprock section. Therefore the air data processing is used for the final TPHI logs in the reservoir section of all wells.

TPHI influences the SIGM processing, because the TPHI logs are input parameters for the subsequently derived SIGM logs (compare Chapter 2.4.2). Therefore, an increasing TPHI increases SIGM as well. The SIGM values increase in the following order of the data processings: "air", "air_OH", "air_OH_8.5" and "air_8.5" in both the reservoir and the caprock section in all wells. The SIGM_air_OH logs are greater than the SIGM_air logs, because the open hole porosity is greater than the porosity derived from the processing algorithm (TPHI_air). In contrast, the SIGM_air_OH_8.5 logs are smaller than the SIGM_air_8.5 logs, because the open hole porosity is smaller than the porosity derived from the processing algorithm (TPHI_air_8.5).

Since the differences between the baseline and the repeat SIGM values (SIGM(b-rx)) are the input parameters for the saturation models, the effect of the different data processings on SIGM(b-rx) is evaluated in detail. The bar charts in the figures A.13, A.16 and A.19 given in the appendix summarize SIGM(b-rx) with different data processings for the repeat runs in the evaluated depth ranges. Moreover similar to the baseline runs, the corresponding DSIG logs with different data processings (Figures A.4, A.12, A.6 and A.8) are taken into account. The bar charts (b) and all following bar charts in the figures A.5, A.7 and A.9 given in the appendix summarize the arithmetic mean of the absolute DSIG values with different data processings for the repeat runs in the evaluated depth ranges.

SIGM in caprock section

Similar to the TPHI_air logs, the SIGM_air logs are close to the baseline SIGM_noair_BSAL logs (SIGM(b-rx), i.e. close to zero). Bar chart (b) in figure A.13) shows this effect in the cemented caprock depth range of Ktzi200. But SIGM(b-rx) is closer to zero for the SIGM_air_OH logs rather than for the SIGM_air logs (Bar chart (b) in Figure A.13). Additionally, DSIG is closest to zero for the "air_OH" data processing (Bar chart (c) in Figure A.5) in the caprock section. Therefore, the "air_OH" data processing is used for the second and all subsequent repeat runs in the caprock section of Ktzi200. Similar to DSIG as mentioned above, SIGM(b-r1) is closest to zero for the noair_OH_BSAL data processing in the caprock section (Bar chart (a) in Figure A.13), validating that the noair_OH_BSAL data processing is the best processing for the first repeat run in the caprock section of Ktzi200.

Similar to the TPHI_air_8.5 logs, the SIGM_air_8.5 logs are closest to the baseline logs of all data processings in the uncemented caprock depth ranges of Ktzi201 and Ktzi202 (Bar chart (a) in Figures A.16 and A.19). The corresponding air_8.5 DSIG values are not closest to zero for all data processings (Bar charts (b) in Figures A.7 and A.9). DSIG is closest to zero for the air_OH_8.5 data processings for all repeats in the caprock section of Ktzi201 and Ktzi202.

DSIG in shales is typically in the range of 1 to 4 cu from zero, because they are not characterized in the RST database (Schlumberger, 2011). The range between the minimum and maximum DSIG values of all data processings for all repeats in the caprock section of Ktzi201 and Ktzi202 are mostly within this DSIG range for shales (Figures A.6 and A.8). Moreover, the arithmetic mean of the absolute DSIG values for all data processings and all repeats in the caprock section of Ktzi201 and Ktzi202 are in the range of 0.3 to 2.2 cu (Bar charts (b) in Figures A.7 and A.9), indicating only minor DSIG differences between the different data

processings. Thus, it seems that the DSIG logs are not well suited for the log quality control in the uncemented caprock section of Ktzi201 and Ktzi202, as opposed to the cemented caprock section of Ktzi200.

Since SIGM(b-rx) is closest to zero for the air_8.5 data processing, this processing is used for the repeat runs in the caprock section of Ktzi201 and Ktzi202, even when the corresponding DSIG values do not indicate that this is the best data processing. In summary, it can be confirmed that different data processings are necessary in the caprock section depending on the nature of the annulus (cemented: air_OH for Ktzi200; uncemented: air_8.5 for Ktzi201 and Ktzi202).

SIGM in reservoir section

As mentioned above, the fifth and the sixth repeat in Ktzi200 are characterized by ideal logging conditions in the upper sandstone layer (SS1), because the corresponding brine levels are above the reservoir section. Therefore, the borehole status is "noair" in SS1. The SIGM logs for these repeat runs nearly overlap in SS1 for all different data processings (Bar chart (c) in Figure A.13 or Figure A.10). Thus, below the brine level, the difference between the different data processings is low in Ktzi200. This is true for all different data processings in all wells below the brine level. Moreover, the corresponding DSIG values for the different data processings are also close to each other in Ktzi200. DSIG is closest to zero for the air_OH and air_OH_8.5 data processings (Bar chart (d) in Figure A.5).

As mentioned above, the task is to find a data processing for the fourth repeat, so that this repeat has nearly the same SIGM reading as the fifth and the sixth repeats in SS1. The fourth repeat SIGM is closest to the fifth and sixth repeat SIGM in Ktzi200 for the air_OH data processing. The same is true for the second and the third repeat in Ktzi200 (Bar chart (c) in Figure A.13 or Figure A.10).

Similar to the fifth and the sixth repeat, the DSIG values for the former repeats are also close to each other, where DSIG is closest to zero for the air_OH and air_OH_8.5 data processings (Bar chart (d) in Figure A.5). DSIG with the air_OH (0.7 cu) and air_OH_8.5 (0.6 cu) data processing are roughly equal, and the air_OH data processing is well suited for the reason described above. Therefore, the air_OH data processing is used for the final repeat logs in Ktzi200. As mentioned above, since all wells are characterized by a partly or uncemented annulus in the reservoir section, the air_OH data processing should also fit to the repeats in the reservoir section of Ktzi201 and Ktzi202. For this purpose, the DSIG values are discussed in detail for Ktzi201 and Ktzi202

Similar to Ktzi200, the repeat DSIG values in the reservoir section of Ktzi201 and Ktzi202 are close to each other for the different data processings. In Ktzi201, DISG is closest to zero for the air_8.5 and the air_OH_8.5 data processing in the reservoir section (Bar chart (c), (d), (e) and (f) in Figure A.7). In Ktzi202, DSIG is closest to zero for the air_OH and air_OH_8.5 data processing in the reservoir section (Bar chart (c) and (d) in Figure A.9). In general, the DSIG logs in Ktzi201 and Ktzi202 for the different data processings do not show in all depth ranges for all repeats that the air_OH data processing is the best processing. Thus, it seems that the DSIG logs are not well suited for the log quality control in the reservoir section. But, the following analysis proves that the air_OH data processing is the best processing for all repeats and all wells in the reservoir section.

The SIGM logs of the fifth and sixth repeat runs in Ktzi200 nearly overlap with the baseline SIGM log in the interbedded, strongly cemented sandstone layers of Ktzi200 and Ktzi201.

5. PNG monitoring results at the Ketzin site

Assuming that no saturation changes have occurred between these repeat runs and all former repeat runs, all processed repeat runs should overlap with the baseline SIGM log as well. The air_8.5 and air_OH_8.5 data processings result in greater repeat SIGM values than the baseline SIGM values. Therefore, the air_8.5 and air_OH_8.5 data processings overestimate the "real" Σ (SIGM) reading. In contrast, the air_OH processed SIGM logs nearly overlap with the baseline SIGM logs in the interbedded, strongly cemented sandstone layers of Ktzi200. The same is true in the interbedded, strongly cemented sandstone layers of Ktzi201 and Ktzi202.

Furthermore, as mentioned above, a greater borehole effect (i.e. greater correction necessity) can be expected in the caprock section rather than in the reservoir section. Thus, the air_8.5 data processing, which is the best processing in the caprock section of Ktzi201 and Ktzi202, cannot be the best data processing in the reservoir section of Ktzi201 and Ktzi202 as well. Additionally, the borehole effect in the caprock section should be smaller in Ktzi200 (cemented annulus) rather than in Ktzi201 and Ktzi202 (uncemented annulus). Therefore, the air_OH data processing, which results in smaller corrections than the air_8.5 data processing, is the best processing in both the caprock and the reservoir section of Ktzi200.

Additionally, the "air" data processing fails the second precondition in the reservoir section of Ktzi201, where the repeat SIGM is greater than or equal to the minimum possible repeat value (Equation 4.18). Using the standard repeat SIGM_air logs would result in unrealistic S_{CO_2} maxima of 1.2 even when ϕ_{irr} is transferred to ϕ_{eff} , thus assuming a pure displacement process in ϕ_{tot} . It is unrealistic that ϕ_{irr} is completely overestimated. Even when assuming that ϕ_{irr} is completely overestimated, S_{CO_2} is still greater than one. Therefore, the air data processing underestimates the "real" Σ reading in Ktzi201. This circumstance also shows that the air_OH data processing is the best method in the reservoir section of Ktzi201.

Based on these log quality controls, the air_OH data processing is the best processing for all repeats in all wells. Müller et al. (2007) also used the porosity from the baseline run for the subsequent repeat runs for a time lapse RST monitoring campaign in a saline aquifer CO₂ storage operation. It should be stated here again that the borehole status "air" is only performed above the brine level. Accordingly the "noair" borehole status describes measurements below the brine level. The open hole porosity is used below and above the brine level.

In Ivanova et al. (2012) the standard repeat SIGM_air logs are used to derive the CO₂ saturations based on the displacement saturation model. The effect of the CO₂ within in the uncemented annuli was compensated for by adding 2.4-7 cu to the SIGM_air values. The same saturation model and data processing procedure is applied in Bergmann et al. (2012) to derive the CO₂ saturations. The differences between the repeat SIGM_air_OH and SIGM_air values in the reservoir section above the brine level are between -0.3 and 5.2 cu in Ktzi200, between 2.0 and 11.4 cu in Ktzi201 and between 2.0 and 3.6 cu in Ktzi202. The greater differences in Ktzi201 occur in the upper and lower part of the upper sandstone layer, where greater SIGM_air_OH and SIGM_air values are evident. The smaller or even negative differences occur close to the brine level in all wells. Except for these depth intervals, the compensation range is in good agreement with the air_OH data processing.

The second precondition is true for the standard air data processing, because the used Σ_{br} value in Ivanova et al. (2012) is with 120 cu (240 ppk) greater than the Σ_{br} value (97.58 cu, 193 ppk) derived from the chemical brine composition after Würdemann et al. (2010). The greater Σ_{br} value, based on first approximation, results in an underestimation of the CO₂ saturations. The small Σ difference between the CO₂ value in Ivanova et al. (2012) (0.03 cu) and the value for the Ketzin reservoir conditions (0.014 cu) is negligible compared to

5. PNG monitoring results at the Ketzin site

the large effect of Σ_{br} . However, the average CO₂ saturations for individual depth intervals in the reservoir section of the Ketzin wells given in Ivanova et al. (2012) and Bergmann et al. (2012) are a good estimation, without taking evaporation/precipitation processes or the performed KCl-preflush in Ktzi201 into account. Details of the saturation profiles based on the environmental corrected intrinsic data with the most appropriate data processings, the conventional and the extended saturation model are discussed in chapter 5.3.

The differences between the repeat SFFA logs and the corresponding repeat SIGM_air_OH logs in the reservoir section above the brine level are between -2.5 and 2.0 cu in Ktzi200, between -3.0 and 2.5 cu in Ktzi201 and between -1 and 2 cu in Ktzi202. Only in the upper (minimum -6.5 cu for all repeat runs) and lower part (minimum -4.5 for all repeats, except sixth repeat run) of the upper sandstone layer and the middle part of the lower sandstone layer (minimum -4.5 cu for second and third repeat runs) of Ktzi201 greater differences occur. These greater differences correspond to higher repeat SFFA readings. Moreover, lower positive differences (between 0.5 and 1.5 cu) correspond to low repeat SFFA readings, which is the case in the middle part of the upper sandstone layer of Ktzi200 and Ktzi201. This circumstance can be expected, since the imprecision and borehole effects decreases as the formation Σ (SFFA) decreases (Kimminau and Plasek, 1992).

For the fifth and the sixth repeat run in Ktzi200 (brine level above upper sandstone section), the differences between the repeat SFFA logs and the corresponding repeat SIGM_air_OH logs is between zero and 1.2 cu in the upper sandstone layer. Thereby, the positive difference (SFFA > SIGM_air_OH) correspond to high DIFF values (DIFF = SBNA - SFFA). It can, therefore, be confirmed that for a SBNA much greater than SFFA (high DIFF), the apparent SFFA logs are greater than the intrinsic SIGM_air_OH logs for the fifth and the sixth repeat run in the upper sandstone layer of Ktzi200 (Neutron Diffusion; Chapter 2.3.1).

As mentioned above (Chapter 5.2.1), the repeat SBNA logs in Ktzi201 have generally higher values than the repeat SBNA logs in the observation wells, except for the fifth and sixth repeat run in Ktzi200. According to the neutron diffusion description in chapter 2.3.1 and similar to the fifth and sixth repeat run in Ktzi200, one would expect that the apparent SFFA logs are greater than the intrinsic SIGM_air_OH logs. This is true in the middle part of the upper sandstone layer of Ktzi201, where the repeat SFFA readings are low as mentioned above.

Moreover, according to the neutron diffusion description, SFFA should be smaller than SIGM, when SBNA is smaller than SFFA. As mentioned above, negative differences (SFFA < SIGM_air_OH) occur in the upper and lower part of the upper sandstone layer and the middle part of the lower sandstone layer of Ktzi201. But in these depth intervals SBNA is greater than SFFA, which does not correspond to the neutron diffusion theory. But the SFFA values are greater in these depth intervals than in the middle part of the upper sandstone layer. Therefore, only the general trend of the neutron diffusion theory can be confirmed for the case SFFA smaller than SIGM. Thus, for an increased SFFA reading by a nearly constant SBNA reading, SFFA is smaller than SIGM_air_OH. It should be stated here again, as mentioned in chapter 5.2.1 that the higher SBNA reading in the upper sandstone layer of Ktzi200 should result from the reservoir. A material with a large Σ value, like halite, could account for the increased SBNA reading in Ktzi201. Thus, SBNA does more reflect the reservoir than the borehole. The higher SBNA reading in the upper sandstone layer of Ktzi200 could be the reason that SBNA is greater than SFFA, and only the general trend of the neutron diffusion theory can be confirmed.

Bonnie (1991) evaluated various PNC logging tools from different service companies under well-defined laboratory conditions. Nearby tools from other service companies, the Thermal

Decay Tool, which is Schlumberger's PNG tool previous to the RST, was evaluated. All tools have problems in handling air- or gas-filled boreholes. For an 8.5 inch borehole size, 7 inch casing and a cemented annulus (most similar well completion compared to the Ketzin site well completion), the difference between the processed and the intrinsic Σ value is in the range of -1 and 3 cu for all evaluated PNC logging tools. The next generation RST has an improved data processing algorithm and further hardware improvements that a better accuracy can be expected for the RST than for the Thermal Decay Tool.

In fact, the "real" intrinsic repeat Σ values of the formation are not known, but the differences between the apparent repeat SFFA logs and the corresponding intrinsic repeat SIGM_air_OH logs are in close agreement with the findings from Bonnie (1991), even when the annuli of the wells at the Ketzin site are partly or not cemented. Moreover, it can be confirmed that for small SFFA readings the corresponding intrinsic SIGM values are closest to SFFA, which is the case in the middle part of the upper sandstone layer of Ktzi200 and Ktzi201. These SIGM values have the greatest accuracy, since the imprecision decreases as the formation Σ (SFFA) decreases (Kimminau and Plasek, 1992).

Below the brine level, the differences between the repeat SFFA logs and the corresponding repeat SIGM_air_OH logs in the reservoir section are between -0.6 and 1.3 cu in Ktzi200, between -0.7 and 0.5 cu in Ktzi201 and close to zero in Ktzi202. Similar to the baseline SFFA and SIGM logs, the differences below the brine level between the repeat SFFA logs and the corresponding repeat SIGM_air_OH logs are small. Thus, similar to the baseline logs the general influence of the environmental corrections on the intrinsic data is also low for the repeat logs below the brine level, because the difference between SFFA and SIGM_air_OH is small.

Figure 5.8 summarizes the environmental corrected intrinsic baseline SIGM (noair_BSAL data processing), repeat SIGM (air_OH data processing), baseline TPHI (noair_BSAL data processing) and repeat TPHI (air data processing) logs for all wells.

5.3. Saturation profiling at the reservoir section

Based on the environmental corrected intrinsic data, the conventional displacement saturation model including the boundary conditions (Chapter 4.1) and the extended displacement and evaporation/precipitation saturation model, the saturation profiles are calculated for the different repeat runs in each well. Since large amounts of dry CO₂ enter the reservoir in the injection well, associated with an evaporation/precipitation tendency, it can be assumed that the extended saturation model is needed for the injection well. In contrast, in the observation wells, only the conventional saturation displacement model should be valid, because it can be assumed that the arriving CO₂ is already water saturated and no water can be further evaporated. But when a S_{CO_2eff} greater than one is calculated in the observation wells, the extended saturation model is applied.

As described in chapter 4.3, information about the remaining water saturation is required for determining the evaporation/precipitation process. This information could be derived from induction, NMR, CHFR or neutron porosity logs. Neutron porosity logs have no special requirements regarding the well completion. In contrast, induction or NMR logs need an electrically non-conductive well completion including casing material (fiberglass) or installations behind casing (no metallic cable). NMR logs can be used to derive water saturation with additional information about the water mobility. Induction logs can be used for brine

5. PNG monitoring results at the Ketzin site

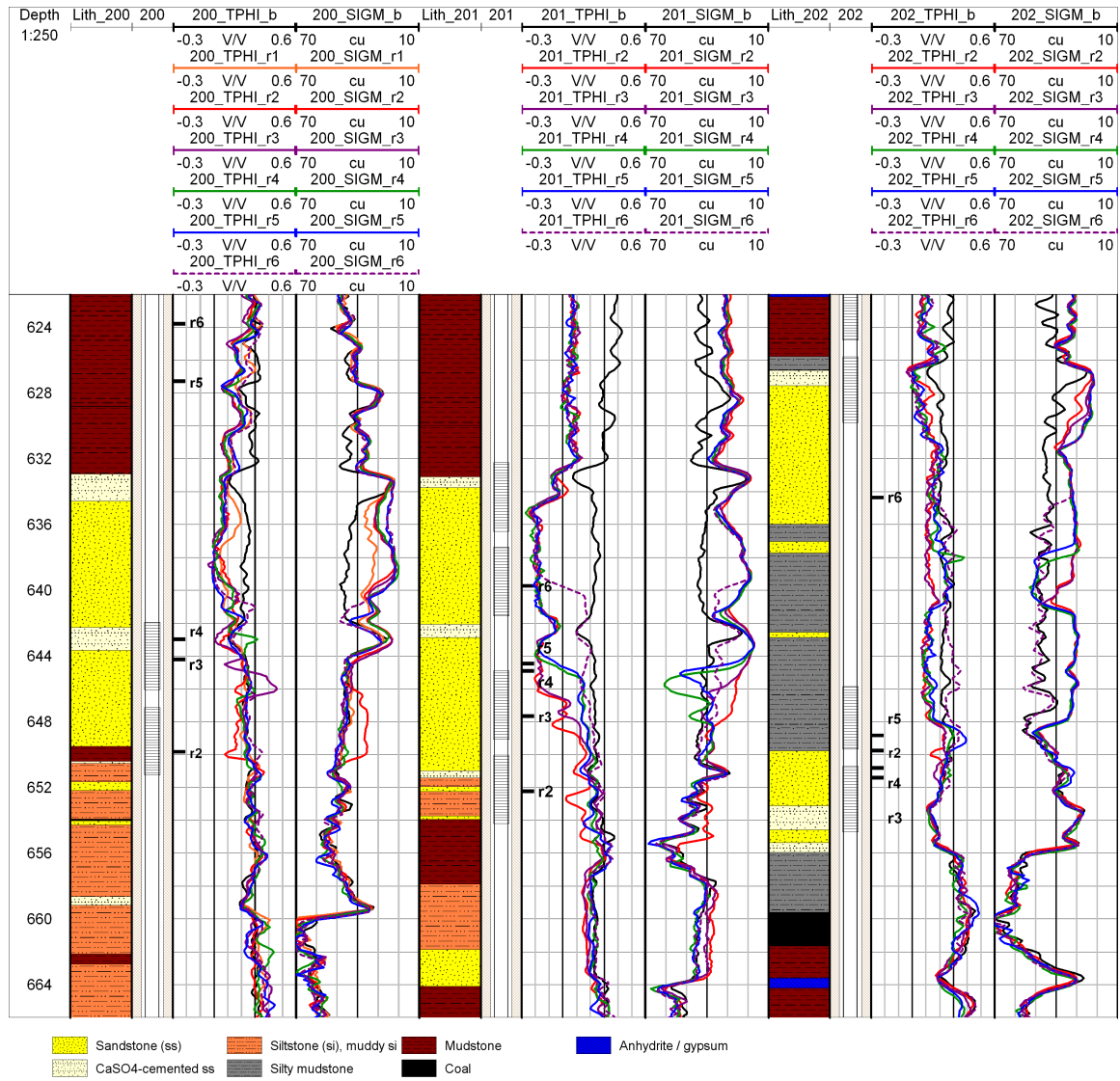


Figure 5.8.: SIGM and TPHI logs for the baseline (SIGM and TPHI with noair_BSAL data processing) and repeat (SIGM with air_OH and TPHI with air data processing) runs for all wells. The brine levels for each repeat run are marked with a black bar on the left side of the TPHI tracks for each well. Lithology after Förster et al. (2010)

determination. CHFR logs are applicable in steel cased wells, where the outside surface of the casing is not coated by electrically isolated materials. Since both the production casings in the reservoir section are steel made and coated, induction, NMR and CHFR measurements are ruled out. Therefore, only the neutron porosity logs (TPHI) are suitable for deriving information about the remaining water saturation for this well completion.

5.3.1. Displacement saturation model

The saturation profiles based on the conventional displacement saturation model including the boundary conditions are calculated after equation 4.6, with the environmental corrected intrinsic baseline, repeat SIGM logs and the Ketzin fluid Σ values (Chapter 5.1.2). Moreover, $S_{CO_2tot-TPHI}$ (Equation 4.38) is derived from the baseline (TPHI_b, noair_BSAL data processing) and repeat (TPHI_r, air data processing) TPHI values, where the fluid HI values of the Ketzin formation brine ($HI_{org}=0.92$) and the CO_2 ($HI_{CO_2}=0$) are used as input parameters (Chapter 2.2.2).

The saturation profiles for the repeat runs are shown in figures 5.9, A.12, 5.12, 5.13 and 5.14 for the wells Ktzi200, Ktzi201 and Ktzi202 respectively. CO_2 (S_{CO_2} in green) and accordingly brine (S_{br} in blue) are shown as fractions of ϕ_{tot} for each repeat run. In the following sections, all saturations are related to ϕ_{tot} . Therefore, the additional subscript "tot" is absent. The orange logs (S_CO2_rx-TPHI) are the CO_2 saturations derived from the TPHI logs for each repeat run.

Negative saturations and saturations greater than one are not possible. The resulting Σ difference between the measured Σ_r and the modeled Σ_{r_m} value, within these saturation boundaries, are described by the Diff logs (solid signature) for each run. Diff is positive when the measured (Σ_r) value is greater than the modeled (Σ_{r_m}) value. Thus, the repeat Σ value is greater than the baseline Σ value, when the saturation boundary S_{CO_2} equal to zero is used. For this situation the extended saturation model with the scenario $\Sigma_r > \Sigma_b$ described in chapter 4.3.2 is applied.

In contrast, Diff is negative when the repeat Σ is smaller than the baseline Σ value, when the saturation boundary S_{CO_2} equal to one is used. Negative differences do not occur for all repeat runs in all wells, except for the second and third repeat run at 643.07 m in Ktzi201, indicating that the second precondition is valid, where the repeat Σ is greater than or equal to the minimum possible repeat value (Equation 4.18). At 643.07 m in Ktzi201, Diff is 0.46 cu small.

The white logs shown in each repeat run are identical for each well. The left hand side of this log is the mobile (ϕ_{eff}/ϕ_{tot}), and the right hand side is the immobile (ϕ_{irr}/ϕ_{tot}) brine. Therefore, a S_{CO_2} value greater than the value from this white log (S_{CO_2} greater than $1 - S_{br_{irr}}$) suggests that, in addition, to displacement, the evaporation/precipitation process is occurring. This "apparent" S_{CO_2} fraction, which can not be displaced, is shown in light green. The corresponding Diff logs (dotted signature) are the remaining differences ($\Delta\Sigma_{r_{irr}}$, Equation 4.21) between the measured Σ_r and the modeled Σ_{r_m} values when only ϕ_{eff} is completely CO_2 saturated ($S_{CO_2_{eff}}=1$) and the saturation in ϕ_{irr} ($S_{CO_2_{irr}}=0$) remains unchanged. Thus, Diff with dotted signature is the Σ correction for the displacement model with the boundary condition $S_{CO_2_{irr}}$ equal to zero. The Diff (dotted signature) values are negative in these depth intervals, because Σ_{r_m} is greater than Σ_r . For this situation the extended saturation model with the scenario $\Sigma_r \leq \Sigma_b$ described in chapter 4.3.1 is applied. When Diff solid signature and

Diff dotted signature are zero, the displacement saturation model is valid. Thus, the derived saturation profile give rise to the Buckley and Leverett (1942) saturation profile, where the brine saturation cannot be reduced below the immobile brine saturation.

The mean S_{CO_2} values (Tables 5.7, 5.8 and 5.9) are based on the S_{CO_2} values derived from Σ . Moreover, The mean S_{CO_2} values include the "apparent" S_{CO_2} fraction (light green signature), because this "apparent" S_{CO_2} fraction is derived from equation 4.6, which is the conventional approach to derive S_{CO_2} without the boundary conditions. Thus, for the case that the displacement saturation model is valid (absent "apparent" S_{CO_2} fraction and scenario $\Sigma_r \leq \Sigma_b$ is valid), the mean S_{CO_2} values are "real". In contrast, for the case that an "apparent" S_{CO_2} fraction exist and/or the scenario $\Sigma_r > \Sigma_b$ is valid, the extended saturation model is needed to derive the "real" S_{CO_2} values and thus the "real" mean S_{CO_2} values. This approach regarding the mean S_{CO_2} values derived from the displacement saturation model is applied to all wells.

5.3.1.1. Ktzi200 observation well

Since the first repeat was only performed in Ktzi200, the corresponding saturation profile based on the conventional displacement saturation model is presented separately in the appendix (Figure A.12). S_{CO_2} has a maximum of 0.53 in SS1 and 0.15 in SS2. The mean S_{CO_2} is 0.36 in SS1 and close to zero (0.03) in SS2. Since Diff with dotted signature is always zero, the extended saturation model with the scenario $\Sigma_r \leq \Sigma_b$ is not needed for the first repeat run.

Compared to the first repeat, S_{CO_2} increases in SS1 for all subsequent repeat runs (Figure 5.9). The shape of the CO_2 saturation profile is roughly equal for the second, third and fourth repeats. In contrast, S_{CO_2} increases in the upper and decreases in the lower part of SS1 for the fifth and the sixth repeat. The mean S_{CO_2} is roughly equal (0.55-0.62) for the second and all subsequent repeats, because the increased and decreased saturations compensate each other. The maximum S_{CO_2} , derived during the fourth repeat, is 0.91 in SS1. The middle part of SS1, S_{CO_2} indicates that the extended saturation model with the scenario $\Sigma_r \leq \Sigma_b$ is needed for the second and all subsequent repeat runs (light green S_{CO_2} signature). The application of the extended saturation model for this depth interval is discussed in chapter 5.3.2.1. Moreover, in the interbedded, strongly cemented sandstone layer, S_{CO_2} indicates that the extended saturation model is needed for the second, third and fifth repeats. Since ϕ_{eff} is close to zero in this cemented sandstone layer, and therefore small Σ changes result in great S_{CO_2} values, the extended saturation model is not applied.

5. PNG monitoring results at the Ketzin site

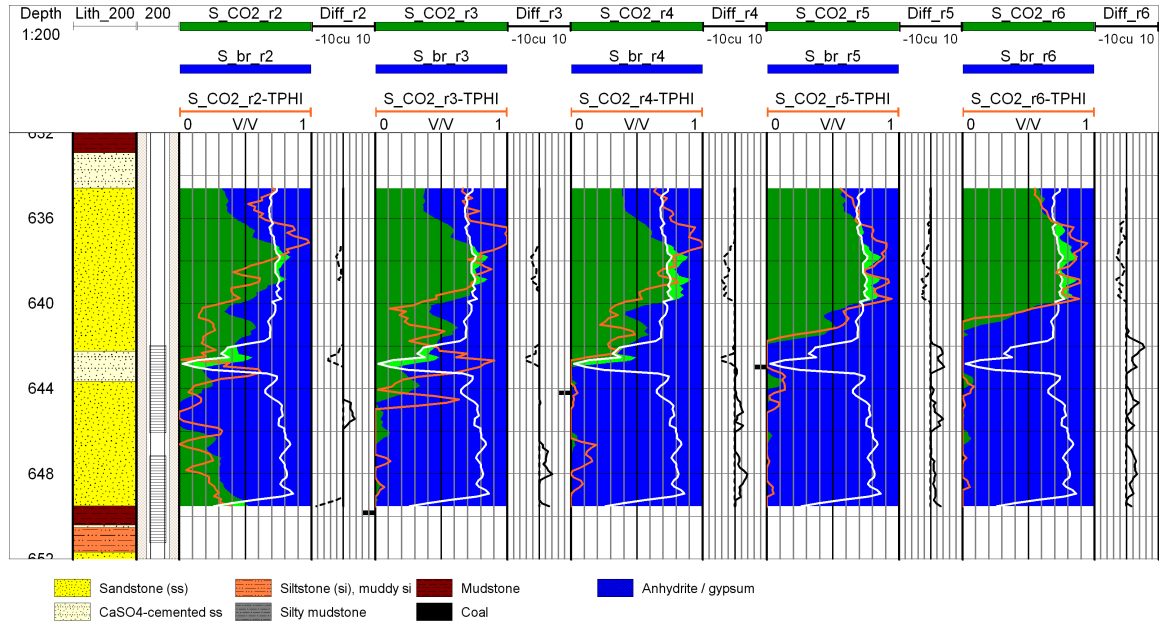


Figure 5.9.: Ktzi200: Saturation profiles as fractions of ϕ_{tot} (displacement conform CO_2 in green, apparent CO_2 in light green and brine in blue), S_{CO_2} derived from TPHI (orange logs) (first track) and the corresponding Diff logs with solid and dotted signature (second track) for five repeat runs based on the *displacement saturation model*. The white log for each repeat run separates the mobile from the immobile brine. The brine levels for each repeat run are marked with a black bar on the right side of the second track. For the fifth and the sixth repeat run, the brine levels are above the displayed depth range. Lithology after Förster et al. (2010)

Compared to the first repeat, S_{CO_2} increases in SS2 for the second repeat and then decreases for all subsequent repeat runs. The maximum S_{CO_2} is 0.53, derived during the second repeat, which is also the repeat with the greatest mean S_{CO_2} (0.22). From the second to the third repeat, S_{CO_2} decreases, especially in the lower part of SS2. The mean S_{CO_2} for the third repeat is 0.06. From the third to all subsequent repeats, S_{CO_2} decreases to practically zero in SS2. Table 5.7 summarizes the mean S_{CO_2} in SS1 and SS2 for all repeat runs.

Diff with solid signature is zero in SS1 for all repeat runs, except for the first and sixth repeat in the lower most part of SS1. In the middle part of SS1, Diff with dotted signature is the Σ fraction on which the extended saturation model is applied.

Small positive (range of 2-6 cu) Diff (solid signature) values occur partially in SS2 for all repeat runs, indicating that the repeat Σ values are greater than the baseline Σ values in these depth intervals. The same is true for the first and sixth repeat runs in the lower most part of SS1. Therefore, using the displacement saturation model, no CO_2 saturation is possible in these depth intervals. However, practically Σ_r and Σ_b overlap, because the imprecision increases as formation Σ increases (Kimminau and Plasek, 1992).

For the first repeat run, S_{CO_2} derived from TPHI (orange log) is mostly greater than S_{CO_2} derived from Σ in SS1 and SS2. The shape of the two S_{CO_2} profiles are similar. For the second, third and fourth repeat runs, S_{CO_2} derived from TPHI is greater than S_{CO_2} derived from Σ in the upper part of SS1. In the remaining depth range of SS1 and in SS2, S_{CO_2}

5. PNG monitoring results at the Ketzin site

Table 5.7.: Ktzi200: Mean S_{CO_2} in the upper (SS1) and lower (SS2) reservoir sandstone sections for six repeats based on the conventional displacement model.

Section	r1	r2	r3	r4	r5	r6
SS1	0.36	0.55	0.58	0.61	0.62	0.58
SS2	0.03	0.22	0.06	0.01	0.01	0.01

derived from TPHI is mostly smaller than S_{CO_2} derived from Σ . The shape of the two S_{CO_2} profiles are relatively similar in SS1 and SS2, except for the third repeat in the upper most part of SS2 (644.2-645.0 m), where the low TPHI reading correspond to high CO_2 saturations (compare Figure 5.8). For the fifth and sixth repeat runs, S_{CO_2} derived from TPHI is closest to S_{CO_2} derived from Σ for all repeat runs in SS1. Moreover, the shape of the two S_{CO_2} profiles are most similar to all repeat runs in SS1.

In contrast to the former repeat runs, the fifth and the sixth repeat runs are characterized by brine levels above SS1. This ideal logging condition is the reason, why S_{CO_2} derived from Σ and TPHI are in good agreement. Similar to S_{CO_2} derived from Σ , S_{CO_2} derived from TPHI is mostly close to zero for the fifth and the sixth repeat in SS2.

Since the brine level for the first repeat is also above the reservoir section, one would expect that S_{CO_2} derived from Σ and TPHI to be in good agreement, as it is the case with the fifth and the sixth repeat. But for the first repeat, S_{CO_2} derived from TPHI is greater than S_{CO_2} derived from Σ in SS1 (Figure A.12). Since TPHI is more influenced by borehole effects than Σ (Chapter 2.4), it can be expected that S_{CO_2} derived from TPHI is greater than S_{CO_2} derived from Σ . Moreover, for the first, fifth and sixth repeat the same data processing (noair_OH) is applied below the brine level. Therefore, there must be a difference in the borehole effects between the first and the fifth/sixth repeat runs. Since the first repeat was performed immediately after the arrival of the CO_2 was observed in this observation well, the brine level within the well is far away from the reservoir, but the partly cemented annulus could contain CO_2 . This is the reason why S_{CO_2} derived from TPHI is greater than S_{CO_2} derived from Σ for the first repeat. Conversely it can be said that for the fifth and the sixth repeat, the annulus contains formation brine in SS1.

5.3.1.2. Ktzi201 injection well

The baseline run was performed on June, 9th 2008. Ten days later (June, 19th) a KCl-preflush was performed in Ktzi201 in order to reduce the brine salinity and thus the amount of NaCl that can precipitate. The first repeat in Ktzi201 (second repeat in general) took place roughly one year later, on June, 24th 2009. Unfortunately, no second baseline run performed immediately after the KCl-preflush is available. This second baseline run would have allowed observation of the sweep efficiency of the mobile brine displacement due the KCl-preflush injection. This situation would be similar to a classical log-injection-log experiment (Dewan et al., 1973), where the properties of the injected fluid are well known. For this purpose, an artificial baseline log is developed in order to factor in the KCl-preflush.

KCl-preflush

From temperature anomalies (derived from the permanent temperature monitoring via the distributed temperature sensing method (DTS)), the KCl-preflush injection intervals can be

5. PNG monitoring results at the Ketzin site

determined (Figure A.20). Since the KCl-preflush has a lower temperature than the reservoir formation, the temperature anomalies are negative. Based on a qualitative analysis (thus depth intervals with high temperature anomalies) the KCl-preflush was mainly injected into SS1 and SS2. Moreover, low temperature anomalies also occur in Silt and SS3. To have a conservative depth range where the KCl-preflush was injected, the complete reservoir section from the upper boundary of SS1 (633.78 m) to the lower boundary of SS3 (664.10 m) is taken into account.

The total KCl-preflush volume is 30.5 m³, with a salinity of 60 ppk KCl (van der Wall et al., 2008). The KCl-preflush density under reservoir conditions, calculated after Mao and Duan (2008), is 1.04 g/cm³. Similar to the formation brine Σ value, the KCl-preflush value (Σ_{br-KCl}) is calculated based on the Σ brine calculation (Chapter 2.2.1.3). Σ_{br-KCl} is 39.50 cu, where the water ($\Sigma_{H_2O_c}$) contributes with 21.64 cu and the dissolved KCl (Σ_{KCl_c}) with 17.86 cu.

It is assumed that the total KCl-preflush volume is injected homogeneously over the depth range. Thus, the individual injection volume (0.152 m³) for each depth increment is derived by dividing the total volume (30.53 m³) by the total number of depth increments (201). It is assumed, that this depth increment volume is only injected in ϕ_{eff} , displacing the mobile brine. The original formation brine in ϕ_{irr} is unaffected by the injection. Moreover, under the assumption that all mobile brine is completely displaced, a KCl-preflush radius can be calculated based on a radially symmetrical geometry. The KCl-preflush radius is always greater than one meter, where large radii correspond to low ϕ_{eff} . Since one meter is the depth of investigation for common PNG tools with high gas saturations in the formation (Knödel et al., 1997), and the KCl-preflush radius is always greater than one meter, no mixture of original brine and preflush brine has to be taken into account in ϕ_{eff} .

A salinity equilibration due to diffusion between the low salinity preflush brine (ϕ_{eff}) and the high salinity formation brine (ϕ_{irr}) is assumed. The following mixing equation account for the salinity equilibration described by the $\Sigma_{KCl_c/NaCl_c}$ log (not shown) , where the dissolved KCl (Σ_{KCl_c}), the Σ salt value for the NaCl-equivalent Ketzin formation brine (Σ_{NaCl_c-eq} , Table 5.1) and the porosity fractions are the input parameter.

$$\Sigma_{KCl_c/NaCl_c} = \Sigma_{KCl_c} \cdot \frac{\phi_{eff}}{\phi_{tot}} + \Sigma_{NaCl_c-eq} \cdot \frac{\phi_{irr}}{\phi_{tot}} \quad (5.1)$$

The corresponding NaCl-equivalent concentrations are calculated as follows:

$$c_{NaCl_{eq}} = \frac{\Sigma_{KCl_c/NaCl_c}}{\sigma_{m_{NaCl}}} \quad (5.2)$$

The flush brine log (SIGM_br_fl), which includes the salinity equilibration, is calculated based on the Σ brine calculation (Chapter 2.2.1.3). SIGM_br_fl is shown in figure 5.23. The final flush baseline SIGM log (SIGM_b_fl) results from $\Sigma_{b_{ma}}$ (Equation 4.15), SIGM_br_fl and ϕ_{tot} . Moreover, Σ_{br} have to be replaced by SIGM_br_fl and the SIGM_b_noair_BSAL by the SIGM_b_fl log for all Σ related equations.

SIGM_b_fl has smaller values than the original baseline SIGM_b_noair_BSAL values (Figure 5.10). Moreover, the repeat SIGM values are greater than the SIGM_b_fl values in the lower and upper part of SS1, Silt and SS3 for all repeat runs. In SS2 the depth range, where the repeat SIGM values are greater than the SIGM_b_fl values, increases from the

5. PNG monitoring results at the Ketzin site

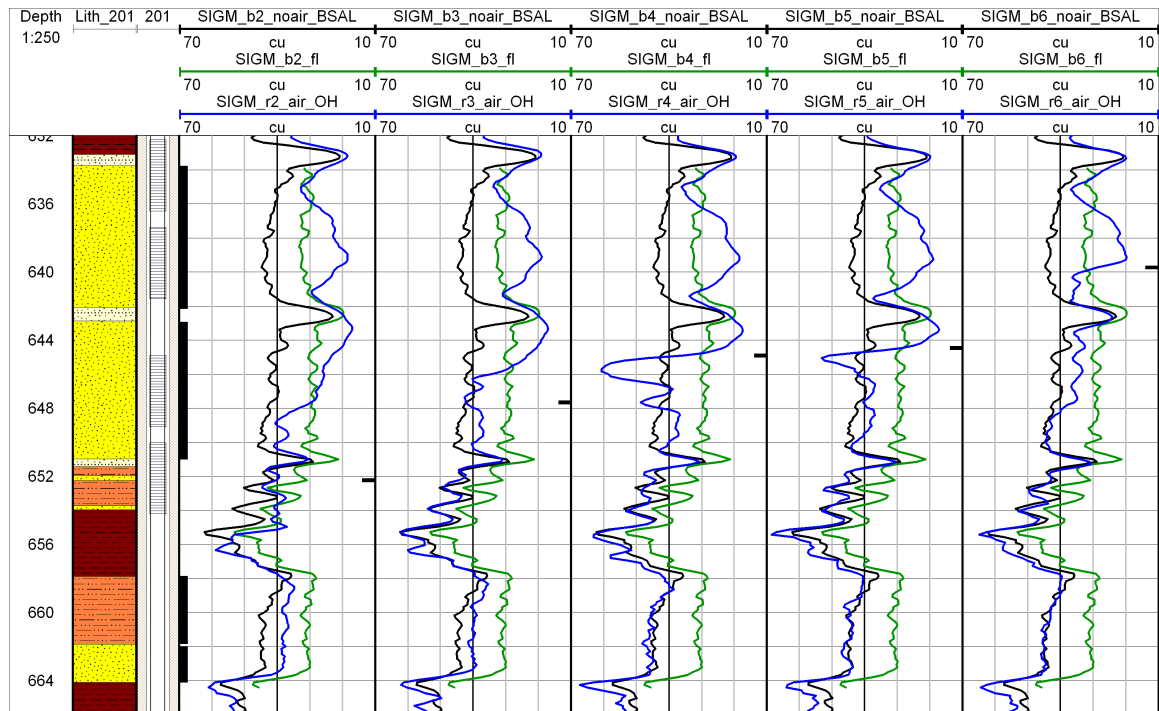


Figure 5.10.: Ktzi201: SIGM baseline log (noair_BSAL data processing), SIGM baseline log including the flush brine salinity (SIGM_b_fl) and the SIGM repeat logs (air_OH data processing). The brine levels for each run are marked with a black bar on the right side of each track. Lithology after Förster et al. (2010)

second to all subsequent repeat runs. In contrast, the repeat SIGM values are smaller than the SIGM_b_noair_BSAL values or nearly overlap with the SIGM_b_noair_BSAL logs in all evaluated depth sections, except for the fourth and the fifth repeat in SS2, which are characterized by peaks (645-648 m) below the brine level that are greater than the baseline log.

Therefore, large differences in the calculated saturation profiles using the displacement saturation model can be expected when using the flush-brine parameters instead of the original brine parameters. Details of the saturation profiles using the displacement saturation model are discussed in the following section. Moreover, using the original brine parameters, the scenario $\Sigma_r \leq \Sigma_b$ is mostly applied (Chapter 4.3.1). In contrast, using the flush brine parameters, the scenario $\Sigma_r > \Sigma_b$ is mostly applied (Chapter 4.3.2). Details of the saturation profiles using the extended saturation model is discussed in chapter 5.3.2.2.

The HI log for the flush-brine (HI_{fl}) is calculated based on equation 2.20 given in the chapter 2.2.2 with SIGM_br_fl as the input parameter. Similar to the final flush baseline SIGM log, the final flush TPhi baseline logs ($TPHI_{b_fl}$) results from equation 4.15, but with $TPHI_{b_{ma}}$ and HI_{fl} instead of $\Sigma_{b_{ma}}$ and SIGM_br_fl as input parameter. $TPHI_{b_{ma}}$ is former calculated from equation 4.15, with the Ketzin NaCl-equivalent HI_{org} brine value (0.92, Chapter 2.2.2) as input parameter. $TPHI_{b_fl}$ is always greater than the initial $TPHI_{b_noair_BSAL}$, because HI_{fl} from the lower flush salinity is always greater than HI_{org} from the original salinity. Furthermore, HI_{org} must be replaced by HI_{fl} in equation 4.38, when $S_{CO_2tot-TPHI}$ is derived with $TPHI_{b_fl}$ as input parameter.

In contrast to the original and flush baseline SIGM logs, the original and flush baseline TPhi logs practically overlap, because TPhi is less affected by changing salinities (Figure 5.11). Therefore, it can expected that minor differences between $S_{CO_2tot-TPHI}$ derived from the original brine or the flush brine parameters occur.

Saturation profile original brine salinity

Since all repeat Σ runs, except the sixth repeat run, nearly overlap in SS1, S_{CO_2} is roughly similar for these repeat runs (Figure 5.12). Moreover, the shape of the CO_2 saturation profile is roughly equal for these repeat runs in SS1. Similar to Ktzi200, S_{CO_2} in the middle part of SS1 is greatest, also indicating that the extended saturation model is needed for all repeats runs (light green S_{CO_2} signature). Moreover, S_{CO_2} indicates in the upper most part of SS1 close to the interbedded, strongly cemented sandstone layer that the extended saturation model is needed for all repeat runs. Since ϕ_{eff} is small, and therefore small Σ changes result in great S_{CO_2} values, the extended saturation model is not applied.

S_{CO_2} in the upper and lower part are smaller than in the middle part of SS1 for all repeat runs, indicating that the middle part of SS1 has the highest injectivity. S_{CO_2} in the upper part of SS1 is roughly similar for all repeats. The highest CO_2 saturations occur for the second repeat run, and then S_{CO_2} decreases for all subsequent repeat runs in the lower part of SS1. S_{CO_2} is lowest for the sixth repeat run in the lower part of SS1, which also correlates with the rising brine level from the fifth to the sixth repeat run. The mean S_{CO_2} is greatest for the second repeat (0.67) and then decreases for all subsequent repeats (Table 5.8). The lowest mean S_{CO_2} occur for the sixth repeat run in SS1 (0.50).

For the second repeat run, S_{CO_2} is maximal in the upper part, also indicating that the extended saturation model with the scenario $\Sigma_r \leq \Sigma_b$ is needed, and decreases with increasing depth in SS2. The same is true for the third, fourth and fifth repeat runs, except in the

5. PNG monitoring results at the Ketzin site

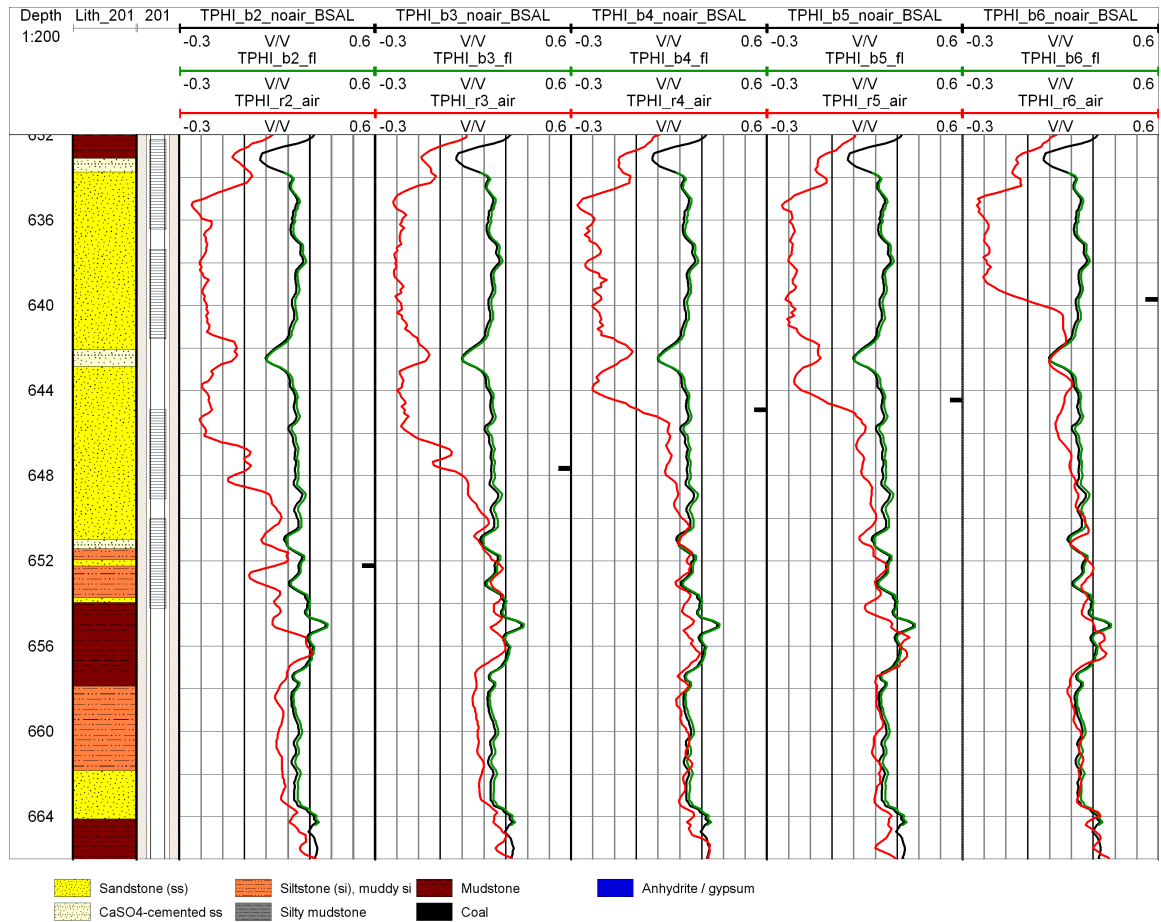


Figure 5.11.: Ktzi201: TPHI baseline log (noair_BSAL data processing), TPHI baseline log including the flush brine salinity (TPHI_b_fl) and the TPHI repeat logs (air data processing). The brine levels for each run are marked with a black bar on the right side of each track. Lithology after Förster et al. (2010)

5. PNG monitoring results at the Ketzin site

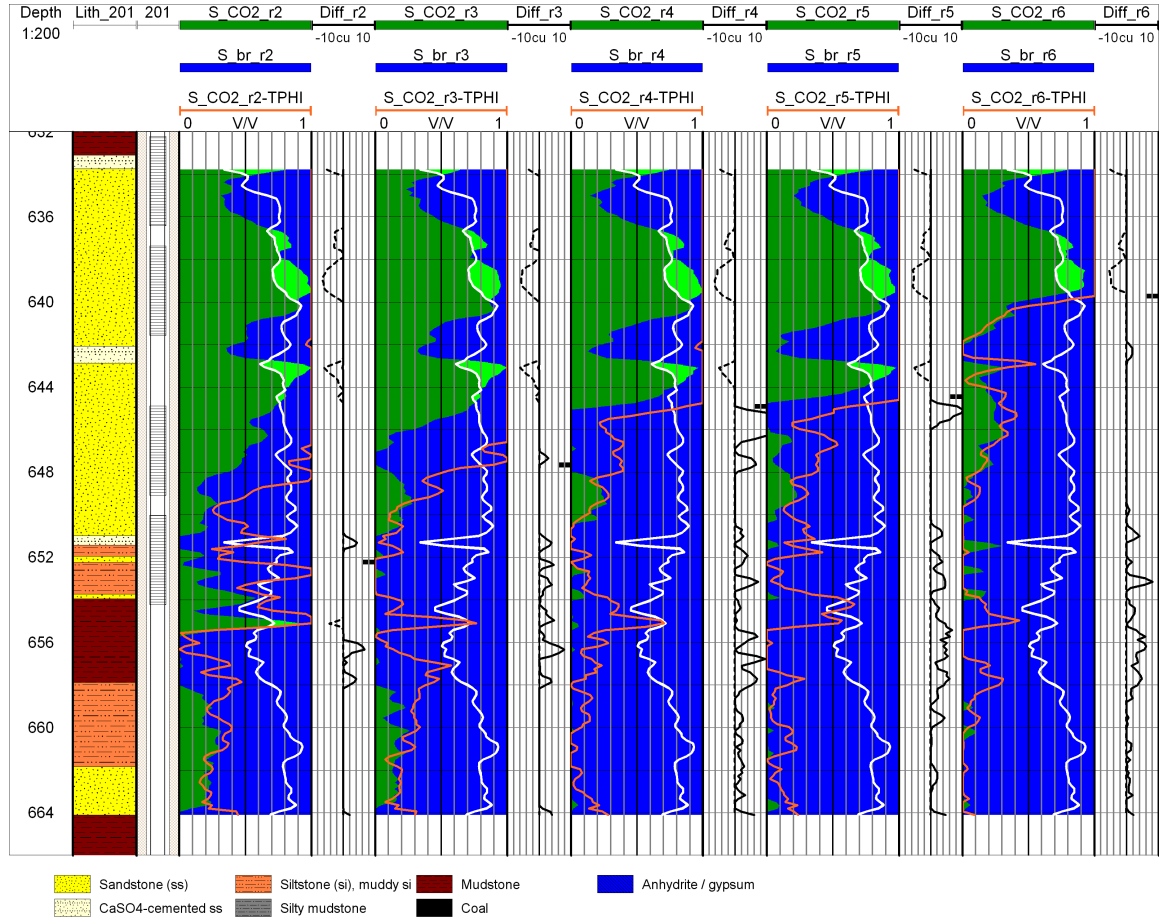


Figure 5.12.: Ktzi201: Saturation profiles as fractions of ϕ_{tot} (displacement conform CO₂ in green, apparent CO₂ in light green and brine in blue), S_{CO_2} derived from TPHI (orange logs) (first track) and the corresponding Diff logs with solid and dotted signature (second track) for five repeat runs based on the *displacement saturation model and the original brine salinity*. The white log for each repeat run separates the mobile from the immobile brine. The brine levels for each repeat run are marked with a black bar on the right side of the second track. Lithology after Förster et al. (2010)

5. PNG monitoring results at the Ketzin site

middle part of SS2 where S_{CO_2} is zero. S_{CO_2} derived from the displacement saturation model is zero, because the repeat Σ values are greater than the baseline Σ values. For this purpose, the extended saturation model with the scenario $\Sigma_r > \Sigma_b$ is needed. In the upper and lower part of SS2, S_{CO_2} is roughly constant for these repeat runs. Compared to the fifth repeat run, S_{CO_2} increases in the middle part for the sixth repeat run, since the repeat Σ values are smaller than the baseline Σ values. In the upper and lower part of SS2, S_{CO_2} decreases for the sixth repeat run. In contrast to all former repeat runs, S_{CO_2} results do not indicate that the extended saturation model with the scenario $\Sigma_r \leq \Sigma_b$ is needed for the sixth repeat run in the upper part of SS2.

In Silt and SS3, the second and third repeat run shows a CO_2 saturation. The CO_2 saturation is relatively constant over the complete depth range of Silt and SS3 for these repeat runs. The mean S_{CO_2} is maximal for the second repeat run in Silt (0.21) and SS3 (0.18) and decreases slightly for the third repeat run. For all subsequent repeat runs, the S_{CO_2} values are close to zero in Silt and SS3. Thus, the mean S_{CO_2} for all subsequent repeats is practically zero. The CO_2 saturation in Silt and SS3 for the second and third repeat runs corresponds to the high injection rate before March 2010. Thus, after the CO_2 enters the open annulus via the lower filter screen section, the CO_2 moves downward in the open annulus and goes into the next neighbored high permeable Silt and SS3.

The calculated S_{CO_2} values, for the second repeat run in the thin sandstone, siltstone and mudstone layers below SS2 and above Silt are influenced by large vertical lithology heterogeneities (compare Figure 5.2) that are in the range of the RST vertical resolution (38.1 cm, Schlumberger (2011)). The mudstone layer especially is not defined by the RST processing algorithm, since the three possible matrices are sandstone, limestone and dolomite (Chapter 2.4.2). Moreover, ϕ_{eff} is relatively low in these layers, and therefore small Σ changes result in great calculated S_{CO_2} values. Due to the rising brine level, all subsequent repeat runs have much lower S_{CO_2} values compared to the S_{CO_2} values from second repeat run in this depth interval. This depth interval, below SS2 and above Silt, is not taken into account for the extended saturation model.

Diff with solid signature is zero in SS1 for all repeat runs. Similar to Ktzi200, in the middle part of SS1, Diff with dotted signature is the Σ fraction on which the extended saturation model is applied. Compared to Ktzi200 (-4 cu), Diff with dotted signature is smaller in Ktzi201 (-6 cu). Therefore, greater S_{NaCl} values can be expected in Ktzi201 than in Ktzi200. In the lower most part of SS2, Diff with solid signature has small positive values (range of 2-4 cu). Similar to SS2 in Ktzi200, Σ_r and Σ_b practically overlap in the lower most part of SS2. For the fourth and the fifth repeat runs, Diff with solid signature have large values in the middle part of SS2 directly below the corresponding brine levels. The maximum value at 645.6 m is 21 cu for the fourth repeat run. In these depth intervals, the extended saturation model with the scenario $\Sigma_r > \Sigma_b$ is needed.

Except in the upper part of SS2, Diff with dotted signature is zero for all repeat runs. Similar to SS1, the minimum value is in the range of -6 cu in the upper part of SS2. In Silt and SS3, Diff with solid and dotted signature is zero for the second and the third repeat runs, indicating that the displacement saturation model is valid. For all subsequent repeat runs, small positive Diff values (solid signature) in the range of 2 to 4 cu occur partially in Silt and SS3. Similar to SS2 in Ktzi200, practically Σ_r and Σ_b overlap.

Due to the very low (mostly negative) repeat TPHI values above the corresponding brine levels in SS1 and SS2, S_{CO_2} derived from TPHI (orange log) has unrealistic values that are much greater than one. Since S_{CO_2} values that are greater than one are not visible in figure

5.12, compare figure A.21 given in the appendix with a larger scale for S_{CO_2} derived from TPHI. The S_{CO_2} values derived from TPHI do not fit to the values derived from Σ . The shape of the S_{CO_2} profile derived from TPHI is relatively similar to the shape of the S_{CO_2} profile derived from Σ , indicating that the general TPHI reading fits qualitatively to the general Σ reading above the brine levels. (Figure A.21). S_{CO_2} derived from TPHI for the third and all subsequent repeat runs range from 1 to 3.5 in SS1 and SS2 above the brine levels. For the second repeat, S_{CO_2} derived from TPHI is greater than one above 648.4 m (3.8 m above the corresponding brine level).

S_{CO_2} derived from TPHI is smaller than one for all repeat runs below the brine levels, except in the depth interval below SS2 and above Silt, which is not taken into account. For the fourth and sixth repeat runs below the brine level in the depth intervals of SS2 where the repeat Σ values are smaller than the baseline Σ values, S_{CO_2} derived from TPHI is relatively close to S_{CO_2} derived from Σ . For the fifth repeat run, S_{CO_2} derived from TPHI is relatively close to S_{CO_2} derived from Σ , except between 646 and 648 m. S_{CO_2} derived from TPHI is relatively close to S_{CO_2} derived from Σ in Silt and SS3 for the second and the third repeat run. For all subsequent repeat runs, S_{CO_2} derived from TPHI is close to or greater than S_{CO_2} derived from Σ in Silt and SS3.

Saturation profile flush brine salinity

In contrast to the S_{CO_2} values based on the original brine salinity ($S_{CO_{2org}}$), the S_{CO_2} values based on the flush brine salinity ($S_{CO_{2flush}}$) are always smaller (Figure 5.13). The ratio of both CO₂ saturation results in:

$$\frac{S_{CO_{2org}}}{S_{CO_{2flush}}} = \frac{\frac{\Sigma_{b-noair-BSAL} - \Sigma_{r-air-OH}}{\phi_{tot}(97.58 - 0.014)}}{\frac{\Sigma_{b-fl} - \Sigma_{r-air-OH}}{\phi_{tot}(\Sigma_{br-fl} - 0.014)}} \quad (5.3)$$

where the original baseline SIGM log (SIGM_b_noair_BSAL; $\Sigma_{b-noair-BSAL}$), the repeat SIGM logs (SIGM_r_air_OH; $\Sigma_{r-air-OH}$), the flush brine Σ log (SIGM_br_fl; Σ_{br-fl}), the flush baseline SIGM log (SIGM_b_fl; Σ_{b-fl}), the ϕ_{tot} log, the Ketzin NaCl-equivalent Σ brine value (97.58 cu, Table 5.1) and the Σ CO₂ value under reservoir conditions (0.014 cu, Chapter 5.1.2) are the input parameters.

Only in the middle and partially in the lower part of SS1 and in the upper part of SS2 is CO₂ saturation derived using the flush brine parameters and the displacement saturation model. Similar to $S_{CO_{2org}}$, $S_{CO_{2flush}}$ indicates in the middle part of SS1 and in the upper part of SS2 that the extended saturation model is needed. The same is true in the upper most part of SS1 close to the interbedded, strongly cemented sandstone layer. Similar to the original brine salinity data set, the extended saturation model is not applied.

In all other depth intervals of SS1 and SS2, the repeat SIGM values are greater than the SIGM_b_fl values, showing that no CO₂ saturation is possible using the displacement saturation model. The same is true in Silt and SS3. Accordingly, the mean S_{CO_2} values using the flush brine parameters are much smaller than the mean S_{CO_2} values using the original brine parameters (Table 5.8).

Where the repeat SIGM values are greater than the SIGM_b_fl values the Diff values with solid signature are not zero. For these positive Diff values, the extended saturation model

5. PNG monitoring results at the Ketzin site

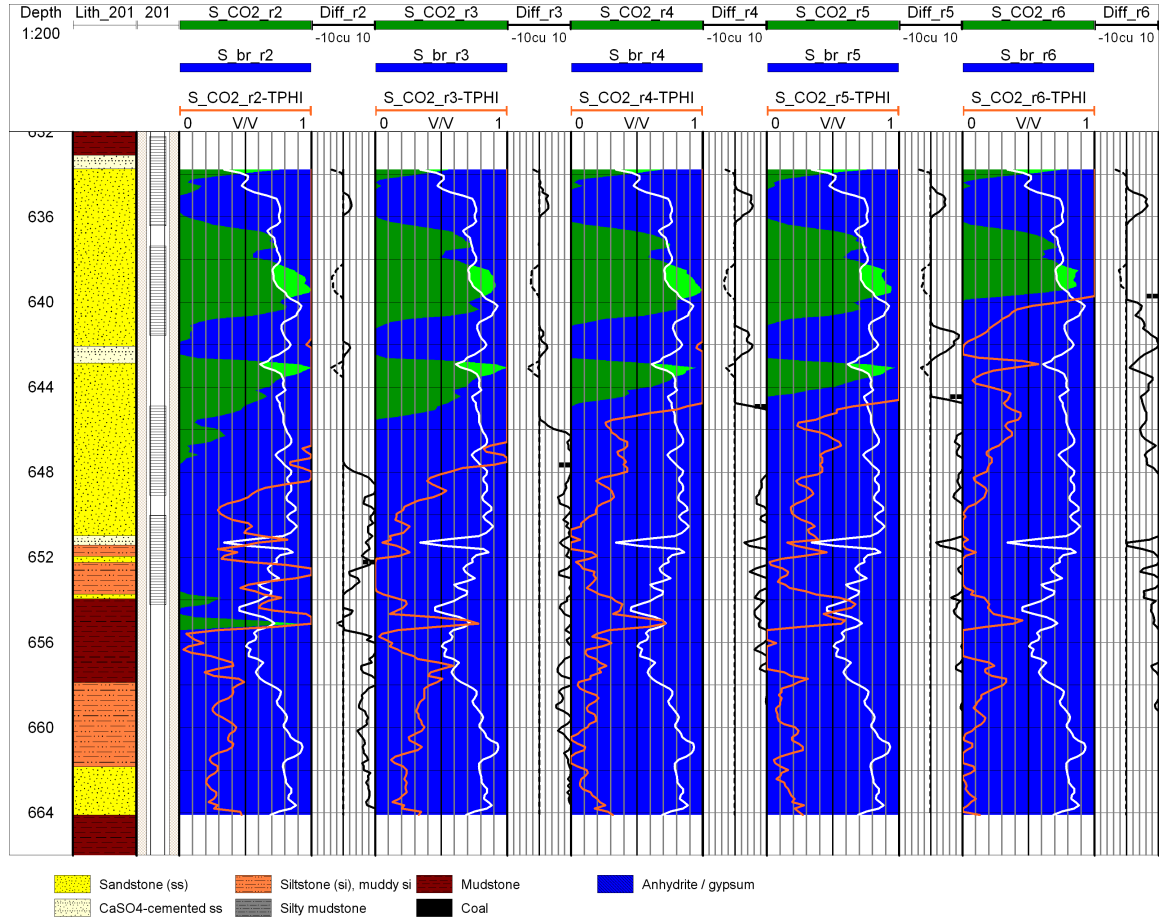


Figure 5.13.: Ktzi201: Saturation profiles as fractions of ϕ_{tot} (displacement conform CO_2 in green, apparent CO_2 in light green and brine in blue), S_{CO_2} derived from TPHI (orange logs) (first track) and the corresponding Diff logs with solid and dotted signature (second track) for five repeat runs based on the *displacement saturation model and the flush brine salinity*. The white log for each repeat run separates the mobile from the immobile brine. The brine levels for each repeat run are marked with a black bar on the right side of the second track. Lithology after Förster et al. (2010)

5. PNG monitoring results at the Ketzin site

Table 5.8.: Ktzi201: Mean S_{CO_2} in the upper (SS1), lower (SS2) reservoir sandstone sections, the silt section (Silt) and the third reservoir sandstone section (SS3) for five repeats based on the displacement model for the original (org) and flush (flush) brine salinity.

Section	brine	r2	r3	r4	r5	r6
SS1	org	0.67	0.63	0.61	0.60	0.50
	flush	0.44	0.40	0.42	0.40	0.30
SS2	org	0.50	0.37	0.25	0.23	0.15
	flush	0.25	0.21	0.14	0.12	0.00
Silt	org	0.21	0.14	0.00	0.01	0.02
	flush	0	0	0	0	0
SS3	org	0.18	0.12	0.01	0.02	0.01
	flush	0	0	0	0	0

with the scenario $\Sigma_r > \Sigma_b$ is needed. Diff with dotted signature has smaller values when using the flush brine parameters instead of the original brine parameters. Therefore, smaller S_{NaCl} values can be expected when using the flush brine parameters instead of the original brine parameters for the extended saturation model with the scenario $\Sigma_r \leq \Sigma_b$.

Similar to equation 5.3, the ratio of $S_{CO_{2org-TPHI}}$ and $S_{CO_{2flush-TPHI}}$ derived from the flush brine adjusted TPHI parameters results in:

$$\frac{S_{CO_{2org-TPHI}}}{S_{CO_{2flush-TPHI}}} = \frac{\frac{TPHI_{b-noair-BSAL}-TPHI_{r-air}}{\phi_{tot}(0.92-0)}}{\frac{TPHI_{b-fl}-TPHI_{r-air}}{\phi_{tot}(HI_{fl}-0)}} \quad (5.4)$$

where the original baseline TPHI log ($TPHI_b_noair_BSAL$; $TPHI_{b-noair-BSAL}$), the repeat TPHI logs ($TPHI_r_air$; $TPHI_{r-air}$), the flush-brine HI log (HI_fl ; HI_{fl}), the flush baseline TPHI log ($TPHI_b_fl$; $TPHI_{b-fl}$), the ϕ_{tot} log, the Ketzin NaCl-equivalent HI_{org} brine value (0.92, Chapter 2.2.2) and the HI CO_2 value under reservoir conditions (0, Chapter 2.2.2) are the input parameters.

Similar to the S_{CO_2} values derived from Σ and the original or flush brine parameters, the S_{CO_2} values derived from TPHI and the original brine parameters are greater than the S_{CO_2} values derived from TPHI and the flush brine parameters. Since TPHI is less affected by changing salinities than Σ , $S_{CO_{2org-TPHI}}$ is closer to $S_{CO_{2flush-TPHI}}$ than $S_{CO_{2org}}$ is to $S_{CO_{2flush}}$. The application of the extended saturation model for both data sets, using both the original and the flush brine parameters, are discussed in chapter 5.3.2.2.

5.3.1.3. Ktzi202 observation well

As mentioned above, in Ktzi202, changes between the baseline and repeat runs have occurred in SS1 and in Mud (Chapter 5.2.1). The fifth and all former repeat Σ logs with the air_OH data processing have lower readings than the baseline Σ log in Mud (Figure 5.8). In contrast, due to the rised brine level from the fifth to the sixth repeat run, the sixth repeat Σ log nearly overlap in Mud for all different data processings with the baseline Σ log.

5. PNG monitoring results at the Ketzin site

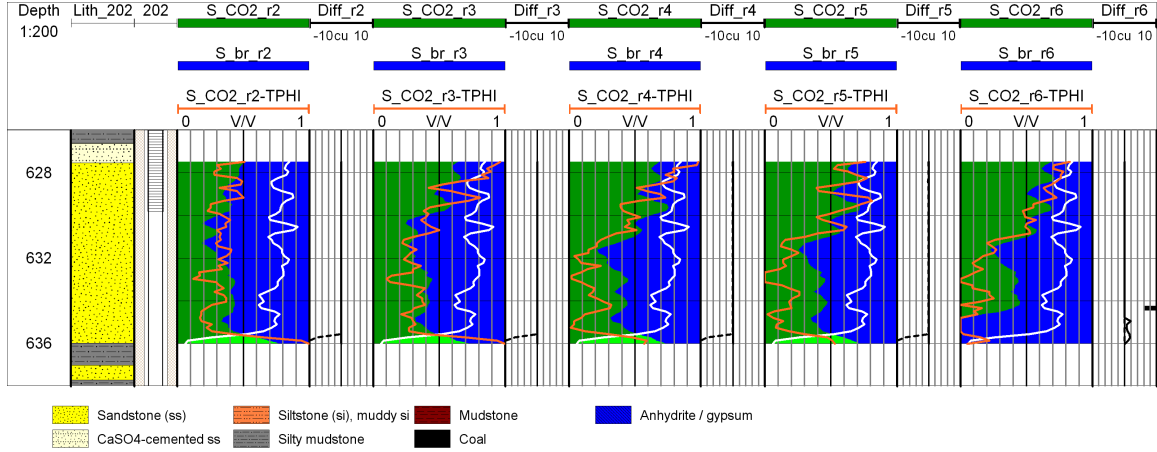


Figure 5.14.: Ktzi202: Saturation profiles as fractions of ϕ_{tot} (displacement conform CO_2 in green, apparent CO_2 in light green and brine in blue), S_{CO_2} derived from TPHI (orange logs) (first track) and the corresponding Diff logs with solid and dotted signature (second track) for five repeat runs based on the *displacement saturation model*. The white log for each repeat run separates the mobile from the immobile brine. The brine levels for each repeat run are marked with a black bar on the right side of the second track. Except for the sixth repeat run, the brine levels are below the displayed depth range. Lithology after Förster et al. (2010)

Due to the low permeability and effective porosity in the Mud section similar to the caprock section (Figure 5.2), it can be assumed that no saturation changes in this formation have occurred. The baseline Σ values in the caprock section and in the Mud section are in the same range. Moreover, for the air_8.5 data processing, which is the best repeat data processing for the caprock section, the fifth and all former repeat Σ logs also roughly overlap with the baseline Σ log in Mud (Figure A.17). If a "real" CO_2 saturation could be anticipated in Mud, the fifth and all former repeat Σ values with the air_8.5 data processing would be smaller than the baseline Σ values, as is the case in the upper part of SS1. Moreover, similar to the mudstone in the caprock section the silty mudstone in the Mud section is not defined by the RST processing algorithm (Chapter 2.4.2). As mentioned above, the sixth repeat Σ log nearly overlap with baseline Σ log, where all former repeat logs with the air_OH data processing have lower readings than the baseline Σ log. It seems unrealistic that all former repeat runs should show a CO_2 saturation in Mud, but then no CO_2 saturation for sixth repeat. Therefore, these Σ differences are probably more associated with the changing brine level than with "real" saturation changes. Moreover, ϕ_{tot} is low in Mud, and therefore small Σ changes result in great calculated S_{CO_2} values. Due to these uncertainties, it seems that the Mud section contains no or only minor amounts of CO_2 , which is why this section is not taken into account for the saturation profile.

Figure 5.14 summarizes the CO_2 saturation profile for the repeat runs in Ktzi202 focused on SS1 without the thin silty mudstone and sandstone layers in the lower most part. For the second repeat run, the CO_2 saturation is relatively constant over the complete depth range of SS1. For all subsequent repeat runs, S_{CO_2} increases in the upper part of SS1, where, in the remaining depth range, the S_{CO_2} values roughly remain unchanged. Only in the lower most part for the sixth repeat run, does S_{CO_2} decrease to zero, which corresponds to the brine level. The mean S_{CO_2} value increases from the second to the fifth repeat (0.50). Then decreases for

5. PNG monitoring results at the Ketzin site

Table 5.9.: Ktzi202: Mean S_{CO_2} in the upper reservoir sandstone section (SS1) without the thin silty mudstone and sandstone layers in the lower most part (new bottom depth 636.02 m) for five repeats based on the displacement model.

Section	r2	r3	r4	r5	r6
SS1	0.39	0.43	0.49	0.50	0.40

the sixth repeat run associated with the rising brine level (Table 5.9).

Except in the lower most part of SS1, Diff with dotted signature is zero for all repeat runs. Diff with dotted signature is not zero, because ϕ_{eff} is close to zero in the lower most part of SS1 (Figure 5.2), and therefore small Σ changes result in great S_{CO_2} values, which are greater than $1 - S_{br_{irr}}$. Diff with solid signature is zero for all repeat runs, except for the sixth repeat in the lower most part, which is a result of the rising brine level associated with a small increased repeat Σ value (2 cu) compared to the baseline Σ value. Since the Diff (dotted signature) anomaly results from the very low ϕ_{eff} value, the displacement saturation model is valid.

The S_{CO_2} values derived from TPHI are mostly larger than the S_{CO_2} values derived from Σ in the upper part of SS1 for all repeat runs. In the lower part of SS1, the S_{CO_2} values derived from TPHI are mostly smaller than the S_{CO_2} values derived from Σ for all repeat runs. The shape of both saturation profiles are relatively similar.

5.3.2. Extended displacement and evaporation/precipitation saturation model

In this section, the application of the extended saturation model is discussed in detail for Ktzi200 and Ktzi201. In addition to CO_2 (S_{CO_2} in green) and brine (S_{br} in blue), the precipitated halite (S_{NaCl} in red) is shown as a fraction of ϕ_{tot} for each repeat run. Since the precipitated halite saturation $S_{NaCl_{pre}}$ is related to ϕ_{irr} in the extended saturation model, S_{NaCl} related to ϕ_{tot} results in:

$$S_{NaCl} = S_{NaCl_{pre}} \cdot \frac{\phi_{irr} + \Delta\phi}{\phi_{tot}} \quad (5.5)$$

Since the S_{NaCl} values are small, a more detailed view of S_{NaCl} with a smaller scale between zero and 0.05 is given in the second track for each repeat run. Additionally, the second track includes the Σ_{br} value. Thus, when S_{NaCl} is calculated, Σ_{br} is accordingly equal to the $\Sigma_{br_{lim}}$ value (131.15 cu). If all dissolved NaCl in ϕ_{irr} is precipitated, S_{NaCl} is greatest and equal to the initial NaCl content (S_{NaCl_b}). Accordingly, S_{br} and Σ_{br} are zero, because all mobile brine has been displaced and the immobile water has been completely evaporated.

As described in chapter 2.4, for a threshold value of 10 cu between SBNA and the SFFA (DIFF > 10 cu) an acceptable neutron porosity (TPHI) determination can be expected. This threshold value is not exceeded for all repeat runs (Chapter 5.2.1). Even when this threshold value is not exceeded, using TPHI to derive CO_2 saturations can be only used with limitations. In general, it can be said that above the brine level, S_{CO_2} derived from TPHI is mostly greater than S_{CO_2} derived from Σ for the observation and injection wells. Moreover, it seems that for high CO_2 saturations occurring above the brine level, S_{CO_2} derived from TPHI is closest to S_{CO_2} derived from Σ for the observation wells. In the injection well above the brine level,

S_{CO_2} derived from TPHI has unrealistic values that are much greater than one. S_{CO_2} derived from TPHI is closest to S_{CO_2} derived from Σ below the brine level for both the observation and injection wells. TPHI is much more affected by borehole effects than Σ . Therefore, due to the open or partially cemented annuli in combination with changing brine levels, TPHI can be used with limitations to derive CO_2 saturations. In contrast, CO_2 saturations derived from Σ are reliable above and below the brine level.

According to chapter 4.3.1, the Σ data are used to derive the saturations for the scenario $\Sigma_r \leq \Sigma_b$ above and below the brine level. The TPHI data are used to get information about the remaining water saturation. Above the brine level, TPHI is used qualitatively, thus can be a remaining water saturation excluded or not. Below the brine level, the S_{CO_2} values derived from TPHI give a more reliable information about the remaining water saturation than above the brine level and are used quantitatively.

According to chapter 4.3.2, the Σ and TPHI data can be used to derive the saturations for the scenario $\Sigma_r > \Sigma_b$. Above the brine level, TPHI is not used, and the model with an assumed backflow rate of brine equal to the evaporation rate is applied ($S_{CO_{2eff}}$ is one and $S_{CO_{2irr}}$ is zero). Below the brine level, the same calculation procedure is applied. Additionally, S_{CO_2} is derived from TPHI, and the Σ data are used to derive Σ_{br} , brine saturation and halite saturation below the brine level.

Diff with dotted signature is absent, because this value is now the input parameter for the extended saturation model with the scenario $\Sigma_r \leq \Sigma_b$. Similar to the displacement saturation model, Diff with solid signature is the resulting Σ difference between the measured Σ_r and the modeled Σ_{r_m} value. For the scenario $\Sigma_r \leq \Sigma_b$, Diff can be negative only, when the modeled Σ_{r_m} value is greater than measured Σ_r value. For this purpose, the affected pore space fractions are adjusted to minimize Diff.

For the scenario $\Sigma_r > \Sigma_b$, Diff can be positive only. After applying the extended saturation model with the scenario $\Sigma_r > \Sigma_b$, the Diff values are closer to zero than the Diff values from the displacement saturation model. Conversely, Diff and the saturation profile remain unchanged (Diff and the saturation profile results from the displacement saturation model), when the extended saturation model with the scenario $\Sigma_r > \Sigma_b$ is not applied. Similar to the extended saturation model with the scenario $\Sigma_r \leq \Sigma_b$, the affected pore space fractions are adjusted to minimize Diff. The dotted white logs describe these porosity adjustments for both scenarios.

5.3.2.1. Ktzi200 observation well

As mentioned in chapter 5.3.1.1, the extended saturation model with the scenario $\Sigma_r \leq \Sigma_b$ is needed for the second and all subsequent repeat runs in the middle part of SS1. For the fifth and sixth repeat runs, S_{CO_2} derived from TPHI is smaller than one, indicating that a remaining water saturation exist in the middle part of SS1 (Figure 5.9). For all former repeat runs, S_{CO_2} derived from TPHI is also smaller than one, except for the fourth and fifth repeat run in the upper most part of the middle of SS1. (Figure 5.9). Since for all former repeat runs the brine level is below this depth interval, S_{CO_2} derived from TPHI is less reliable than for the fifth and the sixth repeat runs. Therefore, step 2.2 (Table 4.2) is not applied for all evaluated repeat runs.

The extended saturation model without adjusting the affected pore space fractions is applied first (Figure 5.15). S_{CO_2} derived from the extended saturation model is greater than S_{CO_2}

5. PNG monitoring results at the Ketzin site

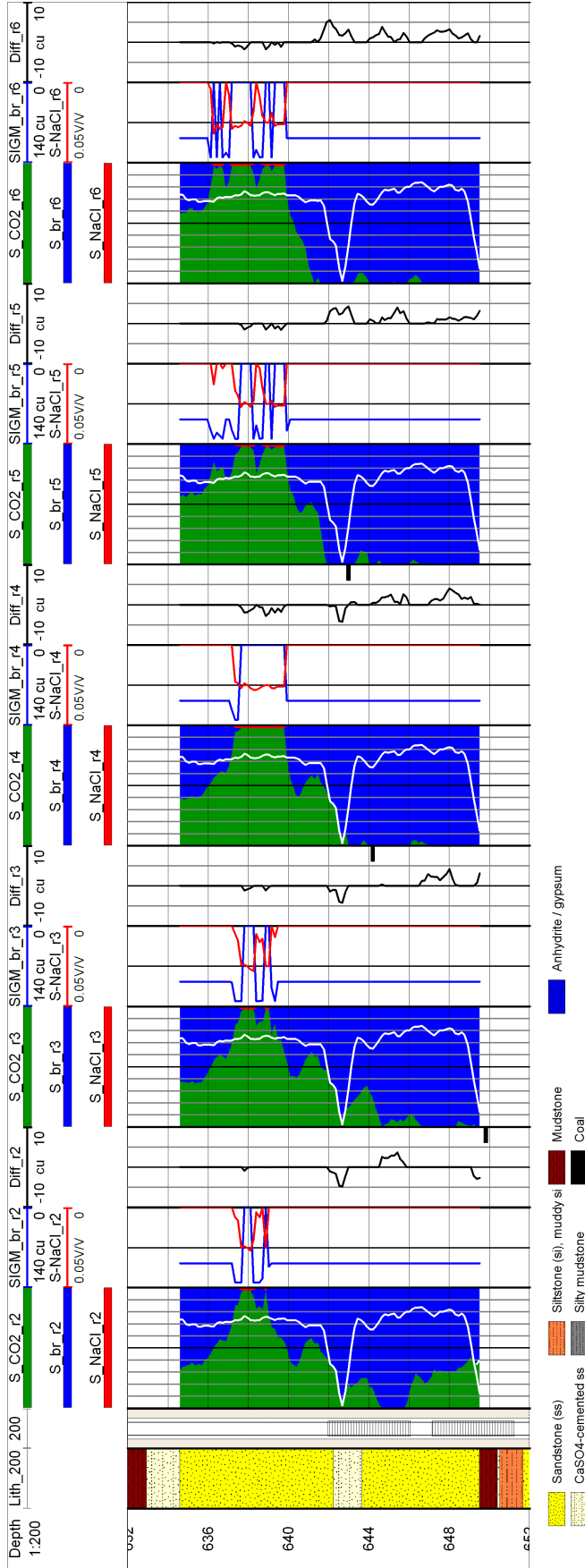


Figure 5.15.: Ktzi200: Saturation profiles as fractions of ϕ_{tot} (CO_2 in green, brine in blue, halite in red) (first track), halite saturations in a smaller scale, Σ_{br} logs (second track) and the corresponding Diff logs (third track) for five repeat runs based on the *extended saturation model without porosity adjustment*. The white solid log for each repeat run separates the mobile from the immobile brine. The brine levels for each repeat run are marked with a black bar on the right side of the third track. For the fifth and the sixth repeat run, the brine levels are above the displayed depth range. Lithology after Förster et al. (2010)

5. PNG monitoring results at the Ketzin site

Table 5.10.: Ktzi200: Mean S_{CO_2} in the upper (SS1) reservoir sandstone section for five repeats based on the extended saturation model.

Section	r1	r2	r3	r4	r5	r6
SS1	-	0.57	0.61	0.66	0.67	0.65

derived from the displacement saturation model in the middle part of SS1 for all evaluated repeat runs. Both situations occur at depth intervals where the evaporation/precipitation process has been completed (S_{NaCl} is greatest, S_{br} and Σ_{br} are zero) and at depth intervals that indicate that the evaporation/precipitation process has not been completed (S_{NaCl} is not greatest, S_{br} and Σ_{br} are not zero). The evaporation/precipitation process has been completed for the fourth repeat run, except in the upper most part of the middle of SS1. Accordingly, S_{NaCl} is greatest (in the range of 0.032) for the fourth repeat run. The same is true for all other repeat runs, when complete evaporation/precipitation is reached.

The other repeat runs have depth intervals where evaporation/precipitation has not been completed. In these depth intervals the brine salinity is increased, or the brine salinity reaches its maximum (NaCl solubility limit is reached) and precipitation occurs. In the depth intervals where precipitation occurs, the S_{NaCl} values are smaller than the S_{NaCl} values when complete evaporation is reached.

When the Diff values are zero, the evaporation/precipitation process with no adjustment of the affected pore space fractions is valid. This is the case for all evaluated repeat runs where evaporation/precipitation has not been completed.

In contrast, Diff is partially negative for all repeat runs where evaporation/precipitation has been completed. Thus, S_{NaCl} , which is greatest and equal to the initial NaCl content (S_{NaCl_b}), overestimates the "real" NaCl saturation. For this purpose, the affected pore space fractions are adjusted to minimize Diff (Table 4.2, Step 2.3). $S_{NaCl_{pre}}$ remains unchanged in ϕ_{irr} , but ϕ_{irr} is decreased ($\phi_{irr} - \Delta\phi$) and ϕ_{eff} is increased ($\phi_{eff} + \Delta\phi$). This porosity adjustment results in a decreased S_{NaCl} value related to ϕ_{tot} (Equation 5.5). Adjusting the affected pore space fractions, S_{NaCl} is partially decreased and Diff is zero for all repeat runs in middle part of SS1 (Figure 5.16).

Table 5.10 summarizes the mean S_{CO_2} values derived from the extended saturation model in SS1. Since S_{CO_2} derived from the extended saturation model is greater than S_{CO_2} derived from the displacement saturation model in the middle part of SS1, the mean S_{CO_2} values are also increased for the extended saturation model.

5.3.2.2. Ktzi201 injection well

As mentioned in chapter 5.3.1.2, the extended saturation model with both scenarios, $\Sigma_r \leq \Sigma_b$ and $\Sigma_r > \Sigma_b$, is needed for the second and all subsequent repeat runs in Ktzi201. For both data sets, the original and flush brine salinity, the extended saturation model with the scenario $\Sigma_r \leq \Sigma_b$ is needed in the middle part of SS1 and the upper part of SS2.

For the original brine salinity data set, the extended saturation model with the scenario $\Sigma_r > \Sigma_b$ is needed for the fourth and fifth repeat runs in the middle part of SS2. In contrast, for the flush brine salinity data set, the extended saturation model with the scenario $\Sigma_r > \Sigma_b$ is needed in SS1, SS2, Silt and SS3 for all repeat runs.

5. PNG monitoring results at the Ketzin site

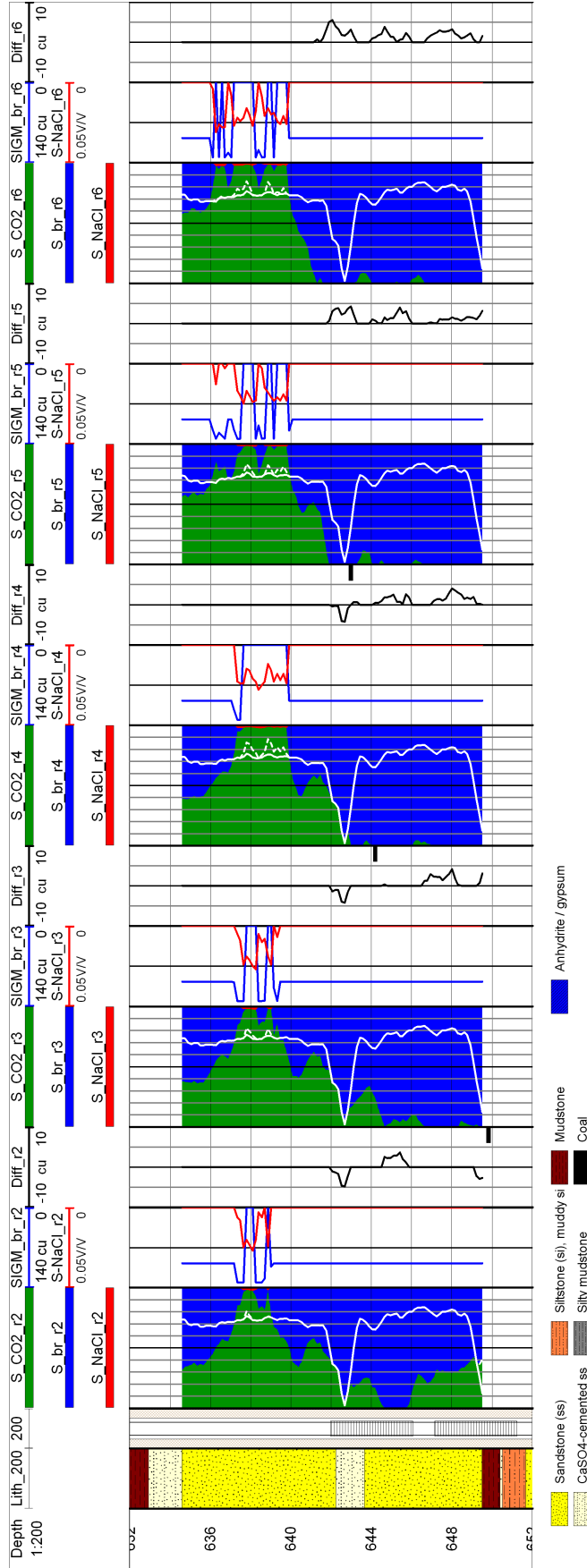


Figure 5.16.: Ktzi200: Saturation profiles as fractions of ϕ_{tot} (CO_2 in green, brine in blue, halite in red) (first track), halite saturations in a smaller scale, Σ_{br} logs (second track) and the corresponding Diff logs for five repeat runs based on the *extended saturation model with porosity adjustment*. The white solid log for each repeat run separates the mobile from the immobile brine. The white dotted logs show the adjustment of the affected porosities. The brine levels for each repeat run are marked with a black bar on the right side of the third track. For the fifth and the sixth repeat run, the brine levels are above the displayed depth range. Lithology after Förster et al. (2010)

For the following reasons, Silt and SS3 are not taken into account for the flush brine salinity data set. The temperature anomalies in Silt and SS3 are low compared to the anomalies in SS1 and SS2 (Figure A.20). Using the original brine salinity data set, Silt and SS3 only show CO₂ saturation for the second and third repeat run. All subsequent repeat Σ logs practically overlap with the original baseline Σ log, indicating no CO₂ saturation. Additionally, the temperature data also show that, for the time period of the subsequent repeat runs, no CO₂ enters Silt and SS3 (Personal communication; Henniges). But without any CO₂ flow in Silt and SS3 no evaporation/precipitation can occur. Moreover, S_{CO_2} derived from TPHI (less affected by salinity) is low or close to zero for all subsequent repeat runs for both the original and flush brine salinity data set. Therefore, the decreased flush brine salinity seems unrealistic in Silt and SS3. Thus, the saturation profile using the original brine salinity and the displacement saturation model is valid in Silt and SS3.

TPHI can not be used quantitatively above the brine level to get information about the remaining water saturation, which is necessary for the scenario $\Sigma_r \leq \Sigma_b$. But the shape of the saturation profiles derived from TPHI (high apparent S_{CO_2} values) correspond to the depth range where the scenario $\Sigma_r \leq \Sigma_b$ is valid for both the original and the flush brine data set. Therefore, TPHI indicates qualitatively, that remaining water saturation can be excluded.

Before the first repeat in Ktzi201 (second repeat in general) took place roughly one year after CO₂ injection started, around 18,000 t of CO₂ was injected (Figure 5.3). For an injection rate of 1 kg/s (3.6 t/h) (Muller et al., 2009), the 18,000 t corresponds to an injection time of 0.57 years. The modeling results for the Ketzin site show that after half a year the dry-out radius is roughly 2 meter for both the original and the flush brine salinity (Muller et al., 2009). The dry-out radius is greater than one meter, which is the depth of investigation for common PNG tools with high gas saturations in the formation (Knödel et al., 1997).

Based on the TPHI analysis and the modeling results, step 2.2 (Table 4.2) is applied for both the original and flush brine salinity data sets for all repeat runs.

Saturation profiles original brine salinity

Similar to Ktzi200, the extended saturation model without adjusting the affected pore space fractions is applied first in Ktzi201 (Figure 5.17). S_{CO_2} derived from the extended saturation model with the scenario $\Sigma_r \leq \Sigma_b$ is greater than S_{CO_2} derived from the displacement saturation model in the middle part of SS1 and in the upper part of SS2 for all repeat runs. For the fourth and fifth repeat run in the middle part of SS2, the saturation profile is calculated without using TPHI. S_{CO_2} derived from the displacement saturation model is zero for the fourth and fifth repeat run in the middle part of SS2. In contrast, S_{CO_2} derived from the extended saturation model is $1 - S_{br_{irr}}$, as defined by the assumed backflow rate of brine being equal to the evaporation rate ($S_{CO_{2eff}}$ is one and $S_{CO_{2irr}}$ is zero).

In the lower most part of SS2, close to the interbedded, strongly cemented sandstone layer, the scenario $\Sigma_r > \Sigma_b$ is not applied for all repeat runs. It is not applied because Diff is small, which is why the repeat Σ logs practically overlap with the baseline Σ log. The same is true for the sixth repeat run in SS1, close to the interbedded, strongly cemented sandstone layer between 642.01 and 642.77 m.

For the third repeat run, Diff has small positive values (greatest 3 cu) between 647.04 and 647.65 m directly above the corresponding brine level. Directly above the Diff anomaly, the S_{CO_2} values derived from Σ are small, and S_{CO_2} derived from TPHI is greater than one (TPHI above the brine level) for the third repeat run. Therefore, the extended saturation

5. PNG monitoring results at the Ketzin site

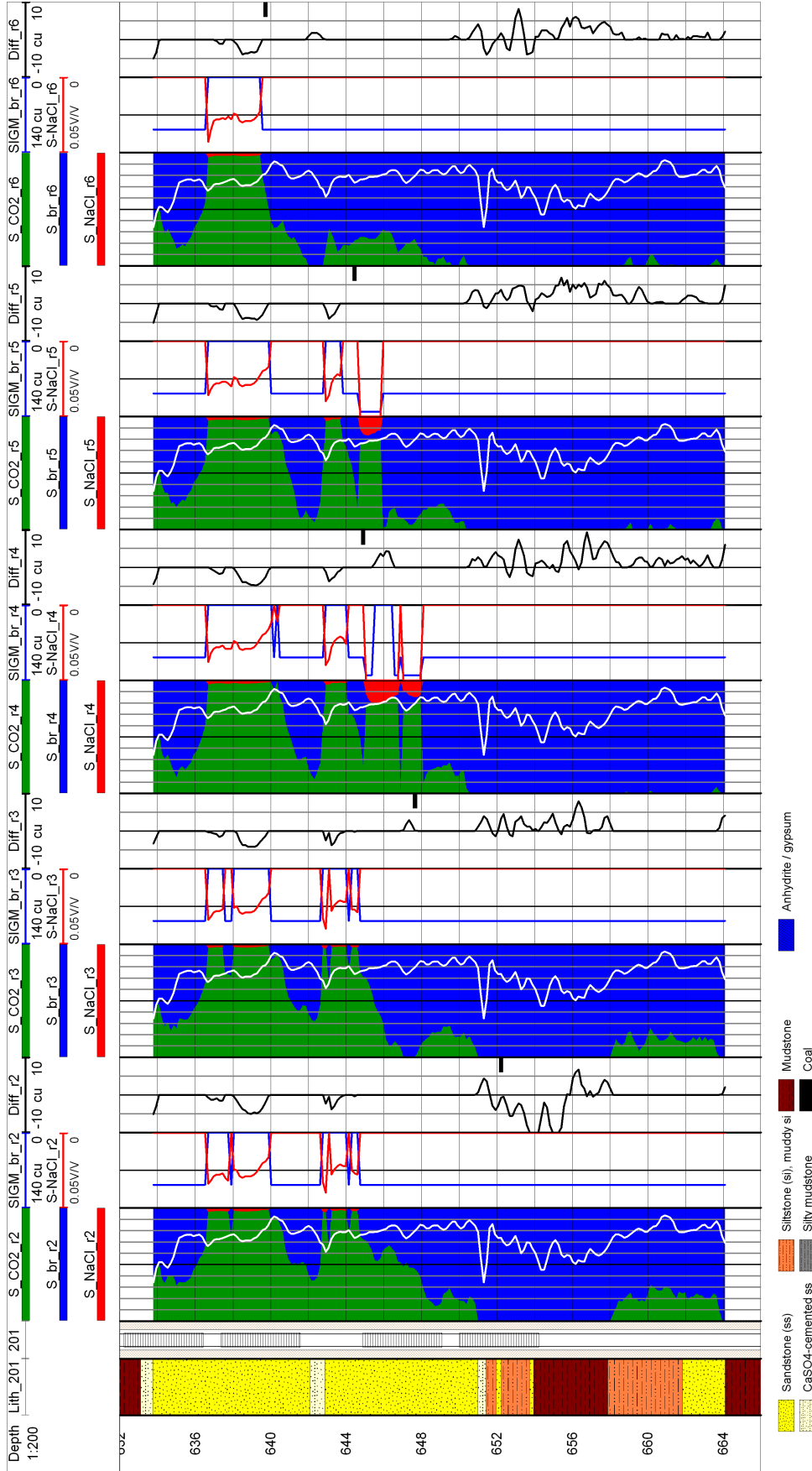


Figure 5.17.: Ktzi201: Saturation profiles as fractions of ϕ_{tot} (CO₂ in green, brine in blue, halite in red) (first track), halite saturations in a smaller scale, Σ_{br} logs (second track) and the corresponding Diff logs (third track) for five repeat runs based on the *extended saturation model and the original brine salinity without porosity adjustment*. The white solid log for each repeat run separates the mobile from the immobile brine. If $\Sigma_r > \Sigma_b$ (occur *only below the brine level for the fourth and the fifth repeat runs*), SCO_{2eff} is set to one and SCO_{2irr} is set zero. The brine levels for each repeat run are marked with a black bar on the right side of the third track. Lithology after Förster et al. (2010)

5. PNG monitoring results at the Ketzin site

model with the scenario $\Sigma_r > \Sigma_b$ is not applied in this depth interval, because the calculation based on the assumption that the backflow rate of brine is equal to the evaporation rate would result in high S_{CO_2} values. S_{CO_2} derived from TPHI is ruled out, because these values are greater than one. These high S_{CO_2} values appear to be unrealistic, as above and below this Diff anomaly the CO_2 saturations are small. But it seems that, due to capillary forces, the brine salinity is slightly increased. This finding also correlates with the large S_{NaCl} values for the subsequent fourth repeat run in this depth interval.

The high CO_2 saturations without any residual brine saturation, indicate that the middle part of SS1 and the upper part of SS2 are dried out for the fourth and all subsequent repeat runs. For the second and the third repeat runs, three small depth intervals with residual brine saturation exist within the middle part of SS1 and the upper part of SS2.

Therefore, the middle part of SS1 and the upper part of SS2, without the depth intervals where a residual brine saturation exist for the second and the third repeat runs, are the dry-out regions (Chapter 3.1.1) in the injection well. The maximum S_{NaCl} values for all repeat runs is in the range of 0.040 and 0.043 in the dry-out regions. The S_{NaCl} maxima occur at the upper edge of the dry-out regions. In the center and at the lower edge of the dry-out regions, S_{NaCl} has lower values.

The maximum S_{NaCl} value for the fourth repeat is 0.214 and for the fifth repeat is 0.166. The large S_{NaCl} values for the fourth and fifth repeat runs occur below the brine level, where Σ_r is greater than Σ_b . For the fourth repeat run between 645.51 and 646.73 m, the complete pore space ϕ_{irr} is clogged by halite. For the fifth repeat run, the S_{NaCl} values decrease in this depth interval.

In the dry-out regions, the Diff values are mostly negative for all repeat runs, indicating that the "real" NaCl saturation is overestimated. In contrast, the Diff values are positive for the fourth repeat run between 645.51 and 646.43 m, indicating that the "real" NaCl saturation is underestimated. For this purpose, the affected pore space fractions are adjusted to minimize Diff for both scenarios.

After adjusting the affected pore space fractions, S_{NaCl} decreases or remains constant, and Diff is zero for all repeat runs in the dry-out regions (Figure 5.18). The maximum S_{NaCl} values in the dry-out regions for all repeat runs are in the range of 0.032 and 0.043. Moreover, after adjusting the affected pore space fractions, the S_{NaCl} maxima occur at the upper edge of the dry-out regions. The maximum S_{NaCl} value (0.043) for all repeat runs is equal for both, with and without adjusting the affected pore space fractions, and occur for the sixth repeat at 636.67 m in the dry-out regions. Since this value is equal for both, no adjustment of the affected pore space fractions is applied and Diff is accordingly zero for both. In the center of the dry-out regions, the S_{NaCl} values are smaller than the S_{NaCl} values without adjusting the affected pore space fractions. The S_{NaCl} values at the lower edge of the dry-out regions also remain unchanged after the adjustment of the affected pore space fractions. The porosity adjustment is applied to mostly the complete dry-out regions and is largest in the center. Thus, the original brine salinity overestimates the "real" formation salinity.

After adjusting the affected pore space fractions, S_{NaCl} increases or remains constant, and Diff is zero for all repeat runs in the middle part of SS2 (Figure 5.18). The maximum S_{NaCl} value for the fourth repeat is 0.223 and for the fifth repeat run is 0.166 occurring below the brine level. The corresponding maximum ϕ_{irr} increasing is 0.006 small and occurs at 646.12 m for the fourth repeat run. These small increased ϕ_{irr} value validates that the complete pore space ϕ_{irr} is clogged by halite for the fourth repeat run, when using the assumption that

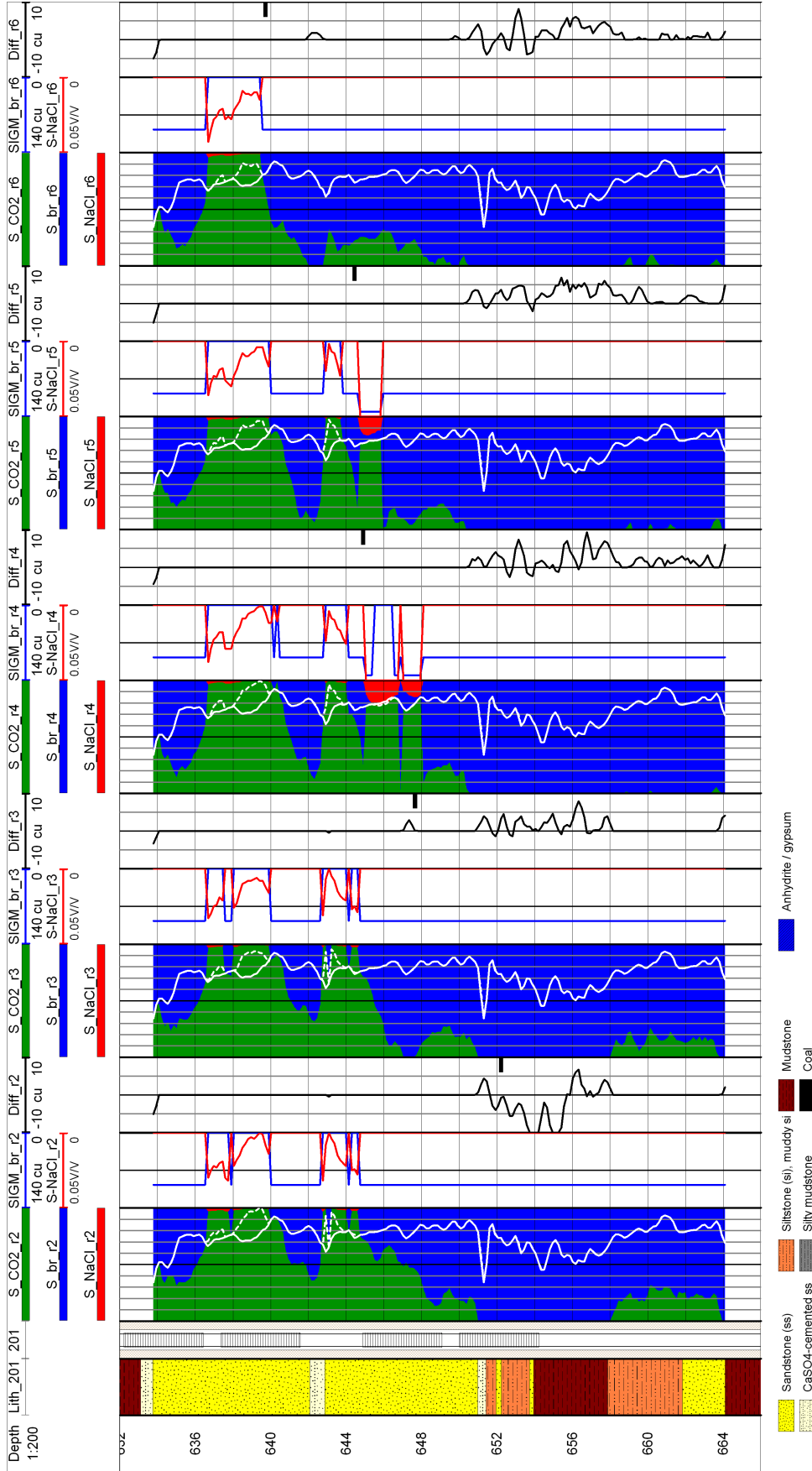


Figure 5.18.: Ktzi201: Saturation profiles as fractions of ϕ_{tot} (CO_2 in green, brine in blue, halite in red) (first track), halite saturations in a smaller scale, Σ_{br} logs (second track) and the corresponding Diff logs (third track) for five repeat runs based on the *extended saturation model and the original brine salinity with porosity adjustment*. The white solid log for each repeat run separates the mobile from the immobile brine. The white dotted logs show the adjustment of the affected porosities. *If $\Sigma_r > \Sigma_b$ (occur only below the brine level for the fourth and the fifth repeat runs), $S_{\text{CO}_2, \text{eff}}$ is set to one and $S_{\text{CO}_2, \text{irr}}$ is set zero.* The brine levels for each repeat run are marked with a black bar on the right side of the third track. Lithology after Förster et al. (2010)

the backflow rate of brine is equal to the evaporation rate. The S_{NaCl} values for the fifth repeat run remain unchanged, because no adjustment of the affected pore space fractions is necessary.

Instead of using the assumption, that the backflow rate of brine is equal to the evaporation rate ($S_{CO_{2eff}}$ is one and $S_{CO_{2irr}}$ is zero), S_{CO_2} can be derived from TPHI, and the Σ data are used to derive Σ_{br} , brine saturation and halite saturation below the brine level. This calculation is applied to the fourth and the fifth repeat runs below the brine level, where Σ_r is greater than Σ_b (Figure 5.19). All other saturations in figure 5.19 are equal to the saturations in figure 5.18.

The S_{CO_2} values derived from TPHI are smaller than the volume weighted sum of the individual CO_2 saturations $S_{CO_{2eff}}$ and $S_{CO_{2irr}}$. This is associated with greater brine and smaller halite saturations. The maximum S_{NaCl} value for the fourth repeat run is 0.135 and for the fifth repeat run is 0.132. In contrast to the S_{NaCl} values derived from the S_{CO_2} assumptions, ϕ_{irr} is not clogged by halite. Diff is zero for the fourth and fifth repeat run in the middle part of SS2. Table 5.11 summarizes the mean S_{CO_2} values shown in figure 5.19 for SS1 and SS2 that include TPHI as input parameter. The mean S_{CO_2} values are greater than the values from the corresponding displacement saturation model.

Saturation profiles flush brine salinity

Similar to the saturation profiles for the original brine salinity, the extended saturation model without adjusting the affected pore space fractions is applied first. Where the repeat SIGM values are greater than the SIGM_b_fl values, the extended saturation model with the scenario $\Sigma_r > \Sigma_b$ without using TPHI is applied. Moreover, this scenario is applied in the interbedded, strongly cemented sandstone layer between SS1 and SS2.

Similar to the CO_2 saturations based on the original brine salinity, the CO_2 saturations based on the flush brine salinity are greater than the CO_2 saturations from the corresponding displacement saturation model in the middle part of SS1 and in the upper part of SS2 for all repeat runs (Figure 5.20). Moreover, the middle part of SS1 and the upper part of SS2 without the depth intervals where residual brine saturation exists are the dry-out regions.

The S_{NaCl} values are smaller compared to the values from the original brine salinity in the dry-out regions. The maximum S_{NaCl} values for all repeat runs are in the range of 0.014 and 0.024 in these dry-out regions. In contrast to the original brine salinity saturation profile, the scenario $\Sigma_r > \Sigma_b$ is applied for the sixth repeat run in the upper part of SS2. This is associated with greater S_{NaCl} values (maximal 0.089) than the derived S_{NaCl} values for the former repeats, where the scenario $\Sigma_r \leq \Sigma_b$ is applied.

Similar to the saturation profiles for the original brine salinity, the S_{NaCl} maxima occur at the upper edge of the dry-out regions. The S_{NaCl} values in the center and at the lower edge of the dry-out regions behave similarly to the S_{NaCl} values using the original brine salinity.

The saturation profiles are equal in the depth interval where Σ_r is greater than Σ_b for both the original and flush salinity. This is the case for the fourth and fifth repeat runs below the brine level. The saturation profiles are equal, because the only measured input parameter in equation 4.30 is the Σ_r value, which is used for both saturation profiles.

The saturation profiles in SS1 and SS2 outside the dry-out regions are different from the corresponding saturation profiles for the original brine salinity. Corresponding to the model assumption, $S_{CO_{2eff}}$ is one and $S_{CO_{2irr}}$ is zero. The S_{NaCl} values are relatively constant

5. PNG monitoring results at the Ketzin site

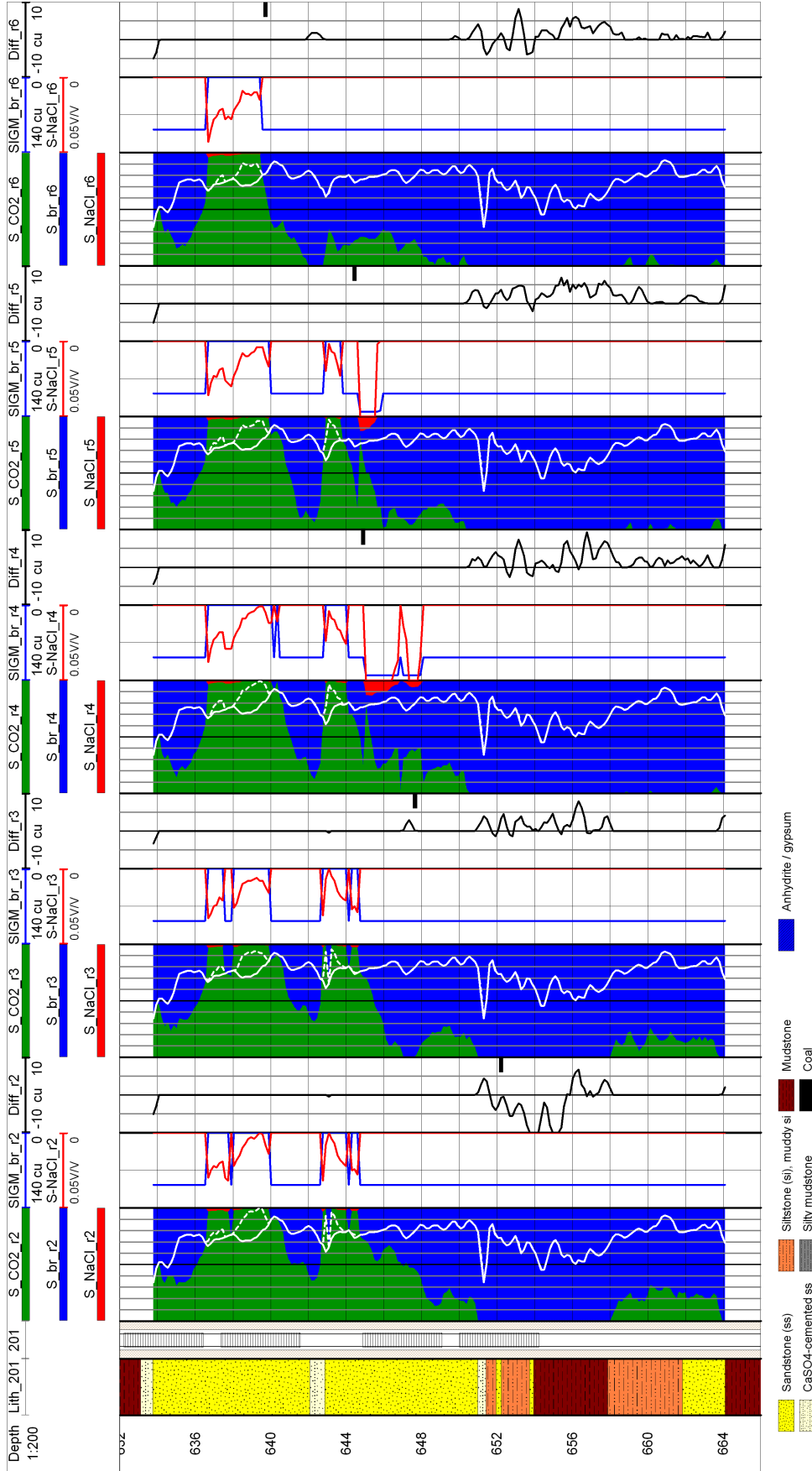


Figure 5.19.: Ktzi201: Saturation profiles as fractions of ϕ_{tot} (CO₂ in green, brine in blue, halite in red) (first track), halite saturations in a smaller scale, Σ_{br} logs (second track) and the corresponding Diff logs (third track) for five repeat runs based on the *extended saturation model and the original brine salinity with porosity adjustment*. The white solid log for each repeat run separates the mobile from the immobile brine. The white dotted logs show the adjustment of the affected porosities. *If $\Sigma_r > \Sigma_b$ (occur only below the brine level for the fourth and the fifth repeat runs), S_{CO_2} is derived from TPHI*. The brine levels for each repeat run are marked with a black bar on the right side of the third track. Lithology after Förster et al. (2010)

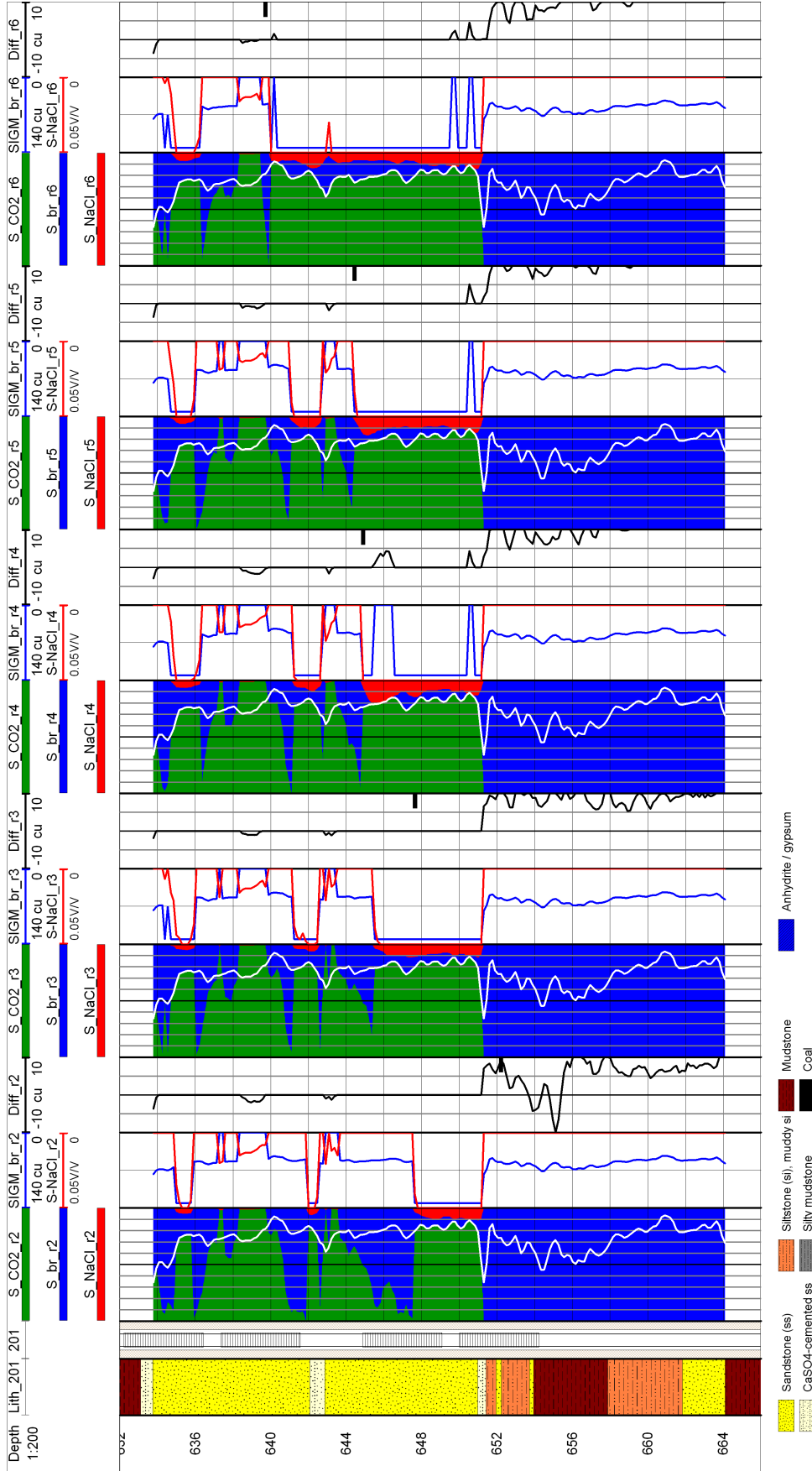


Figure 5.20.: Ktzi201: Saturation profiles as fractions of ϕ_{tot} (CO_2 in green, brine in blue, halite in red) (first track), halite saturations in a smaller scale, Σ_{br} logs (second track) and the corresponding Diff logs (third track) for five repeat runs based on the *extended saturation model and the flush brine salinity without porosity adjustment*. The white solid log for each repeat run separates the mobile from the immobile brine. If $\Sigma_r > \Sigma_b$ (occur above and below the brine level for all repeat runs), $S_{\text{CO}_2, \text{eff}}$ is set to one and $S_{\text{CO}_2, \text{irr}}$ is set zero. The brine levels for each repeat run are marked with a black bar on the right side of the third track. Lithology after Förster et al. (2010)

5. PNG monitoring results at the Ketzin site

(0.1) in SS2 for all repeat runs. In some depth intervals of SS2, slightly smaller or greater S_{NaCl} values occur. In the interbedded, strongly cemented sandstone layer between SS1 and SS2, the S_{NaCl} values are greatest 0.064 for the second repeat run. From the second to all subsequent repeat runs, the S_{NaCl} value increases and also expands into the lower most part of SS1 and the upper most part of SS2. Between 634.2 and 636.3 m in SS1, the maximum S_{NaCl} value is 0.077 for the sixth repeat run.

Compared to the corresponding saturation profiles for the original brine salinity, nearby for the fourth and fifth repeat run, precipitated halite also occurs for all other repeat runs in the middle and lower part of SS2. Especially the third repeat run show halite saturation in the middle part of SS2, which correlates with the halite saturation for the fourth repeat run for both, the original (Figure 5.19) and flush saturation profile. This precipitated halite is absent for the third repeat in the original brine salinity saturation profile, because the scenario $\Sigma_r > \Sigma_b$ is not valid in this depth interval.

The Diff values are partially negative in the dry-out regions for all repeat runs. The positive Diff values are equal to the Diff values from the original brine salinity saturation profiles for the fourth and fifth repeat runs below the brine level. This results from equation 4.30. In the lower most part of SS2 positive Diff values also occur for the fourth, fifth and sixth repeat runs. For this purpose the affected pore space fractions are adjusted.

After adjusting the affected pore space fractions, S_{NaCl} decreases or remains constant, and Diff is zero for all repeat runs in the dry-out regions (Figure 5.21). The maximum S_{NaCl} values for all repeat runs are in the range of 0.008 and 0.024. The S_{NaCl} values are greatest at the upper edge and decrease in the center of the dry-out regions after the porosity adjustment. The relative changes between the S_{NaCl} values with and without the porosity adjustment are comparable to the original and flush brine salinity saturation profiles. But, compared to the porosity adjustment for the original brine salinity, the porosity adjustment for the flush brine salinity is smaller. Thus, the flush brine salinity is closer to the "real" formation salinity than the original brine salinity. In the lower most part of SS2, ϕ_{irr} is slightly increased.

In contrast to the original brine salinity saturation profiles, where the scenario $\Sigma_r > \Sigma_b$ using TPHI is applied for the fourth and the fifth repeat runs below the brine level, the scenario $\Sigma_r > \Sigma_b$ using TPHI is applied for all repeat runs below the brine level.

Some $S_{CO_2flush-TPHI}$ values are smaller than zero (repeat TPHI value greater than baseline TPHI value) for the fourth (last three data points) and the sixth (last seven data points) repeat runs in the lower most part of SS2. The same is true for three data points in SS1 between 642.16 and 642.46 m for the sixth repeat run. Most of the $S_{CO_2flush-TPHI}$ values are close to zero, especially for the data points in SS1. In order to calculate a complete saturation profile in SS1 and SS2 for all repeat runs, $S_{CO_2flush-TPHI}$ is set to zero for these data points. For all these data points the case $\Sigma_x \leq \Sigma_{br_{lim}}$ is valid. Thus, setting $S_{CO_2flush-TPHI}$ to zero, increases the Σ_{br} value.

Some $S_{CO_2flush-TPHI}$ values are greater than one (negative repeat TPHI values). This is the case for the two data points at 644.45 and 644.60 m below the brine level for the fifth repeat run. For the second repeat run, the $S_{CO_2flush-TPHI}$ values are mostly smaller than one above the brine level up to 647.65 m, which is the brine level for the third repeat run. The CO₂ saturation profile derived from TPHI for the second repeat run between the top of SS2 and 647.65 m is comparable to the CO₂ saturation profile derived from TPHI for the third repeat run (Figure 5.13). Therefore, the $S_{CO_2flush-TPHI}$ values for the second repeat are used up to the brine level for the third repeat run. For all other repeat runs, TPHI is used below the

5. PNG monitoring results at the Ketzin site

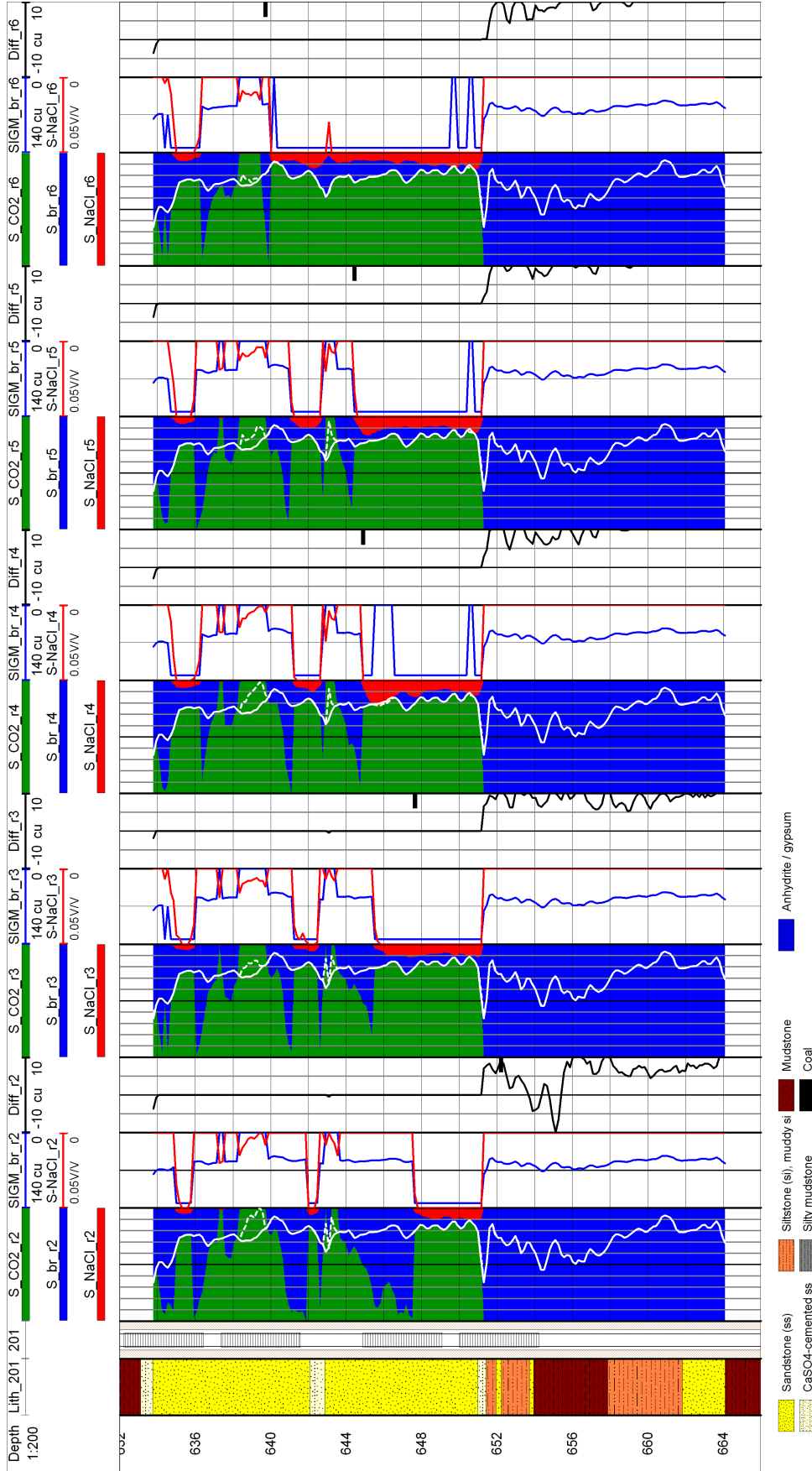


Figure 5.21.: Ktzi201: Saturation profiles as fractions of ϕ_{tot} (CO_2 in green, brine in blue, halite in red) (first track), halite saturations in a smaller scale, Σ_{br} logs (second track) and the corresponding Diff logs (third track) for five repeat runs based on the *extended saturation model and the flush brine salinity with porosity adjustment*. The white solid log for each repeat run separates the mobile from the immobile brine. The white dotted logs show the adjustment of the affected porosities. If $\Sigma_r > \Sigma_b$ (occurs above and below the brine level for all repeat runs), SCO_{2eff} is set to one and SCO_{2irr} is set zero. The brine levels for each repeat run are marked with a black bar on the right side of the third track. Lithology after Förster et al. (2010)

5. PNG monitoring results at the Ketzin site

brine level only. For five data points close to the brine level of the third repeat run (647.65 m), the $S_{CO_2 flush-TPHI}$ values are greater than one for the second repeat run. For the case that the $S_{CO_2 flush-TPHI}$ values are greater than one, the saturation profile is similarly calculated as the former saturation profile with equation 4.30.

The saturation profiles using TPHI is shown in figure 5.22. Except for the second repeat run, the saturations above the brine level in figure 5.22 are equal to the saturations in figure 5.21. The S_{CO_2} values derived from TPHI are smaller than the S_{CO_2} values derived from the model assumption for all repeat runs in SS2. The brine saturations increase and the halite saturations decrease. Especially in the lower part of SS2, the halite saturations are absent for all repeat runs, except for the second and fifth repeat runs.

The maximum S_{NaCl} values are 0.141 for the fourth repeat run and 0.134 for the fifth repeat run. These are located at the same depth as the maximum values for the original brine salinity. Since $S_{CO_2 flush-TPHI}$ is greater than $S_{CO_2 org-TPHI}$, the maximum S_{NaCl} values for the flush brine salinity are slightly greater than the corresponding values for the original brine salinity.

Using the flush brine salinity data set in combination with the scenario $\Sigma_r > \Sigma_b$, results in halite saturation in the middle part of SS2 for the third, fourth and fifth repeat run. The saturation profiles for the fourth and fifth repeat runs are derived using TPHI and without using TPHI for the third repeat run. The vertical expansion of the halite saturation is relatively similar for these repeat runs. Moreover, this halite containing depth interval moves upward with the repeat runs, corresponding to the rising brine level. The S_{NaCl} values are largest for the third repeat run (above the brine level) and decrease for the subsequent fourth and fifth repeat runs (below the brine level). For the sixth repeat run, halite saturation is absent, also correlating with the rising brine level from the fifth to sixth repeat runs. Instead of using the original brine salinity data set, the scenario $\Sigma_r > \Sigma_b$ is only applied for the fourth and the fifth repeat run with comparable halite saturation in the middle part of SS2 (Figure 5.19). For all other repeat runs, halite saturation is absent in the middle part of SS2 when using the original brine salinity data set.

Diff is zero for all repeat runs in SS1 and SS2. Table 5.11 summarizes the mean S_{CO_2} values shown in figure 5.22 for SS1 and SS2, which are greater than the values from the corresponding displacement saturation model.

In the following section, the scenario $\Sigma_r \leq \Sigma_b$ is discussed in detail. The porosity adjustment, applied to minimize Diff, results in a decreased S_{NaCl} value related to ϕ_{tot} (Equation 5.5). The largest porosity adjustment is necessary when using the original brine salinity. Using the flush brine salinity, smaller porosity adjustments are needed. Thus, the flush brine salinity is closer to the "real" formation salinity than the original brine salinity, since the "real" formation salinity is affected by the KCl-preflush.

Based on equation 4.27, a target halite precipitation value (S_{NaCl_x}) can be calculated such that Diff is zero without any porosity adjustment.

$$\Sigma_{r_{irr}} = \phi_{irr} \cdot [S_{NaCl_x} \cdot \Sigma_{NaCl} + (1 - S_{NaCl_x}) \cdot \Sigma_{CO_2}] \quad (5.6)$$

Solving for S_{NaCl_x} with $S_{CO_2} = 1 - S_{NaCl_x}$:

$$S_{NaCl_x} = \frac{\frac{\Sigma_{r_{irr}}}{\phi_{irr}} - \Sigma_{CO_2}}{(\Sigma_{NaCl} - \Sigma_{CO_2})} \quad (5.7)$$

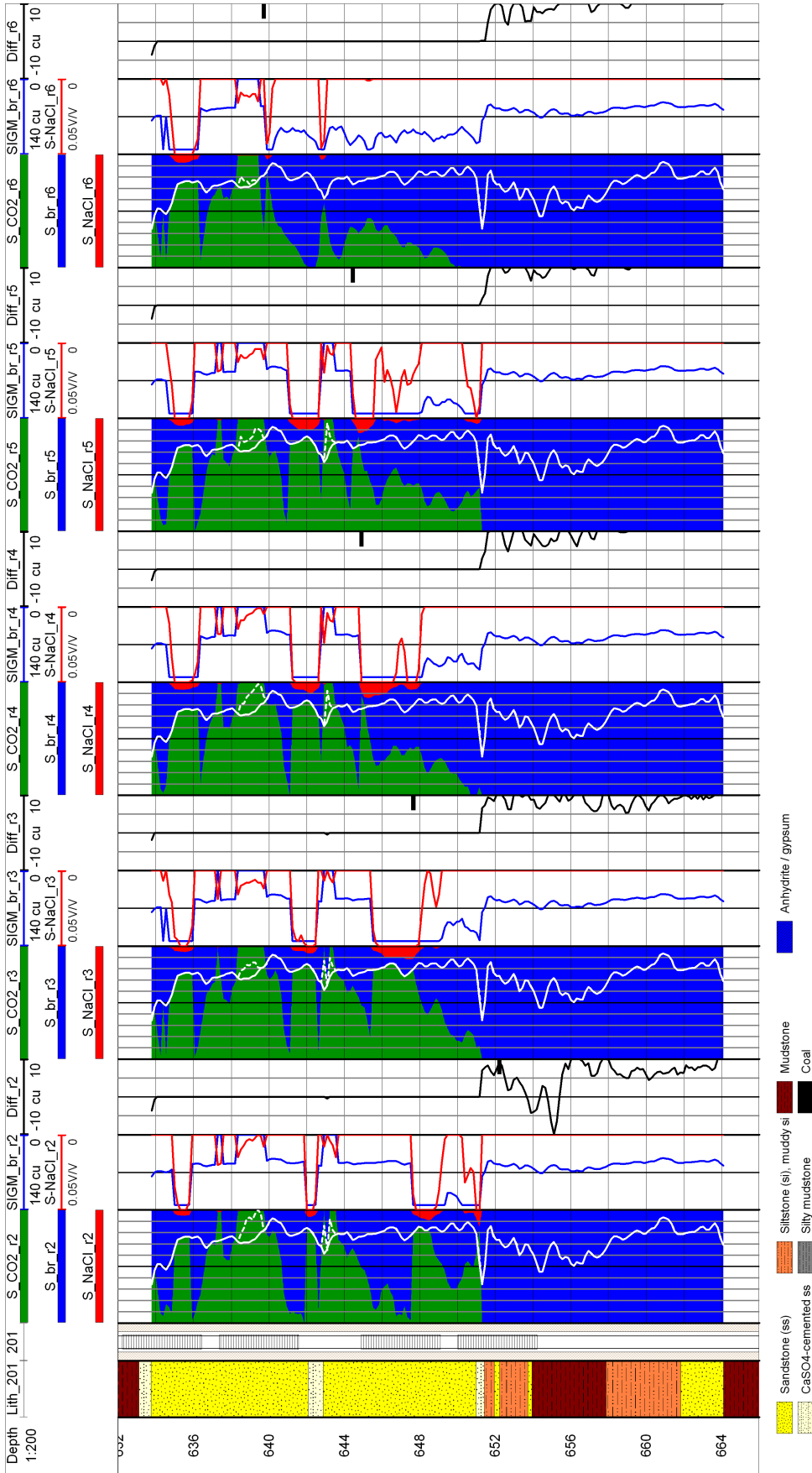


Figure 5.22.: Ktzi201: Saturation profiles as fractions of ϕ_{tot} (CO_2 in green, brine in blue, halite in red) (first track), halite saturations in a smaller scale, Σ_{br} logs (second track) and the corresponding Diff logs (third track) for five repeat runs based on the *extended saturation model and the flush brine salinity with porosity adjustment*. The white solid log for each repeat run separates the mobile from the immobile brine. The white dotted logs show the adjustment of the affected porosities. *If $\Sigma_r > \Sigma_b$, $SCO_{2,eff}$ is set to one and $SCO_{2,irr}$ is set zero (mostly above the brine level) or SCO_2 is derived from TPPI (mostly below the brine level)*. The brine levels for each repeat run are marked with a black bar on the right side of the third track. Lithology after Förster et al. (2010)

5. PNG monitoring results at the Ketzin site

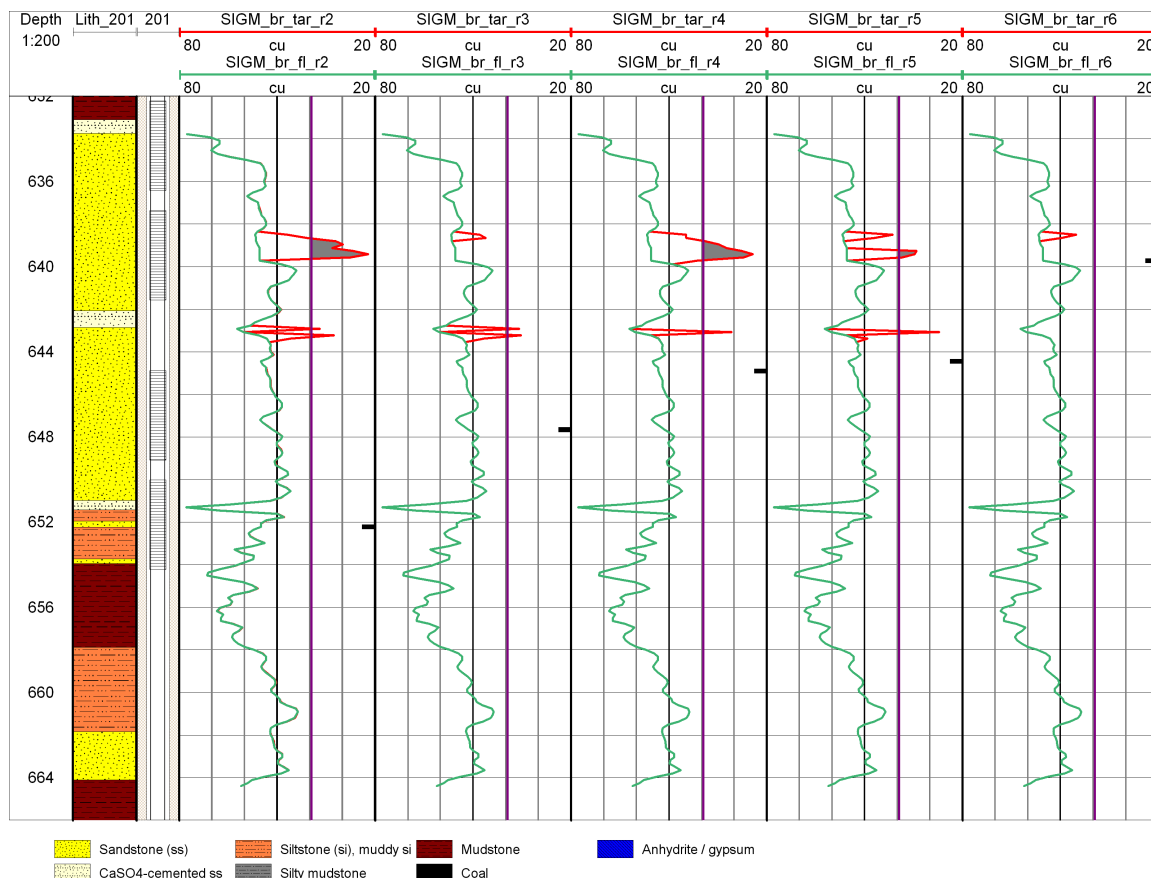


Figure 5.23.: Ktzi201: Flush brine log, which includes the salinity equilibration (SIGM_br_fl) and the target Σ_{br} logs (SIGM_br_tar) for five repeat runs when the affected porosities are not adjusted to minimize Diff. The constant purple curve is Σ_{br-KCl} for the KCl-preflush (39.50 cu). The remaining Σ differences between SIGM_br_tar and Σ_{br-KCl} (grey shading) are the input values for the adjustment of the affected porosities. Lithology after Förster et al. (2010)

The S_{NaCl_x} logs can be transferred to corresponding Σ_{br_x} logs (SIGM_br_tart_r). SIGM_br_tar for the repeat runs as well as the flush brine log (SIGM_br_fl), which includes the salinity equilibration due to diffusion between the low salinity preflush brine (ϕ_{eff}) and the high salinity formation brine (ϕ_{irr}), are shown in figure 5.23.

The SIGM_br_tar values are equal or smaller than the SIGM_br_fl values for all repeat runs. Where a porosity adjustment is applied for the flush brine salinity saturation profiles (Figures 5.22 or 5.21), the SIGM_br_tar values are smaller than the SIGM_br_fl values. For the second, fourth and fifth repeat runs, the SIGM_br_tar values are also smaller than the Σ_{br-KCl} value (39.50 cu) for the KCl-preflush (constant purple log in 5.23) in the middle part of SS1. Except for the sixth repeat run, the same is true for all repeat runs in the upper part of SS2.

The KCl-preflush was performed over a period of about 2.5 days, with changing injection rates and shut-in periods (van der Wall et al., 2008). Assuming multiple salinity equilibrations due to diffusion (diffusion length on pore size scale) between the low salinity preflush brine

Table 5.11.: Ktzi201: Mean S_{CO_2} in the upper (SS1) and lower (SS2) reservoir sandstone sections for five repeats based on the extended saturation model for the original and flush brine salinity data sets shown in figures 5.19 and 5.22.

Section	brine	r2	r3	r4	r5	r6
SS1	org	0.71	0.68	0.67	0.65	0.57
	flush	0.59	0.65	0.69	0.67	0.56
SS2	org	0.51	0.39	0.40	0.31	0.15
	flush	0.50	0.56	0.39	0.45	0.21

(ϕ_{eff}) and the high salinity formation brine (ϕ_{irr}), the Σ_{br} value in ϕ_{irr} decreases for each "cycle". The temperature data for the KCl-preflush (Figure A.20) show the largest temperature anomalies in the middle part of SS1 and the upper part of SS2. Moreover, these depth intervals have the longest warm-back periods. Thus, these findings from the temperature data validate that these depth intervals are most affected by the KCl-preflush. The minimum possible Σ_{br} value is equal to the Σ_{br-KCl} value (39.50 cu). The remaining Σ differences between SIGM_br_tar and Σ_{br-KCl} (grey shading) and the S_{NaCl_x} values are then the input parameters for the adjustment of the affected porosities (Equation 4.27) in order to minimize Diff.

The saturation profiles are unaffected by these porosity adjustments, because the smaller S_{NaCl_x} values in combination with smaller porosity adjustments are equal to the larger S_{NaCl} values from the flush brine salinity and the larger porosity adjustments. Therefore, only the adjusted porosities are different in figure 5.24 compared to the adjusted porosities in figures 5.22 or 5.21 where the scenario $\Sigma_r \leq \Sigma_b$ is valid.

Table summarizes 5.11 the mean S_{CO_2} values shown in figure 5.19 or 5.22 for SS1 and SS2 that include TPHI as input parameter. The mean S_{CO_2} values are greater than the values from the corresponding displacement saturation model for the original and flush brine salinity.

5.4. Discussion of the saturation profiles

In the following section, the saturation profiles for the Ketzin wells are discussed in detail for the investigated period from June 2008 to October 2012. For the Ketzin site, different reservoir modeling results are available that are shortly summarized in table 5.12. All models used a constant injection rate of 1 kg/s. For an injection time of 2 years, this injection rate results in a total amount of 63,000 t CO₂, which is close to the injected amount of CO₂ (60,000 t) for the investigated period. The corresponding dry-out radii (r_{dry}) for 2 years of injection are always smaller than 50 m, which is the distance between the injection well (Ktzi201) and the closest observation well (Ktzi200). All models use a larger formation brine salinity than used for the calculation of the saturation profiles (193 ppk; Chapter 5.1.2). Since the formation brine salinity is, along with the pore size distribution that control the brine's mobility, the most important input parameter for salt precipitation modeling (Zeidouni et al., 2009b), greater halite saturations derived from the models can be expected.

Large halite saturation (0.8) can occur in the lower most reservoir section due to the combined effect of capillary and gravitational forces (Hurter et al., 2007). High halite saturations occur at the edge of the dry-out region and seem to expand vertically due to gravitational forces (Hurter et al., 2007).

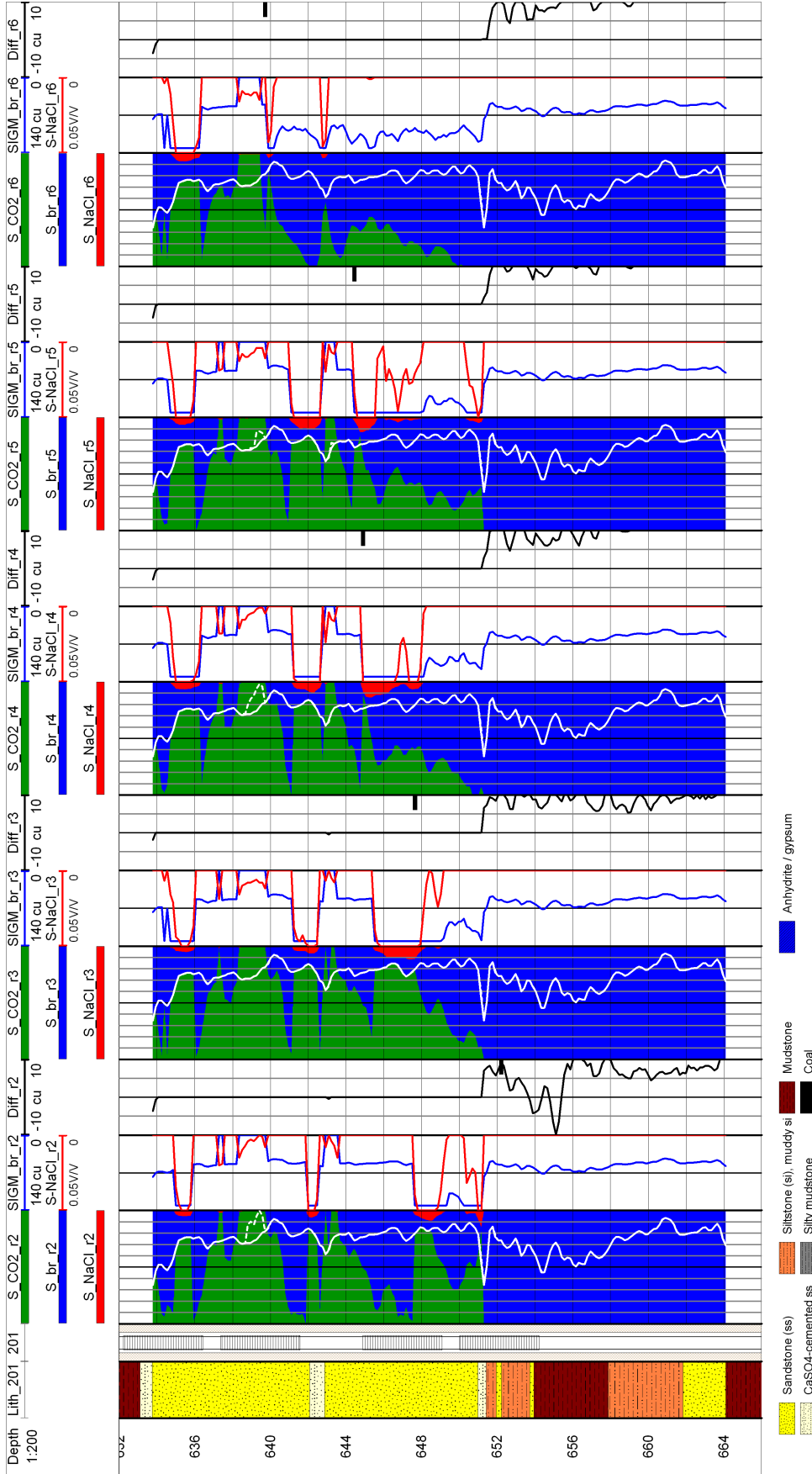


Figure 5.24.: Ktzi201: Saturation profiles as fractions of ϕ_{tot} (CO₂ in green, brine in blue, halite in red) (first track), halite saturations in a smaller scale, Σ_{br} logs (second track) and the corresponding Diff logs (third track) for five repeat runs based on the *extended saturation model and the flush brine salinity with porosity adjustment*. Instead of the *SIGM_br_fl* log, the *SIGM_br_tar* logs and the remaining Σ differences between *SIGM_br_tar* and Σ_{br-KCl} for five repeat runs are the input data for the *simplified evaporation/precipitation saturation model*. The white solid log for each repeat run separates the mobile from the immobile brine. The white dotted logs show the adjustment of the affected porosities. If $\Sigma_r > \Sigma_b$, SCO_{2eff} is set to one and SCO_{2irr} is set zero (mostly above the brine level) or SCO_2 is derived from TPPI (mostly below the brine level). The brine levels for each repeat run are marked with a black bar on the right side of the third track. Lithology after Förster et al. (2010)

5. PNG monitoring results at the Ketzin site

Table 5.12.: Salt precipitation modeling results for the Ketzin site include the input salinity (X_{NaCl}), the dry out radius (r_{dry}) and the greatest precipitated halite saturation (S_{NaCl}).

Reference	X_{NaCl} [ppk]	r_{dry} [m]	S_{NaCl} [V/V]
Hurter et al. (2007)	216	13	0.8
Zeidouni et al. (2009a)	250	3.9	0.03
Muller et al. (2009), org	220	4.0	0.166
Muller et al. (2009), flush	80	3.8	0.04

Zeidouni et al. (2009a) calculated maximum halite saturation of 0.04 by a 1D analytical model, without taking capillary and gravitational forces into account. Muller et al. (2009) derived halite saturation for both the original and flush brine salinity. It should be noted here that the KCl-preflush brine salinity is 20 ppk greater in Muller et al. (2009) than is used for the calculation of the saturation profiles. The halite saturation for the flush brine salinity derived from Muller et al. (2009) is close to the halite saturation derived from Zeidouni et al. (2009a) for the original brine salinity. In contrast, the halite saturation for the original brine salinity derived from Muller et al. (2009) is greater than the value derived from Zeidouni et al. (2009a), because Muller et al. (2009) accounts for capillary and gravitational forces.

The derived saturation profiles for the observation well Ktzi202 (Figure 5.14) give rise to the Buckley and Leverett (1942) saturation profile, indicating that the conventional displacement saturation model is valid. The CO_2 saturation increases in the upper part and decreases in the lower part of SS1 for the investigated period. The mean CO_2 saturation increases from the second to the fourth repeat, and then decreases for all subsequent repeat runs in SS1. The greatest mean CO_2 saturations occur for the third and fourth repeat runs, which also correlates with the deepest brine levels. In contrast the deepest brine levels in Ktzi201 and Ktzi200 occur for the second repeat run. The later derived deepest brine levels associated with the greatest mean CO_2 saturations correspond to the later arrival of the CO_2 at Ktzi202 (Kempka et al., 2010). Compared to Ktzi201 and Ktzi202, the CO_2 saturation is smallest in Ktzi202.

In contrast to the observation well Ktzi202, the derived CO_2 saturations in the observation well Ktzi200, derived from the displacement part of the extended saturation model, show that, in addition to displacement, the evaporation/precipitation process is occurring in some depth intervals above the brine level. In Ktzi200 all three situations occur: the brine salinity is increased, the brine salinity reaches its maximum and precipitation occurs or the evaporation/precipitation process has been completed (Figure 5.16). The maximum derived halite saturation is 0.032.

Compared to the modeling results, the precipitated halite seems unrealistic in Ktzi200, because the dry-out radii are smaller than the distance (50 m) between the injection well Ktzi201 and the observation well Ktzi200. But these models are based on simplifications and do not sufficiently account for the lithological heterogeneities of the reservoir section, or the changing injection rate. Additionally, the Ktzi200 was characterized by a less comprehensive open hole well logging program (Norden et al., 2010) than was performed in the injection well, which is why greater uncertainties can be expected for the derived saturation profiles. Further modeling investigations, including the derived saturation profiles from the PNG monitoring data in combination with the extended saturation model, are needed to validate whether the de-

rived halite precipitations are possible or not. Since the lithology in Ktzi200 and Ktzi201 is relatively similar, and the area of the derived halite saturation in Ktzi200 corresponds to the dry-out region in the middle part of SS1 in Ktzi201, preferential flow paths could account for derived halite saturation. The increasing CO₂ saturation during the investigated period in the upper part of SS1 can result from gravitational forces and the decrease in the lower part of SS1 can result from the decreased injection rate. For the first, second and third repeat runs, SS2 contains CO₂. This corresponds to the high injection rate before March 2010. Due to the uncertainties regarding the derived precipitated halite, no final saturation profiles can be determined for Ktzi200. If precipitated halite can be excluded, the saturation profiles based on the displacement process associated with differences between the modeled and measured data is valid (Figure 5.9).

In contrast to the observation well Ktzi200, the evaporation/precipitation process has been completed in the middle part of SS1 and the upper part of SS2 for both brine salinity data sets of the injection well Ktzi201 (Figures 5.19 and 5.24). In these dry-out regions, the maximum derived halite saturation is 0.043 for the original brine salinity and 0.024 for the flush brine salinity data set. The halite saturations are greatest at the upper edge and decrease in the center of the dry-out regions for both brine salinity data sets. Moreover, for some repeat runs, halite saturations are also increased at the lower edge of the dry-out regions for both brine salinity data sets. The derived halite saturations as well as their distribution are in good agreement with the modeling results from Muller et al. (2009) and Zeidouni et al. (2009a) for the Ketzin site.

The porosity adjustment results always in a decreased halite saturation compared to the possible initial stored amount of NaCl in the original or flush brine. The two performed brine salinity adjustments (starting from original formation brine over flush brine to the minimum possible brine salinity being equal to the KCl-preflush brine salinity) decrease the necessary porosity adjustment. The most appropriate combination of brine salinity and porosity adjustment is reached for the last brine salinity adjustment and is shown in figure 5.24. Since a porosity adjustment is remaining in the dry-out regions, the performed calculation step (i.e. excluding remaining water saturation) is validated. The application of this step is validated because the stored amount of NaCl in brine was continuously decreased due to decreasing the brine salinity. This is associated with a decreasing modeled Σ value to minimize Diff, which is why an additional Σ fraction from remaining water saturation can be excluded. Moreover, the temperature data for the KCl-preflush (Figure A.20) show the largest temperature anomalies and longest warm-back periods in the later dry-out regions, validating that these depth intervals have the highest injectivity corresponding to the expected behavior for dry-out regions.

The second scenario of the extended saturation model occurs partially for the original as well as for the flush brine salinity data sets, indicating an increased pore fluid Σ value as a result of capillary effects. For the original brine salinity data set, the second scenario occurs only below the brine level for two repeat runs. In contrast, for the flush brine salinity data set, the second scenario occurs partially above and below the brine level for all repeat runs. As a result, in more areas of the reservoir section, precipitated halite occurs for the flush than for the original brine salinity data set.

Compared to the CO₂ saturation shape based on the assumption that S_{CO_2eff} is one and S_{CO_2irr} is zero, the CO₂ saturation shape derived from TPHI seems more realistic. It seems more realistic because the CO₂ saturation shape fits better to the overall saturation shape, especially when comparing the neighboring CO₂ saturations where this scenario is not applied.

5. PNG monitoring results at the Ketzin site

Additionally, the TPHI derived CO₂ saturations are based on real measurements and not on an assumption. Therefore, where CO₂ saturations can be derived from TPHI, they are used for the final saturation profiles as shown in figures 5.19 and 5.24. Since the CO₂ saturations derived from TPHI are smaller than the CO₂ saturations based on the model assumption, the correspondingly derived halite saturations are decreased and the brine saturations are increased.

The mean CO₂ saturations in SS1 are smaller for the flush brine salinity data set than for the original brine salinity data sets before March 2010. Subsequently both mean CO₂ saturations are nearly similar in SS1. In contrast, the mean CO₂ saturations are nearly similar for the first year in SS2. For the rest of the investigated time period the mean CO₂ saturations are greater for the flush brine salinity data set than for the original brine salinity data set or nearly similar. In Silt and SS3, only CO₂ saturation exists before March 2010, corresponding to the high injection rate. Moreover, the extended saturation model is needed. Otherwise the CO₂ saturation will be erroneously underestimated.

The greatest halite saturations for both brine salinity data sets occur in the vicinity below the brine level, where large capillary forces occur. The maximum halite saturation is 0.135 for the original brine salinity and 0.141 for the flush brine salinity data set below the brine level, validating an increased salt load due to capillary effects. These greatest halite saturations resulting from capillary forces also agree with the modeling results for the Ketzin site. For the original brine salinity data set, this halite saturation only occurs for the fourth and fifth repeat runs in the middle part of SS2 below the brine level.

For the flush brine salinity data set, halite saturation occurs in the middle part of SS2 above the brine level. This halite containing depth interval moves upward with the repeat runs, corresponding to the rising brine level. For both brine salinity data sets, halite saturation is absent for the sixth repeat run, also correlating with the rising brine level from the fifth to sixth repeat runs. For the flush brine salinity data set in the interbedded, strongly cemented sandstone layer between SS1 and SS2, halite saturation initiates at the beginning of the investigated time period and expands up to the fifth repeat run into the lower most part of SS1 and the upper most part of SS2. For the sixth repeat run, halite saturation is absent in this depth interval corresponding to the rising brine level.

The halite saturation distribution seems to be controlled by the combined effects of changing injection rates associated with changing brine levels, lithology heterogeneities, and different saturation changing processes such as evaporation/precipitation or capillary forces. Due to the rising brine levels precipitated halite goes back into solution. Based on equation 3.4, the relative permeability change ($\frac{k}{k_0}$) due to porosity change is 0.58 for the greatest derived halite saturation (0.141). However, it should be stated here again that the porosity reduction alone is not sufficient to account for the associated permeability effect, especially in heterogeneous lithologies like the reservoir section of the Ketzin site. Additionally, the dynamic distribution of the halite saturations is associated with possible dynamic effects on permeability.

As mentioned in chapter 5.2.1, the higher SBNA reading in SS1 should result from the reservoir. A material with a large Σ value, like halite, could account for the increased SBNA reading. Muller et al. (2009) derived a halite saturation peak at 0.3 m from the borehole for the original brine salinity, whereas for the flush brine salinity no precipitated halite occurs up to one meter distance from the injection point. In fact, the KCl-preflush was performed, but the increased SBNA reading correlates with the findings from Muller et al. (2009) for the original brine salinity. Maybe this salt peak also occurs for the flush brine salinity.

5. PNG monitoring results at the Ketzin site

Additionally, precipitated halite is also derived for the flush brine salinity data set that do not agree with the findings from Muller et al. (2009). For the flush brine salinity, precipitated halite occurs with a maximum of 0.04 at 4.3 m from the injection point (Muller et al., 2009) that is not within the expectable depth of investigation for common PNG tools with high gas saturations in the formation (Knödel et al., 1997).

The lowest halite saturations are derived in the dry-out regions above the brine level, corresponding to low repeat Σ values. The highest halite saturations are derived below the brine level, corresponding to high repeat Σ values. Since the imprecision increases as formation Σ increases (Kimminau and Plasek, 1992), a greater accuracy can be expected for the low rather than for the high derived halite saturations. Additionally, the uncemented or partly cemented annuli in the reservoir section add further environmental effects above the brine level. This mainly affects the neutron porosity, because the neutron porosity is derived from near and far detector, whereas Σ is derived from the far detector only. Moreover, the TPHI values are input parameters for the RST processing algorithm for deriving the Σ values. The data processing for the repeat runs, using the open hole derived porosity as external knowledge, is the most appropriate data processing, bypassing the TPHI influence on Σ . But a negative effect on the PNG accuracy cannot be excluded, even after the extensive log quality control. For this purpose, enhanced PNG tools calibration is needed for gas-filled borehole environments, especially for effects resulting from uncemented annuli. However, the greatest uncertainty results from the missing second PNG baseline run performed immediately after the KCl-preflush. Thus, the saturation profiles derived from the original or flush brine salinity data sets cannot be more specified. The final saturation profiles are probably in between both derived saturation profiles. Such omission should be avoided.

Salt precipitations were previously not detected in situ in connection with CO₂ injection in saline aquifers. At the Ketzin site, salt precipitations are detected in situ. In general, the derived saturation profiles are in good agreement with the modeling results for the Ketzin site. PNG monitoring in combination with the extended saturation model is suited to determine displacement and evaporation/precipitation processes for CO₂ storage operations.

6. Sensitivity study for the Altmark site

The injection of CO₂ into depleted natural gas reservoirs has been proposed as a promising new technology for combining enhanced gas recovery (EGR) and geological storage of CO₂ (van der Burgt et al., 1992). Application of this technology could both lead to environmental and economic benefits by reducing greenhouse gas emissions in the framework of carbon capture and storage (CCS) and increasing the amount of recoverable gas from a reservoir (Oldenburg et al., 2004). Since only few experiences from field-scale experiments do exist until now, the joint research project CLEAN (Kühn et al., 2011, 2012) for evaluation of the EGR potential at the Altmark site, Germany, which is owned and operated by GDF SUEZ E&P Deutschland GmbH (GDF-SUEZ, 2009), has been set up.

The nearly depleted gas field is characterized by a low reservoir pressure (40 bar; GDF-SUEZ (2009)), where low gas densities correspond to low carbon and oxygen concentrations as well as low Σ values. Moreover, natural gas (CH₄, N₂) and CO₂ contain carbon, but only CO₂ contains oxygen. Therefore, the fraction of natural gas displacement by CO₂ contributes only marginally to the total carbon or oxygen concentration and to the overall carbon-oxygen ratio (COR) of the formation. Even for super critical CO₂ only qualitative determinations of CO₂ saturations with the C/O log are applicable (Murray et al., 2010). Under this low pressure conditions the CO₂ is gaseous with a corresponding very low density and carbon concentration.

Hence, both the changes in the total COR as well as the Σ value of the formation by displacement of natural gas by CO₂ can be considered to be low. But since the Σ contrast between CO₂ and brine is large, a good detectability of brine displacement can be expected in Σ logging mode, which is therefore more appropriate than C/O logging under the considered conditions.

Therefore the PNG monitoring potential focused on Σ logging, taking into account evaporation/precipitation effects and changing gas-water-contacts (GWC) in the formation, is evaluated for application under conditions similar to the Altmark site (Baumann et al., 2011; Baumann and Henniges, 2012), which might be representative of many suitable locations for a commercial deployment of the EGR and CCS technologies worldwide.

6.1. Initial saturation conditions and expected saturation changes

The following describes the saturation conditions and possible changes in pore space fluid composition by dry CO₂ injection that then feed in a saturation model described by individual volumetric mixing equations.

The reservoir intervals above the initial GWC at the Altmark site are partially saturated with mobile natural gas (S_{ng}) and immobile brine. The natural gas is predominantly composed of 0.75 N₂ and 0.25 CH₄ by volume (GDF-SUEZ, 2009). The irreducible brine saturation

($S_{br_{irr}}$) has been determined from logging data (GDF-SUEZ, 2009) and ranges between 0-40 % of the total porosity (ϕ_{tot}). Accordingly, the volume-weighted shares (fractions) of natural gas, irreducible brine and the rock matrix result in the first case of the considered baseline model characterizing the section above the GWC.

Due to increased reservoir pressure during CO₂ injection, the initial GWC would be anticipated to move downward. Thus, formerly completely brine-saturated injection layers are flooded with CO₂. Therefore, the baseline model below the initial GWC simplifies to a brine-saturated pore space. In this second case, a similar distinction is made between immobile brine and free mobile brine.

Therefore in summary, two different cases for the baseline model before injection are considered: case 1 refers to the situation above the initial GWC (pore space partially saturated with natural gas and immobile brine), and case 2 to the reservoir section below the initial GWC (completely brine-saturated). Starting from the two different baseline saturation conditions and their individual phase mobilities, different physical mechanisms lead to saturation changes.

6.2. Saturation scenarios and saturation models

The mobile fluid fraction (case 1: natural gas, case 2: brine) is physically displaced by the injected CO₂. In contrast to that, the immobile fluid fraction (case 1 and case 2: brine) is evaporated associated with salt precipitation. Capillary and gravitational effects are neglected. Therefore, only the amount of salt precipitation routed from the original brine is taken into account.

The pore space above the initial GWC ϕ_{eff} is saturated with natural gas (case 1) and below the GWC with brine (case 2). ϕ_{irr} results for both cases from $S_{br_{irr}}$.

Accordingly, the volume-weighted shares of natural gas (case 1) or brine (case 2), the immobile brine and the rock matrix result in the baseline model (Figure 6.1, Baseline). To estimate the effect of saturation changes on Σ measurements, the following two scenarios are assumed for repeat measurements during injection.

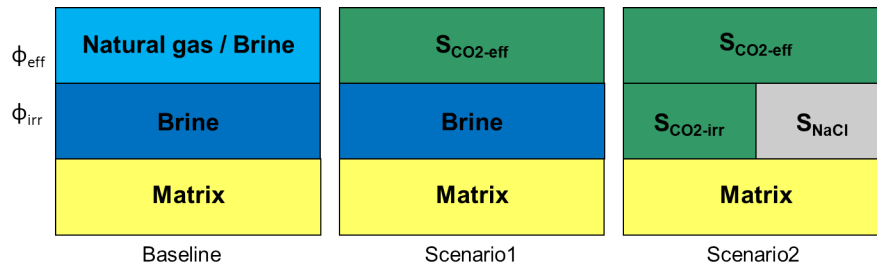


Figure 6.1.: Saturation models: Baseline: in-situ saturation condition before injection. Scenario 1: natural gas/brine displacement (ϕ_{eff}). Scenario 2: natural gas/brine displacement (ϕ_{eff}) and complete evaporation of immobile brine associated with salt precipitation (ϕ_{irr}).

The first scenario takes only the mobile fluid displacement into account, where $S_{br_{irr}}$ is assumed to be unchanged (Figure 6.1, Scenario 1). The second scenario considers not only the

6. Sensitivity study for the Altmark site

in situ fluid displacement, but in addition the evaporation of the immobile brine (Figure 6.1, Scenario 2).

The baseline models is adjusted after equation 4.2

$$\Sigma_b = (1 - \phi_{tot}) \cdot \Sigma_{ma} + \phi_{eff} \cdot \Sigma_{ng/br} + \phi_{irr} \cdot \Sigma_{br} \quad (6.1)$$

where the subscripts ma, ng and br correspond to the rock matrix and the pore fluid components, natural gas and brine, respectively. Under the assumption that N₂ and CH₄ are completely miscible and can therefore be equally effectively displaced, Σ_{ng} results from the volume-weighted Σ values of N₂ and CH₄ (N₂ 0.75 and CH₄ 0.25 by volume; GDF-SUEZ (2009)).

$$\Sigma_{ng} = S_{N_2} \cdot \Sigma_{N_2} + S_{CH_4} \cdot \Sigma_{CH_4} \quad (6.2)$$

To estimate the maximum expectable Σ changes for the sensitivity study, corresponding maximum possible saturation changes are evaluated in each scenario. In the first scenario, the natural gas and brine in ϕ_{eff} is completely replaced by CO₂. Therefore, $S_{CO_{2eff}}$ is equal to one. Accordingly, the first scenario results from equation 4.3 with $S_{br_{eff}}$ equal to zero in

$$\Sigma_{r-sc1} = (1 - \phi_{tot}) \cdot \Sigma_{ma} + \phi_{eff} \cdot \Sigma_{CO_2} + \phi_{irr} \cdot \Sigma_{br} \quad (6.3)$$

with $S_{CO_{2tot}}$

$$S_{CO_{2tot}} = (1 - S_{ng}) \cdot \frac{\phi_{eff}}{\phi_{tot}}$$

In addition to the first scenario's parameters, the second scenario also takes into account the complete evaporation of irreducible brine and resulting salt precipitation. The second scenario results from equation 4.8 with $S_{br_{eff}}$ and $S_{H_2O_r}$ equal to zero in

$$\Sigma_{r-sc2} = (1 - \phi_{tot}) \cdot \Sigma_{ma} + \phi_{eff} \cdot \Sigma_{CO_2} + \phi_{irr} \cdot (S_{salt} \cdot \Sigma_{salt} + S_{CO_{2irr}} \cdot \Sigma_{CO_2}) \quad (6.4)$$

where S_{salt} is the salt saturation and Σ_{salt} is the macroscopic capture cross section of the precipitated salts. $S_{CO_{2tot}}$ is derived as follows

$$S_{CO_{2tot}} = (1 - S_{ng}) \cdot \frac{\phi_{eff}}{\phi_{tot}} + (1 - S_{salt}) \cdot \frac{\phi_{irr}}{\phi_{tot}}$$

In addition to in situ fluid displacement and water evaporation associated with salt precipitation, also mineral trapping of CO₂ can possibly result in Σ_{ma} changes. Beyer et al. (2012) studied the reactive transport by CO₂ injection, including dissolution and precipitation kinetics of mineral reactions. Notable mineral trapping of CO₂ by carbonate precipitation starts after approximately 2000 years for the conditions similar to the Altmark site. Even over a period of 10000 years, the injected CO₂ results in dissolution of the primary silicates associated with the precipitation of clay minerals.

In contrast to the timescale of mineral trapping, displacement and evaporation processes occur more or less simultaneously with the CO₂ injection process. Resulting from these different timescales, mineral dissolution and precipitation are not considered in the sensitivity study. Therefore, Σ_{ma} is assumed to be invariant for the sensitivity study.

6.3. Determination of pore fluid capture cross sections and salt precipitations

According to the saturation models, the involved pore fluid capture cross sections are analyzed in detail. Moreover, to assess the influence of salt precipitation on Σ measurements, the chemical brine composition from the Altmark site (De Lucia et al., 2012) is considered. The Σ values of the pore fluids are calculated based on the Σ brine calculation (Chapter 2.2.1.3).

Similar to many brines from the North German Basin, the Altmark brine is dominated by chlorine. Since chlorine has a large σ_{m_i} in comparison to other typical dissolved ions, the Σ chlorine fraction is dominant. The trace elements boron and lithium only play a subordinate role in the total solution content. But due to their considerably large σ_{m_i} , their contribution to Σ_{salt} is not irrelevant. Overall, Σ_{salt} results in 136.26 cu, where chlorine contributes 89.9 %, boron 6.9 % and lithium 2.0 % to the total value. All other remaining ions contribute less than 1.2 % to the total value.

Table 6.1.: Capture cross sections for brine (Σ_{br}) as the sum of the capture cross sections of fresh water ($\Sigma_{H_2O_c}$) and the dissolved salts for the “true” and the NaCl-equivalent brine ($\Sigma_{salt/NaCl_{c-eq}}$) under ambient (25 °C, 1 bar) and reservoir conditions (125 °C and 40 bar), the corresponding brine densities (ρ_{br}) and total dissolved salt content (TDS). *(Data provided by GDF-SUEZ (2009); adjusted by De Lucia et al. (2012))

Brine	T / p	TDS	ρ_{br}	$\Sigma_{salt/NaCl_{c-eq}}$	$\Sigma_{H_2O_c}$	Σ_{br}
	[°C] / [bar]	[g/l]	[g/cm ³]	[cu]	[cu]	[cu]
“True” brine	25 / 1	347.18*	1.24*	136.26	19.75	156.01
NaCl _{eq} brine	25 / 1	388.59	1.24	136.26	18.92	155.18
NaCl _{eq} brine	125 / 40	369.92	1.18	129.72	18.01	147.73

Since chlorine is the dominant chemical constituent, the saturation state calculations are simplified. Σ_{salt} is presented only as the NaCl-equivalent concentration ($c_{NaCl_{eq}}$). In comparison to the “true” total salt concentration (347.18 g / l; Table 6.1), $c_{NaCl_{eq}}$ results in 388.59 g/l NaCl, which is greater than the “true” total salt concentration. This results from the larger σ_{m_i} of the trace elements boron and lithium compared to chlorine. Compensation for this discrepancy is made by increasing the NaCl-equivalent concentration until it reaches the total Σ_{salt} value.

The brine density for the NaCl-equivalent concentration under ambient conditions (25°C, 1 bar) was calculated after Rowe and Chou (1970). The calculated NaCl-equivalent brine density of 1.24 g/cm³ under ambient conditions is similar to the “true” brine density. To account for the Altmark reservoir conditions (125 °C, 40 bar; GDF-SUEZ (2009)), the brine density was also adjusted after Rowe and Chou (1970) to 1.18 g/cm³. The decreasing brine density under reservoir conditions correspondingly results in a smaller NaCl-equivalent concentration of 369.92 g/l.

Accordingly, Σ_{salt} results in 147.73 cu. In Table 6.1 all relevant brine parameters are summarized. The NaCl-equivalent brine under reservoir conditions is used for the halite precipitation calculation and the sensitivity study in the following section.

The gases’ Σ values (Table 6.2) were also calculated for the reservoir conditions by adjusting

the input densities as a function of pressure and temperature using the approach of Afeefy et al. (2005).

The extended saturation model is not needed, because only the maximum possible saturation changes are evaluated in each scenario. The precipitation of all dissolved NaCl would yield a halite saturation (S_{NaCl}) calculated after equation 3.1. $c_{NaCl_{eq}}$ under reservoir conditions, S_{NaCl} is 0.17, with a corresponding $S_{CO_{2irr}}$ of 0.83 ($1 - S_{NaCl}$).

6.4. Sensitivity study for displacement and evaporation/precipitation processes

To evaluate the assumed saturation models, hypothetical Σ values based on the assumed cases and scenarios are calculated. Case 1 describes the baseline above and case 2 the baseline below the initial GWC. Accordingly, the baseline measurement response was calculated (Table 6.2, S_b , case 1, case 2). The hypothetical repeat measurement response was calculated according to the first and second scenarios (Table 6.2, S_{sc1} , S_{sc2}). The first scenario takes only the physical in situ fluid displacement into account (Figure 6.1, scenario 1). The second scenario considers in addition the evaporation of the immobile brine associated with salt precipitation (Figure 6.1, scenario 2). Subsequently, the differences between baseline and repeat measurements are analyzed.

Table 6.2.: Σ values of different fluids and the associated saturations for the baseline (S_b) above (case 1) and below (case 2) the initial GWC and the two assumed scenarios (S_{sc1} , S_{sc2}) first pure displacement and second displacement and evaporation/precipitation. *Data according to GDF-SUEZ (2009).

Fluid (125 °C, 4 MPa)	Σ [cu]	S_b^* [V/V] case 1	S_b^* [V/V] case 2	S_{sc1} [V/V]	S_{sc2} [V/V]	ϕ [V/V]
N_2	2.722	0.75*	0	0	0	ϕ_{eff}
CH_4	0.984	0.25*	0	0	0	
Natural gas	2.288	1	0	0	0	
NaCl _{eq} brine	147.73	0	1	0	0	
CO_2	0.003	0	0	1	1	ϕ_{irr}
NaCl _{eq} brine	147.73	1	1	1	0	
NaCl	760.92	0	0	0	0.17	
CO_2	0.003	0	0	0	0.83	

To investigate the general behavior of the assumed cases and scenarios, first hypothetical baseline and repeat measurements were calculated as a function of the total porosity ϕ_{tot} . S_{brirr} was set to 50 % of ϕ_{tot} ; therefore, ϕ_{eff} and ϕ_{irr} are equal. The Σ fluid values under reservoir conditions are used and the Σ matrix value (Σ_{ma}) corresponds to clean sandstone (10 cu; Smolen (1996)). It should be noted that an inert matrix was assumed. Therefore, the choice of Σ_{ma} is generally irrelevant for the sensitivity study, since Σ_{ma} is constant for all baseline and repeat measurements.

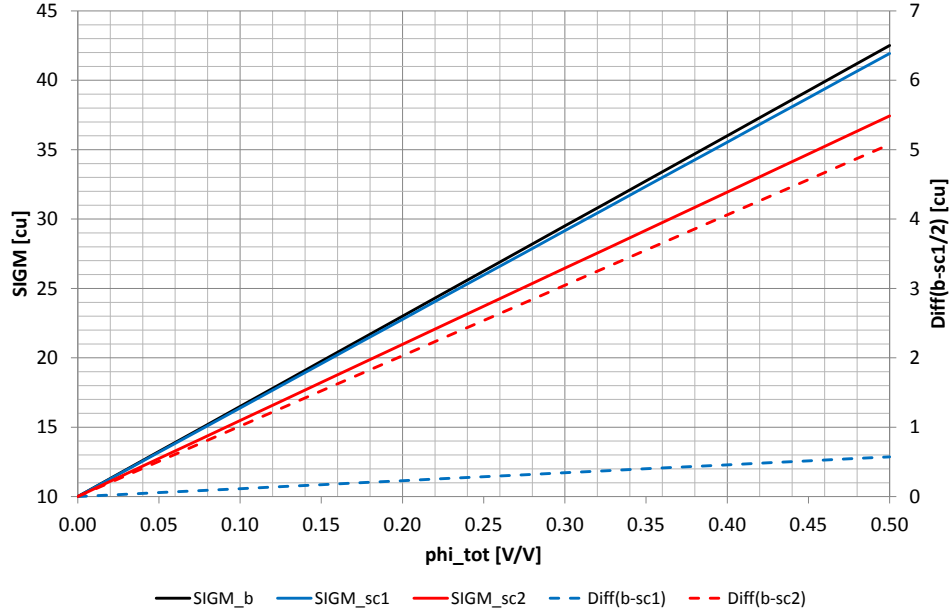


Figure 6.2.: Σ modeling results (left ordinate) for the baseline above the initial GWC (case 1, Σ_b) and the two different scenarios (Σ_{sc1} , Σ_{sc2}) as a function of the total porosity (ϕ_{tot}) and the corresponding differences (right ordinate) between the baseline and two scenarios (Diff(b-sc1)), Diff(b-sc2)). $S_{br_{irr}}$ is set to 50 % of ϕ_{tot} .

6.4.1. Case 1: above the initial GWC

As expected, Σ increases for the baseline as well as for the two scenarios with increasing ϕ_{tot} (Figure 6.2, left ordinate). Also, the Σ differences between the baseline and the two scenarios (Diff(b-sc1), Diff(b-sc2)) increase with ϕ_{tot} . Diff(b-sc1) is much smaller than Diff(b-sc2) (Figure 6.2, right ordinate). For the maximum investigated total porosity of 0.5, Diff(b-sc1) results in 0.6 cu and Diff(b-sc2) in 5.1 cu. The small Diff(b-sc1) result from the small Σ difference between natural gas and CO_2 , since the immobile brine remains unchanged in the first scenario. For the second scenario, the influence of evaporation associated with higher Σ differences between water and CO_2 is evident.

Based on the immobile brine and the given scenarios, $S_{CO_{2tot}}$ results from the volume-weighted sum of the individual CO_2 saturations in ϕ_{eff} and ϕ_{irr} . Therefore, $S_{CO_{2tot}}$ for the first scenario (S_{sc1}) is 0.5 corresponding to $S_{br_{irr}}$ of 50 % of ϕ_{tot} . For the second scenario (S_{sc2}), $S_{CO_{2tot}}$ is 0.915 (Figure 6.2, right ordinate). This greater CO_2 saturation results from the additional volume fraction initially occupied by water, which is then evaporated and replaced by CO_2 in the second scenario. Correspondingly, the remaining volume fraction ($1 - S_{CO_{2tot}}$) is occupied by precipitated halite. Generally, ϕ_{tot} does not influence the saturation values, because the CO_2 volume increases proportional with ϕ_{tot} .

6.4.2. Case 2: below the initial GWC

Similar to case 1, Σ and the corresponding Σ differences in case 2 increase also for the baseline with increasing ϕ_{tot} (Figure 6.3). Also, the difference between the baseline and the first scenario is smaller than the difference between the baseline and the second scenario. For the

6. Sensitivity study for the Altmark site

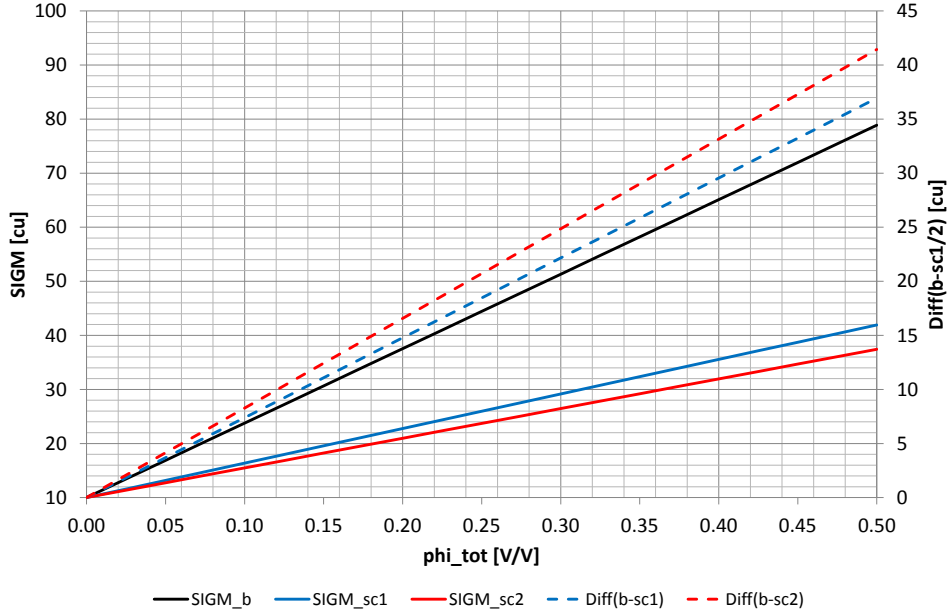


Figure 6.3.: Σ modeling results (left ordinate) for the baseline below the initial GWC (case 2, Σ_b) and the two different scenarios (Σ_{sc1} , Σ_{sc2}) as a function of the total porosity (ϕ_{tot}) and the corresponding differences (right ordinate) between the baseline and two scenarios (Diff(b-sc1)), Diff(b-sc2)). $S_{br_{irr}}$ is set to 50 % of ϕ_{tot} .

maximum investigated total porosity of 0.5, Diff(b-sc1) results in 36.9 cu, and Diff(b-sc2) is 41.4 cu. These differences are an order of magnitude larger than for the natural gas saturated model (case 1). Case 1 and case 2 differ in the mobile fluid fraction that can be displaced by the injected CO_2 . Below the initial GWC (case 2) the larger Σ difference between brine and CO_2 results in larger Σ differences between the baseline and two scenarios.

The influence of evaporation is of course similar for both cases below and above the GWC, since the same scenario is assumed. Therefore, the difference between (Diff(b-sc2)) and (Diff(b-sc1)) is the same and results in 4.5 cu.

Also, the total CO_2 saturation ($S_{CO_{2tot}}$) is equal for both cases but differs between the two scenarios. In the first scenario, only the mobile fluid fraction can be displaced and is occupied by the injected CO_2 . The second scenario considers in addition the evaporation of the immobile brine resulting in an extra CO_2 saturated porosity fraction (ϕ_{irr}). To illustrate the influence of neglecting potential salt precipitation on the estimated CO_2 saturation, the immobile porosity fraction (ϕ_{irr}) is analyzed in detail. $S_{CO_{2irr}}$ calculated after

$$S_{CO_{2irr}} = \frac{1}{\Sigma_{CO_2}} \cdot \left(\Sigma_{H_2O_c} - \frac{\Sigma_{b_{irr}} - \Sigma_{r-sc2_{irr}}}{\phi_{irr}} \right) \quad (6.5)$$

results in 0.830 and is independent of ϕ_{irr} . The remaining porosity fraction (0.17) is occupied by halite. Correspondingly, $S_{CO_{2irr}}$ and $S_{CO_{2eff}}$ weighted by their corresponding porosity fraction result in a total CO_2 saturation $S_{CO_{2tot}}$ of 0.915 as described above.

Conventional PNG saturation models assume a displacement process only. Physically, it is not possible to displace the immobile fluid fraction. But assuming an inverted model where the immobile brine is not evaporated but displaced, $S_{CO_{2irr}}$ can be calculated from

$$S_{CO_{2irr}} = \frac{\Sigma_{b_{irr}} - \Sigma_{r-sc2irr}}{\phi_{irr} (\Sigma_{br} - \Sigma_{CO_2})} \quad (6.6)$$

Here, an “apparent” $S_{CO_{2irr}}$ of 0.122 is calculated, opposed to a value of 0.830 using the inverted model of the second scenario. Neglecting the evaporation process and assuming a displacement process would therefore result in an erroneous underestimation of the CO₂ saturation. Therefore, it is important to account for the dry CO₂ evaporation capability by a saturation model which is extended by a salt precipitation component.

6.4.3. S13 injection well

To assess whether saturation changes are to be expected at the Altmark site above the GWC are detectable with PNG monitoring; baseline (Table 6.2, S_b) and hypothetical repeat measurements according to the described scenarios (Table 6.2, S_{Sc1} , S_{Sc2}) were calculated for the S13 injection well. The log-derived total porosity and residual brine saturation data of well S13 (GDF-SUEZ, 2009) were included. The assumed Σ values of the matrix correspond to clean sandstone (10 cu) in the injection layers and claystone (38 cu) in the non-injection intervals (Smolen, 1996).

Due to the small Σ differences between the gases, the effect of gas displacement alone (scenario 1) is also correspondingly low (Figure 6.4). The largest contrast is 0.30 cu and occurs in the high porosity sandstone layers (X435-X455 m). The difference between the baseline and scenario 1 is in the range of typical PNG tool accuracy (0.22 cu; Plasek et al. (1995)) and would therefore not be detectable in practice.

Taking into account additional evaporation of immobile brine with the dissolved salts precipitating in the pore space (scenario 2), the calculated Σ contrast is an order of magnitude higher. As for the first scenario, the greatest contrast occurs in the high porosity sandstones with high irreducible brine saturations, but for scenario 2, the difference is about 1.48 cu and could be detectable with typical PNG tools.

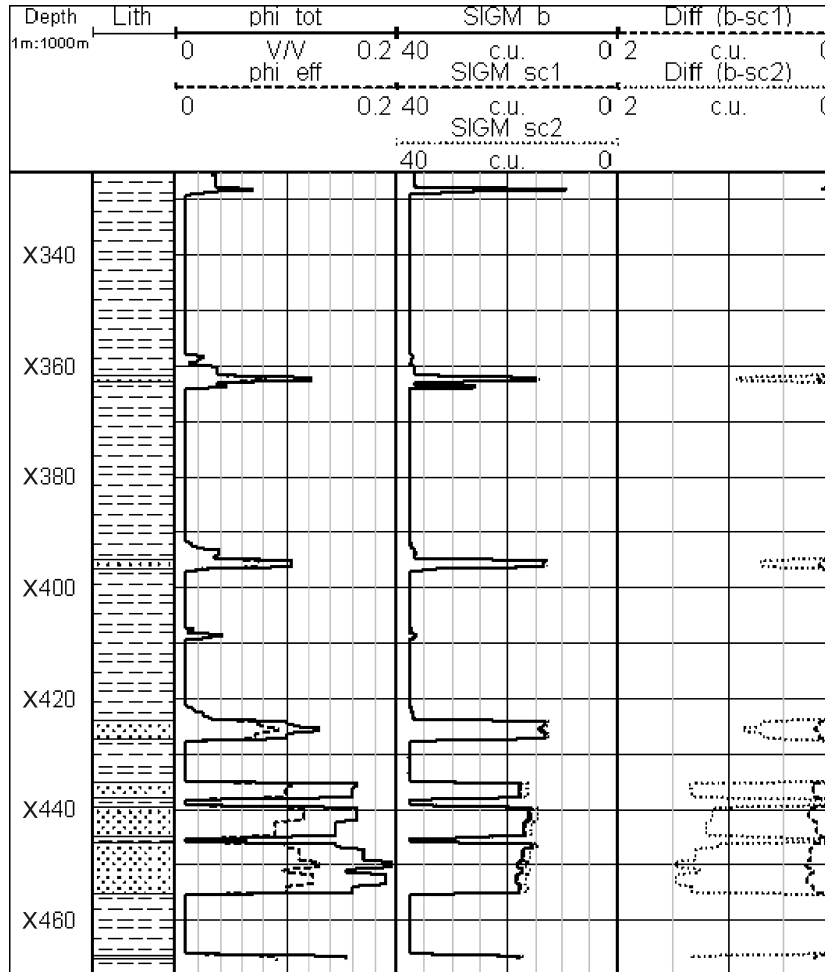


Figure 6.4.: Σ modeling results for the baseline and the two different scenarios for the S13 injection well at the Altmark site. Injection intervals with high permeabilities are indicated by dotted signature. Left track: total porosity (ϕ_{tot})* and effective porosity (ϕ_{eff})*, middle track: baseline (SIGM_b) and repeat Σ (SIGM_sc1, SIGM_sc2), right track: difference between baseline and repeats (Diff_(b-sc1), Diff_(b-sc2)). * Data according to GDF-SUEZ (2009)

6.5. Summary of the sensitivity study

Application of the PNG method for estimation of saturation changes above the GWC is hampered under the considered conditions because of the low contrast between CO₂ and natural gas. The Σ contrast, taking into account only the gas displacement, is in the range of typical PNG tool accuracy and therefore not detectable. This is especially true for observation wells, since the arriving CO₂ is already water saturated. Only the mobile natural gas can be displaced, but the immobile brine is unaffected.

Changes of the gas composition need to be quantified chemically, e.g. by analyzing samples of produced fluids in a laboratory or applying existing tools for downhole fluid analysis to quantify the CO₂ content in the reservoir fluids (Müller et al., 2006).

Considering the evaporation processes associated with salt precipitation, which is expected to

6. Sensitivity study for the Altmark site

occur close to injection wells, the expected effect in the Σ reading is an order of magnitude larger than the effect of gas displacement alone. Potentially, evaporation effects could be monitored with PNG logs depending on the volume of immobile brine. In general, it is important to take the brine evaporation capability of dry CO_2 for injection wells into account. Conventional PNG saturation models based on displacement processes only would result in an erroneous underestimation of the CO_2 saturation. Furthermore, changes in the GWC associated with a high Σ contrast between displaced brine and injected CO_2 can be detected very well.

7. Summary and Conclusion

Pulsed neutron-gamma (PNG) measurements have already been applied successfully for monitoring CO₂ injection in saline aquifers (e.g. Murray et al., 2010; Müller et al., 2007; Sakurai et al., 2005; Vu-Hoang et al., 2009; Xue et al., 2006). For this purpose, the conventional PNG saturation model, based on a displacement process has been used for PNG interpretation in different CO₂ storage projects in saline aquifers. The conventional displacement saturation model accounts for mixing of the fluids in the pore space and ignores any mutual physico-chemical interaction. But the mutual solubility between brine and CO₂ results in evaporation and salt precipitation. Moreover capillary effects can increase the initial salt load. Thus, the conventional displacement saturation model accounts for the displacement of the mobile brine (ϕ_{eff}), but not for the evaporation of the immobile water (ϕ_{irr}) associated with salt precipitation or capillary effects. Therefore, to describe both saturation changing processes, an extended PNG saturation model including both, displacement and evaporation/precipitation, is needed.

The mutual solubility between brine and CO₂, thus the CO₂ and H₂O components in the aqueous and gaseous phases, can be neglected within the typical precision of PNG tools (0.22 cu; Plasek et al. (1995)). Therefore, both the gaseous and the aqueous phase can be simplified by assuming pure CO₂ or pure brine. In contrast, the salt saturated aqueous phase and the associated precipitated solid phase can be detected with PNG measurements. Based on these findings, a PNG saturation model that accounts for the evaporation/precipitation process for NaCl-brines is developed.

Pressure and temperature correspond to the initial reservoir conditions and are assumed to be constant throughout, since the effects of changing temperature and pressure due to CO₂ injection are negligible for the brine and CO₂ Σ values as well as for the amount of precipitated salt itself (Pruess, 2009). From the PNG methodological point of view, it is irrelevant whether the salts are dissolved in brine or precipitated as halite, because the original NaCl content remain unchanged in ϕ_{irr} , where the water of the immobile brine is evaporated. Thus, precipitated or dissolved NaCl give the same Σ reading.

Transferring the concentration based brine Σ values, Σ_{NaCl_c} and $\Sigma_{H_2O_c}$, into apparent volume fractions or rather saturations, S_{NaCl_b} and $S_{H_2O_b}$, in combination with the halite and water Σ values allows inclusion of evaporation/precipitation process in volume fraction based PNG saturation models. The water evaporation results in a "free" volume fraction which is occupied by CO₂. Based on static thermodynamic conditions and a criterion for the NaCl solubility limit to factor in precipitation, the dissolved ($S_{NaCl_{sol}}$) and precipitated NaCl saturations ($S_{NaCl_{pre}}$) are quantified. During evaporation, the transfer from dissolved to precipitated NaCl is controlled by the remaining water saturation ($S_{H_2O_r}$) that decreases with increasing CO₂ saturation ($S_{CO_2_{irr}}$) in ϕ_{irr} . Finally, when all water is evaporated the initial apparent NaCl saturation (S_{NaCl_b}) is equal to the precipitated halite saturation. Therefore, neglecting evaporation/precipitation processes results in an erroneous underestimation of the CO₂ saturation, since the dissolved NaCl is still remaining as halite in the pore space with a corresponding higher Σ reading compared to a displacement process.

7. Summary and Conclusion

The introduced auxiliary water density function in brine, $\rho_{H_2O_{br}}$, which is an input parameter for the water Σ value, accounts for the non-linear brine density change with changing salinity due to the effect of volume change upon mixing. Using the auxiliary water density function in brine, the saturations can be determined iteratively. The Σ error between using the auxiliary water density function in brine and using the constant baseline water density for different initial brine salinities for the Ketzin site reservoir conditions (35 °C and 75 bar) is smaller than a typical PNG tool's precision. Therefore, the effect of volume change upon mixing can be neglected for the Ketzin site reservoir conditions. Using the initial baseline water density, simplifies the evaporation/precipitation saturation model, and the saturations can be determined directly.

This simplified evaporation/precipitation saturation model is used for the extended PNG saturation model that includes both the displacement and evaporation/precipitation processes weighted by their affected porosity proportions. The displacement part of the extended saturation model gives rise to the Buckley and Leverett (1942) saturation profile, where the brine saturation cannot be reduced below the immobile brine saturation. For the immobile brine saturation the simplified evaporation/precipitation saturation model is applied.

The extended PNG saturation model distinguishes between two scenarios. If the repeat Σ value is smaller than the baseline Σ value, first the displacement saturation model (ϕ_{eff}) and subsequently the simplified evaporation/precipitation saturation model (ϕ_{irr}) is applied. The total CO₂ saturation $S_{CO_{2tot}}$ results from the volume weighted sum of the individual CO₂ saturations $S_{CO_{2eff}}$ and $S_{CO_{2irr}}$ derived from the displacement and the simplified evaporation/precipitation saturation model.

If the repeat Σ value is greater than the baseline Σ value, the pore fluid Σ value is increased. The increased pore fluid Σ value can result from capillary effects that increase the initial salt load. For this purpose, two calculation procedures can be applied. Based on the precondition for evaporation, that the mobile brine is completely displaced ($S_{CO_{2eff}}$ is one), and an assumed back flow rate of brine being equal to the evaporation rate ($S_{CO_{2irr}}$ is zero), an overall summarizing Σ value (Σ_x) describes the increased pore fluid Σ value. Transferring Σ_x to thermodynamically reasonable conditions, results in brine and/or halite saturation. Additionally, $S_{CO_{2tot}}$ can be alternatively derived from the neutron porosity (TPHI). Similar to the former calculation procedure, Σ_x describes the increased pore fluid Σ value. For both scenarios, the affected pore space fractions can be adjusted, to minimize the difference between the modeled and measured repeat Σ data. Since the evaporation/precipitation process can be compared with the three phase system in EOR operations (Amadi and Hughes, 2008), additional information about the remaining water saturation, i.e. derived from a set of logging measurements, is required to distinguish between brine, CO₂ and halite.

The Ketzin pilot site for CO₂ storage in the saline aquifer of the Stuttgart formation, has one injection (Ktzi201) and two observation wells (Ktzi200 and Ktzi202), where an extensive PNG monitoring program is performed with the Reservoir Saturation Tool (RST) that is a registered trademark of Schlumberger. Depending on the brine level, the nature of the annulus and the lithology, different data processings are required to transfer the apparent data into the intrinsic data. After analyzing different data processings in combination with an extensive log quality control, the air data processing is found to be the appropriate data processing for all TPHI and the air_OH data processing for all Σ repeat runs in all wells of the reservoir section. These data processings, derived from the RST processing algorithm, include the borehole status air above, noair below the brine level and the open hole porosity as external knowledge for the Σ repeat runs.

7. Summary and Conclusion

The neutron porosity logs (TPHI), also derived from the RST, are suitable for deriving information about the remaining water saturation. Since no second PNG baseline run performed immediately after the KCl-preflush is available, a baseline log based on available temperature data, derived from the permanent temperature monitoring via the distributed temperature sensing method, is developed in order to factor in the KCl-preflush for the injection well (Ktzi201). Therefore, two data sets, the original Ketzin formation brine and the flush brine data sets, are used for saturation profiling in the injection well.

Based on the environmental corrected intrinsic data and the displacement part of the extended saturation model, the saturation profiles are calculated for the repeat runs in each well. The derived saturation profiles for the observation well Ktzi202 give rise to the Buckley and Leverett (1942) saturation profile, indicating that the conventional displacement saturation model is valid.

In contrast, for the injection well Ktzi201 and the observation well Ktzi200, which is closest to the injection well, the derived CO₂ saturations show that, in addition to displacement, the evaporation/precipitation process is occurring in some depth intervals above the brine level. For this purpose the simplified evaporation/precipitation saturation model is applied. In Ktzi200, all three situations occur, the brine salinity is increased, the brine salinity reaches its maximum and precipitation occurs, or the evaporation/precipitation process has been completed. The maximum derived halite saturation is 0.032. Since the Ktzi200 is 50 m far away from the injection well, the partially derived halite saturations seem unrealistic compared to modeling results for the Ketzin site (Hurter et al., 2007; Muller et al., 2009; Zeidouni et al., 2009a). But the Ktzi200 was characterized by a less comprehensive open hole well logging program (Norden et al., 2010) than was performed in the injection well, which is why greater uncertainties can be expected for the derived saturation profiles.

For the injection well the evaporation/precipitation process has been completed in these depth intervals. In these dry-out regions the maximum derived halite saturation is 0.043 for the original brine salinity and 0.024 for the flush brine salinity data set. The halite saturations are greatest at the upper edge and decrease in the center of the dry-out regions for both brine salinity data sets. Moreover, for some repeat runs, halite saturations are also increased at the lower edge of the dry-out regions for both brine salinity data sets.

Additionally, in the injection well (Ktzi201), the second scenario of the extended saturation model occurs partially for the original as well as for the flush brine salinity data sets, indicating an increased pore fluid Σ value as a result of capillary effects. For the original brine salinity data set, the second scenario occurs only below the brine level for two repeat runs. In contrast, for the flush brine salinity data set, the second scenario occurs partially above and below the brine level for all repeat runs. As a result, in more areas of the reservoir section, precipitated halite occurs for the flush than for the original brine salinity data set. The greatest halite saturations for both brine salinity data sets occur in the vicinity below the brine level, where large capillary forces occur. The more reliable CO₂ saturations derived from the TPHI measurements are smaller than the volume weighted sum of the individual CO₂ saturations $S_{CO_{2eff}}$ and $S_{CO_{2irr}}$ based on the model assumption. This is associated with greater brine and smaller halite saturations. The maximum halite saturation using the CO₂ saturations derived from TPHI is 0.135 for the original brine salinity and 0.141 for the flush brine salinity data set below the brine level, validating an increased salt load due to capillary effects.

Moreover, derived halite saturations decrease or are absent when the brine level rises, indicating that the halite goes back into solution. The halite saturation distribution seems to be

7. Summary and Conclusion

controlled by the combined effects of changing injection rates associated with changing brine levels, lithology heterogeneities, and different saturation changing processes such as evaporation/precipitation or capillary forces. In general, the derived saturation profiles are in good agreement with the modeling results for the Ketzin site. Due to the uncertainties from the unavailable second baseline PNG run performed after the KCl-preflush, the saturation profiles derived from the original or flush brine salinity data sets cannot be more specified.

Salt precipitations were previously not detected in situ in connection with CO₂ injection in saline aquifers. At the Ketzin site, salt precipitations, resulting from the evaporation/precipitation process and the combination of capillary effects and the evaporation/precipitation process, are detected in situ. In general, it can be said that PNG monitoring in combination with the extended saturation model is suited to determine displacement and evaporation/precipitation processes for CO₂ storage operations. The extended saturation model is needed, especially for injection wells; otherwise the CO₂ saturation will be erroneously underestimated. In order to improve precision, PNG tools calibration should be improved for gas-filled borehole environments.

The PNG monitoring potential at the Altmark site for estimation of natural gas displacement by CO₂ is in the range of typical PNG tool's precision and therefore not detectable. In contrast, the expected effect in the Σ reading for the evaporation/precipitation process is an order of magnitude larger than the effect of gas displacement. Potentially, evaporation/precipitation effects could be monitored with PNG logs depending on the volume of immobile brine. Furthermore, changes in the gas-water contact (GWC) associated with a high Σ contrast between displaced brine and injected CO₂ can be detected very well. Thus, PNG logs can be applied for determination of changes in brine saturation and water content associated with salt precipitation, whereas changes in the gas composition are below the detection limit.

A. Appendix

Casing schemes fo the Ketzin wells Ktzi200, Ktzi201 and Ktzi202

A. Appendix

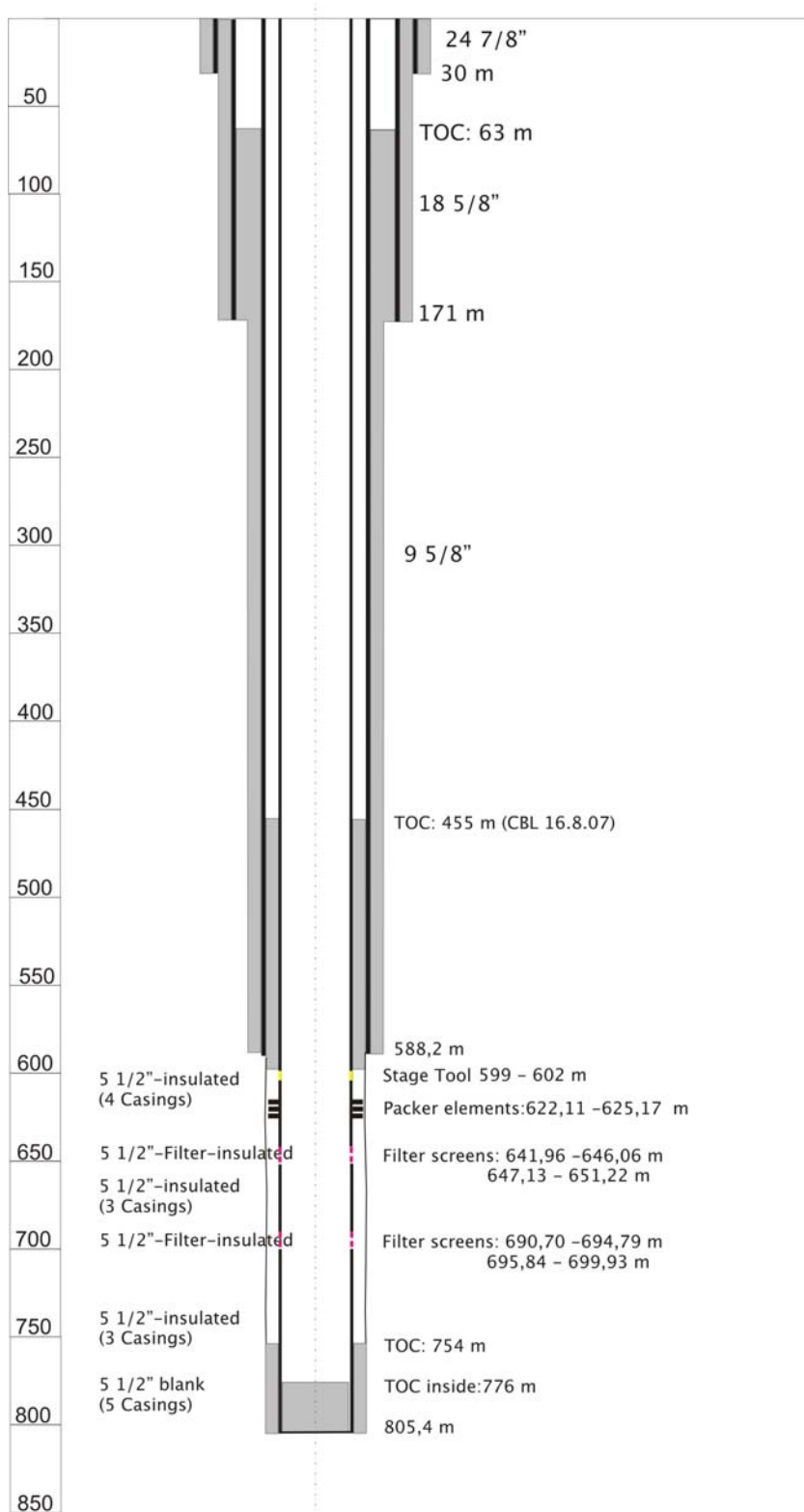


Figure A.1.: Ktzi200: Casing scheme after Prevedel (2008)

A. Appendix

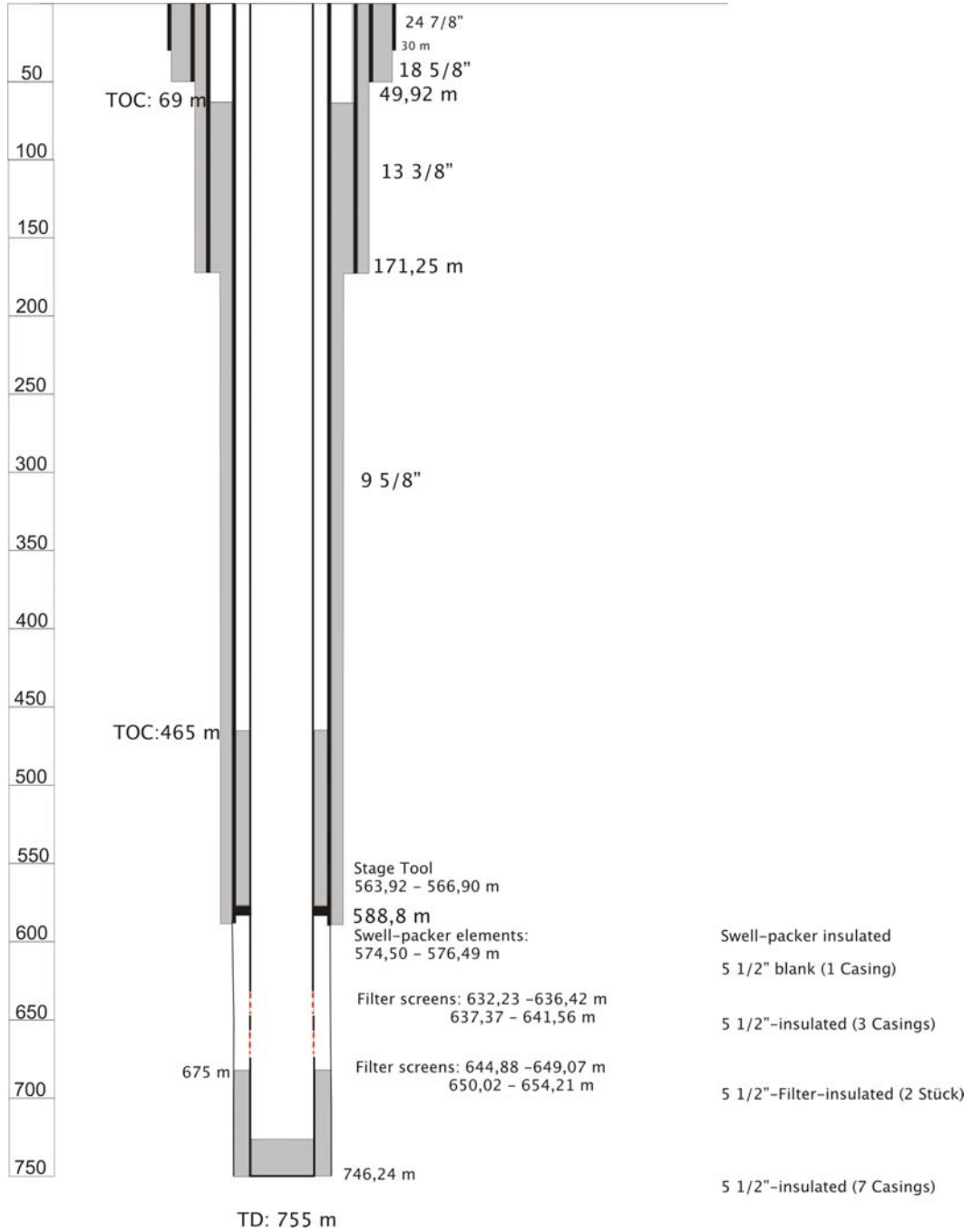


Figure A.2.: Ktzi201: Casing scheme after Prevedel (2008)

A. Appendix

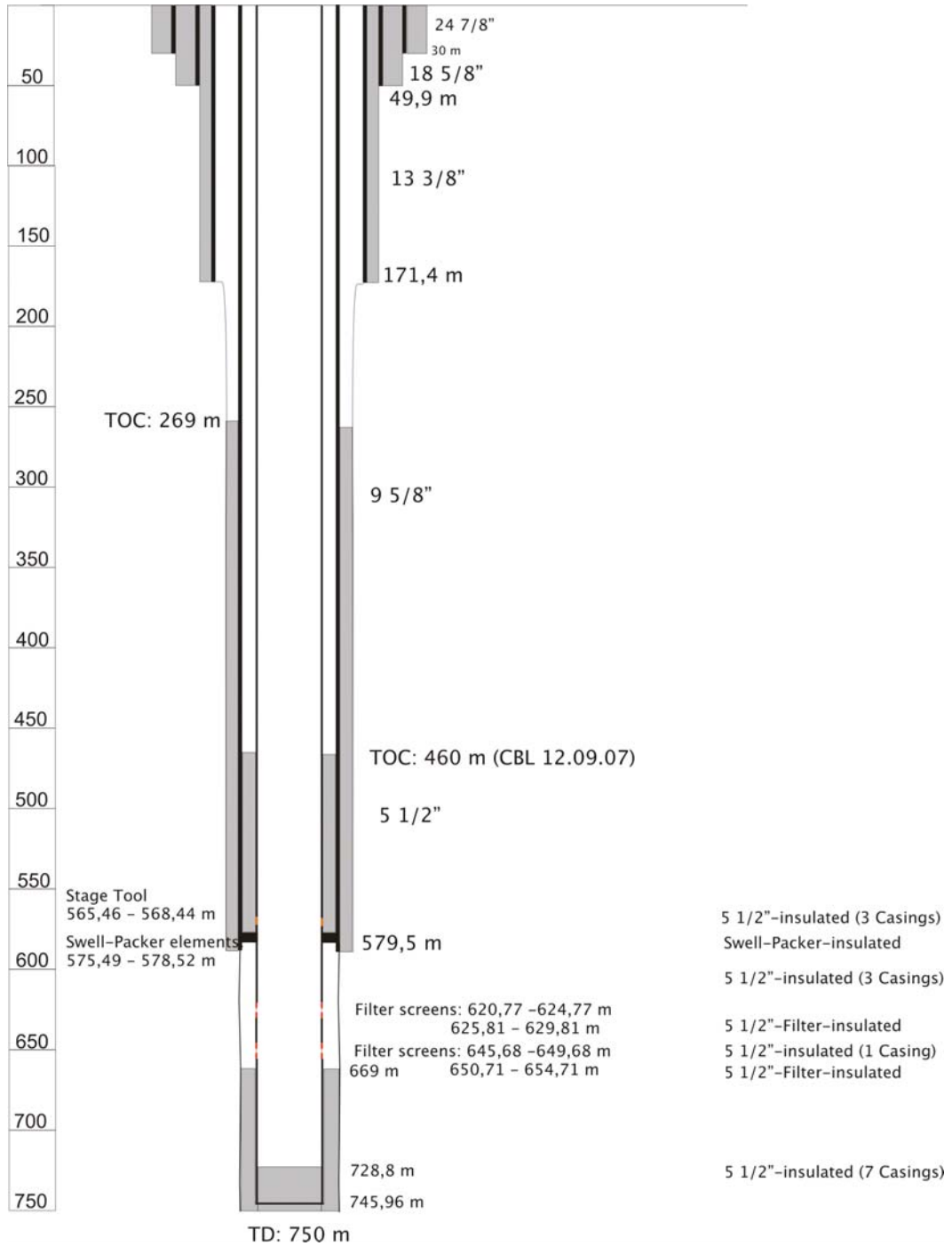


Figure A.3.: Ktzi202: Casing scheme after Prevedel (2008)

DSIG logs with different data processings and the arithmetic mean of the absolute DSIG values in the evaluated depth intervals for all runs of the Ketzin wells

- Evaluated depth intervals in Ktzi200: Cap, SS1, SS2
- Evaluated depth intervals in Ktzi201: Cap, SS1, SS2, Silt, SS3
- Evaluated depth intervals in Ktzi202: Cap, SS1, Mud (Table 5.4)
- Baseline runs data processings: noair, noair_OH, noair_BSAL and noair_OH_BSAL (Table 5.5)
- Repeat runs data processings: air, air_OH, air_8.5 and air_OH_8.5 (Table 5.6)

A. Appendix

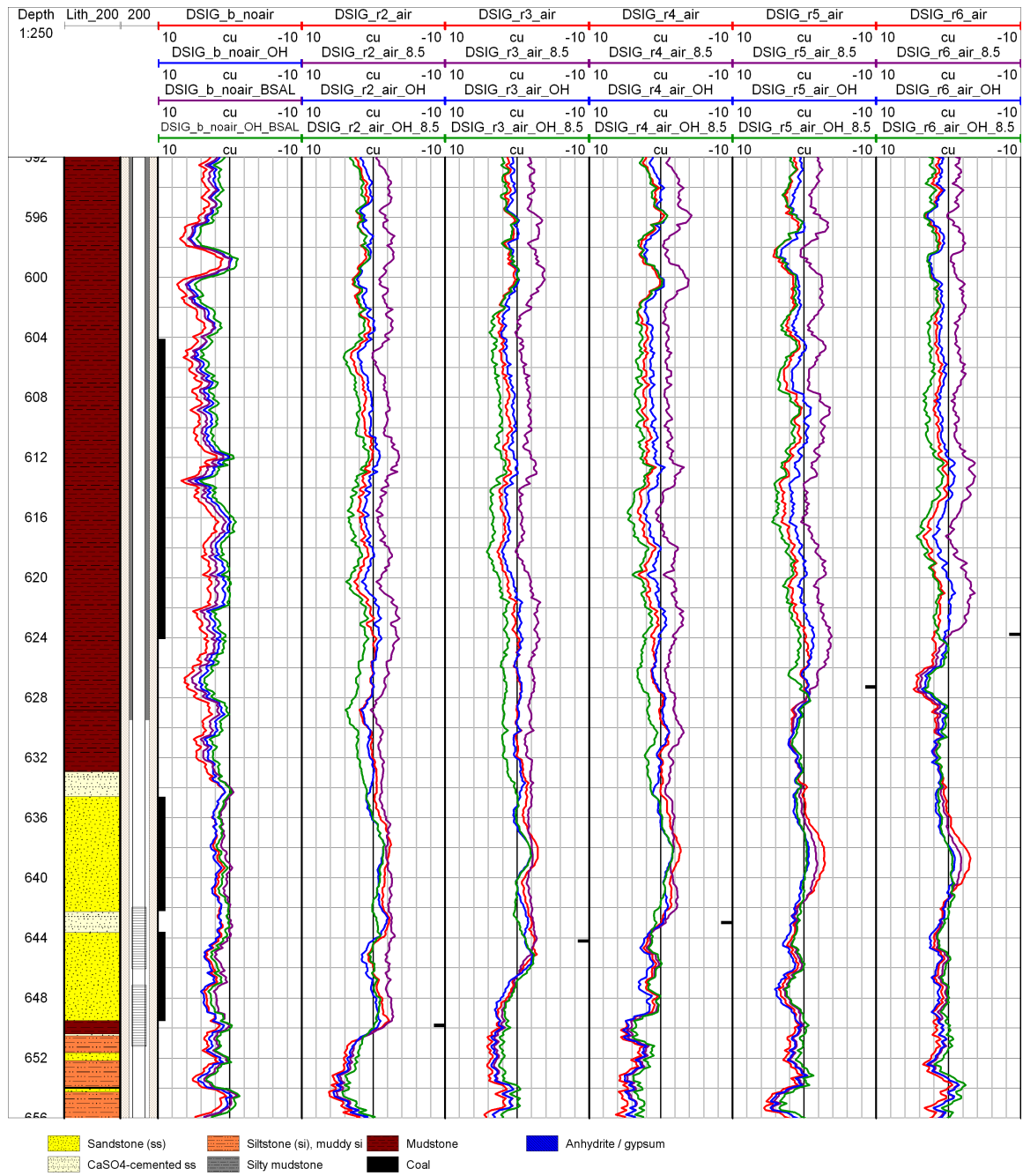
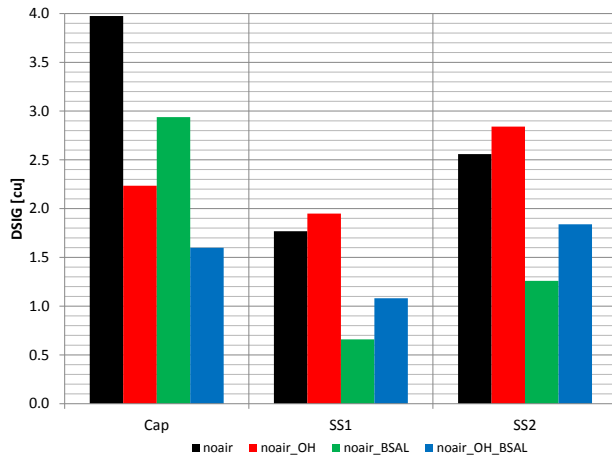
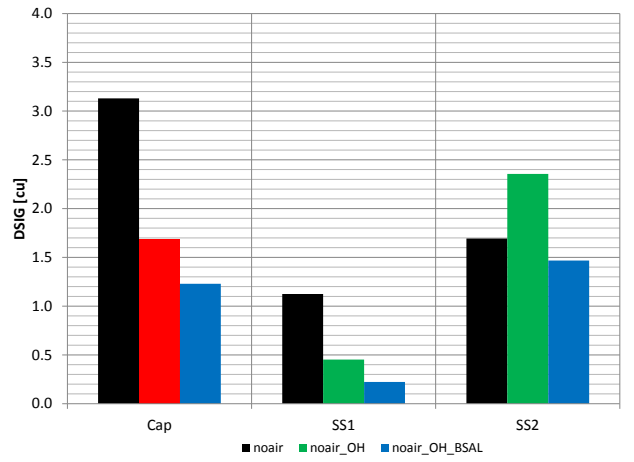


Figure A.4.: Ktzi200: DSIG logs with different data processings for the baseline and the five repeat runs. The brine levels for each run are marked with a black bar on the right side of each track. Lithology after Förster et al. (2010)

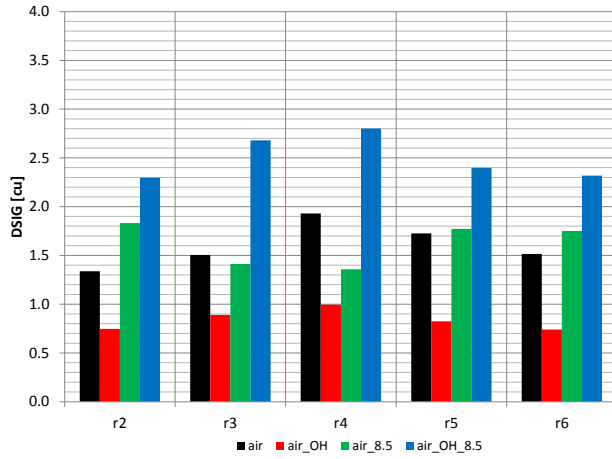
A. Appendix



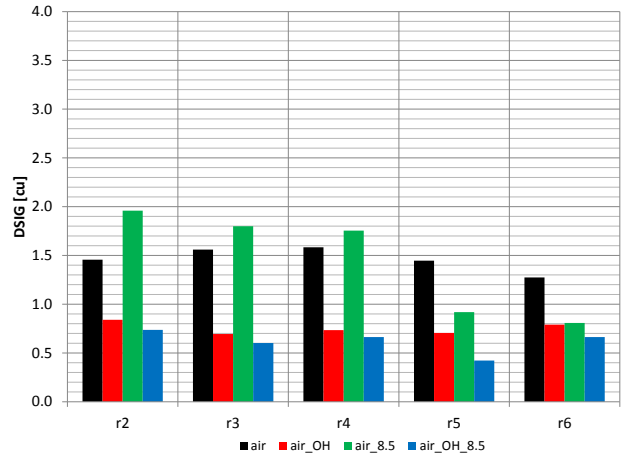
(a) Baseline with different processings in all evaluated depth intervals



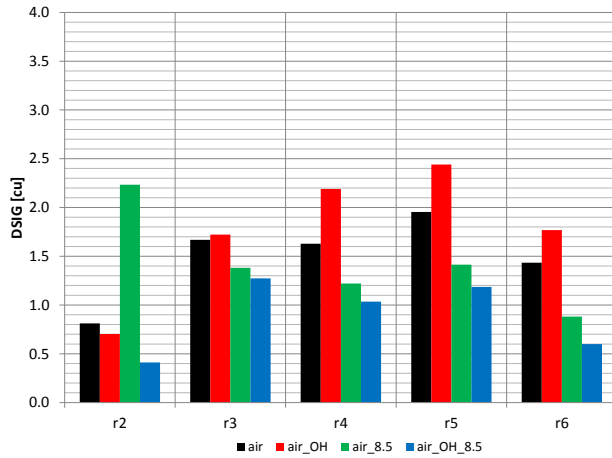
(b) Repeat 1 with different processings in all evaluated depth intervals



(c) Repeats 2-6 with different processings in the Cap interval



(d) Repeats 2-6 with different processings in the SS1 interval



(e) Repeats 2-6 with different processings in the SS2 interval

Figure A.5.: Ktzi200: Arithmetic mean of the absolute DSIG values with different data processings for the baseline and the six repeat runs in the evaluated depth intervals.

A. Appendix

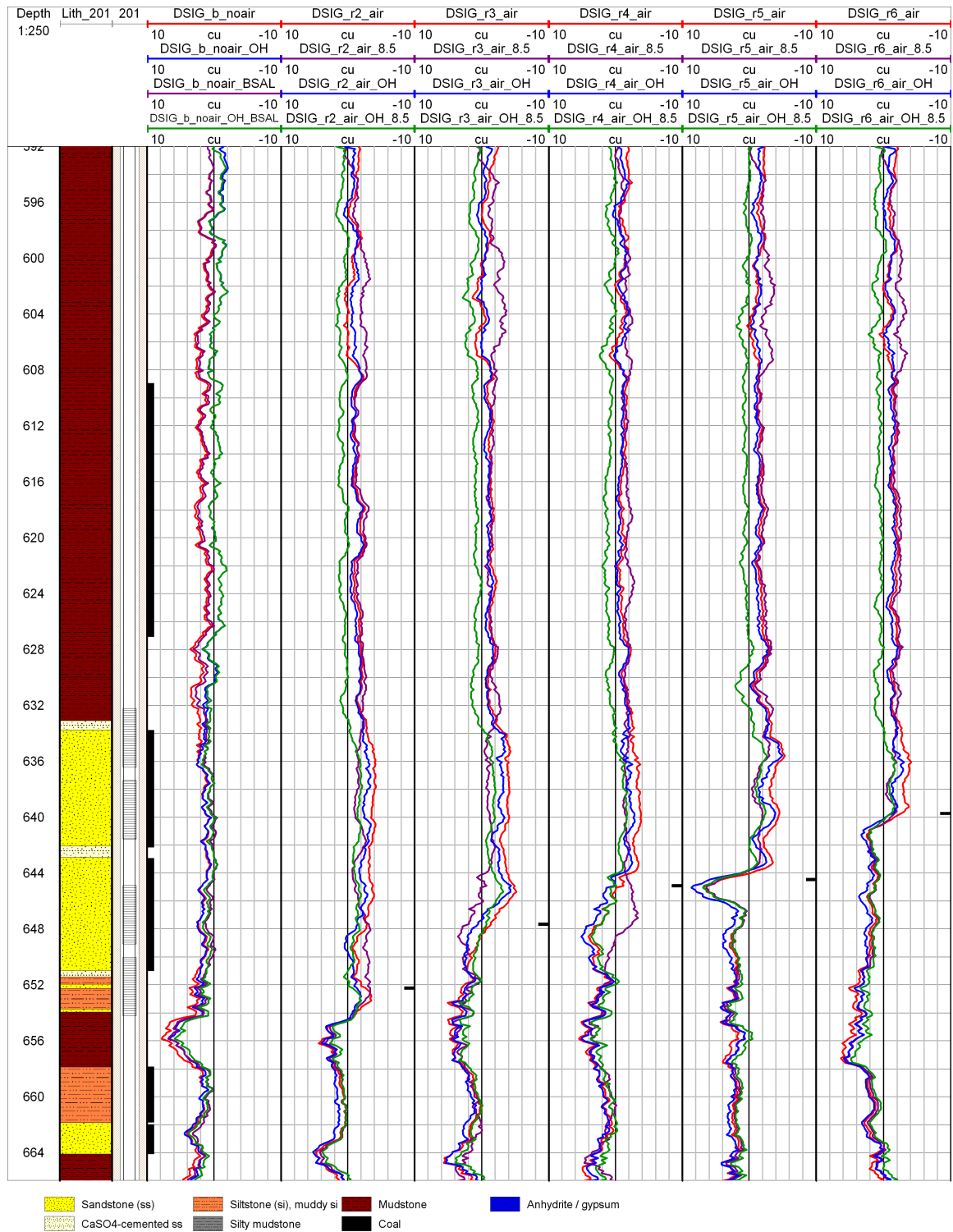
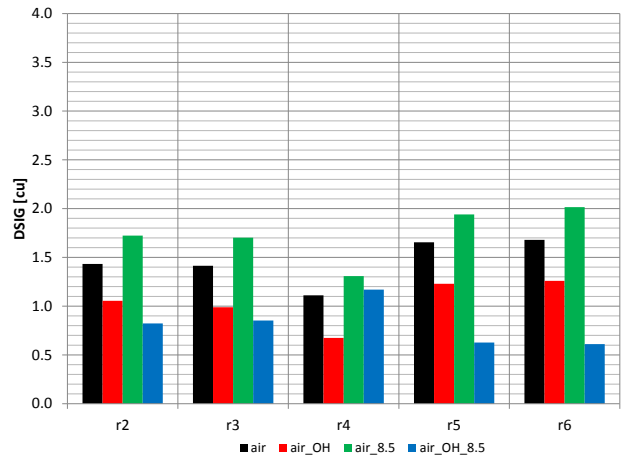
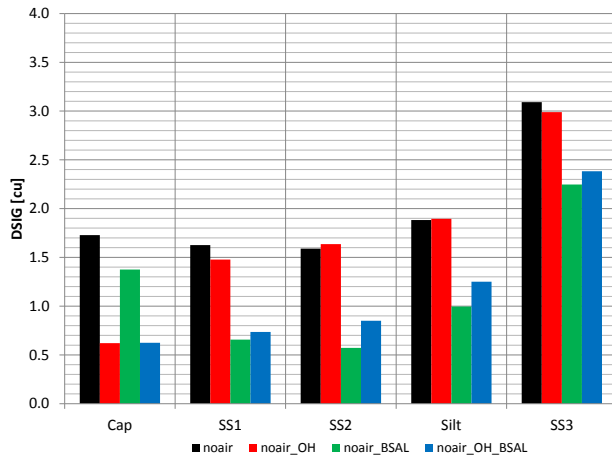
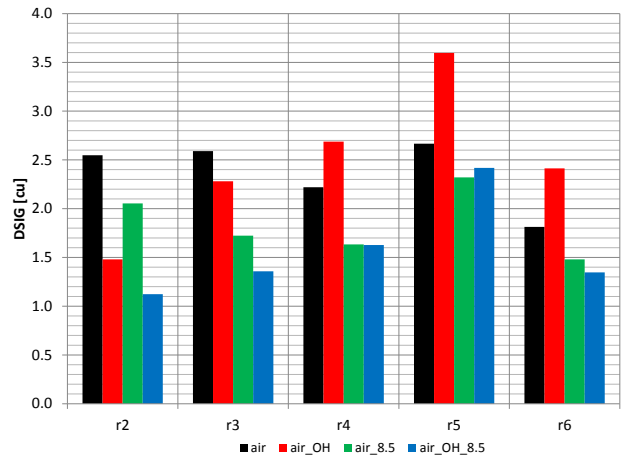
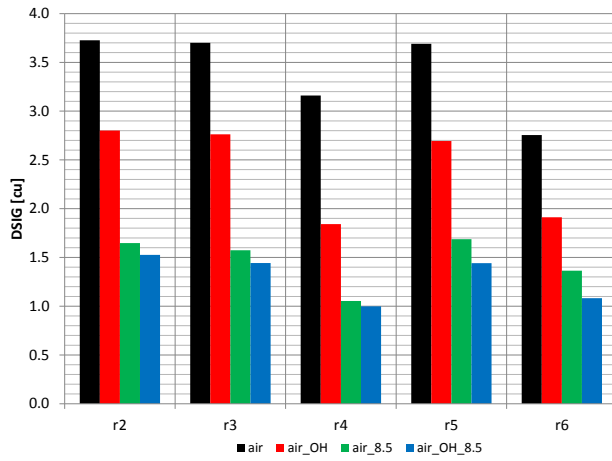


Figure A.6.: Ktzi201: DSIG logs with different data processings for the baseline and the five repeat runs. The brine levels for each run are marked with a black bar on the right side of each track. Lithology after Förster et al. (2010)

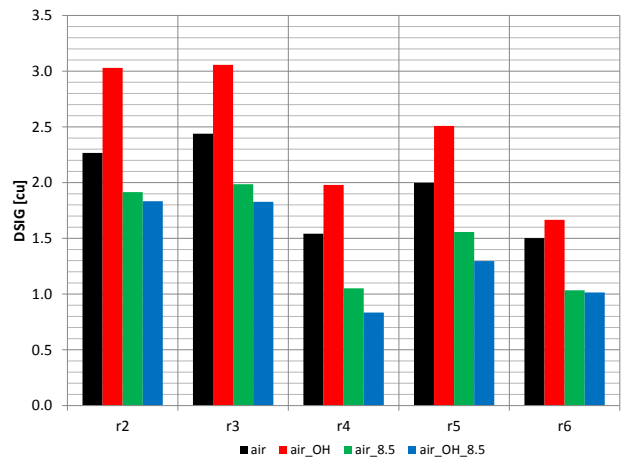
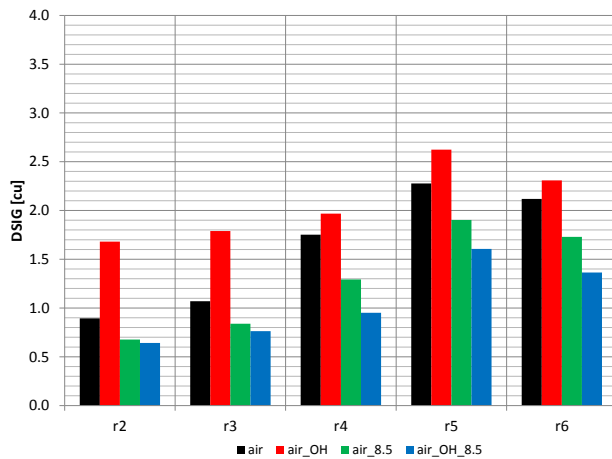
A. Appendix



(a) Baseline with different processings in all evaluated depth intervals (b) Repeats 2-6 with different processings in the Cap interval



(c) Repeats 2-6 with different processings in the SS1 interval (d) Repeats 2-6 with different processings in the SS2 interval



(e) Repeats 2-6 with different processings in the Silt interval (f) Repeats 2-6 with different processings in the SS3 interval

Figure A.7.: Ktzi201: Arithmetic mean of the absolute DSIG values with different data processings for the baseline and the five repeat runs in the evaluated depth intervals.

A. Appendix

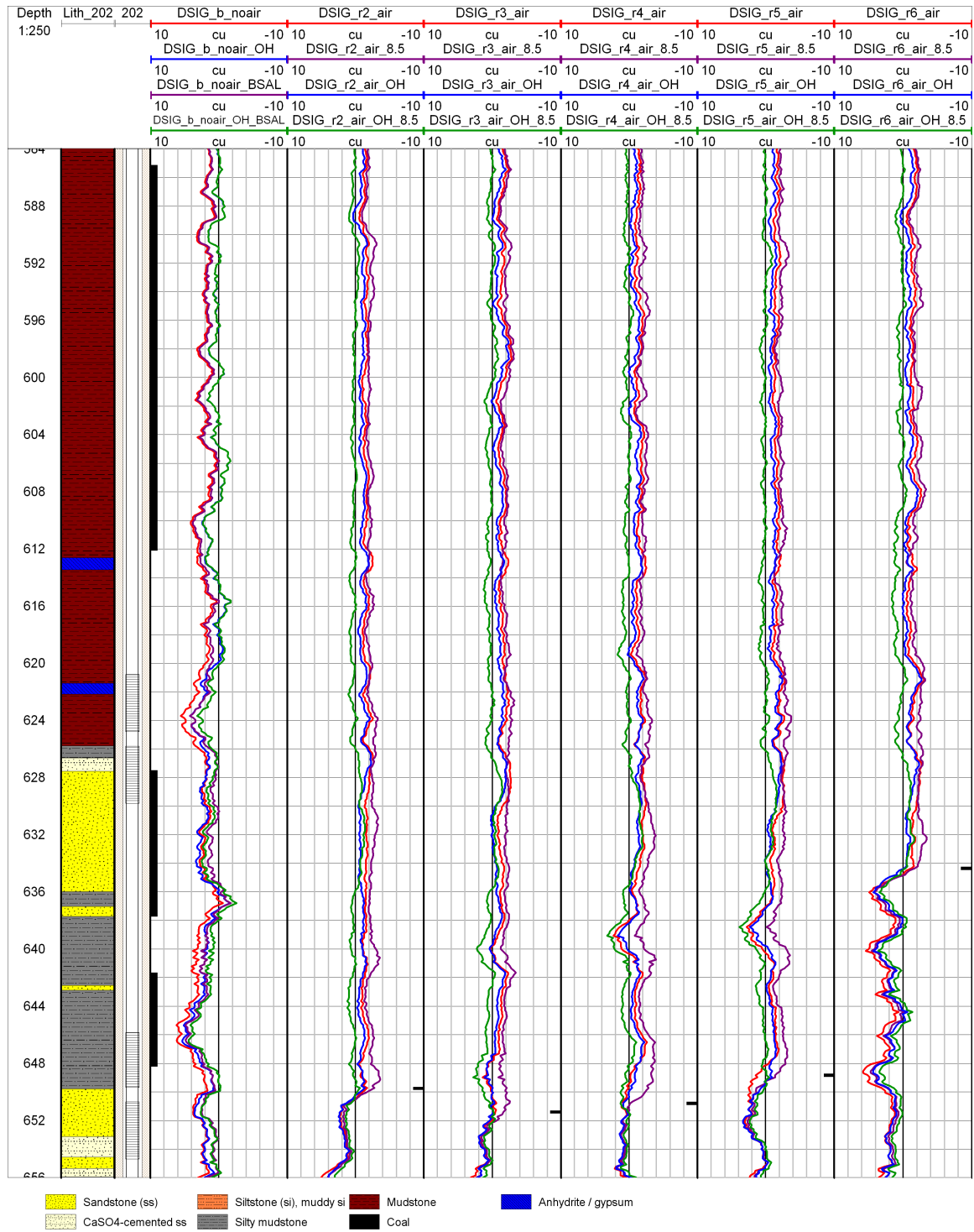
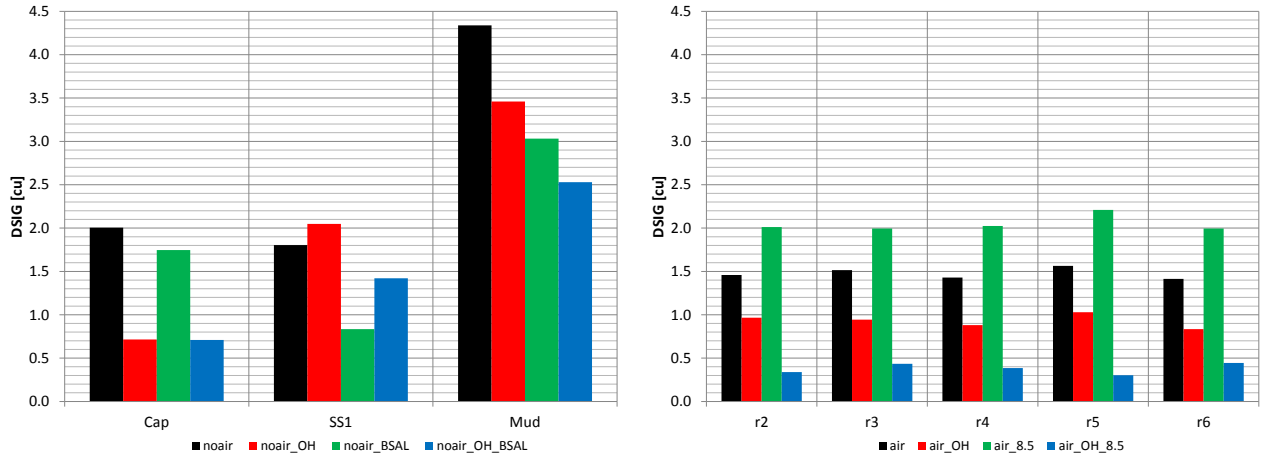
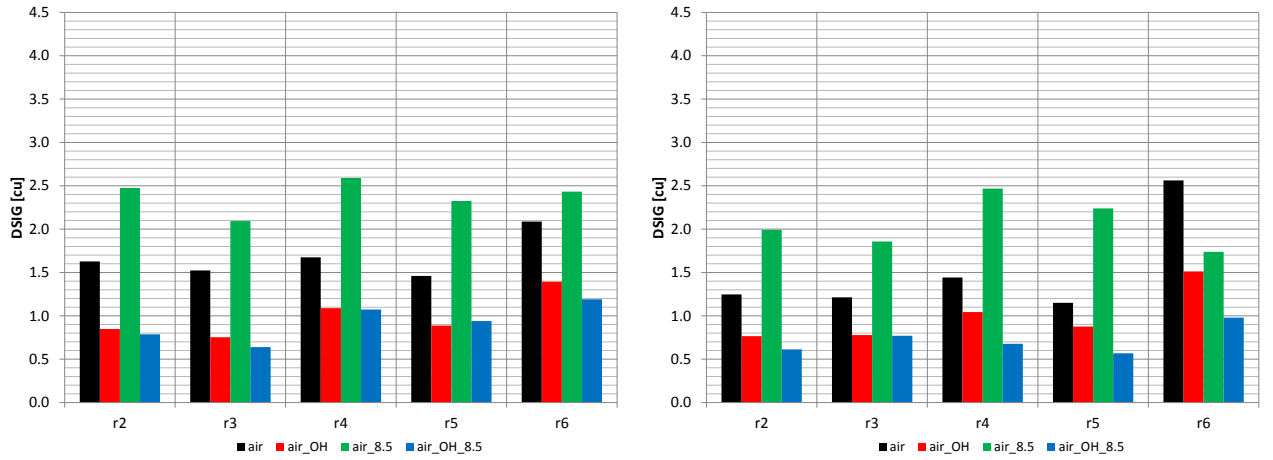


Figure A.8.: Ktzi202: DSIG logs with different data processings for the baseline and the five repeat runs. The brine levels for each run are marked with a black bar on the right side of each track. Lithology after Förster et al. (2010)



(a) Baseline with different processings in all evaluated depth intervals (b) Repeats 2-6 with different processings in the Cap interval intervals



(c) Repeats 2-6 with different processings in the SS1 interval (d) Repeats 2-6 with different processings in the Mud interval

Figure A.9.: Ktzi202: Arithmetic mean of the absolute DSIG values with different data processings for the baseline and the five repeat runs in the evaluated depth intervals.

Environmental corrected intrinsic baseline and repeat SIGM and TPHI logs with different data processings and the differences between the baseline and the repeat SIGM values (SIGM(b-rx)) in the evaluated depth intervals for the repeat runs of the Ketzin wells

- Evaluated depth intervals in Ktzi200: Cap, SS1, SS2
- Evaluated depth intervals in Ktzi201: Cap, SS1, SS2, Silt, SS3
- Evaluated depth intervals in Ktzi202: Cap, SS1, Mud (Table 5.4)
- Final SIGM and TPHI baseline runs data processing: noair_BSAL (Table 5.5)
- Repeat runs data processings: air, air_OH, air_8.5 and air_OH_8.5 (Table 5.6)

A. Appendix

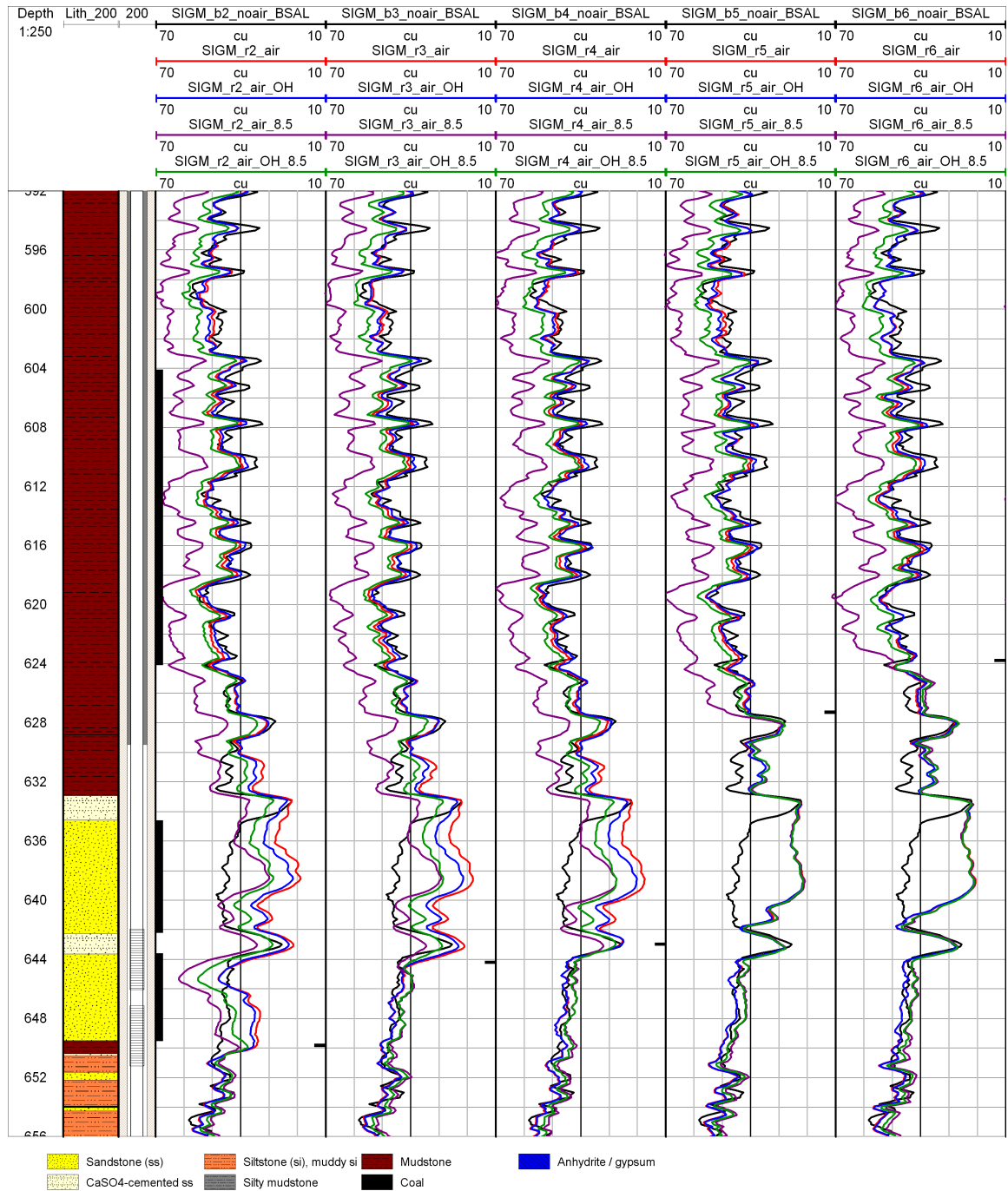


Figure A.10.: Ktzi200: SIGM baseline log (noair_BSAL data processing) and five repeat SIGM logs with different data processings. The brine levels for each run are marked with a black bar on the right side of each track. Lithology after Förster et al. (2010)

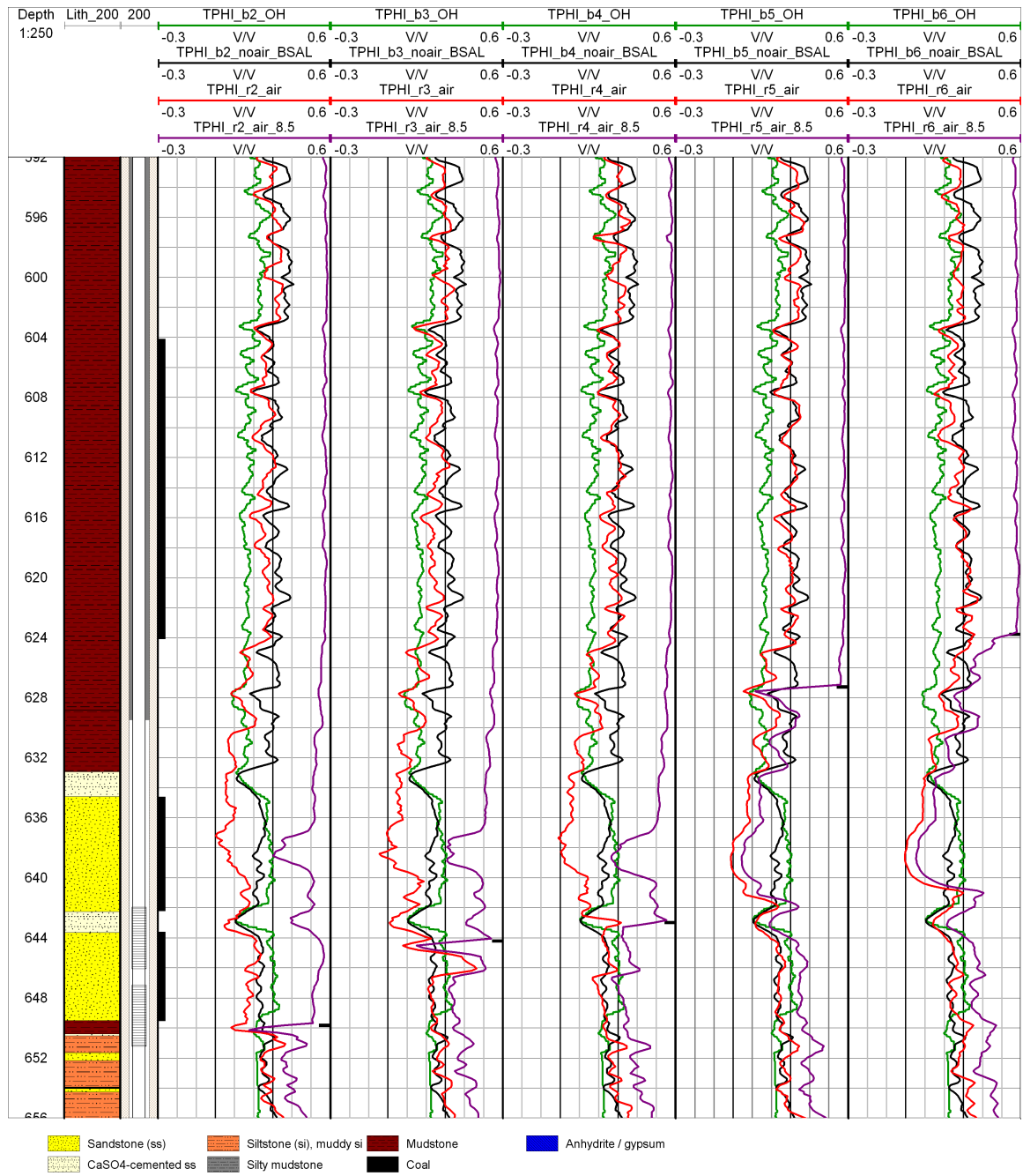


Figure A.11.: Ktzi200: TPHI baseline log (noair_BSAL data processing), open hole derived porosity log after Norden et al. (2010) and five repeat TPHI logs with different data processings. The brine levels for each run are marked with a black bar on the right side of each track. Lithology after Förster et al. (2010)

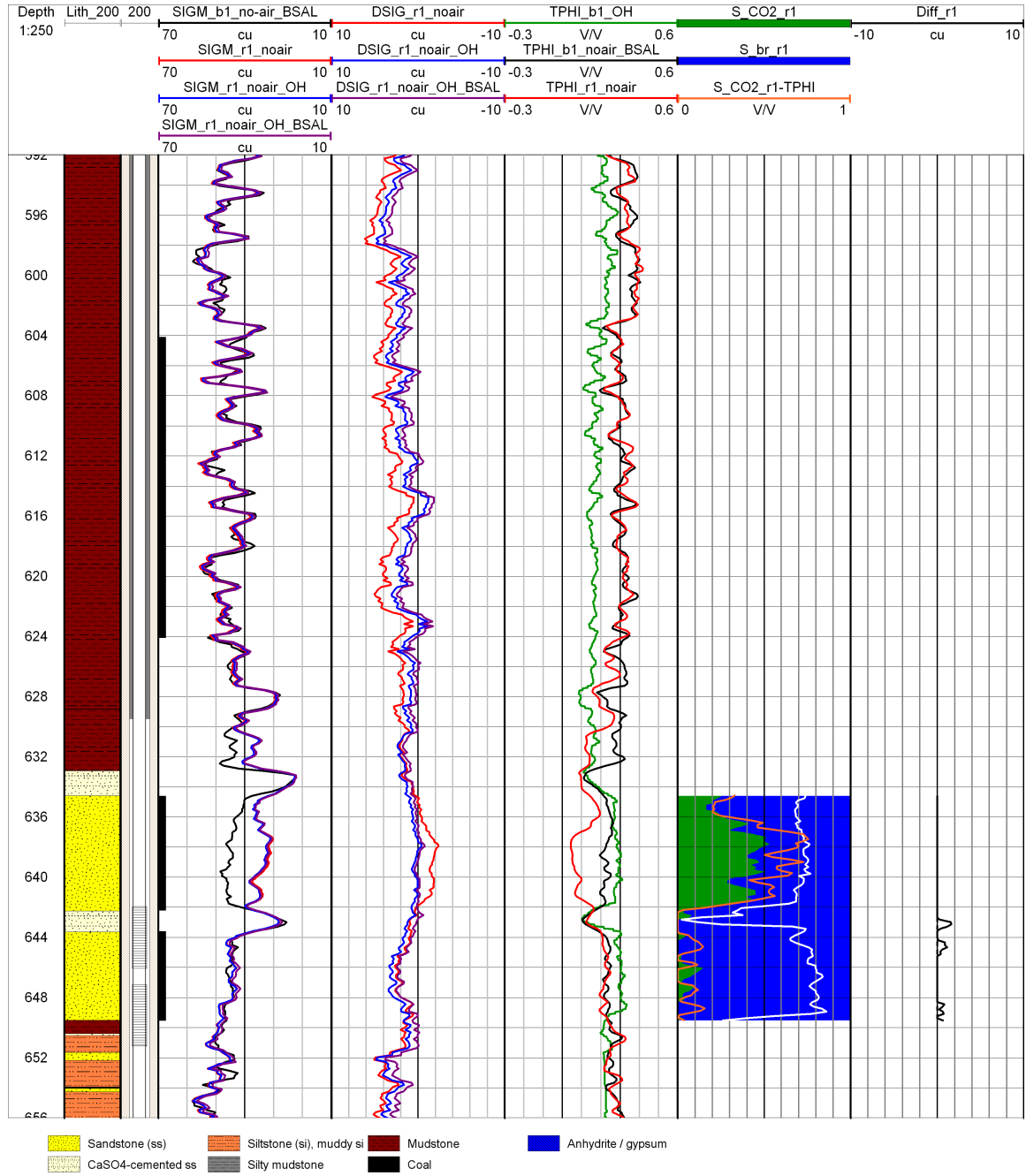
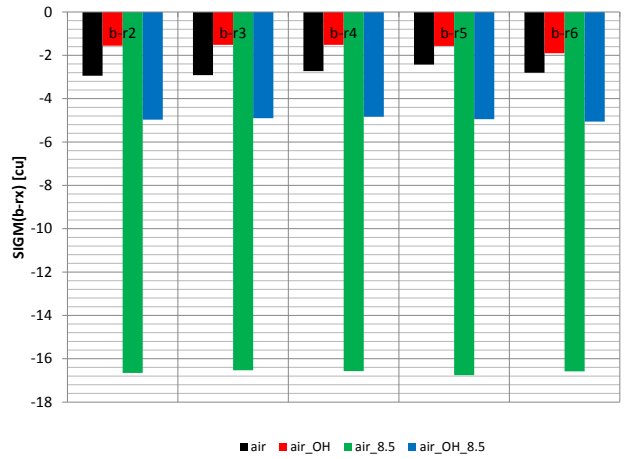
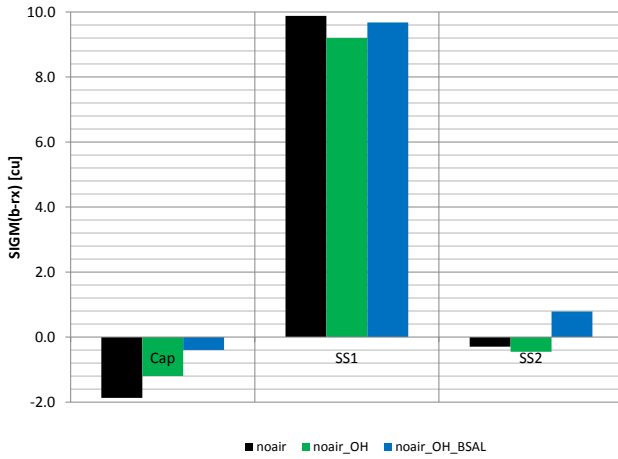
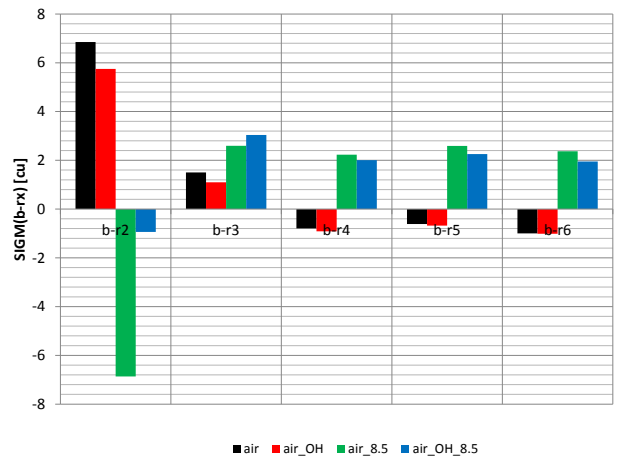
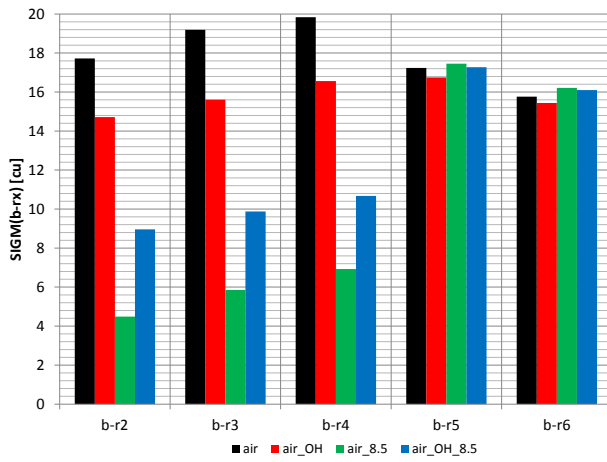


Figure A.12.: Ktzi200: SIGM baseline log (noair_BSAL), SIGM first repeat logs with different data processings (noair, noair_OH and noair_OH_BSAL), corresponding DSIG logs, open hole derived porosity log after Norden et al. (2010), TPHI baseline log (noair_BSAL), TPHI first repeat log with noair data processing, the corresponding saturation profile based on the *displacement saturation model*, S_{CO_2} derived from TPHI (orange logs) and the corresponding Diff log. Lithology after Förster et al. (2010)

A. Appendix



(a) Repeat 1 with different processings in all evaluated depth intervals (b) Repeats 2-6 with different processings in the Cap interval intervals



(c) Repeats 2-6 with different processings in the SS1 interval (d) Repeats 2-6 with different processings in the SS2 interval

Figure A.13.: Ktzi200: Arithmetic mean of the differences between the baseline and the six repeat SIGM runs, $SIGM(b-rx)$, with different data processings in the evaluated depth intervals. Note the different scale in each depth interval.

A. Appendix

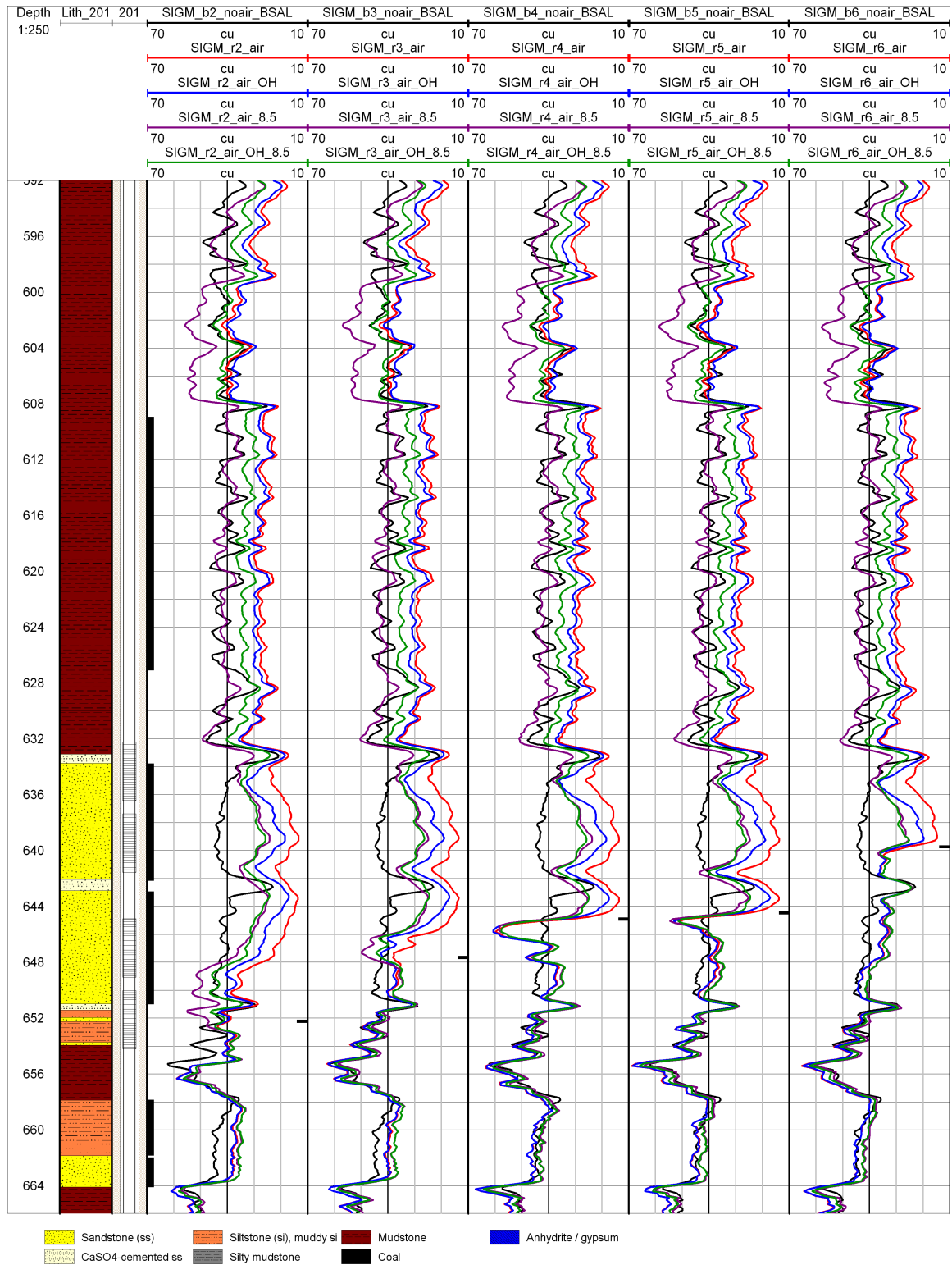


Figure A.14.: Ktzi201: SIGM baseline log (noair_BSAL data processing) and five repeat SIGM logs with different data processings. The brine levels for each run are marked with a black bar on the right side of each track. Lithology after Förster et al. (2010)

A. Appendix

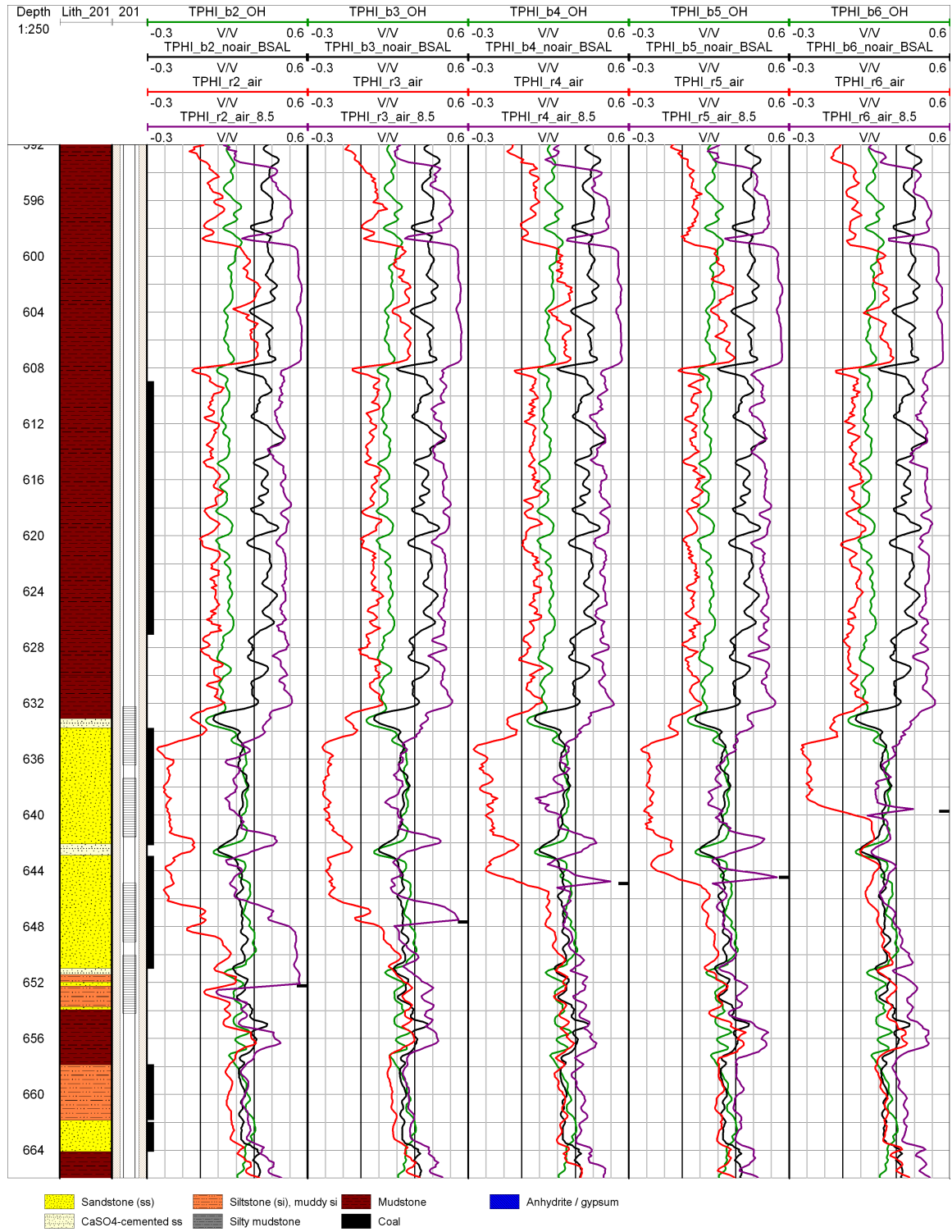
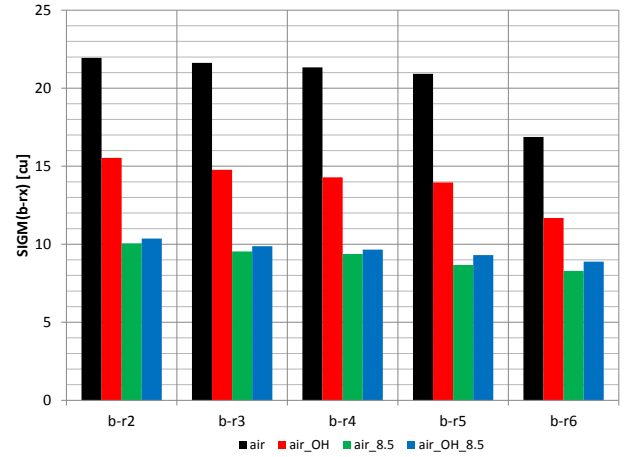
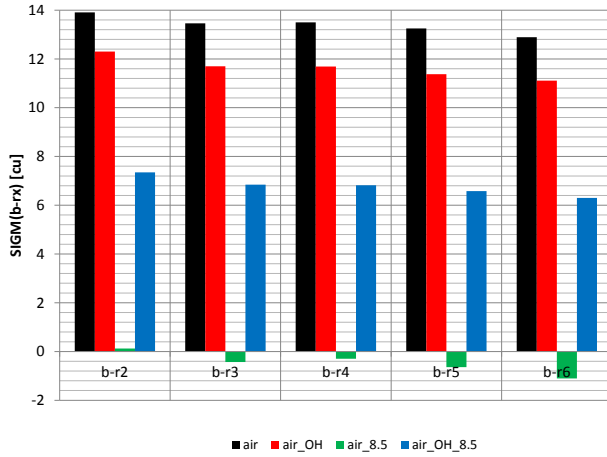
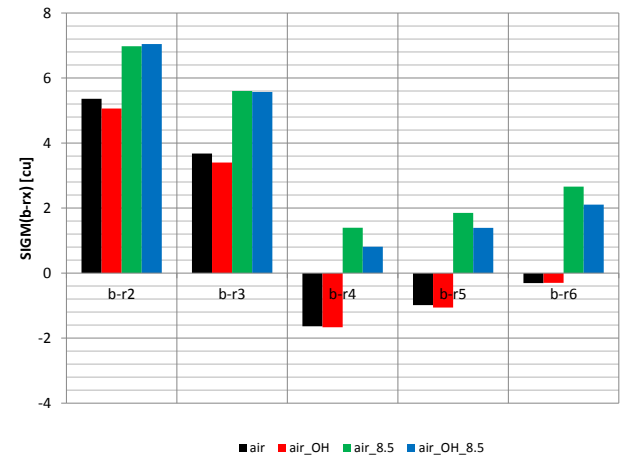
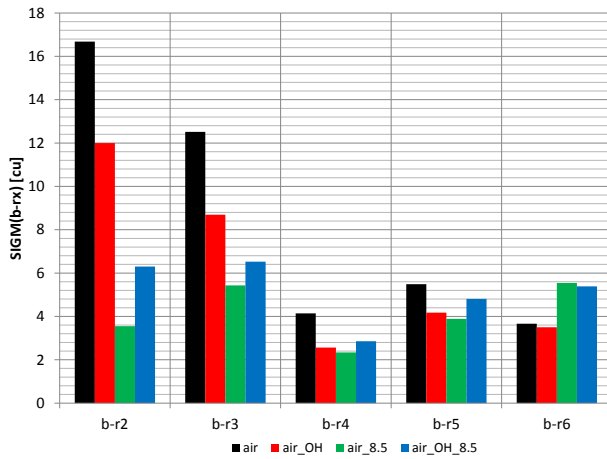


Figure A.15.: Ktzi201: TPHI baseline log (noair_BSAL data processing), open hole derived porosity log after Norden et al. (2010) and five repeat TPHI logs with different data processings. The brine levels for each run are marked with a black bar on the right side of each track. Lithology after Förster et al. (2010)

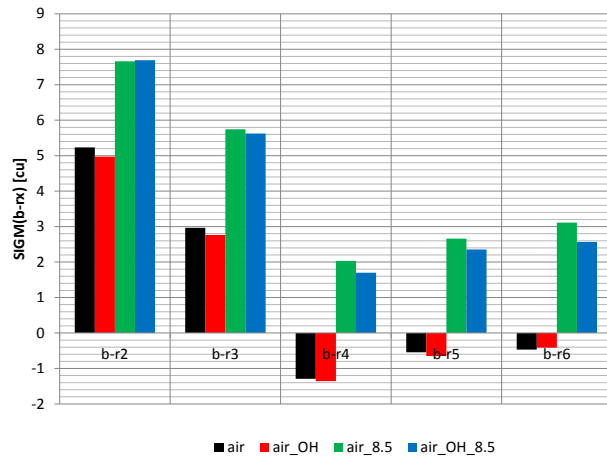
A. Appendix



(a) Repeats 2-6 with different processings in the Cap interval (b) Repeats 2-6 with different processings in the SS1 interval



(c) Repeats 2-6 with different processings in the SS2 interval (d) Repeats 2-6 with different processings in the Silt interval



(e) Repeats 2-6 with different processings in the SS3 interval

Figure A.16.: Ktzi201: Arithmetic mean of the differences between the baseline and the five repeat SIGM runs, $SIGM(b-rx)$, with different data processings in the evaluated depth intervals. Note the different scale in each depth interval.

A. Appendix

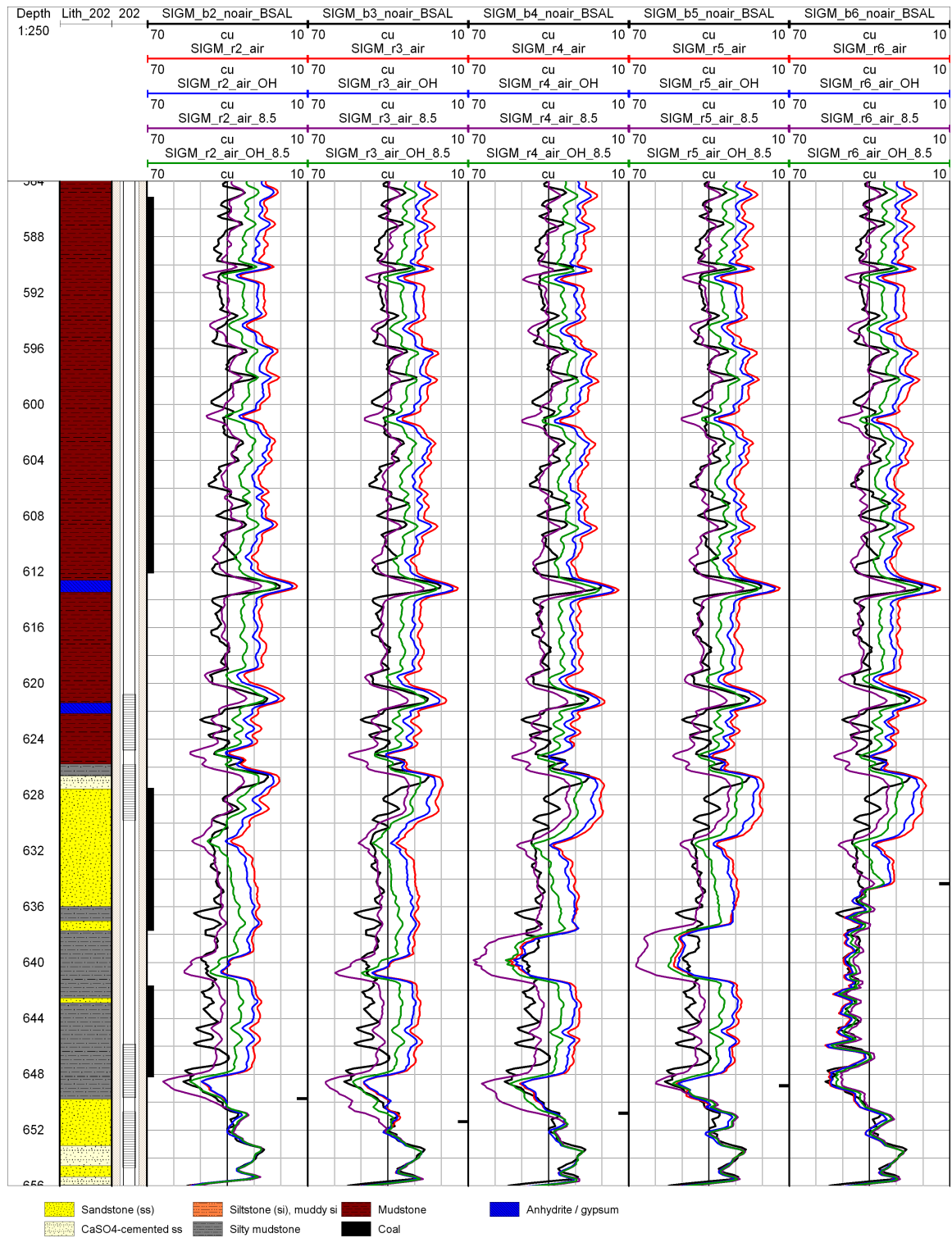


Figure A.17.: Ktzi202: SIGM baseline log (noair_BSAL data processing) and five repeat SIGM logs with different data processings. The brine levels for each run are marked with a black bar on the right side of each track. Lithology after Förster et al. (2010)

A. Appendix

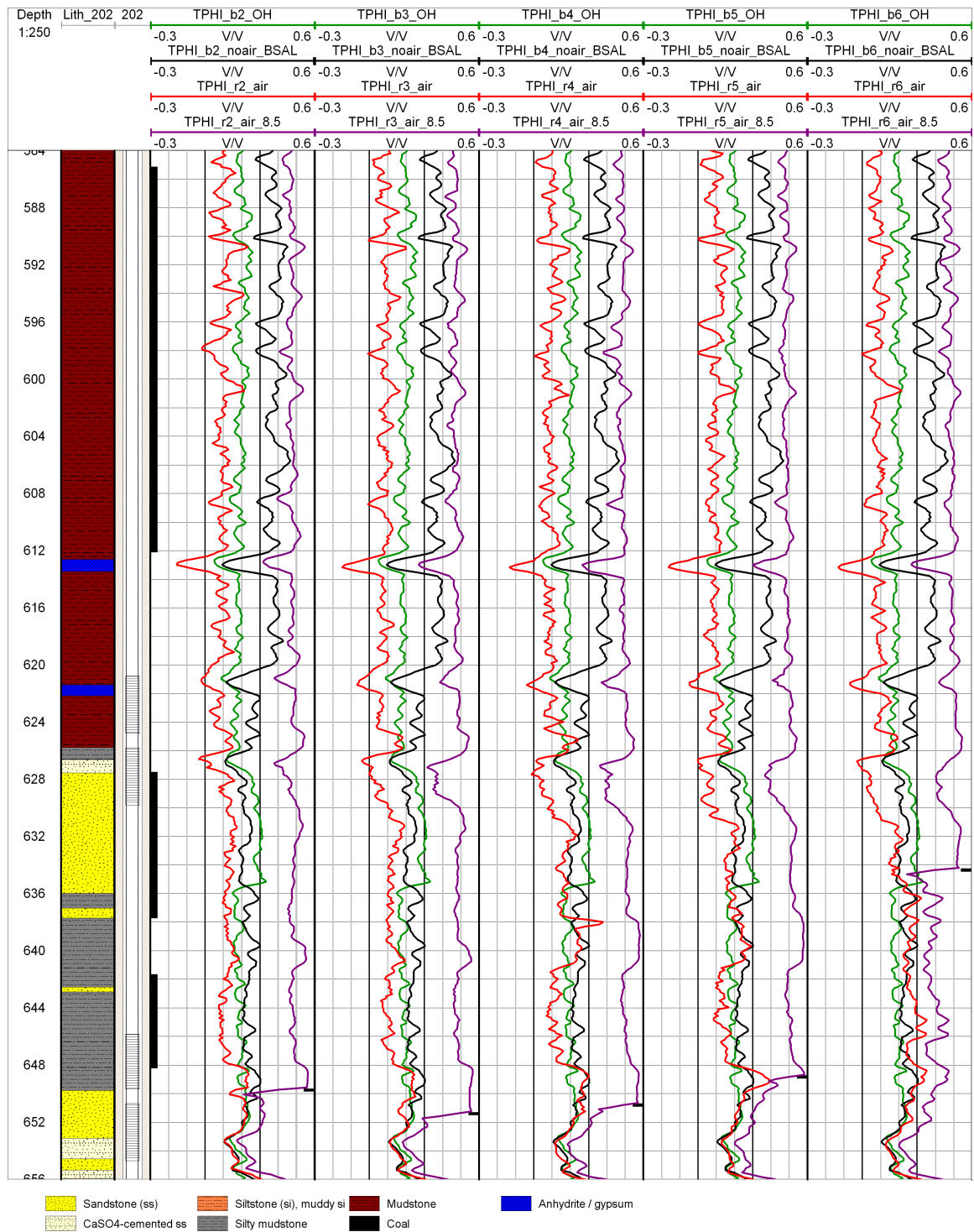
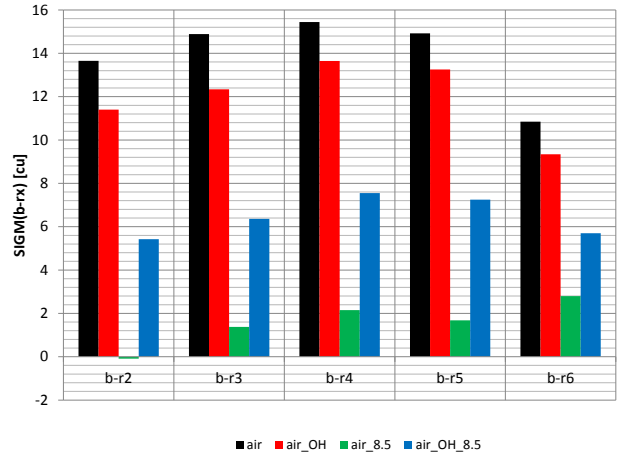
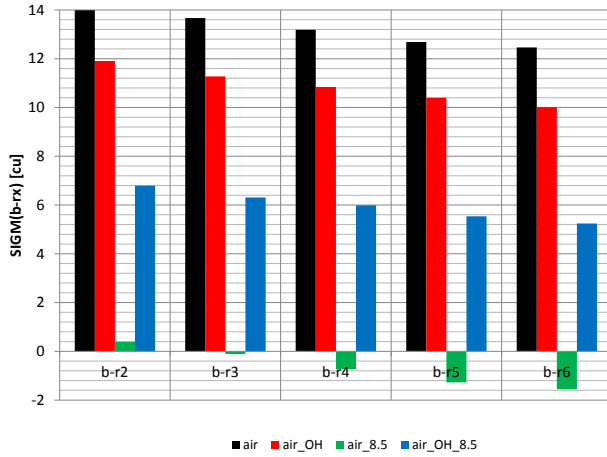
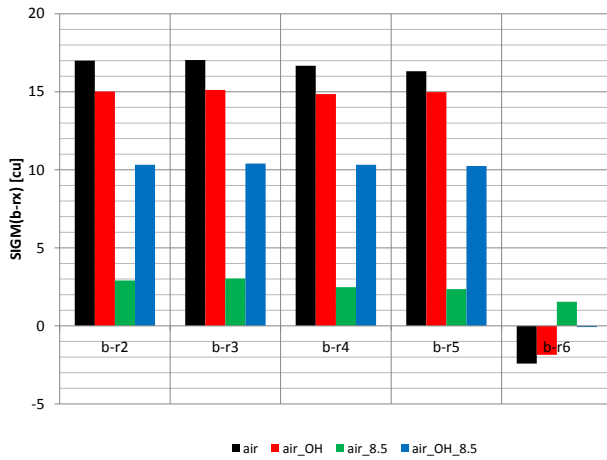


Figure A.18.: Ktzi202: TPHI baseline log (noair_BSAL data processing), open hole derived porosity log after Norden et al. (2010) and five repeat TPHI logs with different data processings. The brine levels for each run are marked with a black bar on the right side of each track. Lithology after Förster et al. (2010)

A. Appendix



(a) Repeats 2-6 with different processings in the Cap interval (b) Repeats 2-6 with different processings in the SS1 interval



(c) Repeats 2-6 with different processings in the Mud interval

Figure A.19.: Ktzi202: Arithmetic mean of the differences between the baseline and the five repeat SIGM runs, $SIGM(b-rx)$, with different data processings in the evaluated depth intervals. Note the different scale in each depth interval.

A. Appendix

Temperature differences for the KCl-preflush and the beginning of CO₂ injection and figure 5.12 with a larger scale for S_{CO_2} derived from TPHI for the injection well Ktzi201

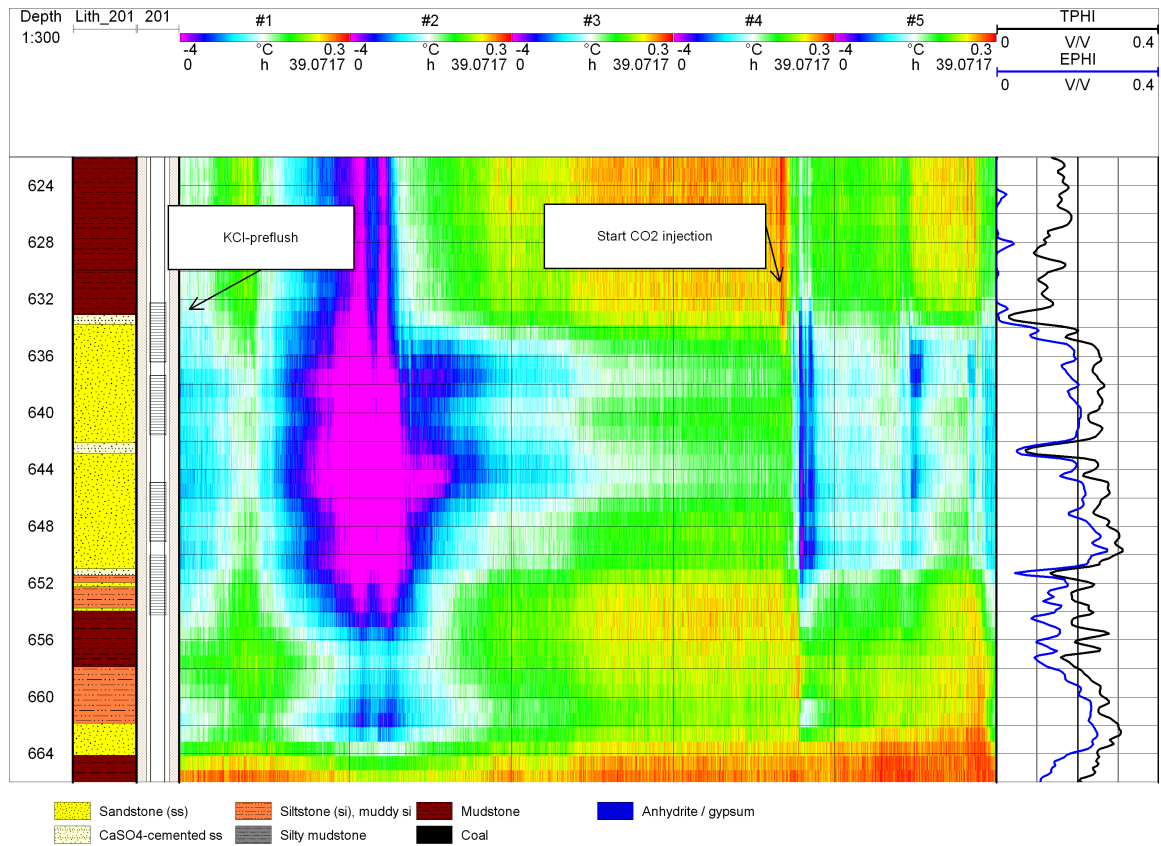


Figure A.20.: Ktzi201: DTS derived temperature differences for the time period 12:03 June, 18th, 2008 to 15:37 June, 26th, 2008. Each track includes a time period of 39.0717 hours. The temperature differences result from a baseline temperature profile before and the actual derived temperature during this time period. Courtesy of Henninges, Lithology after Förster et al. (2010), TPHI and EPHI after Norden et al. (2010)

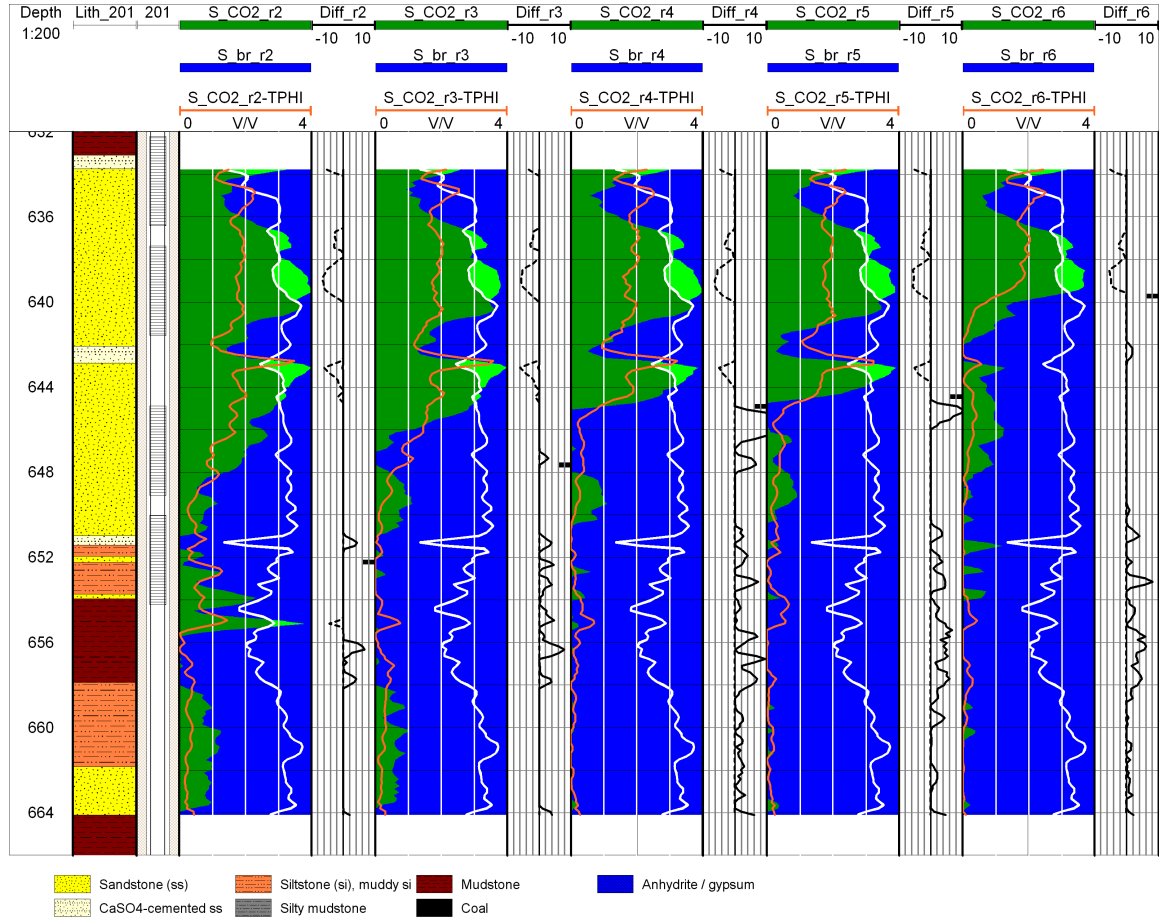


Figure A.21.: Ktzi201: Saturation profiles as fractions of ϕ_{tot} (displacement conform CO₂ in green, apparent CO₂ in light green and brine in blue), S_{CO_2} derived from TPHI with a larger scale (orange logs) (first track) and the corresponding Diff logs with solid and dotted signature (second track) for five repeat runs based on the *displacement saturation model and the original brine salinity*. The brine levels for each repeat run are marked with a black bar on the right side of each track. Lithology after Förster et al. (2010)

Bibliography

- Afeefy, H. Y., Liebman, J. F., and Stein, S. E.: Neutral Thermochemical Data, in NIST Chemistry WebBook, NIST Standard Reference Database Number 69, (Eds. P. J. Linstrom and W. G. Mallard), National Institute of Standards and Technology, Gaithersburg MD, 20899, (<http://webbook.nist.gov>), 2005.
- Amadi, S. and Hughes, R. G.: Evaluation of Behind-Pipe Saturation in a Miscible CO₂ Flood, SPE/DOE Symposium on Improved Oil Recovery, 20-23 April 2008, Tulsa, Oklahoma, USA, p. 12, doi: 10.2118/113887-MS, 2008.
- Badruzzaman, A., Logan, J., Bean, C., Adeyemo, A., Zalan, T., Barnes, D., and Platt, C.: Is Accurate Gas/Steam Determination Behind Pipe Feasible with Pulsed Neutron Measurements?, SPE Asia Pacific Oil and Gas Conference and Exhibition, p. 17, 2007.
- Battistelli, A., Calore, C., and Pruess, K.: The simulator TOUGH2/EWASG for modelling geothermal reservoirs with brines and non-condensable gas, *Geothermics*, 26, 437–464, doi: 10.1016/S0375-6505(97)00007-2, 1997.
- Baumann, G. and Henninges, J.: Sensitivity study of pulsed neutron-gamma saturation monitoring at the Altmark site in the context of CO₂ storage, *Environmental Earth Sciences*, 67 (2), 463–471, doi: 10.1007/s12665-012-1708-x, 2012.
- Baumann, G., Henninges, J., and De Lucia, M.: Sensitivity study of pulsed neutron gamma monitoring to evaluate saturation changes for depleted gas field conditions in the context of CO₂ storage, EGU Geophysical Research Abstracts, EGU General Assembly 2011 (Vienna, Austria), 13, 2011.
- Benson, S. M. and Cook, P.: Underground geological storage. In: Metz B, Davidson O, de Coninck HC, Loos M, Meyer LA (eds) IPCC Special Report on Carbon Dioxide Capture and Storage. Prepared by Working Group III of the Intergovernmental Panel on Climate Change., Cambridge University Press, Cambridge, UK and New York, NY, USA, pp. 195–276, 2005.
- Bergmann, P., Schmidt-Hattenberger, C., Kiessling, D., Rücker, C., Labitzke, T., Henninges, J., Baumann, G., and Schütt, H.: Surface-downhole electrical resistivity tomography applied to monitoring of CO₂ storage at Ketzin, Germany, *Geophysics*, 77, B253–B267, 2012.
- Beyer, C., Li, D., De Lucia, M., Kühn, M., and Bauer, S.: Modelling CO₂-induced fluid-rock interactions in the Altensalzwedel gas reservoir: Part II - coupled reactive transport simulation, *Environmental Earth Sciences*, 67 (2), 573–588, doi: 10.1007/s12665-012-1684-1, 2012.
- Bolton, E. W., Lasaga, A. C., and Rye, D. M.: Long-term flow/chemistry feedback in a porous medium with heterogeneous permeability: kinetic control of dissolution and precipitation, *American Journal of Science*, 299, 1–68, 1999.
- Bonnie, R. J. M.: Evaluation of various Pulsed Neutron Capture logging tools under well-defined laboratory conditions, Society of Petrophysicists and Well-Log Analysts, SPWLA 32nd Annual Logging Symposium, June 16-19, p. 11, 1991.

Bibliography

- Brimage, R. C. and Blackburn, J. S.: Estimation of formation pressures in clean gas sands from dual-spacing TDT log, SPWLA, p. 14, 1978-V, 1978.
- Buckley, S. and Leverett, M.: Mechanism of Fluid Displacement in Sands, Transactions of the AIME, 146, 107–116, doi: 10.2118/942107-G, 1942.
- Butsch, R. and Vacca, H.: Experimental Pulsed Neutron Porosity for Gas-Filled Boreholes in the Gulf Coast, SPE Annual Technical Conference and Exhibition, 23-26 September 1990, New Orleans, Louisiana, 1990.
- Charlson, G. S., Jr. Bilhartz, H. L., and Stalkup, F. I.: Use of Time-Lapse Logging Techniques in Evaluating the Willard Unit CO₂ Flood Mini-Test, SPE Symposium on Improved Methods of Oil Recovery, 16-17 April 1978, Tulsa, Oklahoma, p. 15, doi: 10.2118/7049-MS, 1978.
- De Lucia, M., Bauer, S., Beyer, C., Kühn, M., Nowak, T., Pudlo, D., Reitenbach, V., and Stadler, S.: Modelling CO₂-induced fluid-rock interactions in the Altensalzwedel gas reservoir. Part I - from experimental data to a reference geochemical model, Environmental Earth Sciences, 67 (2), 563–572, doi: 10.1007/s12665-012-1725-9, 2012.
- Dewan, J. T., Jacobson, L. A., and Johnstone, C. W.: Thermal neutron decay logging using dual detection, Society of Petrophysicists & Well Log Analysts, 14, 22, 1973-vXIVn5a2, 1973.
- Dunn, K. J., Guo, D. S., and Zalan, T. A.: Gas / Steam Saturation Effect On Pulsed Neutron Capture Count Rates, SPWLA 32nd Annual Logging Symposium, p. 24, 1991.
- Dunn, K. J., Guo, D. S., and Zalan, T. A.: Gas / Steam Saturation Effect On Pulsed Neutron Capture Count Rates, The Log Analyst, 35, 1994.
- Ellis, D. and Singer, J.: Well Logging for Earth Scientists, Springer, Dordrecht, Netherlands, 2 edn., 2008.
- Ellis, D. V., Faum, C., Galford, J. E., and Scott, H.: The Effect of Formation Absorption on the Thermal Neutron Porosity Measurement, SPE Annual Technical Conference and Exhibition, p. 16, doi: 10.2118/16814-MS, 1987.
- Ellis, D. V., Case, C. R., and Chiamonte, J. M.: Porosity from Neutron Logs I: Measurement, Petrophysics, 44, 13, 2003-v44n6a5, 2003.
- Ellis, D. V., Case, C. R., and Chiamonte, J. M.: Porosity from Neutron Logs II: Interpretation, Petrophysics, 45, 14, 2004-v45n1a5, 2004.
- Ennis-King, J. and Paterson, L.: Role of Convective Mixing in the Long-Term Storage of Carbon Dioxide in Deep Saline Formations, SPE Annual Technical Conference and Exhibition, p. 12, doi: 10.2118/84344-MS, 2003.
- Fitz, D. E. and Ganapathy, N.: Quantitative Monitoring of Fluid Saturation Changes using Cased-hole Logs, SPWLA 34th Annual Logging Symposium, p. 25, 1993.
- Fricke, S. and Schön, J.: Praktische Bohrlochgeophysik, Enke im Thieme Verlag, 1999.
- Förster, A., Norden, B., Zinck-Jørgensen, K., Frykman, P., Kulenkampff, J., Spangenberg, E., Erzinger, J., Zimmer, M., Kopp, J., Borm, G., Juhlin, C., Cosma, C., and Hurter, S.: Baseline characterization of the CO₂SINK geological storage site at Ketzin, Germany, Environmental Geosciences, 13, 145–161, doi: 10.1306/eg.02080605016, 2006.

Bibliography

- Förster, A., Schöner, R., Förster, H.-J., Norden, B., Blaschke, A.-W., Luckert, J., Beutler, G., Gaupp, R., and Rhedea, D.: Reservoir characterization of a CO₂ storage aquifer: The Upper Triassic Stuttgart Formation in the Northeast German Basin, *Marine and Petroleum Geology*, 27, 2156–2172, 2010.
- Galford, J. E., Flaum, C., Gilchrist Jr., W. A., and Duckett, S. W.: Enhanced Resolution Processing of Compensated Neutron Logs, *SPE Formation Evaluation*, 4, 131–137, doi: 10.2118/15541-PA, 1989.
- GDF-SUEZ: CLEAN DMS Data Management System, GFZ German Research Centre for Geosciences, 2009.
- Giese, R., Henninges, J., Lüth, S., Morozovaa, D., Schmidt-Hattenberger, C., Würdemann, H., Zimmer, M., Cosma, C., Juhlin, C., and CO₂SINK Group: Monitoring at the CO₂SINK Site: A Concept Integrating Geophysics, Geochemistry and Microbiology, *Energy Procedia*, 1, 2251–2259, 2009.
- Giorgis, T., Carpita, M., and Battistelli, A.: 2D modeling of salt precipitation during the injection of dry CO₂ in a depleted gas reservoir, *Energy Conversion and Management*, 48, 1816–1826, doi:10.1016/j.enconman.2007.01.012, 2007.
- Hashem, M. and Gilchrist, W.: PNC Log Evaluation in Gas-Filled Borehole Environments: A Case Study, *SPE Annual Technical Conference and Exhibition*, 1994.
- Henninges, J., Liebscher, A., Bannach, A., Brandt, W., Hurter, S., Köhler, S., Möller, F., and CO₂SINK Group: P-T- ρ and two-phase fluid conditions with inverted density profile in observation wells at the CO₂ storage site at Ketzin (Germany), *Energy Procedia*, 4, 6085–6090, 2011.
- Hilchie, D., Mills, W. R., Dennis, C. L., and Givens, W. W.: Some Aspects of Pulsed Neutron Logging, *The Log Analyst*, X, 11, 1969-vXn2a2, 1969.
- Hurter, S., Labregere, D., and Berge, J.: Simulations for CO₂ Injection Projects With Compositional Simulator, *Society of Petroleum Engineers*, p. 8, doi: 10.2118/108540-MS, 2007.
- IPCC: Intergovernmental Panel on Climate Change - Special report on carbon dioxide capture and storage, IPCC, Cambridge, England, 2005.
- Ivanova, A., Kashubin, A., Juhonjuntti, N., Kummerow, J., Henninges, J., Juhlin, C., Lüth, S., and Ivandic, M.: Monitoring and volumetric estimation of injected CO₂ using 4D seismic, petrophysical data, core measurements and well logging: A case study at Ketzin, Germany, *Geophysical Prospecting*, 60, 957–973, doi: 10.1111/j.1365-2478.2012.01045.x, 2012.
- Jarrell, P. M., Fox, C., Stein, M., and Webb, S.: Practical Aspects of CO₂ Flooding, *SPE Monograph*, 22, 214, 2002.
- Jeckovich, G. and Olesen, J.-R.: Enhancing Through-Tubing Formation Evaluation Capabilities With the Dual-Burst Thermal Decay Tool, *SPE Annual Technical Conference and Exhibition*, 1989.
- Juhlin, C., Giese, R., Zinck-Jørgensen, K., Cosma, C., Kazemeini, H., Juhojuntti, N., Lüth, S., Norden, B., and Förster, A.: 3D baseline seismics at Ketzin, Germany: The CO₂SINK project, *Geophysics*, 72, B121–132, doi: 10.1190/1.2754667, 2007.
- Kempka, T., Kühn, M., Class, H., Frykman, P., Kopp, A., Nielsen, C., and Probst, P.: Modelling of CO₂ arrival time at Ketzin - Part I, *International Journal of Greenhouse Gas Control*, 4, 1007–1015, doi: 10.1016/j.ijggc.2010.07.005, 2010.

Bibliography

- Kühn, M., Förster, A., Großmann, J., Meyer, R., Reinicke, A., Schäfer, D., and Wendel, H.: CLEAN: Preparing for a CO₂-based Enhanced Gas Recovery in a depleted gas field in Germany, *Energy Procedia*, 4, 5520–5526, doi: 10.1016/j.egypro.2011.02.538, 2011.
- Kühn, M., Tesmer, M., Pilz, P., Meyer, R., Reinicke, K., Förster, A., Kolditz, O., and Schäfer, D.: CLEAN: project overview on CO₂ large-scale enhanced gas recovery in the Altmark natural gas field (Germany), *Environmental Earth Sciences*, 67 (2), 311–321, doi: 10.1007/s12665-012-1714-z, 2012.
- Kimminau, S. and Plasek, R.: The Design of Pulsed Neutron Reservoir Monitoring Programs, *SPE Formation Evaluation*, 7, 93–98, 20589-PA, 1992.
- Kleinitz, W., Koehler, M., and Dietzsch, G.: The Precipitation of Salt in Gas Producing Wells, *SPE European Formation Damage Conference*, p. 7, 2001.
- Klinkenberg, L.: The permeability of porous media to liquids and gases, *API Drilling and Production Practice*, pp. 200–213, 1941.
- Knödel, K., Krummel, H., and Lange, G.: *Handbuch zur Erkundung des Untergrundes von Deponien und Altlasten*, Geophysik, vol. 3, Springer Verlag Berlin, 1997.
- Lorentz, S. and Muller, W.: Modelling of halite formation in natural gas storage aquifers, *Proceedings TOUGH2 symposium*, Berkeley, CA, May 12-14, 2003.
- Mao, S. and Duan, Z.: The p, v, T, x properties of binary aqueous chloride solutions up to T= 573 K and 100 MPa, *The Journal of Chemical Thermodynamics*, 40, 1046–1063, 2008.
- Martens, S., Liebscher, A., Möller, F., Henniges, J., Kempka, T., Lüth, S., Norden, B., Prevedel, B., Szizybalskia, A., Zimmer, M., Kühn, M., and the Ketzin Group: CO₂ storage at the Ketzin pilot site, Germany: Fourth year of injection, monitoring, modelling and verification, *Energy Procedia*, p. 10, 2013.
- McKeon, D. C. and Scott, H. D.: SNUPAR - A Nuclear Parameter Code for Nuclear Geophysics Applications, *Nuclear Geophysics*, 2, 215–230, 1988.
- Michael, K., Golab, A., Shulakova, V., Ennis-King, J., Allinson, G., Sharma, S., and Aiken, T.: Geological storage of CO₂ in saline aquifers - A review of the experience from existing storage operations, *International Journal of Greenhouse Gas Control*, 4, 659–667, 2010.
- Möller, F., Liebscher, A., Martens, S., Schmidt-Hattenberger, C., and Kühn, M.: Yearly Operational Datasets of the CO₂ Storage Pilot Site Ketzin, Germany, Helmholtz Centre Potsdam GFZ German Research Centre for Geosciences, *Scientific Technical Report STR12/06 - Data*, p. 14, doi: 10.2312/GFZ.b103-12066, 2012.
- Müller, N., Elshahawi, H., Dong, C., Mullins, O. C., Flannery, M., Ardila, M., Weinheber, P., and Chinn McDade, E.: Quantification of Carbon Dioxide Using Downhole Wireline Formation Tester Measurements, *SPE Annual Technical Conference and Exhibition*, p. 10, 100739-MS, 2006.
- Müller, N., Ramakrishnan, T., Boyd, A., and Sakurai, S.: Time-lapse carbon dioxide monitoring with pulsed neutron logging, *International Journal of Greenhouse Gas Control*, 1, 456–472, doi: 10.1016/S1750-5836(07)00071-0, 2007.
- Morris, C., Aswad, T., Morris, F., and Quinlan, T.: Reservoir Monitoring with Pulsed Neutron Capture Logs, *SPE Europec/EAGE Annual Conference*, p. 16, doi: 10.2118/94199-MS, 2005.

Bibliography

- Muller, N., Qi, R., Mackie, E., Pruess, K., and Blunt, M. J.: CO₂ injection impairment due to halite precipitation, *Energy Procedia*, 1, 3507–3514, 2009.
- Murdoch, W., Randall, C. J. H. K., and Towsley, C. W.: Diffusion Corrections to Pulsed Neutron Capture Log: Methodology, Society of Petrophysicists and Well-Log Analysts, SPWLA 31st Annual Logging Symposium, p. 24, 1990.
- Murray, D., Wang, Y. X., Horie, T., Yoshimura, T., and Mito, S.: CO₂ Sequestration Monitoring in a Low Formation Water Salinity Reservoir, Society of Petroleum Engineers, p. 9, 2010.
- Nelson, P. H.: Permeability-Porosity Relationships in Sedimentary Rocks, *The Log Analyst*, 35, 38–62, 1994.
- Norden, B., Förster, A., Vu-Hoang, D., Marcelis, F., Springer, N., and Nir, I. L.: Lithological and Petrophysical Core-Log Interpretation in CO₂SINK, the European CO₂ Onshore Research Storage and Verification Project, SPE Reservoir Evaluation & Engineering, 13, 179–192, 115247-PA, 2010.
- Oldenburg, C. M., Stevens, S. H., and Benson, S. M.: Economic feasibility of carbon sequestration with enhanced gas recovery (CSEGR), *Energy*, 29, 1413–1422, doi: 10.1016/j.energy.2004.03.075, 2004.
- Olesen, J.-R., Mahdavi, M., and Steinman, D. K.: Dual-Burst Thermal Decay Time Data Processing and Examples, Society of Petrophysicists and Well-Log Analysts, SPWLA 28th Annual Logging Symposium, June 29-July 2, p. 25, 1987.
- Plasek, R., Adolph, R., Stoller, C., Willis, D., Bordon, E., and Portal, M.: Improved Pulsed Neutron Capture Logging With Slim Carbon-Oxygen Tools: Methodology, SPE Annual Technical Conference and Exhibition, p. 15, 30598-MS, 1995.
- Potter, R. W., Babcock, R. S., and Brown, D. L.: A new method for determining the solubility of salts in aqueous solutions at elevated temperatures, *J. Research U. S. Geol. Surv.*, 5, 389–395, 1977.
- Pregg, W. and Scott, H.: Computing Thermal Neutron Decay Time Environmental Effects Using Montecarlo Techniques, Society of Petroleum Engineers, SPE Formation Evaluation, pp. 35–42, doi: 10.2118/10293-PA, 1986.
- Prevedel, B.: Final Report for the drilling of Ketzin 200 (Ktzi200), Ketzin 201 (Ktzi201) and Ketzin 202 (Ktzi202), 2008.
- Pruess, K.: Formation dry-out from CO₂ injection into saline aquifers: 2. Analytical model for salt precipitation, *Water Resources Research*, 45, 6, doi: 10.1029/2008WR007102, 2009.
- Pruess, K. and Müller, N.: Formation dry-out from CO₂ injection into saline aquifers: 1. Effects of solids precipitation and their mitigation, *Water Resources Research*, 45, 11, doi: 10.1029/2008WR007101, 2009.
- Roscoe, B. A., Stoller, C., Adolph, R. A., Boutemy, Y., Cheeseborough III, J. E., Hall, J. S., McKeon, D. C., Pittman, D., Seeman, B., and Thomas Jr., S. R.: A New Through-Tubing Oil-Saturation Measurement System, Society of Petroleum Engineers, Middle East Oil Show, 16-19 November 1991, Bahrain, p. 10, doi: 10.2118/21413-MS, 1991.
- Rowe, A. M. and Chou, J. C. S.: Pressure-volume-temperature-concentration relation of aqueous sodium chloride solutions, *Journal of Chemical and Engineering Data*, 15, 61–66, doi: 10.1021/jc60044a016, 1970.

Bibliography

- Sakurai, S., Hovorka, S., Ramakrishnan, T. S., Boyd, A., and Mueller, N.: Monitoring Saturation Changes for CO₂ Sequestration: Petrophysical Support of the Frio Brine Pilot Experiment, SPWLA 46th Annual Logging Symposium, p. 16, 2005.
- Schilling, F., Borm, G., Würdemann, H., Möller, F., Kühn, M., and CO₂SINK Group: Status report on the first European on-shore CO₂ storage site at Ketzin (Germany), *Energy Procedia*, 1, 2029–2035, 2009.
- Schlumberger: Cased Hole Log Interpretation Principles/Applications, Schlumberger Wireline & Testing, P.O. Box 2175, Houston, Texas 77252-2175, 1989.
- Schlumberger: Log Interpretation Charts, Schlumberger Oilfield Marketing Communications, Schlumberger, 225 Schlumberger Drive, Sugar Land, Texas 77478, 2009.
- Schlumberger: Wireline Log Quality Control Reference Manual, Schlumberger Oilfield Marketing Communications, Schlumberger, 225 Schlumberger Drive, Sugar Land, Texas 77478, 2011.
- Schmidt-Hattenberger, C., Bergmann, P., Kiessling, D., Krüger, K., Rücker, C., Schütt, H., and CO₂SINK Group: Application of a vertical electrical resistivity array (VERA) for monitoring CO₂ migration at the Ketzin site: First performance evaluation, *Energy Procedia*, 4, 3363–3370, 2011.
- Schmidt-Hattenberger, C., Bergmann, P., Labitzke, T., Schröder, S., Krüger, K., Rücker, C., and Schütt, H.: A modular geoelectrical monitoring system as part of the surveillance concept in CO₂ storage projects, *Energy Procedia*, 23, 400–407, doi: 10.1016/j.egypro.2012.06.062, 2012.
- Schwanitz, B. J.: A combination of logging measurements for quantitative monitoring of CO₂ floods, SPE Permian Basin Oil and Gas Recovery Conference, 10-11 March 1988, Midland, Texas, p. 7, doi: 10.2118/17276-MS, 1988.
- Sears, V. F.: Neutron scattering lengths and cross sections, *Neutron News*, 3, 29–37, 1992.
- Serra, O.: Fundamentals of well-log interpretation, vol. 1, Elsevier Science Publishers B. V., 1984.
- Smith, Jr., H. D., Wyatt, Jr., D. F., and Arnold, D. M.: Obtaining intrinsic formation capture cross sections with pulsed neutron capture logging tools, SPWLA 29th Annual Logging Symposium, p. 24, 1988.
- Smolen, J.: Cased Hole and Production Log Evaluation, Pennwell Publishing Company, Tulsa, Oklahoma, 1996.
- Spycher, N. and Pruess, K.: CO₂-H₂O mixtures in the geological sequestration of CO₂. II. Partitioning in chloride brines at 12 - 100°C and up to 600 bar, *Geochimica et Cosmochimica Acta*, 69, 3309–3320, 2005.
- Spycher, N., Pruess, K., and Ennis-King, J.: CO₂-H₂O mixtures in the geological sequestration of CO₂. I. Assessment and calculation of mutual solubilities from 12 to 100°C and up to 600 bar, *Geochimica et Cosmochimica Acta*, 67, 3015–3031, 2003.
- Steinman, D., Adolph, R., Mahdavi, M., and Preeg, W.: Dual-Burst Thermal Decay Time Logging Principles, SPE Formation Evaluation, 3, 377–385, 1988.
- Svor, T. and Globe, M.: A Three-Phase Quantitative Monitoring Method for CO₂ Floods, SPE Enhanced Oil Recovery Symposium, 4-7 April 1982, Tulsa, Oklahoma, doi: 10.2118/10684-MS, 1982.

Bibliography

- van der Burgt, M. J., Cantle, J., and Boutkan, V. K.: Carbon dioxide disposal from coal-based IGCC's in depleted gas fields, *Energy Conversion and Management*, 33, 603–610, doi: 10.1016/0196-8904(92)90062-2, 1992.
- van der Wall, R., Ebeling, K., Wolf, P., and Lenne, S.: *Ketzin-KCl-Injection in Ktzi201*, Golder Associates, 2008.
- Vu-Hoang, D., Henniges, J., and Hurter, S.: Monitoring carbon dioxide saturation through wireline logging techniques, *EGU Geophysical Research Abstracts*, EGU General Assembly 2009 (Vienna, Austria), 11, 2009.
- Wang, Y., Mackie, E., Rohan, J., Luce, T., Knabe, R., and Appel, M.: Experimental study on halite precipitation during CO₂ sequestration, *International Symposium of the Society of Core Analysis*, p. 12, 2009.
- Wang, Y., Luce, T., Ishizawa, C., Shuck, M., Smith, K., Ott, H., and Appel, M.: Halite precipitation and permeability assessment during supercritical CO₂ core flood, *International Symposium of the Society of Core Analysis*, p. 12, 2010.
- Wildenborg, T., Bentham, M., Chadwick, A., David, P., Deflandre, J., Dillen, M., Groenenberg, H., Kirk, K., and Gallo, Y.: Large-scale CO₂ injection demos for the development of monitoring and verification technology and guidelines (CO₂ReMoVe), *Energy Procedia*, 1, 2367–2374, 2009.
- Würdemann, H., Möller, F., Kühn, M., Heidug, W., Christensen, N. P., Borma, G., Schilling, F. R., and the CO₂SINK Group: CO₂SINK - From site characterisation and risk assessment to monitoring and verification: One year of operational experience with the field laboratory for CO₂ storage at Ketzin, Germany, *International Journal of Greenhouse Gas Control*, 4, 938–951, 2010.
- Xue, Z., Tanase, D., and Watanabe, J.: Estimation of CO₂ saturation from time-lapse CO₂ well logging in an onshore aquifer, Nagaoka, Japan, *Exploration Geophysics*, 37, 19–29, 2006.
- Youmans, A. H., Hopkinson, E. C., Bergan, R. A., and Oshry, H. I.: Neutron Lifetime, a New Nuclear Log, *Journal of Petroleum Technology*, 16, 319–328, doi: 10.2118/709-PA, 1964.
- Zeidouni, M., Pooladi-Darvish, M., and Keith, D.: Analytical solution to evaluate salt precipitation during CO₂ injection in saline aquifers, *International Journal of Greenhouse Gas Control*, 3, 600–611, doi: 10.1016/j.ijggc.2009.04.004, 2009a.
- Zeidouni, M., Pooladi-Darvish, M., and Keith, D.: Sensitivity Analysis of Salt Precipitation and CO₂-Brine Displacement in Saline Aquifers, *SPE International Conference on CO₂ Capture, Storage, and Utilization*, p. 16, 126690-MS, 2009b.